Design and Application of Advanced Disturbance Rejection Control for Small Fixed Wing UAVs

by

Jean Smith

A doctoral thesis submitted in partial fulfilment of the requirements for the award of the degree of Doctor of Philosophy (PhD) of Loughborough University.

Control and Reliability Group,
Department of Aeronautical and Automotive Engineering,
Loughborough University, Loughborough,
Leicestershire, UK, LE11 3TU

To my loving wife and parents...

Acknowledgements

I am very grateful to Dr Cunjia Liu who has been my supervisor throughout my PhD. He has been a constant source of knowledge, guidance and motivation at all times. His uncanny ability to identify the root cause of problems which I had been working on for many days was very much appreciated during some of the more challenging points during my studies. I am also very thankful for the opportunities to work alongside him as an RA on his projects which have taught me many valuable lessons for the future.

I would also like to thank Prof. Wen-Hua Chen for his guidance during my studies, and his hard work in facilitating my research within LUCAS. It was through his lectures during my undergraduate studies that I was introduced to the field of control engineering and which ultimately led to my PhD studies. I am also very thankful to Dr Jun Yang, with whom I have worked closely during his time within LUCAS. His assistance and guidance during my research is highly appreciated.

I also am grateful to Dr Peter Render for his role in monitoring my progress. He also offered many insightful points during our annual meetings, which have helped me keep the work and its' outcomes in context for my future.

I am very pleased to have known all researches within LUCAS. They helped to make this a great place to work. The willingness of everyone to help anyone where possible made for a great sense of teamwork. My particular thanks to Matthew Coombes, Paweł Ładosz and Michael Hutchinson for their help in my work and for making work enjoyable. I do hope they find a suitable replacement for me on the hourly tea run. I also am very grateful to Jinya Su, who was always willing to help with the more challenging theoretical understanding.

To my close friends Alex, Dan and Owen, I am also very thankful. I'm very grateful for their help in proof reading my writing, as well as for helping me make the most of time away from my research.

I am forever thankful to my parents, John and Loraine, who have supported me in every way possible. Without them I would not have had the opportunities to chase my dreams and fulfil them. I will always remember and appreciate their many sacrifices and constant encouragement.

Finally, to my wife Kayleigh, I am truly thankful for her constant love and support. I could never have hoped or asked for more during all my studies. Thank you for always keeping me sane and smiling, even during the most difficult times. I promise that my student days are finally over!

Abstract

Small Unmanned Aerial Vehicles (UAVs) have seen continual growth in both research and commercial applications. Attractive features such as their small size, light weight and low cost are a strong driver of this growth. However, these factors also bring about some drawbacks. The light weight and small size means that small UAVs are far more susceptible to performance degradation from factors such as wind gusts. Due to the generally low cost, available sensors are somewhat limited in both quality and available measurements. For example, it is very unlikely that angle of attack is sensed by a small UAV. These aircraft are usually constructed by the end user, so a tangible amount of variation will exist between different aircraft of the same type. Depending on application, additional variation between flights from factors such as battery placement or additional sensors may exist. This makes the application of optimal model based control methods difficult.

Research literature on the topic of small UAV control is very rich in regard to high level control, such as path planning in wind. A common assumption in such literature is the existence of a low level control method which is able to track demanded aircraft attitudes to complete a task. Design of such controllers in the presence of significant wind or modelling errors (factors collectively addressed as *lumped disturbances* herein) is rarely considered.

Disturbance Observer Based Control (DOBC) is a means of improving the robustness of a baseline feedback control scheme in the presence of lumped disturbances. The method allows for the rejection of the influence of unmeasurable disturbances much more quickly than traditional integral control, while also enabling recovery of nominal feedback control performance. The separation principle of DOBC allows for the design of a nominal feedback controller, which does not need to be robust against disturbances. A DOBC augmentation can then be applied to ensure this nominal performance is maintained even in the presence of disturbances. This method offers highly attractive properties for control design, and has seen a large rise in popularity in recent years.

Current literature on this subject is very often conducted purely in simulation. Additionally, very advanced versions of DOBC control are now being researched. To make the method attractive to small UAV operators, it would be beneficial if a simple DOBC design could be used to realise the benefits of this method, as it would be more accessible and applicable by many.

This thesis investigates the application of a linear state space disturbance observer to low level flight control of a small UAV, along with developments of the method needed to achieve good performance in flight testing. Had this work been conducted purely in simulation, it is likely many of the difficulties encountered would not have been addressed or discovered.

This thesis presents four main contributions. An anti-windup method has been developed which is able to alleviate the effect of control saturation on the disturbance observer dynamics. An observer is designed which explicitly considers actuator dynamics. This development was shown to enable faster observer estimation dynamics, yielding better disturbance rejection performance. During initial flight testing, a significant aeroelastic oscillation mode was discovered. This issue was studied in detail theoretically, with a proposed solution developed and applied. The solution was able to fully alleviate the effect in flight. Finally, design and development of an over-actuated DOBC method is presented. A method for design of DOBC for over actuated systems was developed and studied. The majority of results in this thesis are demonstrated with flight test data.

Contents

List of Figures

Nomenclature

$\bar{c}$	Standard mean chord	m
$\boldsymbol{\eta}$	A vector containing the actuator states from a model with second order dynamics.	
$\boldsymbol{A}$	General state space system dynamics matrix	
$\boldsymbol{B}$	General state space control matrix	
$\boldsymbol{B}_d$	General state space external disturbance mapping vector	
$\boldsymbol{C}$	General state space output matrix	
$\boldsymbol{D}$	General state space feedthrough matrix	
$\boldsymbol{d}$	General state space external disturbance vector	
$\boldsymbol{F}$	A vector containing forces applied along 3 axes.	
$\boldsymbol{I}_b$	The inertial tensor matrix for a body	kgm^2
$\boldsymbol{M}$	A vector containing the moments applied along 3 axes of a body	Nm
$\boldsymbol{N}_w$	A vector of n white noise sources given by N_w^{1-n}	
$\boldsymbol{u}$	General state space input vector	
$\boldsymbol{W}$	A weighting matrix used in the pseudoinverse calculation of the disturbance rejection gain.	
$\boldsymbol{x}$	General state space state vector	
$\boldsymbol{y}$	General state space output vector	
ϵ	A variable or vector to denote true actuator states.	
γ	The angle between a given glide slope and the horizon.	
$\mathcal{F}^b$	The body reference frame	
$\mathcal{F}^i$	The inertial reference frame	
$\mathcal{F}^v$	The vehicle reference frame	
$\mathcal{F}^w$	The wind reference frame	
$C_{(\cdot)}$	Coefficient associated with the $(\cdot)$ quantity	
g	Gravitational acceleration constant	$9.81ms^2$

rho	Air density	kg/m^3
S	Wing plan form area	m^2
u_{min}, u_{max}	Minimum and maximum control amplitudes	

Acronyms

6DOF Six Degrees of Freedom

AC Adaptive Control

ADOBC Actuator Augmented Disturbance Observer Based Control

ADRC Active Disturbance Rejection Control

AoA Angle of Attack

AoS Angle of Sideslip

ARE Algebraic Riccati Equation

BIBO Bounded Input Bounded Output

CFD Computational Fluid Dynamics

COTS Commercial off the Shelf

DCM Direction Cosine Matrix

DFT Discrete Fourier Transform

DLC Direct Lift Control

DO Disturbance Observer

DOBC Disturbance Observer Based Control

EID Equivalent Input Disturbance

EKF Extended Kalman Filter

EPP Expanded Polypropylene

ESO Extended State Observer

FFT Fast Fourier Transform

FPS Frames Per Second

GPS Global Positioning System

IMU Inertial Measurement Unit

LQ Linear Quadratic

LQG Linear Quadratic Gaussian

LQI Linear Quadratic Integral

LQR Linear Quadratic Regulator

LTI Linear Time-Invariant

LUCAS Loughborough University Centre for Autonomous Systems

MAV Micro Aerial Vehicle

MIMO Multi Input Multi Output

NASA National Aeronautics and Space Administration

NDI Nonlinear Dynamic Inversion

NDO Nonlinear Disturbance Observer

NED North East Down

NRMSE Normalised Root Mean Square

ParID Parametric Identification

PEM Prediction Error Method

PID Proportional Integral Derivative

PO Perturbation Observer

RC Radio Control

ROS Robot Operating System

ROTH Run on Target Hardware

RPi Raspberry Pi

RPM Rotations Per Minute

SISO Single Input Single Output

SPPO Short Period Pitching Oscillation

UAV Unmanned Aerial Vehicle

UCAV Unmanned Combat Aerial Vehicle

UDP User Datagram Protocol

UIO Unknown Input Observer

URL Uniform Resource Locator

VFA Very Flexible Aircraft

X8 Skywalker X8

Chapter 1

Introduction

1.1 Background

Research, development and operation of small Unmanned Aerial Vehicles (UAVs) have been ongoing for around 20 years. Initially, military organisations were the main operators due to the high cost and complexity of operation. As it is today, UAVs are accessible to almost anyone. Due to continual advancement in micro electronics and manufacturing methods, the barrier to entry has been significantly lowered.

This has resulted in UAVs seeing a far wider range of applications, including remote monitoring, security and search and rescue. Flight control of UAVs is an active area of research, with many advanced methods being developed. Initial flight control for UAVs was based on methods developed for full size manned aircraft, as this was the state of the art at that time. However, there are many factors of UAV operation which mean control design does not need to be restricted in the same way as manned aviation. Generally, manned aviation is focused heavily on safety, reliability, comfort and robustness. This is of course reasonable, as preservation of human life is paramount concern for commercial operation. Clearly, UAVs are not to the same degree.

Small UAVs are uniquely positioned to be very attractive platforms for research. They offer low cost and much less operational risks compared to full size aircraft. They can be easily and widely obtained. Furthermore, with the widespread availability of autopilot systems for small UAVs, they can be operated with much less training than traditional aircraft. This has led to rapid developments in flight control in recent years, which is set to continue. This offers many opportunities for new developments.

1.2 Motivation

Due to the rapid pace of development, simulation studies are the most common method for studying the resulting performance. Development of custom control hardware along with the extensive work needed to apply it to physical aircraft results in flight testing being expensive and laborious. Numerical simulation offers a good alternative to easily and quickly study the performance of control methods. Ideally, a simulation environment will represent the true plant very well. However, this requires consideration of all possible elements of the physical plant which leads to highly complex simulation environments, which are also costly and time consuming to develop. Instead, many factors are often assumed negligible and ignored. Typical examples include external disturbances such as wind, modelling errors and actuator dynamics.

The work in this thesis studies some of the effects which can result from ignoring these factors. When it comes to flight testing, these factors can no longer be assumed negligible. As demonstrated in this thesis, falsely ignoring these factors can lead to instability of

controllers and potentially the loss of the aircraft. While small UAVs are generally much cheaper to replace than full scale aircraft, there are many other reasons to avoid crashes. Danger to the operators or members of the public or damage to property for example, are still undesirable.

To study these effects, a suitable advanced control method was needed. Disturbance Observer Based Control (DOBC) is a highly practical and applicable control method which offers the ability to reject both external and internal disturbances. As will be discussed, small UAVs are very sensitive to external disturbances such as wind. Further, due to the nature of their operation, small UAVs do not commonly have highly accurate models available for control design. It is also likely that a degree of variation exists between different aircraft of the same type, as they are typically hand built. Therefore the effect of internal disturbances resulting from these modelling errors are much more likely to occur. This makes DOBC a highly attractive method in this area. It also provides a large scope to demonstrate and study the effects of common assumptions in advanced flight control.

1.2.1 Aims

DOBC is a highly active research area with many opportunities for contributions. The work in this thesis was driven by some key aims, designed to focus attention on a particular area:

- Improve the robustness and stability of DOBC when applied to physical systems
- Improve DOBC performance in disturbance rejection for small UAVs
- Produce practical data for the performance of DOBC on small UAVs.

1.2.2 Objectives

The objectives which must be met to achieve the aims are:

- Develop a method to improve DOBC stability in the presence of control saturation
- Develop the DOBC method using known actuator dynamics
- Investigate a situation where the advantages of small UAVs can be leveraged for performance improvement
- Conduct flight testing of proposed advancements to demonstrate DOBC performance in application to small UAVs.

These objectives were successfully completed in this research. Several important contributions to the topic were made, which are summarised in the following section.

1.3 Research Contributions

This thesis has contributed an anti-windup method for state space disturbance observers. This development improves the robustness and stability of disturbance observers applied to a physical plant, all of which have unavoidable physical constraints on their actuators. It was designed with implied stability proof, by basing the solution on methods established in other areas of control research.

Another important contribution of this work is the development of the DOBC method to utilise actuator dynamics to improve the disturbance estimation and rejection performance. A study is conducted into the considerations of such a design as well as demonstrations of the performance benefits which can result. This is shown even when using intentionally erroneous actuator models.

An additional extension of the DOBC method is provided in a method for calculating disturbance rejection gain for over actuated systems. The proposed method also allows for selection of the control action distribution to achieve disturbance rejection performance. This is supported by a study into the resulting performance benefits when selecting control action to favour faster actuators.

This thesis provides an additional contribution to the wider area of flight control for small fixed wing UAVs. During initial flight testing, a structural oscillation was identified which endangered the aircraft and limited the progress of research. Although there is scope for future work to better understand the characteristics of such oscillations, a method for mitigating the effect is demonstrated. The proposed method is shown to be sufficient to suppress the oscillation.

1.4 Outline

The thesis outline is provided below, along with the main contributions of each chapter.

Chapter 2 - Literature Review

Within the literature review, examples of UAV control are studied with a focus on disturbance rejection. Of particular interest are the limitations of the work with respect to physical application of the developed methods. Additionally, an overview of the DOBC method is given with relevant development and applications of the technique.

Chapter 3 - Flight Test Platform

Flight testing of control algorithms has generally been expensive and slow. Here, the platform developed as part of this thesis to allow for rapid development and assessment of advanced flight control techniques is discussed.

Chapter 4 - Modelling and System Identification

An overview of the mathematical modelling principles needed for simulation of aircraft and flight control is provided. Although the thesis is motivated by application, simulation is still an essential part of the development process. The methods for obtaining the models used in later work through system identification are also discussed.

Chapter 5 - Anti-Windup Disturbance Observer

The feedback control method which is used as a baseline for DOBC development throughout the thesis is presented in detail along with the design process for the standard DOBC method. The first development of the DOBC technique contributed by this thesis then looks at the effect of saturated physical controls on the internal state of the disturbance observer. A solution is proposed and investigated with both simulation and flight test results.

Chapter 6 - Actuator Augmented Disturbance Observer

Continuing the contributions to DOBC development, dynamic models of the physical actuators are introduced to the observer. Simulations and flight test data are used to demonstrate the necessity for this development, as well as discussion on the design and tuning considerations.

Chapter 7 - Aircraft Structural Oscillation

During flight testing of the initial control developments, an aircraft structural oscillation issue was identified. This section aims to determine the root cause of the problem, with a proposed solution. Frequency domain analysis is conducted to understand the initial problem and proposed solution. A simulation and flight testing demonstration of the solution and resulting control performance is then conducted. This chapter serves as a very good example on issues which arise in flight testing which would not be identified from simulation alone.

Chapter 8 - Direct Lift Control

The final contribution to DOBC development uses Direct Lift Control (DLC) as a case study on the design and function of an over-actuated DOBC application. The over-actuated problem is presented and discussed along with a proposed solution. Initial study is conducted using numerical simulation and validated with an industry recognised simulation environment. This chapter also presents an advancement of the control scheme used in earlier chapters to allow for tracking of non-continuous references.

1.5 Publications

Book Chapters

Ladosz, P., Coombes, M., Smith J. and M. Hutchinson, 2018. A Generic ROS based System for Rapid Development and Testing of Algorithms for Autonomous Ground and Aerial Vehicles. In: *Robot Operating System (ROS) The Complete Reference*. Springer International Publishing, pp.99-101.

Journal Paper

Smith, J., Su, J., Liu, C. and Chen, W.H., 2017. Disturbance observer based control with anti-windup applied to a small fixed wing UAV for disturbance rejection. *Journal of Intelligent & Robotic Systems*, 88(2-4), pp.329-346.

Conference Papers

Smith, J., Yang, J., Liu, C. and Chen, W.H., 2018, February. Actuator Dynamics Augmented DOBC for A Small Scale Fixed Wing UAV. In *Industrial Technology, 2018 IEEE International Conference on* IEEE.

Smith, J., Liu, C. and Chen, W.H., 2016, June. Disturbance observer based control for gust alleviation of a small fixed-wing UAS. In *Unmanned Aircraft Systems (ICUAS), 2016 International Conference on* (pp. 97-106). IEEE.

Chapter 2

Literature Review

Within the literature review, the problem of small UAV flight control is studied first. Then, a review of the proposed solution method is conducted and relevant limitations are identified. From this, the research motivations are formed. This plan is summarised in Fig. 2.1.

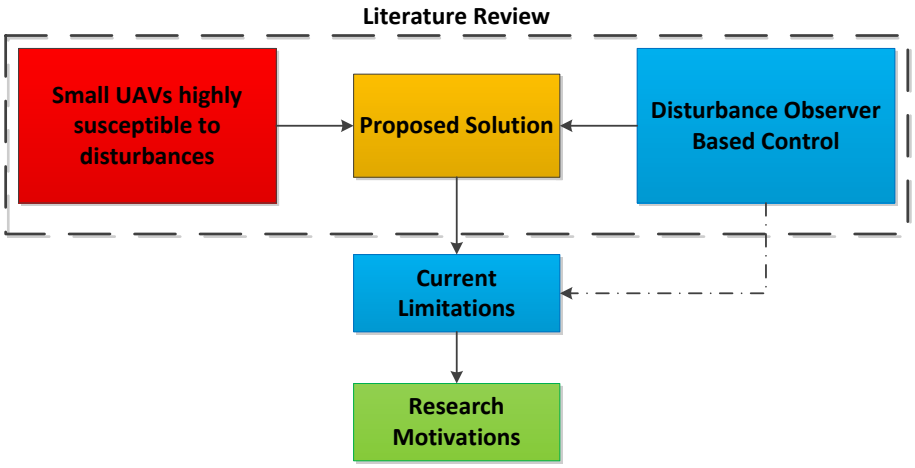

Figure 2.1: A brief summary of the aim of the literature review.

2.1 The Effect of Wind on Aircraft

By the very nature of their operation, the effect of wind on aircraft flight has been well studied. Of particular interest is the problem of wind gust disturbances, which are an unavoidable component of flight outdoors. The most commonly cited works which study the effects of gusts and their effects on aircraft can be found by Etkin [9], Frost [10] and Hoblit [11]. Generally wind disturbances are considered in three constituent part: mean wind, discrete gusts and continuous gusts [12]. Mean wind generally poses minimal risk to aircraft as it can easily be accounted for in trim flight conditions, as it varies slowly enough to be accounted for with basic control. Discrete gusts are akin to step disturbances, which act for a discrete time period. Continuous gusts, also referred to as turbulence [11], are the unpredictable and continual fluctuations of the wind. Both discrete gusts and turbulence present a disturbance rejection problem in flight control, as they act on the aircraft as an external disturbance. As this is an unavoidable feature of flight, it has been studied extensively in literature.

One of the earliest commonly referenced works by Frost [10] produced detailed adaptations to the general aircraft equations of motion to include both wind velocity and rotation; wind gradients are also considered. Frost is cited by a great number of later papers and

used as the basis for modelling the effect of wind on aircraft, as well as flight control in wind gusts [13–15]. However, measurement of wind gusts on aircraft is non-trivial, so some work exists which attempts to estimate the gusts online. One work by Mulgund [16] utilised an Extended Kalman Filter (EKF) to estimate wind components to be used in flight control, although it was determined that the nonlinear model used was very sensitive to parameter uncertainty which would limit performance. Pourtakdoust [15] studied the affect of microburst wind shear during aircraft landing, where it was shown that without proper accommodating action, these conditions were dangerous to aircraft during landing.

2.1.1 The Effect of Wind on UAVs

Although they operate on the same principles, the flight considerations for small UAVs are vastly different to general aviation. Their small size reduces their inertia, making them more susceptible to disturbances. Additionally, the operating airspeed of a small UAV is generally much lower than conventional aircraft. It has approached the point where the velocity of wind and gusts may match or even exceed the airspeed of a small UAV. Generally this means that for a given disturbance, a small UAV will be more affected.

This issue has been studied in literature. For example, Mueller [1] provided a detailed investigation into the aerodynamic considerations of small UAVs. Fig. 2.2 is reproduced from this work, and demonstrates that small UAVs operate in a different flight regime than traditional aircraft. This means small UAVs are designed differently, for example using aerofoils specifically tailored for this flight regime. The impact of this, as also discussed by Broeren [17], is that small (and indeed micro) UAVs have different responses to wind gusts than conventional aircraft. This means that flight control methods which are suitable for traditional aircraft may no longer be sufficient. For example, the relatively slow response of a Proportional Integral Derivative (PID) controller which was suitable for attitude control of a conventional aircraft may no longer offer sufficient response times when applied to small UAVs. The work done by Lissaman [18] also demonstrates clearly that as wingspans decrease, the associated roll response magnitude to a given disturbance increases.

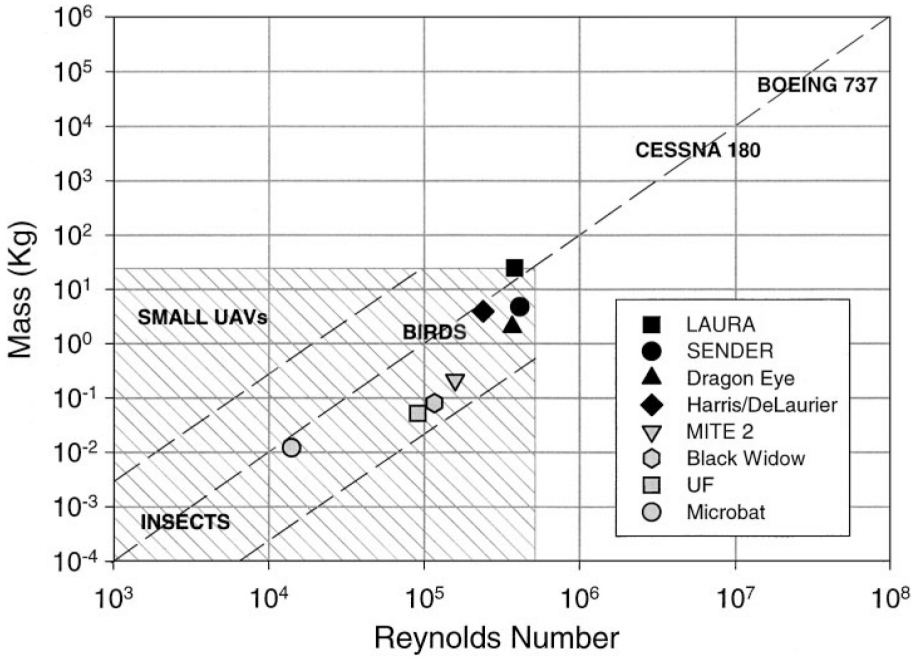

Figure 2.2: The relationship between mass and Reynolds number with some example small UAVs included. This indicates well how different the considerations of wind on small UAVs are when compared to full sized aircraft. Reproduced from [1]

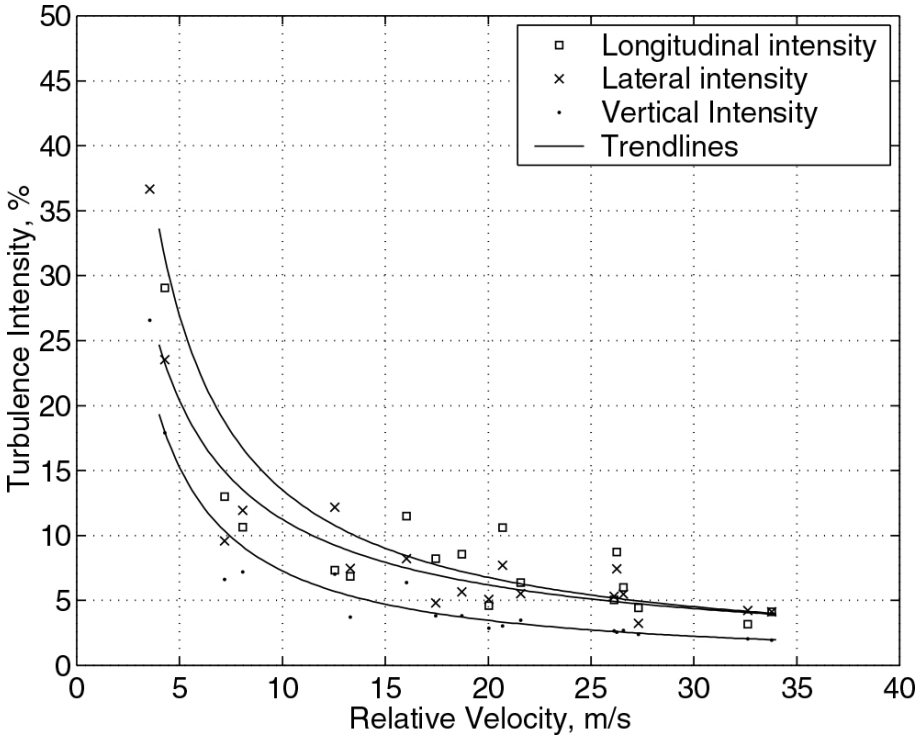

Figure 2.3: Top: Variations in experienced turbulence intensity for a given velocity of vehicle. Bottom: Variations in experienced pitch angle in wind for a stationary probe with wind speed of 7.8m/s. Reproduced from [2]

A recent and detailed investigation [19] into the effects of UAV characteristics and their effects on gust response made some interesting conclusions. It was found that a reduced wing loading reduced UAV response to gust in all metrics apart from pitch; a result which is not necessarily expected. A number of other aircraft design considerations were also discussed specifically regarding wind turbulence handling. Although this information is useful in the design of future aircraft, quite often the small UAVs operated use a generic airframe, adapted for purpose. If this problem could be addressed through control design, the solution would be more generic and cheaper to implement. A detailed study by Mohamed [20] concluded that current sensors, such as gyroscopes and accelerometers may be insufficient for counteracting turbulence for Micro Aerial Vehicles (MAVs). However, MAVs are substantially smaller than UAVs and therefore even more susceptible to wind disturbances. It was concluded that combining multiple sensor readings together would provide far better response. This means that a multiple input control system is preferable, as the effect of turbulence may not easily be obtained from a single sensor. Traditional control methods such as PID are limited in this sense.

Watkins [2] conducted an investigation into the turbulent winds within the atmospheric boundary layer. This is the layer of wind close enough to the ground that it may be affected by obstacles such as trees or buildings. The traditional methods of wind turbulence modelling do not explicitly consider these effects. Shown in Fig. 2.3 is data from the work by Watkins, which demonstrates that the typical operating speed for small UAVs ($10-20m/s$) is in the region where turbulence is becomes more intense. Previous literature indicated that for a given wind, small UAVs are more affected than conventional aircraft. The data from Watkins shows that the problem of wind disturbance is indeed worse for small UAVs, as the turbulence at speeds which small UAVs operate is even higher, compounding the issue. Further work in the area [21] found that, for a given gust applied to each axis, the roll axis will exhibit the most response for aircraft of a conventional configuration. This is something to be considered in later work in the thesis.

Overall, the body of work studying the effects of wind and turbulence on small UAVs demonstrates clearly that the problem is significantly worse for these aircraft. Not only are the aircraft more affected by a given disturbance due to their size, but the operating speed means they are more likely to encounter larger disturbances. This means that traditional control methods applied to conventional aircraft may no longer be sufficient.

The next area of investigation therefore is control methods for mitigation of wind disturbances for aircraft and specifically small UAVs.

2.2 Flight Control Design with Disturbances

The general area of disturbance mitigation in flight control has been studied for some time. An area where this is paramount concern is Very Flexible Aircraft (VFA) control. Due to their size and lightweight construction, these aircraft are extremely flexible and sensitive to wind disturbances [22]. A notable recent paper by Cook [23] developed a H_∞ controller with the aim of reducing root bending moments when subjected to gusts. A reduction of 9% resulted. This is of note as it demonstrates that control design can be used to reduce the influence of disturbances on an aircraft. This is a more universally applicable solution than the physical design constraints proposed in [19].

Research has also been conducted for some time involving the addition of specialised control surfaces for the reduction of structural stress. Moulin [24] demonstrated that a reduction of up to 16% in wing bending stress was possible. The stress studied in [23, 24] is closely related to the transfer of unavoidable gust loads on the wings to the aircraft fuselage. Control design to reduce this stress suggests it is feasible to reduce the overall effect on the aircraft too.

Okamoto studied optimal aircraft control in stochastic weather [25], specifically addressing microbursts during landing. However, this approach was concerned with the generation of an optimal path and the aircraft attitude needed to achieve this path; no consideration is made for the low level controller which must be able to track these commands, particularly in the presence of such severe disturbances.

Yoon [26] studied controller design for wind disturbance rejection, which also considered actuator saturation. Yoon also considered the effect of actuator failures. With less control authority to use, it was more likely that the remaining surfaces would undergo saturation, meaning the control design had to consider this explicitly. Without considering actuator faults, it is more likely that a small UAV will undergo control saturation in a normal flight due to the relatively larger effect of disturbances. This would be a good point to consider in any flight control for small UAVs.

On the whole, literature for disturbance rejection in attitude control of full scale aircraft is somewhat limited. Research into the reduction of structural stress [27–30] is the most common consideration for disturbance alleviation in conventional aircraft. The lack of literature aimed at disturbance rejection in aircraft attitude control would suggest that it is not seen as a problem worth studying.

2.2.1 Flight Control for UAVs Subject to Disturbances

Due to the additional considerations for UAVs, a large amount of research can be found on path following in wind. One of the few practical works in the area is by Nelson [31]. Nelson developed a vector field guidance method which demonstrated that robustness to wind disturbances could yield good path following in the presence of high wind (46% of airspeed in [31]). Vector field guidance is an attractive control method when there is no constraint on the time at which the vehicle should reach a location. An additional benefit is that the aircraft can maintain a given airspeed, which can be selected as desired.

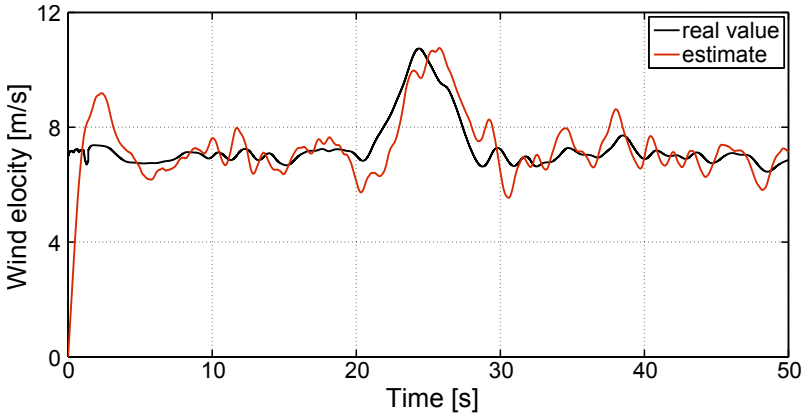

Figure 2.4: Performance of the wind estimator from the work by Brezoescu [3].

Flight tests demonstrated that the proposed method translated to practical application, despite no direct wind information being used. Hota [32] also investigated path planning in a constant, known wind with Dubins paths. This demonstrated good robustness in the presence of winds which approached the airspeed of the investigated vehicle. Similar work was done by Jennings [33], using dynamic programming to generate feasible paths in the presence of wind.

Ceccarelli [34] demonstrated in simulation that path planning using a known wind field allowed for a significant improvement in trajectory tracking. Similar work was conducted by Jackson [35] using spatial sliding mode controllers. Both demonstrate that with ideal knowledge of the wind, performance need not be affected substantially. Earlier work by McGee produced similar results [36]. The limitation with these methods are the reliance on ideal knowledge of a assumed constant wind, neither of which are practical.

Mills [37] studied path following in the presence of wind using visual servo control, where positional information is derived from image processing. In this work, it was shown that using the estimated wind component directly in the control scheme was far better than traditional integral augmentation. The limitation with this particular method is that few aircraft will have the required hardware for visual servo control. Some improvement can be found in the work by Brezoescu [3], where an online estimator was used to obtain measurements of the wind. Fig. 2.4 shows the estimator performance. The estimator performance is reasonable, although there is room for improvement as there is some steady state error and a tangible delay in the estimate. However, this work is far more practically applicable than all previous works which assumed a known constant wind field. Liu [38] investigated the applicability of the DOBC technique to this problem. A nonlinear observer is designed and tested in simulation and crucially flight testing. Within this work, the flight test demonstrated very good performance which was similar to the simulation results. The disturbance observer was able to estimate the truly stochastic wind, which was shown to have a large effect on the aircraft when the observer augmentation was not active. This is a promising result for DOBC in application to flight control.

The main limitation of all these works is the assumption that a low level controller exists which is able to track the demanded attitudes. This is somewhat justifiable as most of this considers steady or quasi-steady winds only. However, in the initial literature review it was shown that this is only one component of wind; step gusts and continuous turbulence must also be considered, where the assumption that the inner loop controller is able to track commands can not be assumed to hold.

Inner Loop Control

While inner loop control for UAVs is widely studied in literature, work regarding disturbance rejection in this area is more sparse. Sadraey [39] studied a combination of nonlinear dynamic inversion control with a robust outer loop H_∞ controller. This approach made no direct consideration of wind in the attitude controller, relying on the H_∞ controller to drive the system to the reference in the presence of disturbances. This yielded sub-optimal, yet robust, performance. More recently, Yang [40] compared the performance of a baseline PID controller to a robust H_∞ scheme. Mixed results were obtained, with the PID controller offering better performance in some areas while the H_∞ controller was better in others. These works demonstrate that, while H_∞ control works well for robustness in terms of disturbance rejection, nominal performance is usually sacrificed. This would limit the ability of an autopilot to track references accurately in the presence of disturbances.

Brezoescu [41] studied the performance of an adaptive backstepping controller in the presence of wind. The propsed method was able to estimate and account for the effect of an unknown wind within $7s$ when tracking a straight line. Some overshoot is also seen in the estimation of the parameter. This tracking response is somewhat slow. Indeed, when tracking multiple paths and subject to wind with a small amount of variance, positional errors resulted. This is a result of the slow estimation response, which suggests this method is not suitable for rejection of stochastic disturbances.

Hervas [42, 43] investigated the performance of a sliding mode controller subjected to stochastic disturbances, with an EKF used to estimate the wind. In this work, slow disturbance estimation was seen again, with errors present in the output for around $100s$. Clearly this response is too slow for proper estimation and attenuation of a stochastic disturbance. Earlier work using a similar methodology by Gavilan [44] demonstrated that this control scheme was well suited to modelling uncertainty, with good performance recovery demonstrated. Ideally, a control method which is able to account for both internal and external disturbances would be preferred.

An amount of work exists around Active Disturbance Rejection Control (ADRC) in this area; this is a method which is intended to account for uncertain plants and external disturbances. Xiong [45] designed and compared an ADRC scheme to a PID method. In the simulation results, the ADRC method improved on the performance of the PID controller in velocity and pitch angle tracking and had similar performance in roll. The effects of the disturbances were still quite prominent in both cases. In [4], the ADRC controller was applied to the tracking of a glideslope in the presence of disturbances. The disturbance rejection performance was limited, with a constant bias in both lateral and vertical directions when disturbances were present. This is shown in Fig. 2.5. In this simulation, wind disturbance was active to the point where the aircraft reached approximately $4800m$ in position. It is quite evident that the disturbance effect was not removed from the output while the disturbance was active. Wang [46] presents some simulation studies for the performance to parameter uncertainty, where the method offers good performance. Later flight testing of this method by Zhang [47] demonstrated that the effect of external disturbances shown by Xiong carried across to flight testing, with lateral and vertical errors present throughout.

Liu [48] evaluated the performance of a nonlinear disturbance observer approach coupled with nonlinear dynamic inversion control. The simulation results demonstrated very good performance of the DOBC method compared to the baseline controller as well as an integral augmented Nonlinear Dynamic Inversion (NDI) approach. The DOBC method was able to estimate and entirely remove the effect of external disturbances very quickly. The approach was applied in a situation similar to that investigated by Xiong [4]. The performance improvement of the DOBC approach compared to the baseline controller and integral augmentation is very clear.

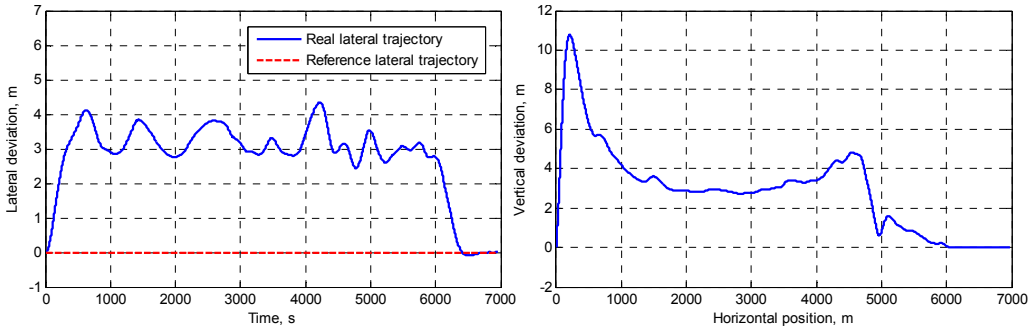

Figure 2.5: Data of reference deviation of an ADRC controller with wind disturbances active (up to $\approx 6000s/4800m$). Reproduced from [4].

From the few items of literature regarding disturbance rejection in attitude control, the DOBC approach has shown the best performance. Other methods are able to show some improvement, but the responses are either too slow or do not fully remove the disturbance. The limitation of the DOBC work for attitude control is that has only been demonstrated in simulation, whereas the ADRC methods have some flight test results. However, there is significant scope for improvement over these results.

2.3 Disturbance Estimation and Attenuation

When control design is taken from theory to practical application, disturbances and uncertainties are always present [49–51]. The degree to which they affect the system being controlled is however not certain and depends on a range of factors. In most control cases, the timely and accurate rejection of disturbance effects is an important factor in control design. Traditional control design methods such as PID and Linear Quadratic Regulators (LQRs) are unlikely to be capable of maintaining high degrees of control performance in the presence of significant disturbances and uncertainties [52]. However, many applications require accurate and timely attenuation of disturbances, which are generally unknown. In some cases, measurement of the disturbances is prohibitively difficult or costly; more often however, there is simply no means of direct measurement of the disturbances. Consequently, a range of methods have been developed which estimate the disturbances based on the measurable states. Within this section, the most notable of these methods are discussed.

2.3.1 Disturbance Estimation Methods

In the 1960s, investigations were ongoing within National Aeronautics and Space Administration (NASA) [53] to develop the optimal linear regulator (now commonly referred to as the Linear Quadratic Regulator (LQR)). At that time, the regulator was only able to effectively deal with known disturbances as part of the initial condition of the system, or to stabilise the system subjected to unknown impulse disturbances. Constant unknown external disturbances, such as plant damage, were not handled effectively. The result of the work was an extension to the LQR which was akin to traditional proportional integral control. This was further developed to account for a more general class of disturbances [54]. These advances were achieved through an implicit *internal* estimation of the external disturbance acting on the system. This was later expanded to an explicit, simultaneous estimation of the system state and disturbance states [55]. It was demonstrated there that the explicit formulation of the disturbance estimation produced the same closed loop performance as the earlier implicit methods. However, the explicit design method was found to be more intuitive and simpler to use by designers [53]. It is on these principles

to which the many methods of disturbance observers mentioned previously can trace their origins.

Development of disturbance estimation techniques continued with many different methods being developed including the Unknown Input Observer (UIO) [56], Perturbation Observer (PO) [57], Equivalent Input Disturbance (EID) estimator [58], Extended State Observer (ESO) [50, 52] and the Disturbance Observer (DO) [59–61]. Of these methods, DOs and ESOs have seen the most contributions in theoretical application and development [51]. The ESO was proposed by Han in [62] and formed a fundamental component of what is now known as ADRC [52]. Non-linear DOBC was originally proposed by Chen [59], and has become very popular in recent years.

Adaptive Control (AC) is another method of disturbance estimation control. The AC approach is aimed at estimating unknown and time varying model parameters [63]. Good performance in the presence of time varying model parameters is a key feature of AC [64]. The method estimates parameters of the controlled plant, then updates the associated control laws to improve performance. However, AC performance may suffer when unknown parameters enter the system [65]. The problem is most noticeable with unknown/unmodelled uncertainties which are non-linear [66]. This significantly restricts the application of this methodology to the rejection of stochastic wind disturbances. The performance of the control method also depends very much on the design of the estimation laws [51], often requiring trial and error. The design of these laws requires use, and consequently understanding of Lyapunov [67] stability theory. A key limitation of AC in the scope of this work is the lack of explicit consideration of external disturbances.

The general principle of disturbance estimation can be illustrated by Fig. 2.6 [68], where $G(s)$ is a plant being controlled by a feedback strategy $C(s)$, $G_n(s)$ is the nominal model of the true plant used in control design, $Q(s)$ is a filter to be designed, y is the system state, y_r is the reference command, c is the controller demand, u is the total control demand, n is the measurement noise, d is an external disturbance, d_l is the lumped disturbance and $\hat{d}_l$ is the lumped disturbance estimate. In this context, *lumped* disturbances are defined to be the sum of the unknown external disturbances and the plant modelling errors. This may include both unmodelled dynamics as well as uncertainty in the modelled parameters. By applying the inverse of the plant model to the system output, the unmeasurable lumped disturbances can be estimated, allowing for the calculation of a feedback control signal to eliminate their effect. A more in depth discussion is presented in Section 2.3.3

A key feature of DOBC can be seen from Fig. 2.6. If external disturbances are removed, and we assume that the nominal model is correct (i.e. $G_n(s) = G(s)$), no action is taken by the disturbance observer. This is the so called "separation principle" [51]. This allows for design of the feedback control and disturbance rejection control for nominal performance and disturbance rejection, respectively. Theoretically, this allows for the use of optimal feedback control which does not need to sacrifice performance for robustness against disturbances. This is a distinguishing feature of the DOBC method. For example, in traditional PID control the integral term is added to remove the effect of disturbances. In doing so, however, nominal performance is sacrificed as the integral term introduces undesirable effects such as overshoot, control saturation and additional phase lag.

2.3.2 Nonlinear Disturbance Observers

In [59], a nonlinear robotic manipulator was studied and a Nonlinear Disturbance Observer (NDO) was proposed to estimate the disturbances. It was shown that the use of these disturbance estimates in the control strategy resulted in substantially improved performance. Additionally, stability was demonstrated for the proposed NDO when subject to constant disturbances. Later developments [69] expanded capabilities to disturbances generated by

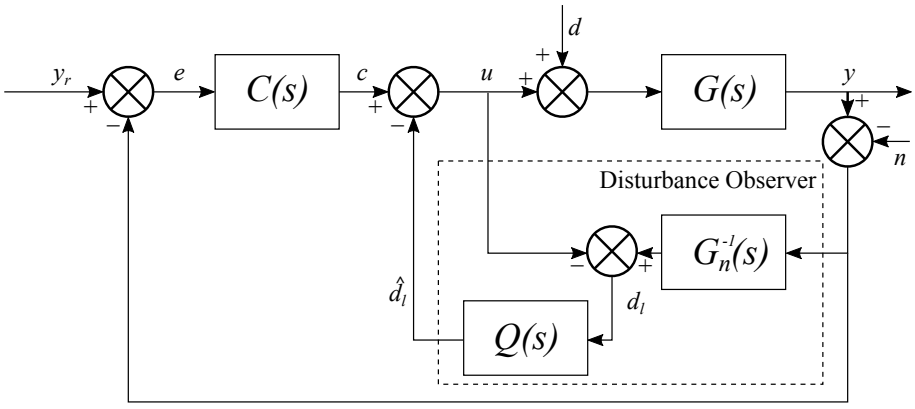

Figure 2.6: The general operating principle of disturbance estimation

an exogenous system, by a proposed NDO with a nonlinear observer gain function. These developments have formed the basis of a significant amount of research on the NDO, including estimation of harmonic disturbances [69] for a class of Single Input Single Output (SISO) systems, an NDO for a class of Multi Input Multi Output (MIMO) systems subjected to disturbances generated by an exogenous system [70]. A recent development by Kim [71] resulted in an NDO which is able to estimate higher order disturbances, such as ramps; from this a generalised method was produced which is able to estimate general order disturbances [71].

One drawback of the NDO method is that it can be somewhat complex in design, analysis and application. Considering the target audience for this thesis, it would be more appropriate to use a simpler method. Additionally, the NDO lack rigorous stability analysis [51], which would severely limit its application in flight control. This issue is not carried over to the linear DO.

2.3.3 Frequency Domain Observers

The original frequency domain disturbance observer was proposed in the 1980s [60, 72], depicted as the "disturbance observer" in Fig. 2.6. This was designed for the estimation of unmeasurable external disturbances by passing the difference between demanded control u and the calculated input (given by $G_n^{-1}(s)$) through a filter, $Q(s)$. This filter is generally designed as a low pass filter with relative degree greater or equal to that of the nominal plant. This is required for $Q(s)G_n^{-1}(s)$ to be proper and realisable.

The benefits of this method were the relatively straight forward design and implementation, as well as compatibility with traditional frequency domain analysis methods. The main drawbacks are its limited application to a class of linear systems and limited performance with transient disturbances [73].

Performance of this observer is also very dependant on the chosen filter $Q(s)$. Ideally, this filter would be designed such that it has unity gain across the entire frequency range, as this would theoretically result in the best disturbance rejection performance. In practice however, the application of such a filter will result in the detection of high frequency sensor noise as disturbances which is likely to give worse performance. Furthermore, such a filter would not satisfy the relative degree requirement and is therefore not implementable. The use of a low pass filter is common, as this allows for attenuation of the (usually) low to medium frequency disturbances while not being affected by the (usually) high frequency sensor noise. The design of this filter is a well researched subject [61, 74]. The frequency domain observer has seen many notable applications including high speed direct drive positioning tables [75], machine tool control [76] and robot manipulators [61].

2.3.4 Time Domain Observers

In the 1990s, the ESO was proposed [62] to estimate all the states of a system, along with the lumped disturbances. For design of the ESO, only the relative degree of the system is needed which allows for design without detailed knowledge of the system being studied. The ESO forms a key component of the ADRC method [52]. This method has been applied in many areas due to its low requirements and simple structure [77]. However, the main challenges facing the ESO based ADRC are a lack of rigorous theoretical stability proof [52] and difficulty in dealing with mismatched disturbances [68, 77]. For flight control, proof of stability is essential, particularly in the application of control methods in commercial applications. Additionally, as is discussed later in Chapter 5, mismatched disturbances are generally found in flight control. Furthermore, although the model free requirements of ADRC are beneficial in instances where models are not available, if a model *is* available it may enable improved disturbance estimation, and therefore disturbance attenuation performance.

State Space Disturbance Observers

In 2000, Lee proposed a state space based disturbance observer [78] which did not require modelling of the disturbances. This demonstrated good recovery of nominal performance in the presence of external disturbances. This was later applied to track following for computer hard drives [79, 80], as well as a generalised approach [81]. There are several important advantages to the use of the disturbance observer in state space, as opposed to the closely related frequency domain. First, inverse plant dynamics are no longer required. Instead, a state space model of the system is needed, which is commonly available in flight control design (as used in the initial works by Johnson [82]). Second, the design of an associated filter $Q(s)$, which is needed to make the system proper in the frequency domain, is also removed. This filter was responsible for the robustness and disturbance rejection performance [81], but the structure of the observer constrained the design to particular forms. Formulation of the observer in state space allows for more advanced methods of designing the disturbance attenuation component. An additional significant benefit of the state space observer is that the system is no longer restricted to SISO applications. This expands the possible applications significantly.

An essential advancement in the state space disturbance observer was developed by Yang [83], in the form of mismatched disturbance attenuation. Prior to this work, only disturbances which entered the system through the same channels as the controls were considered. In [84, 85], a hybrid DOBC and H_∞ approach was used to address the mismatched disturbances. However, in this case, the DOBC component was used to act upon the matched disturbances only, while the H_∞ control addressed the mismatched disturbances. Additionally, this method required that the disturbances adhered to certain constraints such as a bounded H_2 norm. This is problematic, as mismatched disturbances are far more general than the matched disturbances and are widely found in practical applications such as flight control [86]. The solution proposed by Yang is therefore more widely applicable than DOBC methods which assume matched disturbances. The approach is briefly described here. We model the dynamics of a bank to turn missile as in [83]

$$\begin{aligned} \dot{x} &= Ax + B_u u + B_d d_x, \\ y &= Cx + D_u u + D_d d_y, \end{aligned} \tag{2.1}$$

where $x = \begin{bmatrix} \omega_z & \alpha & \omega_y & \beta \end{bmatrix}$ is the state vector, $u = \begin{bmatrix} \delta_z & \delta_y \end{bmatrix}$ is the control input, $y = \begin{bmatrix} n_z & n_y \end{bmatrix}$ is the output, $d_x = \begin{bmatrix} d_{\omega_z} & d_\alpha & d_{\omega_y} & d_\beta \end{bmatrix}$ is the external disturbance on the states and $y = \begin{bmatrix} d_{n_z} & d_{n_y} \end{bmatrix}$ is the disturbance on the outputs, with A,B,C and D being the state,

control, output and feedthrough matrices associated with the system, $B_d = I^{4\times4}$ and $D_d = I^{2\times2}$ are the state and disturbance mapping matrices, respectively. Assume that observers have been designed following traditional DOBC methods to estimate the lumped output disturbances, given by

$$\hat{d}_{l_y} = y - Cx - D_n u,$$

where $\hat{d}_{l_y}$ is the lumped output disturbance estimate and D_n is the nominal model of D. Also assume that lumped state disturbances are estimated by

$$\begin{cases} \dot{z} = -LB_d(z + Lx) - L(A_n x + B_n u), \\ \hat{d}_{lx} = z + Lx, \end{cases}$$

where $\hat{d}_{lx}$ is the estimate of the lumped state disturbances, L is the observer gain matrix, A_n and B_n are the nominal system and control matrices and z is an internal state of the observer. Also presume that a state feedback controller has been designed which provides sufficient feedback control to track reference commands in the absence of disturbances, subject to the control law

$$u = K_x x.$$

To deal with the mismatched disturbances, a control law was designed as

$$u = K_x x + K_d \hat{d}, \tag{2.2}$$

where $K_d = \begin{bmatrix} K_{dx} & K_{dy} \end{bmatrix}$ and $\hat{d} = \begin{bmatrix} \hat{d}_{lx} & \hat{d}_{ly} \end{bmatrix}^T$. Based on the assumption that the lumped disturbances vary slowly, which is to say $\dot{d}_{lx} \approx 0$, and that the observer gain L has been chosen to yield a stable observer, it is possible to design a gain vector K_d such that the disturbances are attenuated from the output. This is achieved if we select the elements of K_d as

$$\begin{aligned} K_{dx} = &\left[D_n - (C_n + D_n K_x)(A_n + B_n K_x)^{-1} B_n \right]^{-1} \\ &\times (C_n + D_n K_x)(A_n + B_n K_x)^{-1} B_d, \end{aligned} \tag{2.3}$$

and

$$K_{dy} = -\left[D_n - (C_n + D_n K_x)(A_n + B_n K_x)^{-1} B_n \right]^{-1} D_d. \tag{2.4}$$

First, we substitute (2.2) into (2.1), allowing the state to be expressed as

$$x = (A_n + B_n K_x)^{-1} \left[\dot{x} - B_n K_d \hat{d} - B_d d_{lx} \right], \tag{2.5}$$

combining this with (2.1), (2.3) and (2.4) yields

$$\begin{aligned} y =& (C_n + D_n K_x)(A_n + B_n K_x)^{-1} \dot{x} \\ &+ \left(D_n - (C_n + D_n K_x)(A_n + B_n K_x)^{-1} B_n \right) K_d \hat{d} \\ &- (C_n + D_n K_x)(A_n + B_n K_x)^{-1} B_d d_{lx} + D_d d_{ly}, \\ =& (C_n + D_n K_x)(A_n + B_n K_x)^{-1} \dot{x} \\ &+ (C_n + D_n K_x)(A_n + B_n K_x)^{-1} B_d e_{d_{lx}} - D_d e_{d_{ly}}. \end{aligned} \tag{2.6}$$

Recalling that, for a constant disturbance, we can say that as $t \to \infty$, $\dot{x} = 0$, which reduces (2.6) to

$$y = (C_n + D_n K_x)(A_n + B_n K_x)^{-1} B_d e_{d_{lx}} - D_d e_{d_{ly}}.$$

It is also assumed that the observers which have been designed are able to track step disturbances (the stability is proven in [83]), which means that $\left(e_{d_{lx}}, e_{d_{ly}}\right) \rightarrow 0$. This important result demonstrated that a state space disturbance observer is able to remove the effect of slowly varying mismatched disturbances from the output of a system. Formulation of the proof in terms of output rather than state is needed, as the system is only able remove disturbances from as many outputs as there are control inputs (or indeed less outputs).

It is also important to note that this method does not result in any loss of generality, as it is also suitable for the matched disturbance case. This can be demonstrated by setting $B_n = B_d$ (the matched condition) and $D_n = D_d = 0$, from which it can be shown by (2.3) and (2.4) that $K_{dx} = -1$ and $K_{dy} = 0$. This is the particular form used in prior literature considering the matched case. It was later demonstrated that this linear state space DO was able to account for non-linearity in a magnetic levitation trains' suspension system [87]. In this work, the train suspension was modelled as a non-linear system, which was linearised for the design of the observer. Simulation results using the non-linear plant dynamics were conducted and it was shown that the linear DO was able to accurately estimate external load disturbances as well as the internal modelling disturbances. The DOBC method was shown to perform much better than traditional integral augmentation of an LQR controller.

2.3.5 Disturbance Observer Methods in Flight Control

Disturbance observer control has also been applied to attitude control for small UAVs in wind, conducted by Liu [48]. A nonlinear DOBC method was shown to offer significant improvement in disturbance rejection when compared to a nonlinear dynamic inversion control in simulation. The method was able to estimate and quickly reject disturbances, allowing restoration of the nominal baseline performance of the feedback controller. This is a promising initial result in the area.

DOBC has been applied to a range flight control problems on platforms other than small UAVs. One of the earliest applications was by Chen [86] to improve robustness of missile control. In this paper, the method demonstrated good performance in the face of large parameter variance. More recently Zhang [88] has applied a nonlinear DO to estimate acceleration of moving missile targets to guarantee convergence in a finite time. Furthermore, the outputs from the observer were used successfully to reduce chattering of the baseline sliding mode control.

Yang [5] demonstrated the added robustness of a model predictive controller for a hypersonic air breathing vehicle. Such aircraft operate at very critical flight conditions and are very susceptible to both parameter uncertainty and external disturbances. Shown in Fig. 2.7 is a simulation from this work. Here, the system has been subjected to a step change in reference velocity and altitude, with a range of disturbances applied. Clearly, the addition of the disturbance observer controller has resulted in a substantial increase in robustness. With the DOBC scheme active, the aircraft is able to mitigate the effect of the unknown disturbances rapidly while also maintaining stability. This is not true for the control without DOBC augmentation.

The advantages of DOBC augmentation over a baseline controller as well as integral augmentation was demonstrated by Liu [6] when applied to small scale helicopters. A figure from this work is reproduced in Fig. 2.8. Here it is demonstrated that the DOBC augmentation was far better than integral augmentation for disturbance rejection. The ability of the NDO to estimate both the modelling errors and external disturbances produced a very clear performance improvement over the integral method. A later development on small scale helicopter control expanded the observer capabilities to estimate the unmeasurable flapping angles [89]. Classically, these angles are unmeasurable. They are, however, critical in governing the helicopter response. By estimating these angles, it was

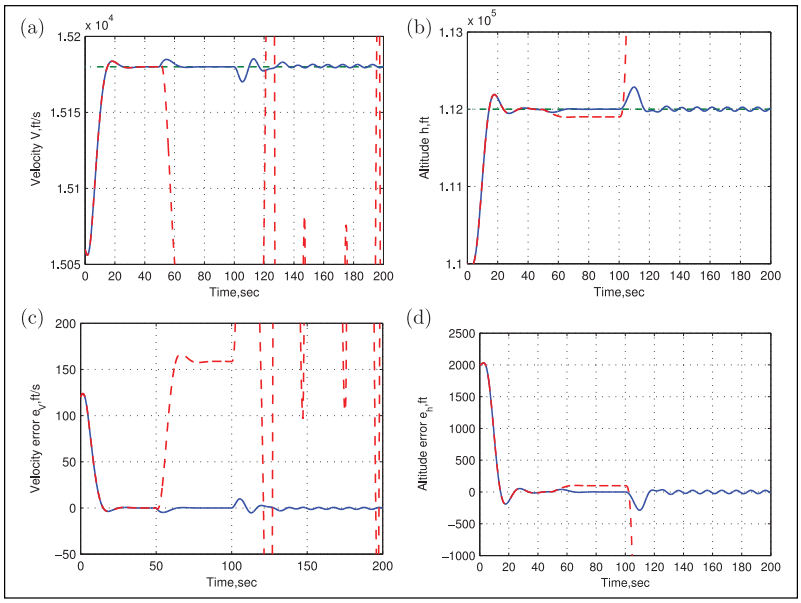

Figure 2.7: A response comparing feedback control without and with DOBC augmentation. Reproduced from [5].

shown that further performance improvement was possible.

Overall, DOBC has been applied to a range of flight control applications, for both external and internal disturbance mitigation. Furthermore, flight demonstrations of the method to small scale helicopters has been conducted with impressive results. As yet, it has not been shown that this performance translates to physical application of small fixed wing UAVs. The investigated work suggests that this method would be very capable of improving robustness and performance of attitude control for small fixed wing UAVs.

Limitations of Current DOBC Methods

Some initial work in the application of DOBC to small UAVs has been conducted. However this work was done in simulation, and limited to the longitudinal channel. No work in this area has been conducted for the lateral channel of small UAV control. The lateral channel is critically important in accurate trajectory and path following; it would be highly beneficial to investigate this area.

Additionally, some further practical constraints have not yet been addressed for the application of DOBC to small UAV flight control. First, most methods in literature are concerned with the nonlinear DO. Although it is known that this method is better able to deal with nonlinear systems if designed well, it is also very clear that its application is more involved. Furthermore, the lack of rigorous stability proof would limit the application in flight control where proof of stability and safety is essential. It has been shown in literature that linear DOBC methods are able to account for some nonlinearity. The design of the state space DOBC is a far more convenient form for use in flight control, as these models are likely to already exist or can be more easily obtained. This makes the linear DOBC an attractive option for practical application, particularly for operators who may not be in the field of advanced flight control research.

Some additional considerations exist in the application of this method to small UAV flight control. One of the key findings of the literature review was that small fixed wing UAVs are far more susceptible to external disturbances. Coupled with reduced actuator effectiveness, control saturation is highly probable in this application. There is a lack of consideration for the effect of control saturation on the performance, and indeed stability, of the linear DOBC. As with overall proof of stability, this issue would need to be addressed

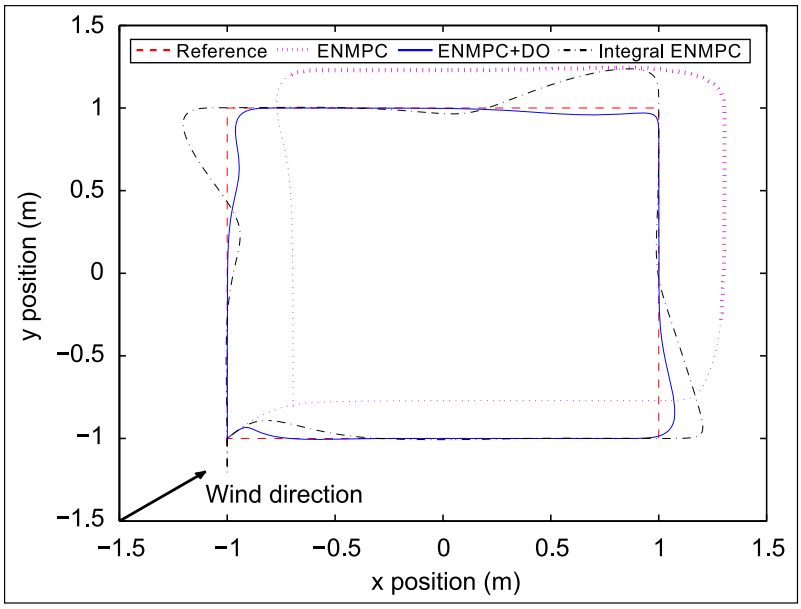

Figure 2.8: A comparison of a baseline controller to integral and DOBC augmentation when subjected to a wind disturbance. Reproduced from [6].

to enable application of this method in the wider area of flight control for small UAVs.

As well as saturation, control surfaces are subject to dynamics themselves. This issue has not been considered for the DOBC method. Some initial work exists which has investigated a means for estimating some unmeasurable dynamics which affect the system output. On small UAVs, it is highly unlikely that direct measurement of control position is available. The effect of the mismatch between demanded and applied control is a topic which is rarely addressed in literature for a wide range of flight control research. An investigation into the effect of actuator dynamics on the performance of the system, as well as any necessary augmentations would be extremely beneficial to this research topic. One of the key items of literature in this regard is by Lu [89], where approximations of helicopter flapping angles were combined into a nonlinear disturbance observer. An adaptation of this method may be possible to include known actuator dynamics. Analysis of the detailed function of the observer with respect to flapping angle estimation was not conducted in [89], meaning there is significant scope for an in depth analysis on this topic in terms of design and possibly tuning.

2.3.6 Summary of Key Methodologies Considered

Table 2.1 shows a broad comparison of the key control methods considered during this literature review, along with a comparison of their strengths and limitations. PID is one of the most applied control methods. It has many benefits including simple design and intuitive tuning. However, with these benefits come the limitations in performance. This control method cannot compete with the more advanced methods when it comes to disturbance rejection. ADRC is closely related, and famously seeked to combine the benefits of simple PID design and tuning with improved performance. ADRC has seen many successful applications. However much of the literature in the area of flight control does not demonstrate substantial performance improvements. Additionally, the lack of rigorous stability proof is a key limitation in the application to flight control.

Robust control is a widely studied and used method. It is popular as it maintains an acceptable level of performance when subjected to significant parameter uncertainty and disturbances. The trade off for this performance is the loss of optimal performance. In applications where this is acceptable, robust control is an attractive choice. An alternative

Table 2.1: A brief summary of the key control methods considered during the literature review

Method	Strengths	Limitations
AC	Handling time varying model parameters, maintaining control performance	Handling of unmodelled uncertainty, external disturbance consideration
ADRC	Simplicity, ease of application	Lack of rigorous stability proof, handling mismatched disturbances
PID	Ease of use, widely understood	Optimal performance not guaranteed
Robust Control	Robustness to uncertainty, guaranteed performance	Disturbance removal from system outputs
DOBC	Total rejection of unknown disturbances, patching into existing controller	Model requirement, limited applied flight control literature

is AC, which seeks to maintain optimal performance in the presence of unknown and possibly time varying model parameters. The design process for AC is more complex than PID and ADRC, but it offers recovery of nominal performance when designed appropriately. In situations where unknown and unmodelled variations enter the system, AC may suffer performance degradation. This might prove problematic in the application to small UAVs subjected to a wide range of disturbances.

DOBC offers a good compromise between all of these methods. It can be applied to an existing feedback controller to regain nominal (potentially optimal) performance in the presence of disturbances. There are many examples of design of DOBC methods in literature which can be adapted to new systems easily. Additionally, once designed the tuning process is very simple, with only the observer gain to tune. The DOBC method guarantees removal of non-varying disturbances completely from the system output, and can be proved stable in these situations. Additionally, the method has been shown to have very good disturbance rejection performance when subjected to time varying disturbances, if the observer dynamics are fast enough. The DOBC method does require a model of the system unlink PID and ADRC control. In flight control however, such models are commonly available. The improved performance offered by DOBC is then a very attractive option.

2.4 Control Design with Actuator Dynamics

In practice, every actuator has limited capabilities such as a motor with a maximum torque which can be applied, or an aircraft elevator with a maximum deflection angle [90]. Small UAVs are more prone to actuator saturation when compared to their full sized counterparts, as the magnitude of disturbances relative to the aircraft state are much higher, requiring significantly more control effort for rejection. Under actuator saturation, control performance degradation such as large overshoot or limit cycle may be encountered; in extreme cases, it is possible for instability to arise. Actuator saturation can also lead to the appearance of the controller windup phenomenon. With windup, internal controller states continue increasing in magnitude which can cause overshoot and instability, among other issues.

2.4.1 Actuator Saturation and Windup

Saturation is a control problem which has been studied for some time, the earliest sources appearing in the 1930s [90]. This occurs when a controller demands more control action

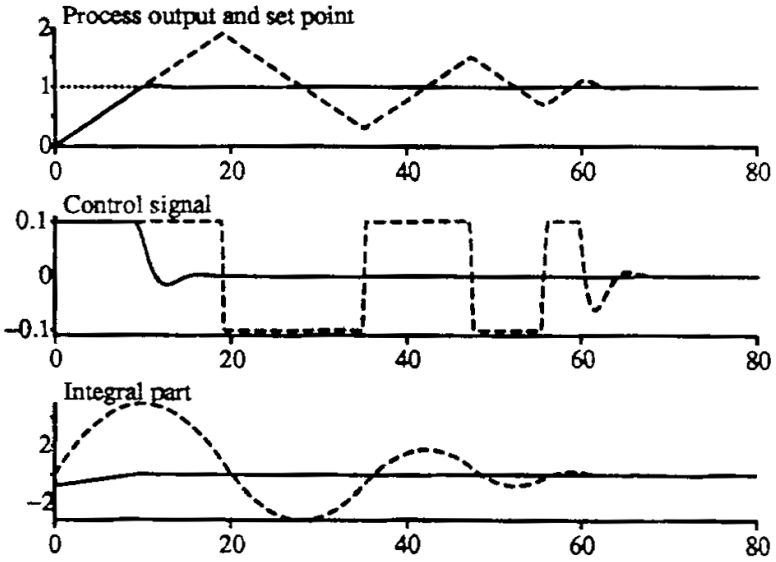

Figure 1. Illustration of integrator windup (dashed line) and control with anti-windup (solid line).

Figure 2.9: An illustration of integral windup for a plant with maximum input of ± 0.1. Reproduced from [7].

than the physical system is capable of. In many situations, this can lead to degraded performance or even instability. Groves [91] demonstrated the performance degradation and instability which might arise from control saturation. Serrani [92] also demonstrated that saturation can lead to dangerous states within a plant being controlled. An additional risk exists for controllers in the presence of actuator saturation, known as "windup". The term "windup" was coined to describe the internal state of a controller, particularly a controller with integral action, which arises from actuator saturation. A widely cited description of the problem is available by Astrom [7]. Shown in Fig. 2.9 is a figure reproduced from this paper which demonstrates integral windup clearly. Here the overshoot and significantly increased settling time are demonstrated as a result of integral windup. As DOBC features an integral component within the observer, it may also be susceptible to internal windup due to control saturation in this way. This internal windup due to saturation presents a significant risk to phyiscal systems; some recent examples [93] are the Saab Gripen fighter during initial flight tests, and the failure of the Chernobyl nuclear reactor.

This clearly presents a significant problem in control design, and has been the subject of research. Classically, two main schools of thought exist. One method, termed the "one step" approach [93] is generalised as designing a controller to avoid saturation entirely. This is generally criticised as resulting in overly conservative solutions [93]. An alternative approach is "anti-windup" control. Generally, in this situation the baseline controller is designed for optimal performance without consideration for saturation. An anti-windup method is then designed to ensure stability is maintained when saturation results.

As maintaining optimal control performance is a key benefit of DOBC methods, it would be counter-intuitive to then design a suboptimal controller to avoid saturation. Instead, the anti-windup method offers a more suitable approach. It has been well studied in literature. Krikelis [94] studied the performance of an "intelligent" integrator, which was disabled in the presence of saturation. Later, Hanus [95] presented the "conditioning" technique, which added a corrective signal to attenuate the effect of windup rather than altering the integrator behaviour. The work of Astrom and Campo [7, 96] presented a generalised approach to accounting for windup due to saturation. These methods provide a good groundwork for development of the linear disturbance observer for anti-windup.

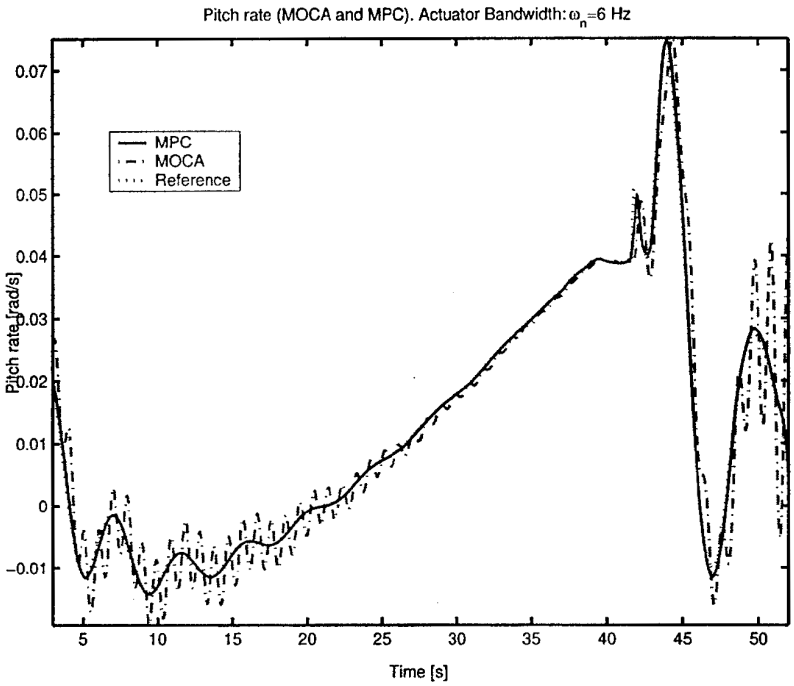

Fig. 3. Performance of MPC and MOIC with $\omega_n = 6Hz$: pitch rate.

Figure 2.10: A comparison of controller performance with explicit actuator consideration (MPC) and without (MOCA) when the controlled plant has low actuator bandwidth, demonstrating the resulting performance degradation not seen for higher bandwidths. Reproduced from [8].

2.4.2 Actuator Dynamics

Some literature can be found which makes use of actuator dynamics in control design. Groves [97] studied the design of a linear quadratic controller for a hypersonic air breathing vehicle. In this work, actuator dynamics models were embedded in the plant model used for control design. The actuator augmentation was not the main focus of the study, so no comparison of performance with or without the consideration of the dynamics is conducted. It is discussed that inclusion of the dynamics allows for consideration of the actuator bandwidth in control design, with anecdotal discussion regarding improved respect for saturation. No consideration is made of the availability of the actuator states for feedback; however in the case of the plant being studied it would not be unreasonable to assume these states are measured aboard such a vehicle. The same could not be said for small UAVs. Goh [98] conducted an in depth analysis on the effect of ignoring actuator dynamics on system stability. It was also shown that a large body of prior work falsely assumed that actuator dynamics could be assumed negligible. Lou demonstrated [8] that a model predictive controller with explicit consideration of actuator dynamics was able to outperform control schemes without actuator dynamics. The study conducted by Lou demonstrated that this was a function of the modelled actuator dynamics, as the performance difference decreased as the actuator bandwidth increased (i.e. tended toward no actuator dynamics).

The key point of these investigations is that actuator dynamics play a critical role in the application of theoretical controllers to a physical plant. As was demonstrated by Lu [89], a consideration of actuator dynamics allows for improved DOBC performance. In the literature, the unmodelled actuator dynamics was shown to degrade control performance. It is possible that not accounting for actuator dynamics in the observer may limit disturbance estimation performance. As with saturation, it may be that not considering actuator dynamics would require the observer to be tuned for suboptimal performance to avoid stability problems. In essence, actuator dynamics is a similar problem to windup

due to saturation, as it represents a difference between the controller demand and the applied action. As shown by Lu [89], there is scope for including actuator dynamics within the observer. The work by Groves [97] also demonstrates that it is possible to include actuator dynamics in a state space model for control design. The combination of these ideas may yield similar improvements to observer performance as was seen through explicit anti-windup design [93].

2.5 Research Motivations

From the conducted literature review, the problem of small UAV vulnerability to external disturbances has been demonstrated. It was also shown that a large body of work exists which studies the effect of external disturbances on high level UAV control. However, in this research it is generally assumed that an appropriate low level controller exists which is able to track the demanded aircraft attitude.

With small UAVs being far more accessible to a wider range of people than conventional aircraft, some different considerations are also needed for control design. It is more likely that these aircraft will be operated by small companies or individuals, who may not have the understanding needed to apply some of the more advanced control schemes. A key motivation in this research then is to determine if the simpler, linear versions of controller and DOBC augmentation are suitable for application to flight control in these instances. Obtaining a linear state space model is more achievable than a fully non-linear model, and will make the method more accessible. Additionally, the DOBC augmentation will allow for robustness and recovery of nominal control performance in the presence of modelling errors, which is also expected.

The literature review has shown that DOBC is a method which is able to account very well for both internal and external disturbances. It has been shown in many applications of flight control that the addition of DOBC makes a system much more robust to large disturbances which may otherwise lead to instability. This suggests that it would be highly beneficial to apply this method to the flight control of small UAVs which are subject to significant disturbances. Less considered are the internal disturbances resulting from modelling uncertainty. Due to the nature of their operation and construction, it is expected that the flight characteristics of a small UAV will vary between flights. Changes to payload, battery location or even light damage are potential sources for these disturbances, which would need to be accounted for.

Application of this method to flight control brings with it some additional considerations which are not thoroughly studied in literature. The problem of control saturation needs to be studied in more detail. It is likely to have a significant effect on the performance and stability of the applied DOBC. An investigation into these effects would be very beneficial to the future development and application of the method to small UAV flight control. Such a solution would be applicable to nearly all physical systems subject to actuator constraints.

Closely related to saturation are the dynamics of the actuators themselves. A large portion of research on flight control is conducted in simulation, where actuator dynamics are often neglected. When it comes to flight testing, it is no longer possible to simply assume the actuator dynamics are negligible. It would be of great benefit to the research topic of DOBC if the effects of actuator dynamics could be investigated.

Ultimately, the best proof of any results from such research should come from flight test data, as these problems are concerned with the physical application of the method. Flight testing will form a significant portion of the research work, as such a suitable flight test platform must be developed.

Chapter 3

Advanced Low Level Control Flight Test Platform

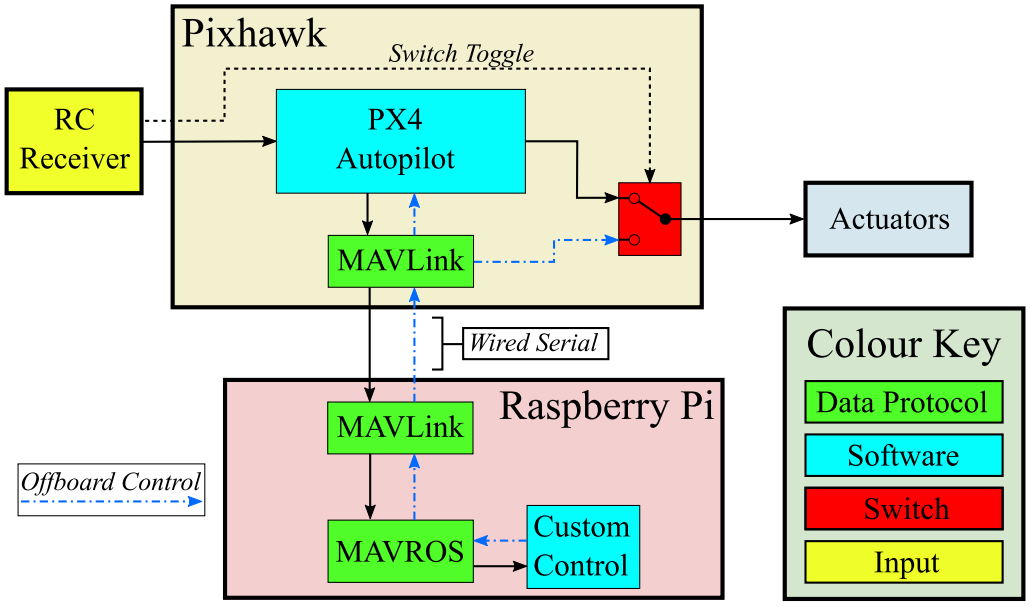

Figure 3.1: Data flow within the ROS enabled autonomous vehicle system used in aerial vehicles within LUCAS. General data flow is shown along with the offboard control path (dash-dot) and the manual override switch (dash-dash).

Within Loughborough University Centre for Autonomous Systems (LUCAS), a standard autopilot is used for all airborne vehicles, both rotary and fixed wing. At the heart of the system is a Pixhawk Commercial off the Shelf (COTS) autopilot which is very popular in the hobbyist autonomous flight area. The Pixhawk provides a range of sensors including Inertial Measurement Unit (IMU), Global Positioning System (GPS) and airspeed. In the standard configuration, commands can be taken directly from the pilot through a radio control link, to a range of autopilot modes from direct actuator control to high level position commands. The Pixhawk can track these user inputs, as well as offering the ability to complete fully autonomous missions which have been uploaded to the autopilot. With the use of the PX4 firmware, additional features are enabled. Most notably, an additional input route becomes available in the "offboard" control mode. In this mode, an external companion system (such as a Raspberry Pi) can replace the human inputs. This means the external source can provide inputs ranging from high level position commands down to low level direct actuator commands. This is a key feature in allowing research of experimental low level control methods.

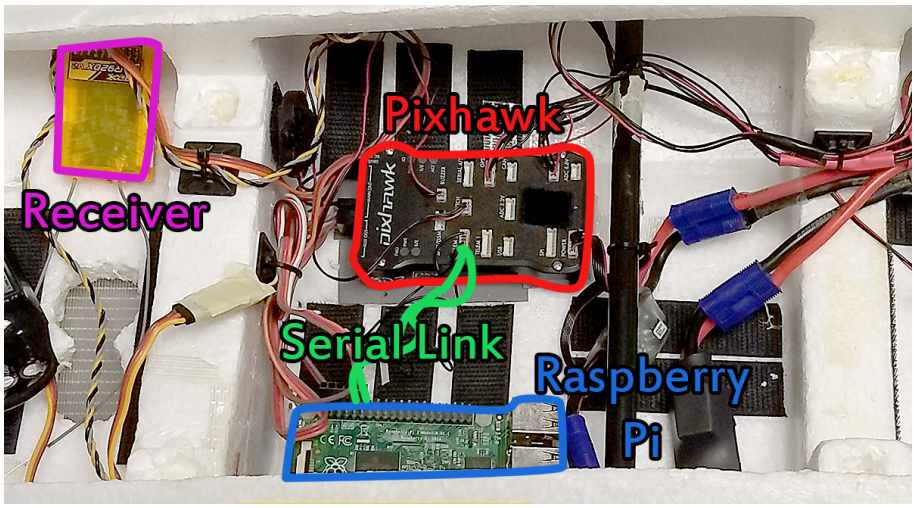

Figure 3.2: The internal components of the Skywalker X8 which allow for remote control and autonomous flight.

The physical manifestation of this system is shown in Fig. 3.2. Data is transferred between the companion system and the Pixhawk with a wired serial connection, using the industry standard MAVLink protocol. This means the companion system can be fairly generic, in that it is only required to support MAVLink communication. Within LUCAS, the Robot Operating System (ROS) framework has been utilised to provide a standardised means for data reception and transmission within the companion system. Due to excellent support from MATLAB/Simulink, controllers can be designed within Simulink and then compiled to run aboard the companion system. This is a considerable advance over previous methods, which required the control to run on a desktop/laptop computer, relying on WiFi for communication. This prior method had significant latency as well as being prone to connection loss. This limited its application to the study of high level control algorithms, with the Pixhawk being used for low level control. With the system described herein, low level controllers run onboard the companion system with a reliable, high speed data link. This allows for testing of low level control algorithms.

Another key feature of this system is the reliable manual override of offboard control. As depicted in Fig. 3.1, a permanent remote is able to switch back to the Pixhawk autopilot at any time. This is crucial, as experimental control algorithms are by nature sometimes unreliable and unpredictable. Keeping the Pixhawk autopilot separate and unaltered provides a reliable backup control solution in case of failure of the custom control. This allows safe flight testing of experimental control methods.

3.1 Key System Components

The key aspects of the described system are discussed herein. Of particular focus is the methodology for design and application of custom control code and the supporting components thereof.

3.1.1 Pixhawk Autopilot

The Pixhawk is a widely available and commonly used autopilot which can be configured to operate a range of vehicles. A key aspect of this autopilot is the internal processor, which is capable of not only running the low level control algorithms but also of converting its sensor data to the MAVLink data protocol, as well as reading data input using the same protocol. This allows the companion system to interface directly with the autopilot,

Table 3.1: A summary of the key Pixhawk autopilot operation modes.

Mode	Human Input	Pixhawk Function
Manual	Actuator Deflections	Pass through
Fly By Wire	Attitude angle commands, throttle setting	Low level control to track given attitude angles
Mission	Pre-defined mission trajectory	Low level attitude control and high level trajectory tracking

with low latency access to the onboard sensors. Data is available at a reliable 50Hz for fixed wing aircraft. This is a sufficient data rate for accurate low level control. Previous autopilots used in LUCAS allowed for data at around 10Hz, with additional latency due to the interface method. This was not sufficient for external low level control.

The Pixhawk also features onboard logging of all its data at the same 50Hz. This is extremely useful for collection and post processing of flight test data. Further, in flight monitoring of the aircraft is also possible through additional radio communication hardware.

The Pixhawk offers a range of control modes, the most relevant of which are summarised in Table 3.1. In offboard mode, the Pixhawk can perform all of the given functions, taking input from the companion computer instead of the operator.

The Pixhawk also has safety features. For example, in case of loss of signal with the operator (due to equipment fault or excessive range), the Pixhawk can return to the launch location and circle overhead until communication is restored. Further, in case of failure of the autopilot itself, the Pixhawk fails to a pass through condition, allowing the operator to regain control in manual mode and return the aircraft to land.

Overall, the Pixhawk autopilot is a very good choice due to the flexibility it offers the operator for a reasonable entry price. A large community exists which is able to provide support to users.

3.1.2 Raspberry Pi Companion Computer

The Raspberry Pi (RPi) 2 is used as the companion computer for all vehicles in LUCAS. This system runs Ubuntu 14.04 as the operating system. Another key aspect is ROS, which is primarily a system of transferring data between various autonomous vehicles. Within this work, it is mainly used to interface between Simulink controllers and MAVLink, allowing connection to the Pixhawk.

The RPi has a low power consumption of 5 watts in operation, and is very light, so does not affect aircraft flight time in a noticeable way. Despite the low power and small size, the system is very capable. A fully featured low level control algorithm running at 50Hz typically operates on less than 25% of a single core capacity, of which the RPi has four. The result is that the RPi is able to run low level algorithms at a consistent rate, while running all the data protocols necessary for operation, with plenty of processing power to spare. This consistency is critical for low level control testing. Once a controller has been compiled to the RPi, it can be configured to run automatically at boot. This allows for controllers to be compiled within the LUCAS facilities. The aircraft is then ready to be taken to the flight testing area and will automatically activate the controllers when the aircraft is powered.

3.1.3 Simulink Control Design

MATLAB and Simulink are software packages widely used in control design, analysis and simulation which are ubiquitous in industry. Simulink in particular allows for easy

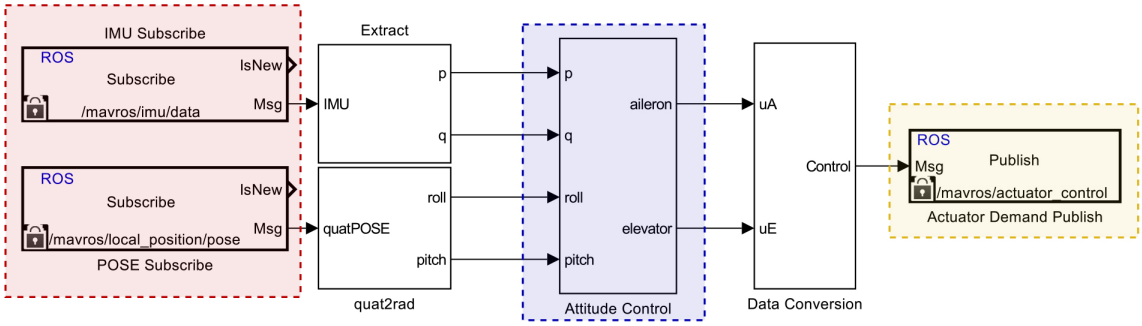

Figure 3.3: An example Simulink model showing data input from ROS (red), control calculations (blue) and publishing control demands back to ROS (yellow).

design of control systems using a graphical input system. The most important feature of Simulink used in this work is support for the ROS framework of communication, and auto-code generation.

ROS Integration

Assuming that the vehicle or system to be controlled has been appropriately configured for use with ROS (as is the case for the Pixhawk and RPi used herein), Simulink integration is straightforward. Using "Subscribe" and "Publish" blocks provides data input to Simulink and output to ROS, respectively. This is shown in Fig. 3.3, with attitude data being read in, control calculations performed to generate the demanded aileron and elevator commands which are then published back into the ROS network.

Depending on configuration, it is also possible to combine data from multiple sources. For example, two UAVs could exhange position data as long as they had an established network connection. This was used during the course of this thesis to obtain VICON motion capture data about the aircraft actuators. However, this also relied on an established network link between the aircraft and the VICON PC. This is easily facilitated through the RPi, which can be connected to an appropriate network device.

An additional benefit of this structure is that initial controller development can be conducted by running the controller in Simulink on a desktop PC, with data being read from and published to the aircraft over a network connection. This could be used for debugging and initial investigations into the controller function. This method was not suitable for flight testing, as it relied too heavily on the network connection.

Simulink Auto Code Generation

To take advantage of the low latency serial connection, controllers in Simulink could be converted to code which could be compiled and run onboard the RPi, as shown by the "Custom Control" element in Fig. 3.1. Generally this process is seamless, with Simulink ensuring that the code is transferred to the RPi and compiled onboard. However, issues were encountered. Certain blocks caused failure of the compiled controller when trying to run on the RPi.

Due to the auto code generation process, determining which elements caused these issues was slow and difficult. It generally required a process of elimination to be conducted until the offending element was identified. One such example was the "Absolute Value" block, which simply calculates the absolute value of a real number. This was solved by implementing the absolute calculation using basic mathematical blocks instead. However, identifying the block as the source of the error was not trivial.

Additionally, continuous time blocks required discretisation to run successfully in the discrete controller. Integrators and filters were the most common sources of this. Ad-

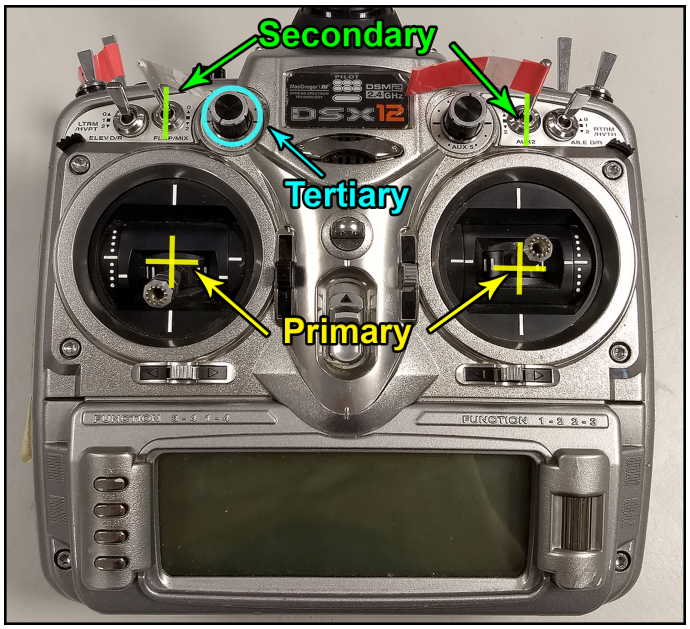

Figure 3.4: The RC transmitter generally used in flight testing.

Table 3.2: An overview of the available control inputs on the RC transmitter, the number of that type of input, the range (and number of discrete steps in the range) along with the common use for that input type.

	Count	Range (Resolution)	Common Use
Primary	4	$-1 \leq x \leq 1$ (1000)	Roll, pitch, yaw and throttle input
Secondary	2	$0 \leq x \leq 1$ (3)	Autopilot modes
Tertiary	2	$0 \leq x \leq 1$ (100)	Control gains

ditionally, it was necessary to ensure the controllers ran at their pre-determined discrete pace. This feature is well supported by Simulink, as it would be a common consideration for all users. Use of the "Simulation Pace" block with appropriate parameters ensured that the controllers ran at a consistent discrete pace.

Operator Control Interface

An additional consideration was the need for the aircraft pilot commands to be entered into the offboard controllers. As shown in Fig. 3.1, Radio Control (RC) transmitter inputs could be read by the custom control systems running on the RPi. The transmitter used for flight control is shown in Fig. 3.4, with primary, secondary and tertiary flight controls highlighted. Table 3.2 contains some additional information on the control availability.

The range of control inputs allowed for selectable control modes in flight, even in offboard mode. For example, once control had been handed to the offboard control system, a secondary control switch could be used to toggle between 3 separate controller modes (e.g. enabling DOBC). Furthermore, use of the tertiary inputs allowed for in flight gain tuning, if the controller was designed appropriately. Overall, this system allowed for a large range of tests to be conducted in a single flight. Apart from saving time, this was essential for comparing the performance of various controllers in similar external conditions.

Simulink Simulation Interface

In Chapter 4, simulation environments are described. The numerical simulation environments are produced in Simulink. The additional verification simulation, X-Plane, is also

designed to work with Simulink. The result of this is that a controller can be designed and tested quickly in numerical simulation. From there, it can be transferred on to the X-Plane validation simulations and on to flight testing. No work is needed to redesign/recode the designed autopilot during this process. The only changes required are data sources and sinks, which is trivial for the most part. This allows for rapid and seamless transition between the environments, making for very efficient work flow.

3.2 Conclusions

The platform described has been the subject of a large portion of the work during this thesis. It was essential to develop a method which was suitable to low level control testing, while allowing for rapid development of controllers.

A system has been designed which requires minimal effort to move from initial numerical simulation, to verification and eventually flight testing. Control schemes can be developed and tested very quickly. Most issues are identified during numerical simulation and can be addressed easily. Once the controller has reached flight testing, it becomes difficult and time consuming to iterate on control design if testing produces issues.

The developed system is a key enabler in a number of the developments in this thesis. Without flight testing, the true importance of many benefits herein are lost and additionally some would never have been identified.

Chapter 4

Modelling and System Identification of a Small Fixed Wing UAV

Figure 4.1: The Skywalker X8 fixed wing UAV.

4.1 Platform Introduction

The majority of the work in this thesis is conducted using the Skywalker X8 (X8) shown in Fig. 4.1. This aircraft is representative of small fixed wing UAVs, which are booming in research and commercial applications. Although the majority of work is conducted on a single platform, the techniques and methods are equally valid and applicable for any small UAV. Furthermore, some of the developments herein (particularly those associated with actuator dynamics) would have more noticeable benefits for larger aircraft with slower dynamics and actuators. This will be discussed in the appropriate sections of the work.

Unlike a conventional aircraft configuration, the X8 is a flying wing which has no tailplane. Conventionally, an aircraft has 3 aerodynamic control surfaces: ailerons for roll, elevator for pitch and a rudder for yaw. The X8 is equipped only with elevons on the main wing; this means that both roll and pitch control is provided by deflection of these surfaces. The X8 has no direct yaw control although passive stabilisation is given by the winglets. However it is worth noting that the aircraft is still suitably modelled by the general aircraft dynamics models usually used in flight dynamics work. The aircraft has no landing gear and is generally hand launched, although catapult systems exist for heavier configurations. Landing is performed by sliding the aircraft belly along the floor; this requires careful and precise piloting to ensure the aircraft is not damaged.

The wingspan of the aircraft is 2.12m, and is generally operated at a weight of around 3kg, depending on sensors being used. Elevon actuation is provided by a pair of electronic servo actuators. The servos are connected to the control surface through a rigid pinion bar. These electronic servo motors offer very rapid deflection rates compared to hydraulic systems typically used on larger aircraft, which suggests they would offer faster and better flight control. Thrust is provided by a 3 phase brushless motor rated at 780 watts driving a 12 inch propeller. This powerful propulsion system allows the aircraft to take off rapidly and overcome non-ideal hand launches. A sustained climb of 60° is easily possible.

4.2 Aircraft Dynamic Modelling

To accurately model the aircraft dynamics, a range of issues must be considered. Generally, the motion of a body through space is governed by Newton's second law of motion, which states

$$F = ma,$$

better known as "*force is equal to mass times acceleration*". However, for an aircraft, the forces which govern translation result from the motion of the aircraft through the air. Therefore, we must establish reference frames which allow for the calculation of such forces correctly. Further, the inclusion of wind into the model makes relation of the motion relative to the world even more complicated.

To address this task, a host of required reference frames are defined along with the operations to transfer between them. Following this, the kinematic and dynamic motion of the aircraft is quantified, which must consider the interactions brought about by a model which allows for not only translation, but also rotation. From this, relating forces generated relative to the aircraft to the motion relative to the world is considered.

4.2.1 Coordinate System Definitions

To describe the motion of a UAV, several coordinate systems will be needed.

Inertial Frame - Γ^i
The inertial, also referred to as the world frame, is Earth fixed with an arbitrarily defined origin. This frame is indicated in Fig. 4.2 by x^i, y^i and z^i, which are directed to face North, East and down to the Earth centre. respectively. This is referred to as a North East Down (NED) coordinate system. The NED system is chosen as it follows the convention used in the majority of aeronautical research and textbooks. It is generally assumed that such a coordinate frame is based on the assumption of a flat non-rotating earth. This is assumed in this work, and is a valid assumption for UAV dynamics.

Vehicle Frame - Γ^v
The vehicle frame origin is defined as the centre of gravity for the aircraft; however, the rotation is such that Γ^v axes align with the inertial frame axes Γ^i. This frame is used to describe translational motion.

Body Frame - Γ^b
The body frame also has its origin at the vehicle centre of gravity, thus coinciding with the origin of Γ^v. The axes of Γ^b are described by x^b,y^b and z^b, where x^b is defined to point out of the aircraft nose, y^b points along the starboard wing and z^b points out of the aircraft belly. However, Γ^b differs from Γ^v in that it also describes the rotation of the

aircraft body. In Fig. 4.2, the two frames are shown with the aircraft having undergone a $\psi_1 = 90°$ rotation about the z^b axis.

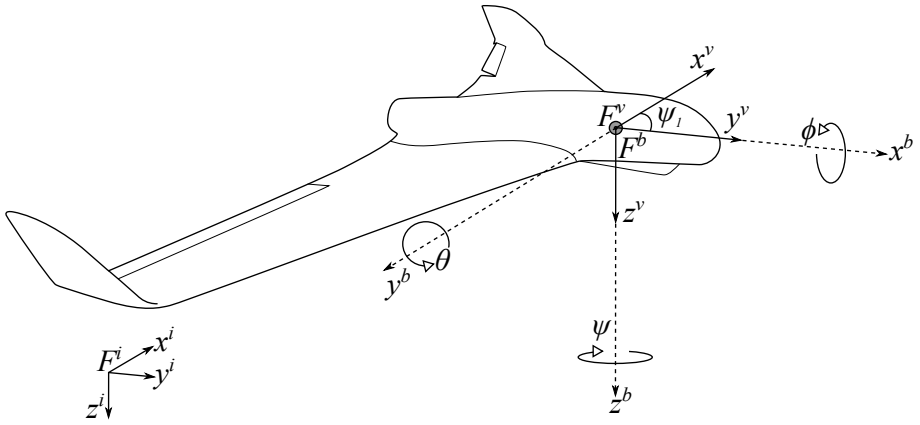

Figure 4.2: The three main reference frames used in derivation of aircraft dynamics, imposed on the Skywalker X8.

The angle ψ is part of a more general system of describing aircraft orientation, known as the Euler angles. The three angles are roll, pitch and yaw which are denoted as ϕ, θ and ψ respectively. These are indicated in Fig. 4.2. The Euler angles are commonly used in aircraft dynamic literature [99], as they offer an intuitive and clear description of the aircraft attitude. The body frame orientation is defined by a series of rotations to transform from either $\mathcal{F}^i$ or $\mathcal{F}^v$. In the case of rotation, as $\mathcal{F}^v$ and $\mathcal{F}^i$ are aligned in orientation they are equivalent in the transformation. The order of rotations is significant in this operation; commonly in flight dynamic ZYX, or yaw-pitch-roll, is used as the rotation ordering. Using this system we can transform from the inertial to body frame angles. First by rotating about z by ψ. The result is an intermediate rotation frame. In this new intermediate frame, now rotate about y by θ, which gives the second intermediate rotation frame. Finally, from the second intermediate frame, rotate about x by ϕ, which completes the transformation. This can be expressed compactly by a rotation matrix $\boldsymbol{R}_i^b$, where

$$\begin{aligned}\boldsymbol{R}_i^b &= \begin{bmatrix}1 & 0 & 0\\ 0 & \cos\phi & \sin\phi\\ 0 & -\sin\phi & \cos\phi\end{bmatrix}\begin{bmatrix}\cos\theta & 0 & -\sin\theta\\ 0 & 1 & 0\\ \sin\theta & 0 & \cos\theta\end{bmatrix}\begin{bmatrix}\cos\psi & \sin\psi & 0\\ -\sin\psi & \cos\psi & 0\\ 0 & 0 & 1\end{bmatrix},\\ &= \begin{bmatrix}\cos\theta\cos\psi & \cos\theta\sin\psi & -\sin\theta\\ \sin\phi\sin\theta\cos\psi - \cos\phi\sin\psi & \sin\psi\sin\theta\sin\psi + \cos\phi\cos\psi & \sin\phi\cos\theta\\ \cos\phi\sin\theta\cos\psi + \sin\phi\sin\psi & \cos\phi\sin\theta\sin\psi - \sin\phi\cos\psi & \cos\phi\cos\theta\end{bmatrix}.\end{aligned}$$

$\boldsymbol{R}_i^b$ is often referred to as the Direction Cosine Matrix (DCM). This represents a very important and often used coordinate transformation in aircraft dynamics. Positive angles are defined by the right hand rule; more intuitively, all angles of rotation would be positive in a coordinated climbing turn to the right, from a North facing orientation.

Wind Frame - $\mathcal{F}^w$

The majority of the work surrounding aerodynamics is conducted in the wind frame. The x^w axis of the wind frame is aligned with the airspeed vector, $\boldsymbol{V}_a$. The relationship is shown in Fig. 4.3. The transformation is achieved by first rotating about the y^b axis by α, then about the z^b axis by β. This is defined as a rotation matrix $\boldsymbol{R}_b^w$,

$$\boldsymbol{R}_b^w = \begin{bmatrix} \cos\alpha\cos\beta & \sin\beta & \sin\alpha\cos\beta \\ -cos\alpha\sin\beta & \cos\beta & -\sin\alpha\sin\beta \\ -\sin\alpha & 0 & \cos\alpha \end{bmatrix}$$

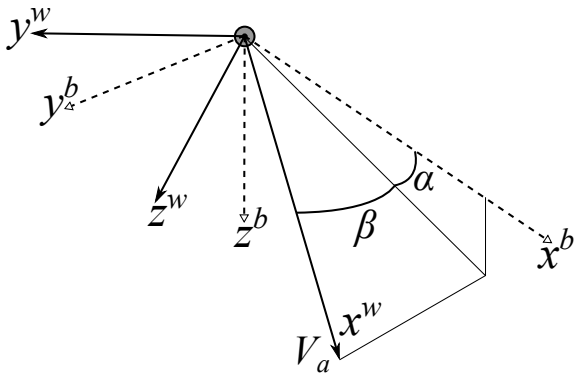

Figure 4.3: The relationship between body and wind frames described by the angles of attack and sideslip.

4.2.2 Relating Air, Wind and Ground Speed

Generally, the motion of a body is modelled in the inertial frame. For aircraft, however, the forces and moments which govern the inertial motion are most readily expressed relative to the motion of the aircraft in the surrounding air. This requires careful consideration in the modelling process. Consider a seagull which is able to hover motionless relative to a beach on a windy day; this is only possible as the velocity of the wind relative to the beach (inertial frame) is high, allowing the seagull to generate the required lift to resist gravity with no inertial motion. This must be explicitly accounted for in calculations of aircraft dynamics. This effect is substantially more influential on small UAVs than larger aircraft. To understand why, consider the formulation of the airspeed vector

$$\boldsymbol{V}_a = \boldsymbol{V}_g - \boldsymbol{V}_w, \tag{4.1}$$

where $\boldsymbol{V}_a$ is the velocity of the UAV relative to the air, $\boldsymbol{V}_g$ is the velocity of the UAV relative to the ground and $\boldsymbol{V}_w$ is the velocity of the wind relative to the ground. A small aircraft will generally have an airspeed vector which is much smaller in magnitude than that of a larger aircraft. As described by (4.1), as $\boldsymbol{V}_a \to 0$, the effect of $\boldsymbol{V}_w$ on the motion of the aircraft over the earth, $\boldsymbol{V}_g$, becomes increasingly more significant; the magnitude of the wind speed is independent of the aircraft flying through it. If this work were considering the motion of a hypersonic vehicle in the atmosphere, it would not be an unreasonable assumption to disregard the $\boldsymbol{V}_w$ term in (4.1) as $\boldsymbol{V}_g >> \boldsymbol{V}_w$, therefore $V_a \approx V_g$.

First, we express the aircraft velocity relative to the ground as

$$\boldsymbol{V}_i^b = \begin{bmatrix} u_r \\ v_r \\ w_r, \end{bmatrix}$$

where the velocities are expressed in the body frame. If we let w_n, w_e and w_d be the wind velocity components in the x_i, y_i and z_i (or north,east and down) directions, the wind components in the body frame would then be given by

$$\boldsymbol{V}_w^b = \begin{bmatrix} u_w \\ v_w \\ w_w \end{bmatrix} = \boldsymbol{R}_i^b \begin{bmatrix} w_n \\ w_e \\ w_d \end{bmatrix}.$$

If we also define V_a as the total airspeed of the aircraft, then V_a can be expressed in the wind frame as

$$\boldsymbol{V}_a^w = \begin{bmatrix} V_a \\ 0 \\ 0 \end{bmatrix}.$$

Further, defining u, v and w as the body frame components of the airspeed vector we can write

$$\boldsymbol{V}_a^b = \begin{bmatrix} u \\ v \\ w \end{bmatrix} = \begin{bmatrix} u_r - u_w \\ v_r - v_w \\ w_r - w_w \end{bmatrix}. \tag{4.2}$$

In the later developed simulations, u, v and w are key quantities used to calculate the dynamics of the aircraft, as it is the airspeed components which define the forces and moments which govern the dynamics of the aircraft. Typically, airspeed is the measured quantity supplied by aircraft; we can express the body components as

$$\begin{aligned} \boldsymbol{V}_a^b = \begin{bmatrix} u \\ v \\ w \end{bmatrix} &= \boldsymbol{R}_w^b \begin{bmatrix} V_a \\ 0 \\ 0 \end{bmatrix} \\ &= \begin{bmatrix} \cos\alpha\cos\beta & -cos\alpha\sin\beta & -\sin\alpha \\ \sin\beta & \cos\beta & 0 \\ \sin\alpha\cos\beta & -\sin\alpha\sin\beta & \cos\alpha \end{bmatrix} \begin{bmatrix} V_a \\ 0 \\ 0 \end{bmatrix}, \end{aligned}$$

more compactly, this equates to

$$\begin{bmatrix} u \\ v \\ w \end{bmatrix} = V_a \begin{bmatrix} \cos\alpha\cos\beta \\ \sin\beta \\ \sin\alpha\cos\beta \end{bmatrix}. \tag{4.3}$$

Commonly, the calculations for aerodynamic forces and moments are functions of airspeed, α and β. We can rearrange (4.3) to

$$\begin{aligned} V_a &= \sqrt{u^2 + v^2 + w^2} \\ \alpha &= \tan^{-1}\left(\frac{w}{u}\right) \\ \beta &= \sin^{-1}\left(\frac{v}{\sqrt{u^2 + v^2 + w^2}}\right) \end{aligned} \tag{4.4}$$

4.2.3 Dynamics and Kinematics

First, considering the position of the aircraft in the inertial frame, we can define

$$\begin{bmatrix} \dot{p}_x \\ \dot{p}_y \\ \dot{p}_z \end{bmatrix} = \boldsymbol{R}_b^v \begin{bmatrix} u_r \\ v_r \\ w_r \end{bmatrix} = \left(\boldsymbol{R}_i^b\right)^T \begin{bmatrix} u_r \\ v_r \\ w_r \end{bmatrix}, \tag{4.5}$$

where p_x, p_y and p_z are the positions in $\mathcal{I}^i$ along the respective axes. $\boldsymbol{R}_b^v$ would be the rotation matrix to move from the body frame $\mathcal{I}^b$ to the vehicle frame $\mathcal{I}^v$; as $\mathcal{I}^b$ and F_i are aligned, we can use the transpose of the DCM to relate the body axis velocities to the inertial frame. To aid intuitive discussion later, we define the altitude h as

$$h = -p_z,$$

a common approach in the literature.

Due to the nature of Euler angle representations, with each being defined based on a different set of previous rotations, subsequent definition of the angular rates is not as simple as taking the derivative of the angle. By taking this into consideration, we can define

$$\begin{bmatrix} p \\ q \\ r \end{bmatrix} = \begin{bmatrix} \dot{\phi} \\ 0 \\ 0 \end{bmatrix} + \begin{bmatrix} 1 & 0 & 0 \\ 0 & \cos\phi & \sin\phi \\ 0 & -\sin\phi & \cos\phi \end{bmatrix} \begin{bmatrix} 0 \\ \dot{\theta} \\ 0 \end{bmatrix} + \begin{bmatrix} 1 & 0 & 0 \\ 0 & \cos\phi & \sin\phi \\ 0 & -\sin\phi & \cos\phi \end{bmatrix} \begin{bmatrix} \cos\theta & 0 & -\sin\theta \\ 0 & 1 & 0 \\ \sin\theta & 0 & \cos\theta \end{bmatrix} \begin{bmatrix} 0 \\ 0 \\ \dot{\psi} \end{bmatrix},$$

which compacts to

$$\boldsymbol{\omega}_b = \begin{bmatrix} p \\ q \\ r \end{bmatrix} = \begin{bmatrix} 1 & 0 & -\sin\theta \\ 0 & \cos\phi & \sin\phi\cos\theta \\ 0 & -\sin\phi & \cos\phi\cos\theta \end{bmatrix} \begin{bmatrix} \dot{\phi} \\ \dot{\theta} \\ \dot{\psi} \end{bmatrix}, \tag{4.6}$$

where p,q and r are the roll, pitch and yaw rates. From inspection it is quite clear that when the angles are small, (4.6) can be approximated by

$$\begin{aligned} p &= \dot{\phi}, \\ q &= \dot{\theta}, \\ r &= \dot{\psi}. \end{aligned}$$

For clearer use in later definition of the full model, it is beneficial to rewrite (4.6) to describe the rate of change of the Euler angles

$$\begin{bmatrix} \dot{\phi} \\ \dot{\theta} \\ \dot{\psi} \end{bmatrix} = \begin{bmatrix} 1 & \sin\phi\tan\theta & cos\phi\tan\theta \\ 0 & \cos\phi & -\sin\phi \\ 0 & \frac{\sin\phi}{\cos\theta} & \frac{\cos\phi}{\cos\theta} \end{bmatrix} \begin{bmatrix} p \\ q \\ r \end{bmatrix} \tag{4.7}$$

4.2.4 Rigid Body Model

Application of Newton's second law requires that the motion is calculated relative to a fixed frame of reference. Using the ground may seem like the obvious choice, as it has no capacity to move in our definition. However, the forces and moments are generated according to the aircraft body motion, as well as containing the sensors and control surfaces which interact with these forces. For these reasons, the derivation is carried out entirely in the aircraft body frame. We therefore use $\boldsymbol{V}_i^b$ for velocities, and define $\boldsymbol{F} = \begin{bmatrix} f_x & f_y & f_z \end{bmatrix}^T$ as a vector containing the forces acting on the principle axes of $\mathcal{I}^b$.

Translation

First, to describe the translation of the aircraft, we write Newton's second law as

$$m\frac{d\boldsymbol{V}_i^b}{dt_i} = \boldsymbol{F}, \tag{4.8}$$

where m is the (assumed) constant mass of the aircraft. It is important to note that the derivative $\frac{d}{dt_i}$ is based in the inertial frame, as required by the second law. However, it

would be more useful to also express this in the aircraft body frame. To achieve this, angular velocity must also be taken into account

$$\frac{d\boldsymbol{V}_i^b}{dt_i} = \frac{d\boldsymbol{V}_i^b}{dt} + \boldsymbol{\omega}_b \times \boldsymbol{V}_i^b, \tag{4.9}$$

Substitution of (4.9) into (4.8) yields

$$m\left(\frac{d\boldsymbol{V}_i^b}{dt} + \boldsymbol{\omega}_b \times \boldsymbol{V}_i^b\right) = \boldsymbol{F}. \tag{4.10}$$

Here, $\frac{d\boldsymbol{V}_i^b}{dt}$ is the derivative of inertial velocity in the body frame, as observed from the moving body. As it was earlier defined that u, v and w are the components of $\boldsymbol{V}_i$ in the body frame. This leads to

$$\frac{d\boldsymbol{V}_i^b}{dt} = \begin{bmatrix} \dot{u} \\ \dot{v} \\ \dot{w} \end{bmatrix}, \tag{4.11}$$

combining (4.11) with (4.10) results in

$$\begin{bmatrix} \dot{u} \\ \dot{v} \\ \dot{w} \end{bmatrix} = \begin{bmatrix} rv - qw \\ pw - ru \\ qu - pv \end{bmatrix} + \frac{1}{m}\begin{bmatrix} f_x \\ f_y \\ f_z \end{bmatrix}. \tag{4.12}$$

With (4.12), the acceleration of the aircraft has been described in $\mathcal{F}^b$ by forces acting in the same axes. This allows for intuitive description of the motion based on forces calculated in a convenient frame.

Rotation

As with translation, we aim to derive the rotational accelerations in $\mathcal{F}^b$ based on moments in the same frame. First, the rotational acceleration is given by

$$I\ddot{\theta} = M$$

where M is the sum of moments acting on a body with moment of inertia I and rotational acceleration $\ddot{\theta}$, where θ is used here to represent a generalised angle.

Before developing the method, it is useful to define an auxiliary variable to simplify the appearance of the subsequent derivations, so let

$$\boldsymbol{j} = \boldsymbol{I}_b\boldsymbol{\omega}_b,$$

where

$$\boldsymbol{I}_b = \begin{bmatrix} I_{xx} & I_{xy} & I_{xz} \\ I_{yx} & I_{yy} & I_{yz} \\ I_{zx} & I_{zy} & I_{zz} \end{bmatrix},$$

is the inertial tensor matrix. Generally, aircraft are symmetrical about the x_bz_b plane, so $I_{xy} = I_{yz} = I_{yx} = I_{zy} = 0$. Further, for the Skywalker X8 the aircraft is almost entirely symmetrical about the x_by_b plane due to the mostly symmetrical fuselage, lack of landing gear and small vertical stabilisers. Therefore we also assume that $I_{xz} = I_{zx} = 0$.

To begin, we once again define the derivative of the motions

$$\frac{d\boldsymbol{j}}{dt_i} = \boldsymbol{M}, \tag{4.13}$$

where $\boldsymbol{M} = \begin{bmatrix} L & M & N \end{bmatrix}^T$ is the vector containing the moments applied on each axis. Transforming (4.13) to the body frame gives

$$\frac{d\boldsymbol{j}}{dt_i} = \frac{d\boldsymbol{j}}{dt_b} + \boldsymbol{\omega}_b \times \boldsymbol{j} = \boldsymbol{M}. \tag{4.14}$$

The moments of inertia for the aircraft are assumed constant, as was assumed with the overall mass. This is important as, to expand the derivative term, we must employ the chain rule

$$\frac{d\boldsymbol{j}}{dt_b} = \frac{d\boldsymbol{I}_b}{dt_b}\boldsymbol{\omega_b} + \frac{d\boldsymbol{\omega}_b}{dt_b}\boldsymbol{I}_b,$$

where $\frac{d\boldsymbol{I}_b}{dt_b} = 0$. Taking this into (4.14) gives

$$\boldsymbol{I}_b\frac{d\boldsymbol{\omega_b}}{dt_b} + \boldsymbol{\omega}_b \times (\boldsymbol{I}_b\boldsymbol{\omega}_b) = \boldsymbol{M}.$$

Now we can rearrange the equation as

$$\frac{d\boldsymbol{\omega_b}}{dt_b} = \boldsymbol{I}_b^{-1}\left[-\boldsymbol{\omega}_b \times (\boldsymbol{I}_b\boldsymbol{\omega}_b) + \boldsymbol{M}\right].$$

Finally, we can write

$$\begin{aligned}
\begin{bmatrix} \dot{p} \\ \dot{q} \\ \dot{r} \end{bmatrix} &= \begin{bmatrix} \frac{1}{I_{xx}} & 0 & 0 \\ 0 & \frac{1}{I_{yy}} & 0 \\ 0 & 0 & \frac{1}{I_{zz}} \end{bmatrix} \left(\begin{bmatrix} 0 & r & -q \\ -r & 0 & p \\ q & -p & 0 \end{bmatrix} \begin{bmatrix} I_{xx} & 0 & 0 \\ 0 & I_{yy} & 0 \\ 0 & 0 & I_{zz} \end{bmatrix} \begin{bmatrix} p \\ q \\ r \end{bmatrix} + \begin{bmatrix} L \\ M \\ N \end{bmatrix} \right) \\
&= \begin{bmatrix} \frac{I_{yy}-I_{zz}}{I_{xx}}rq + \frac{L}{I_{xx}} \\ \frac{I_{zz}-I_{xx}}{I_{yy}}rp + \frac{M}{I_{yy}} \\ \frac{I_{xx}-I_{yy}}{I_{xx}}qp + \frac{L}{I_{zz}} \end{bmatrix}.
\end{aligned} \tag{4.15}$$

The Six Degrees of Freedom (6DOF) dynamics of the aircraft have been defined by (4.5), (4.7), (4.12) and (4.15). The definition is complete, and aligns with the general fixed wing UAV model [99], but relies on as yet undefined forces and moments. The contributions to these forces and moments will come from aerodynamics, gravity and the propulsion system.

4.2.5 Forces and Moments

The dynamics equations defined previously can be used to model almost any fixed wing aircraft, regardless of size or configuration. The difference is described by the forces and moments which govern the dynamic responses. Several sources must be considered,

$$\boldsymbol{F} = \boldsymbol{F}_a + \boldsymbol{F}_p + \boldsymbol{F}_g,$$
$$\boldsymbol{M} = \boldsymbol{M}_a + \boldsymbol{M}_p,$$

where the superscripts a, p and g represent the contributions from aerodynamic, propulsive and gravitational forces. In this section, all forces and moments are taken to act in $\mathcal{F}^b$, unless explicitly stated otherwise.

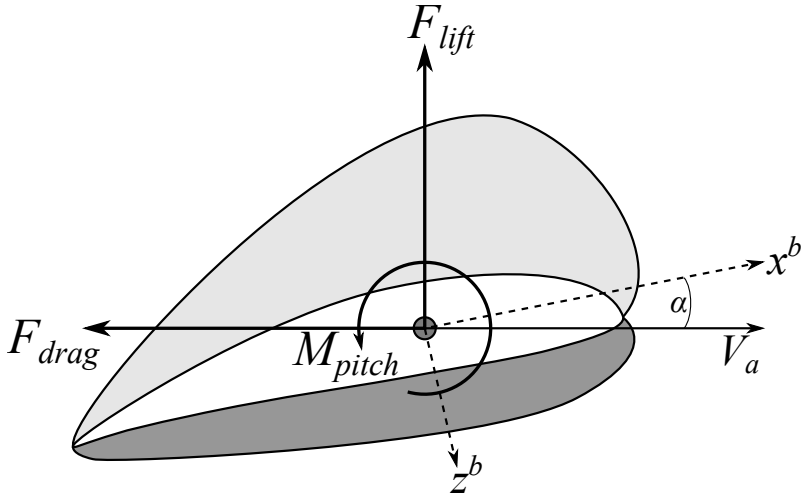

Figure 4.4: A typical pressure distribution over an aerofoil. High and low pressure is indicated by the dark and light areas, respectively.

Gravity

The effect of gravity only depends on the mass of the aircraft, and the gravitational constant. The force acts directly along the z^v axis, so must be transformed into $\mathcal{F}^b$ by (4.16).

$$\boldsymbol{F}_g = \boldsymbol{R}_v^b \begin{bmatrix} 0 \\ 0 \\ mg \end{bmatrix}. \tag{4.16}$$

Since gravity acts on the origin of $\mathcal{F}^b$, it produces no moment.

Aerodynamics

For conventional aircraft, the aerodynamic forces stem from the main wing, body, tailplane and potentially landing gear. The X8, as a flying wing without undercarriage, does not need to consider the tailplane or landing gear; the fuselage contributions can be also combined with the wing contributions. In Fig. 4.4, a typical wing section is shown along with the pressure distribution and associated forces and moments.

Forces produced by the wing result the sum of high and low pressure distributions which act on the lower and upper sections, respectively. As the Angle of Attack (AoA) of the wing changes, the pressure distribution also varies, altering the net forces on the wing. Studying the forces in terms of pressure distributions would be rather cumbersome. Instead, the net effect can be represented by 3 components: the lift force, F_{lift}, the drag force F_{drag} and the pitching moment M_{pitch}. These forces can be expressed as

$$\begin{aligned} F_{lift} &= \frac{1}{2}\rho V_a^2 S C_L, \\ F_{drag} &= \frac{1}{2}\rho V_a^2 S C_D, \\ M_{pitch} &= \frac{1}{2}\rho V_a^2 S C_M, \end{aligned} \tag{4.17}$$

where ρ is the air density, S is the plan form wing are and $C_{(\cdot)}$ represents the coefficient associated with the subscript. The coefficients are usually non-linear; an example lift-curve slope is given in Fig. 4.5. In the region of $-5^\circ \leq \alpha \leq 9^\circ$ for the curve shown, the slope is mostly linear. As the stall point of $\alpha \approx 15^\circ$ is approached, the slope reverses, with lift

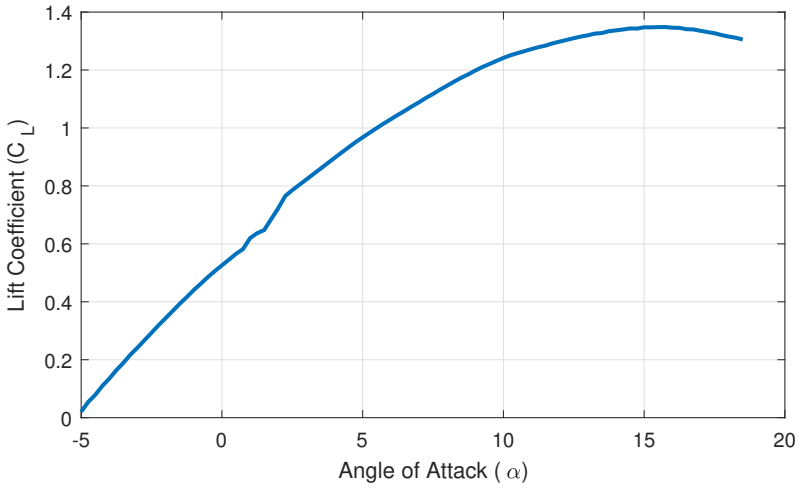

Figure 4.5: An example lift coefficient for the NACA 4415 aerofoil demonstrating how lift coefficient changes with angle of attack.

coefficient reducing. For the work in this thesis, it is assumed that the aircraft is always operating well below the stall point, and as such only the linear region is considered. A similar assumption is conducted for the remaining coefficients as well.

Doing so means that the considered flight envelope can be modelled accurately with a linear function; an example for C_L is given as

$$C_L = C_{L_0} + \frac{\partial C_L}{\partial \alpha}\alpha + \frac{\partial C_L}{\partial q}q + \frac{\partial C_L}{\partial \delta_e}\delta_e. \tag{4.18}$$

$$\tag{4.19}$$

Typically this is then non-dimensionalised to be a function of coefficients and flight variables. Only q requires adjustment to non-dimensionalise; using $\frac{\bar{c}}{2V_a}$, where $\bar{c}$ is the standard mean chord, is commonplace. The resulting functions for C_L, C_D and C_M are then given as

$$\begin{aligned} C_L &= C_{L_0} + C_{L_\alpha}\alpha + C_{L_q}\frac{\bar{c}}{2V_a}q + C_{L_{\delta_e}}\delta_e, \\ C_D &= C_{D_0} + C_{D_\alpha}\alpha + C_{D_q}\frac{\bar{c}}{2V_a}q + C_{D_{\delta_e}}\delta_e, \\ C_M &= C_{M_0} + C_{M_\alpha}\alpha + C_{M_q}\frac{\bar{c}}{2V_a}q + C_{M_{\delta_e}}\delta_e. \end{aligned} \tag{4.20}$$

These forces must be converted to the body frame to be compatible with the equations developed previously. This is done by applying a transformation,

$$\begin{bmatrix} F_x \\ F_z \end{bmatrix} = \begin{bmatrix} \cos\alpha & -\sin\alpha \\ \sin\alpha & \cos\alpha \end{bmatrix} \begin{bmatrix} -F_{drag} \\ -F_{lift} \end{bmatrix}. \tag{4.21}$$

The relationships in (4.17) and (4.21) fully describe the longitudinal motion of the aircraft, completing 3 of the 6 degrees of freedom. The remainder of the motion is contained in the lateral dynamics. These are described similarly to the longitudinal dynamics, give as

$$F_y = \frac{1}{2}\rho V_a^2 S C_y,$$
$$L = \frac{1}{2}\rho V_a^2 S C_l,$$
$$N = \frac{1}{2}\rho V_a^2 S C_n,$$

where F_y is the force along the z^b axis, L is the moment about x^b and N is the moment about z^b which are governed by their associated coefficients C_y, C_l and C_n. The components of these coefficients are given as

$$\begin{aligned} C_y &= C_{y_0} + C_{y_\beta}\beta + C_{y_p}\frac{b}{2V_a}p + C_{y_r}\frac{b}{2V_a}r + C_{y_{\delta_a}}\delta_a + C_{y_{\delta_r}}\delta_r, \\ C_l &= C_{l_0} + C_{l_\beta}\beta + C_{l_p}\frac{b}{2V_a}p + C_{l_r}\frac{b}{2V_a}r + C_{l_{\delta_a}}\delta_a + C_{l_{\delta_r}}\delta_r, \\ C_n &= C_{n_0} + C_{n_\beta}\beta + C_{n_p}\frac{b}{2V_a}p + C_{n_r}\frac{b}{2V_a}r + C_{n_{\delta_a}}\delta_a + C_{n_{\delta_r}}\delta_r. \end{aligned} \tag{4.22}$$

where δ_a and δ_r are the aileron and rudder deflection angles respectively. It is important to note that the lateral components are already aligned with $\mathcal{F}^b$ and as such require no transformation into the body axis to apply the dynamics equations of (4.12) and (4.15). This property makes formulation of these forces in $\mathcal{F}^b$ preferable.

It is possible to transform the relationships in (4.20) to the body frame. This is given as

$$\begin{aligned} C_z &= C_{z_0} + C_{z_\alpha}\alpha + C_{z_q}\frac{c}{2V_a}q + C_{z_{\delta_e}}\delta_e, \\ C_x &= C_{x_0} + C_{x_\alpha}\alpha + C_{x_q}\frac{c}{2V_a}q + C_{x_{\delta_e}}\delta_e, \\ C_m &= C_{m_0} + C_{m_\alpha}\alpha + C_{m_q}\frac{c}{2V_a}q + C_{m_{\delta_e}}\delta_e. \end{aligned} \tag{4.23}$$

As the pitching moment was already based in $\mathcal{F}^b$ it remains unchanged. The model of aerodynamic forces and moments on the aircraft is now fully described by (4.22) and (4.23), although it remains to define the coefficients themselves. The formulation of these coefficients determines the accuracy of the simulation model produced. A fully non-linear model results when, for all coefficients, variations in both α and β are considered. For example, it is possible to define

$$C_x = C_{x_0} + f(\alpha, \beta, p, q, r, \delta_a, \delta_e, \delta_r), \tag{4.24}$$

which would be necessary to fully define the behaviour of the aircraft. However, such a detailed formulation is not conducive to control design. The application of these formulae assume that the C_x and C_z coefficients are not affected by variations in β. While this results in a small loss in accuracy, the model becomes much simpler. This compromise is deemed reasonable as the magnitude of sideslip introduced by wind gusting is quite small, while lasting for short periods of time. This results in minimal effect on the aircraft dynamics for most operating conditions. These effects can then be considered as part of the *lumped disturbances*, which can be mitigated by DOBC.

Due to the assumptions made in this section, the resulting model will not be fully accurate. It will, however, provide a highly representative model of the aircraft in the considered flight envelope. Additionally, simulation results are verified with flight test data where sideslip effects will be present. Sufficient performance in flight testing will alleviate any concern on modelling accuracy.

Wind Gust Modelling

In some later work, control performance in the presence of stochastic wind gust disturbances are considered. The nature of wind gust disturbances has been studied and is well understood in literature. One method for modelling gusts as a statistical model is the von Karman turbulence spectrum [100]. As an overview, this model produces wind gusts by passing white noise through a time invariant filter given by the von Karman model. The major drawback of this system is that it does not result in a rational transfer function, which can limit its application. A rational approximation of this method is given by the Dryden model, which is widely known to produce acceptably accurate results [101]. The Dryden transfer functions are given by

$$
\begin{aligned}
G_u(s) &= \sigma_u \sqrt{\frac{2V_a}{W_u}} \frac{1}{s + \frac{V_a}{L_u}}, \\
G_v(s) &= \sigma_v \sqrt{\frac{3V_a}{W_v}} \frac{\left(s + \frac{V_a}{\sqrt{3}L_v}\right)}{\left(s + \frac{V_a}{L_u}\right)^2}, \\
G_w(s) &= \sigma_w \sqrt{\frac{3V_a}{W_w}} \frac{\left(s + \frac{V_a}{\sqrt{3}L_w}\right)}{\left(s + \frac{V_a}{L_w}\right)^2},
\end{aligned}
$$

where $W_{(\cdot)}$ and $\sigma_{(\cdot)}$ are the spatial wavelengths and turbulence intensities for the associated axes and V_a is the vehicle airspeed. This formulation implies that a constant airspeed is used. Further definitions of these parameters can be found in MIL-F-8785C, a US Military specification. More conveniently, parameters applicable to small UAVs are specified in [102]. Expanding the formulation of $\boldsymbol{V}_w$ from (4.1) gives

$$
\boldsymbol{V}_w = \boldsymbol{V}_{w_c} + \boldsymbol{V}_{w_g}, \tag{4.25}
$$

where $\boldsymbol{V}_{w_c}$ is a constant wind vector and $\boldsymbol{V}_{w_g}$ is a gusting component. It makes most sense to define $\boldsymbol{V}_{w_c}$ in $\mathcal{I}^i$, as global wind acts in this frame. The gusting component is conventionally formulated in $\mathcal{I}^b$. To relate the global and gusting components we first define

$$
\boldsymbol{N}_w^3 = \begin{bmatrix} N_w^1 \\ N_w^2 \\ N_w^3 \end{bmatrix}, \tag{4.26}
$$

where $\boldsymbol{N}_w^3$ is vector of three separate white noise sources, N_w^{1-3}. Now, let

$$
\boldsymbol{V}_{w_g} = \begin{bmatrix} G_u \\ G_v \\ G_w \end{bmatrix} \boldsymbol{N}_w, \tag{4.27}
$$

which then allows the definition of

$$
\boldsymbol{V}_w^b = \boldsymbol{R}_i^b \begin{bmatrix} w_n \\ w_e \\ w_d \end{bmatrix} + \boldsymbol{V}_{w_g}, \tag{4.28}
$$

where $w_{(\cdot)}$ is the wind in the North, East and Down (global x, y and z) directions. This formulation allows the effects of random gusts to enter the aircraft dynamics as they would in the physical system: by affecting the dynamics through the wind angles given by (4.2) and (4.4).

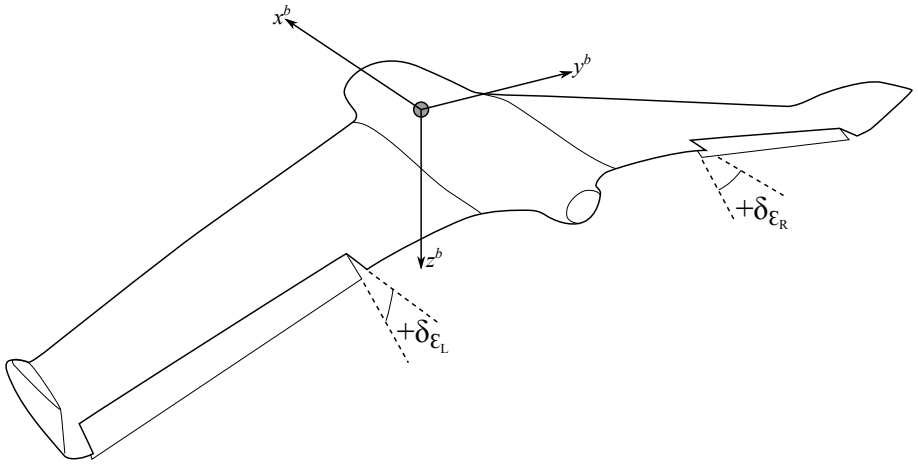

Figure 4.6: The directionality of the Skywalker X8 Elevons

Control Surfaces

The force and moment equations for dynamics are formulated in the traditional control inputs of aileron, elevator and rudder so that they can be applied to a larger range of aircraft configurations. For the Skywalker X8, some additional considerations are needed to map the elevons to the standard control functions. First, the rudder is entirely disregarded for the X8, leaving only the aileron and elevators to be considered. The mapping is simple, given as

$$\begin{bmatrix} \delta_e \\ \delta_a \end{bmatrix} = \begin{bmatrix} 1 & 1 \\ -1 & 1 \end{bmatrix} \begin{bmatrix} \delta_{\epsilon_L} \\ \delta_{\epsilon_R} \end{bmatrix}, \tag{4.29}$$

where δ_ϵ denotes the left and right elevon deflection with directionality defined in Fig. 4.6. This relationship assumes that the effect of the control surface is linear with deflection, as well as assuming superposition applies. The majority of the work in this thesis will be conducted in small regions around a trim condition - the same assumption which has enabled the use of a linear lift coefficient. The same assumption applies in the control surface model, enabling the use of the mixing relationship given in (4.29).

An additional control surface, or more appropriately actuator, is the aircraft motor. This is discussed in detail in Section 4.4.

4.2.6 Obtaining Force and Moment Coefficients

The final element to be completed in the aircraft dynamic modelling is the acquisition of the coefficients. A range of methods are available, from Computational Fluid Dynamics (CFD) to Parametric Identification (ParID) from flight testing. Another viable source of data is Bihrle SimGen; a software package intended for producing stability derivatives for flight simulation environments. Each of these methods have their benefits and drawbacks, a summary of which is given in Table 4.1.

To decide on the appropriate source, the intended use of the simulation must be considered for context. The nonlinear simulations will be used to ensure that any designed controllers which work in a linear environment are generally stable in a non-linear environment as well. From there, performance will be demonstrated through either flight testing or industry standard simulation software. The main requirement of the nonlinear simulation is therefore to capture nonlinear dynamics, and to be easy to use. The extensive work needed to conduct CFD or ParID analysis to obtain the model would not be an efficient use of time. SimGen offers a better solution in that it is fast and relatively

Table 4.1: An overview of the various considerations in sources for simulation coefficients

	CFD	**Parametric ID**	**SimGen**
Acquiring Data	Difficult. Requires additional development of CAD model and definition of CFD simulation.	Somewhat difficult. Relies on flight testing data which needs good weather and proper aircraft operation. May need multiple data sources	Quite simple: the software requires some learning but is straight forward as input is geometric.
Processing Data	Quite difficult. Output requires processing to transfer to stability derivatives	Middling: relevant data must be extracted from entire flight tests, with conditioning then applied. May also need to synchronise multiple sources	Minimal: data is intended for use in flight simulation environments and is supplied in stability derivative form.
Time to Implement	Very long: time to produce CAD model, define CFD environment, run simulations and analyse data	Quite long: flight tests must be planned and executed, dependant on weather, data must be processed	Short, requiring only 3 view photographs and basic information on the aerodynamic setup of the aircraft. Output in required form
Accuracy	Very good - assuming model and simulation were done accurately	Variable; highly dependant on sensor quality, flight test regime and data processing	Good in linear regions, non-linear region must be estimated

simple, while resulting in a sufficiently accurate nonlinear model. SimGen was therefore the clear choice. A brief overview of the SimGen process is given in the following section.

SimGen Methodology

The first stage of SimGen application is entry of the geometric model into the software. This is demonstrated for an Embraer 195 in Fig. 4.7. Once the layout of the aircraft has been specified, SimGen converts the model to a suitable format to be used in the model prediction software. For the non-US version used, this is conducted using HASC2002 - an open source software package jointly developed by a consortium of US aerospace and research institutions.

The open source version of HASC2002 combines a vortex lattice approach with semi-empirical strake/wing vortex analysis for its aerodynamic modelling. An additional non-linear module exists but is not available as open access.

Geometry for the X8 was obtained with three view photographs and measurements of the aircraft. Whilst data on the exact aerofoil used was not available, by matching the cross section at the root and tip to predefined aerofoils in the UIUC Airfoil Coordinate Database, a good approximation was reached.

All that remains is to specify the range of AoA and Angle of Sideslip (AoS) to be studied. A range of $-6^\circ \leq \alpha \leq 12^\circ$ and $|\beta| \leq 10^\circ$ was selected as it covered the region of the flight envelope considered in this thesis. SimGen then outputs the full range of stability derivatives in the body frame; an example of this is given in Table 4.2 for C_z. Data for C_z and the remaining coefficients are stored in data tables in comma separated value format, which enables direct input into MATLAB.

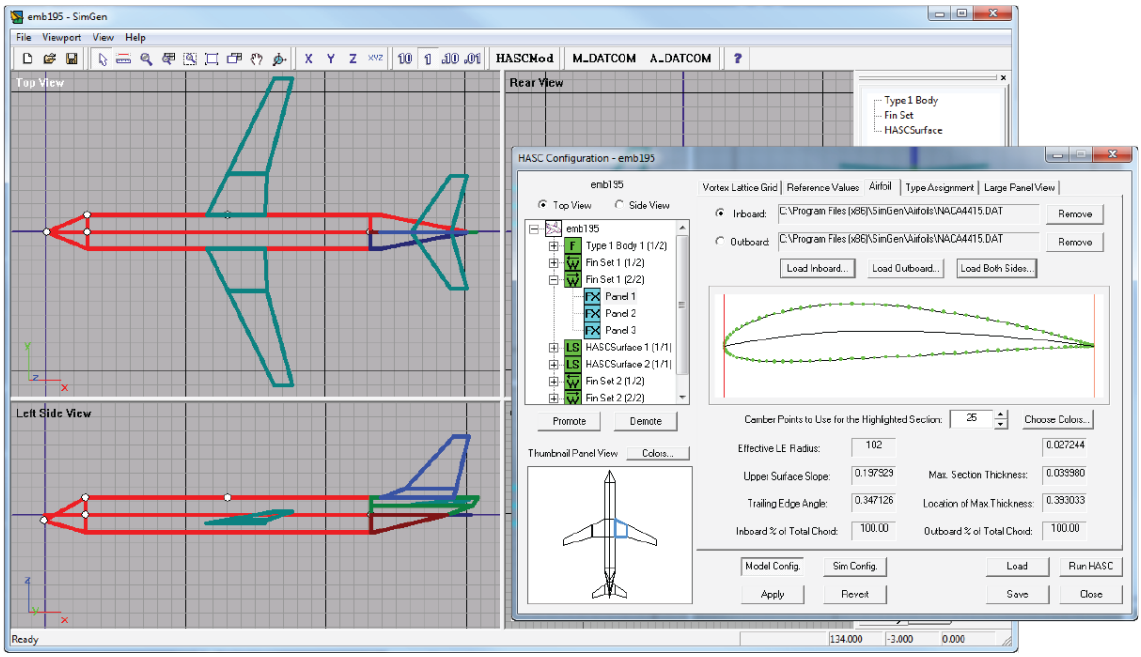

Figure 4.7: An example screen of SimGen model configuration[1]

Table 4.2: The values of C_z for the Skywalker X8 with α and β, resulting from SimGen analysis.

		β (degrees)						
		-10	**-7**	**-4**	**0**	**4**	**7**	**10**
α (degrees)	**-6**	-0.484	-0.496	-0.504	-0.507	-0.504	-0.498	-0.489
	-4	-0.281	-0.290	-0.295	-0.297	-0.295	-0.291	-0.286
	-2	-0.076	-0.082	-0.085	-0.086	-0.085	-0.083	-0.081
	0	0.129	0.127	0.126	0.126	0.126	0.126	0.124
	2	0.333	0.335	0.337	0.338	0.336	0.334	0.329
	4	0.537	0.542	0.546	0.548	0.545	0.540	0.532
	6	0.738	0.747	0.753	0.756	0.752	0.744	0.732
	8	0.936	0.948	0.956	0.961	0.955	0.945	0.930
	10	1.130	1.146	1.155	1.162	1.154	1.141	1.123
	12	1.320	1.338	1.349	1.358	1.347	1.333	1.311

4.2.7 Non-Linear Flight Simulation Environment

Shown in Fig. 4.8 is the data flow for the non-linear flight simulation environment, which has been implemented in Simulink. MATLAB/Simulink was chosen as it is widely used in the industry and is a very well suited environment for this exact purpose. The environment is highly flexible, allowing simulations to be run in either real time, or significantly above real time. This means running large batches of tests (e.g. Monte Carlo runs) can be conducted relatively quickly.

Simulink was set to calculate at a fixed 1ms time step, providing sufficient resolution to capture the behaviour of the X8 with high fidelity. Although variable time stepping would have provided faster operation of the simulator environment, it would be very limiting in the application of control schemes in a way which is consistent with the discrete nature of their true operation. This time step was also chosen as it scales well with common autopilot operating rates (25, 50 or 100Hz). This allows for the simulation of control schemes at the rate at which they would operate on the physical platform. This can then be used to investigate the suitability of a chosen discretisation time step for a controller.

[1]Reproduced from SimGen Brochure - www.bihrle.com/brochures/Bihrle_SimGen.pdf

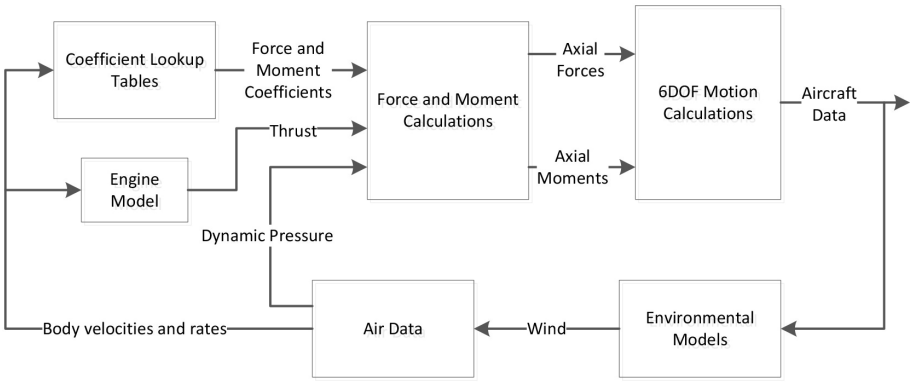

Figure 4.8: The overview of calculations and data flow within the non-linear flight simulation environment.

FlightGear Visualisation

For better intuitive understanding and operation of the flight simulation environment, FlightGear was used as a data visualisation platform. FlightGear is a free, open source flight simulation platform with good Simulink integration. FlightGear is by default configured to use its own internal flight simulation models, which is then displayed graphically in 3D. Through some basic modifications, it was possible to reconfigure FlightGear to take all aircraft orientation and location information from an external source - in this case the designed Simulink environment. This provided a good 3D visualisation of the aircraft motion, which was much simpler to interpret than the purely numerical output of Simulink.

4.2.8 Linear Flight Simulation Environment

Linear flight simulation in this work is conducted using Linear Time-Invariant (LTI) state space models. A general formulation is given in Section 4.3.1, while specific models are defined in the appropriate sections.

4.3 System Identification

The non-linear simulation model developed in Section 4.2 captures some of the finer details of the X8's flying characteristics, but is not a verified simulation environment. For this reason, it could only be used to test linear controllers in a non-linear environment. Further, the complex non-linear nature means that this model is not well suited to control design - it has too many features to consider. A widely used model in control design is the linear state space model. This model has a convenient and widely used mathematical form and is able to capture behaviour well around a linearisation point. As the work herein generally considers a particular flight condition, a state space model would provide sufficient detail for control design around these operation points.

In this section the general form of the state space model and its key features are discussed. Then, the method by which the appropriate parameters for the model were obtained is also outlined.

4.3.1 State Space Model Definition

State space modelling is the representation of n dimensional system dynamics as first order differential equations, with state variable of an n dimension vector. In this work, only the

LTI form of the state space model is used. This is generally done with a system in the form

$$\dot{\boldsymbol{x}}(t) = \boldsymbol{A}\boldsymbol{x}(t) + \boldsymbol{B}\boldsymbol{u}(t),$$
$$\boldsymbol{y} = \boldsymbol{C}\boldsymbol{x}(t) + \boldsymbol{D}\boldsymbol{u}(t),$$

where $\boldsymbol{x} \in \mathbb{R}^n$ is the state vector, $\boldsymbol{u} \in \mathbb{R}^m$ is the system input vector, $\boldsymbol{y} \in \mathbb{R}^p$ is the system output vector, $\boldsymbol{A} \in \mathbb{R}^{n\times n}$ is the system dynamics matrix, $\boldsymbol{B} \in \mathbb{R}^{n\times m}$ is the input matrix, $\boldsymbol{C} \in \mathbb{R}^{p\times n}$ is the output matrix and $\boldsymbol{D} \in \mathbb{R}^{p\times m}$ is the feedthrough matrix. In most work, $\boldsymbol{D}$ is ignored; that is true for all work herein unless otherwise explicitly stated. For simplicity, explicit notation of time varying parameters is dropped. Unless stated otherwise, only $\boldsymbol{x}$,$\boldsymbol{y}$ and $\boldsymbol{u}$ will be time varying.

One significant additional consideration for this work is how external disturbances are included in the system. If we define $\boldsymbol{d}$ as a vector of external disturbances, then the state space model with disturbances is given by

$$\dot{\boldsymbol{x}} = \boldsymbol{A}\boldsymbol{x} + \boldsymbol{B}\boldsymbol{u} + \boldsymbol{B}_d\boldsymbol{d},$$
$$\boldsymbol{y} = \boldsymbol{C}\boldsymbol{x},$$

where $\boldsymbol{B}_d$ is the disturbance mapping matrix. The disturbance term is considered more thoroughly in Section 5.2.

The described state space model can be used to model a large variety of systems, depending on the states and associated matrices chosen. The states are chosen as required by the system being modelled. The matrices associated with these states must then be determined. Generally, a state space model is produced in one of three ways:

1. First principles modelling
2. Linearisation of an existing non-linear model
3. System identification

First principle modelling and linearisation of an existing model are closely related. For example, the model developed in 4.2 is a model from first principles, which could then be linearised to produce an LTI model. The drawback of this method is that the accuracy depends entirely on the accuracy of the stability derivatives produced by SimGen, which have not been validated. System identification is akin to parametric identification (which was discarded as a viable modelling method). The benefit of system identification is that it is much simpler to apply. Furthermore, the state space model is very well suited to system identification methods of a linear model. The benefit of this approach is that the model which is produced can be easily verified with additional flight data. Therefore, any control design conducted using such a model can be done with confidence. Simulation results using the same model also become far more relevant. For these reasons, system identification was chosen as the means for obtaining the state space model. The techniques and methodology to obtain this model are discussed in Section 4.3.3

4.3.2 Decoupled State Space Model Configuration

In flight dynamics it is common to assume that the longitudinal and lateral dynamics are decoupled, so are modelled separately. This allows for simpler analysis and control design. Furthermore, it allows the system identification to be conducted on two reduced order models which aids the identification process.

To properly design the system identification tests, the desired models must first be defined. The standard longitudinal model for aircraft dynamics in state space form is given as

$$\boldsymbol{A} = \begin{bmatrix} X_u & X_w & X_q & -g\cos\theta^* \\ Z_u & Z_w & Z_q & -g\sin\theta^* \\ M_u & M_w & M_q & 0 \\ 0 & 0 & 1 & 0 \end{bmatrix}, \qquad \boldsymbol{x} = \begin{bmatrix} u \\ w \\ q \\ \theta \end{bmatrix},$$
$$\boldsymbol{B} = \begin{bmatrix} 0 & X_{\delta_t} \\ Z_{\delta_e} & 0 \\ M_{\delta_e} & 0 \\ 0 & 0 \end{bmatrix}, \qquad \boldsymbol{u} = \begin{bmatrix} \delta_e \\ \delta_t \end{bmatrix}, \tag{4.30}$$

where * denotes the steady state value of the associated parameter at the linearisation point. It should be noted that the majority of the $\boldsymbol{B}$ matrix has calculable coefficients. In this work, the form shown is taken for two reasons. First, these are the most significant contributing factors by a significant margin. Second, intentional elimination of the weak cross coupling terms gives a natural way to later demonstrate the performance advantages of DOBC methods, which are expected to deal with unknown modelling errors. Without system identification, coefficients would be calculated from the trim conditions and stability derivatives. For example, X_u is calculated as

$$X_u = \frac{u^*\rho S}{m}\left[C_{x_0} + C_{x_\alpha}\alpha^* + C_{x_{\delta_e}}\delta_e^*\right] - \frac{\rho S w^* C_{x_\alpha}}{2m} + \frac{\rho S \bar{c} C_{x_q} u^* q^*}{4mV_a^*} - \frac{\rho S_{prop} C_{prop} u^*}{m}, \tag{4.31}$$

which relies entirely on quantities described in Section 4.2 and the chosen aircraft trim condition. The definition of the remaining coefficients take a similar form, but are not published herein for brevity; the full expansions of each can be found in most aerodynamics reference texts e.g. [99]. It is clear from (4.31) that the calculation of these variables relies on a substantial number of parameters. This approach could lead to more accurate modelling of the flight dynamics. However, this requires more effort in the identification process, while yielding relatively small benefits. State space models which only utilise only the resulting coefficients are sufficiently accurate for control design. They are also more easily obtained, which makes them the more attractive option in this use case.

As for the longitudinal dynamics, we can define the lateral state space model as

$$\boldsymbol{A} = \begin{bmatrix} Y_v & Y_p & Y_r & g\cos\theta^*\cos\phi^* & 0 \\ L_v & L_p & L_r & 0 & 0 \\ N_v & N_p & N_r & 0 & 0 \\ 0 & 1 & \cos\phi^*\tan\theta^* & q^*\cos\phi^*\tan\theta^* - r^*\sin\phi^*\tan\theta^* & 0 \\ 0 & 0 & \cos\phi^*\sec\theta^* & p^*\cos\phi^*\sec\theta^* - r^*\sin\phi^*\sec\theta^* & 0 \end{bmatrix}, \quad \boldsymbol{x} = \begin{bmatrix} v \\ p \\ r \\ \phi \\ \psi \end{bmatrix},$$
$$\boldsymbol{B} = \begin{bmatrix} 0 & 0 \\ L_{\delta_a} & L_{\delta_r} \\ N_{\delta_a} & N_{\delta_r} \\ 0 & 0 \\ 0 & 0 \end{bmatrix}, \qquad \boldsymbol{u} = \begin{bmatrix} \delta_a \\ \delta_r \end{bmatrix}. \tag{4.32}$$

Again, only the most significant control contributions have been considered in this model.

4.3.3 System Identification Methodology

The system identification was conducted using the MATLAB System Identification toolbox [103], and makes use of the common Prediction Error Method (PEM). In general terms,

PEM aims to reduce the output error between a model (to be estimated) and the supplied data. PEMs aim to minimise

$$\hat{\theta} = \arg\min V(\theta, Z^N),$$

where V is a function of the difference between Z, the recorded data, and θ, the parameters tuned as part of the estimation routine. We define

$$V(\theta, Z^N) = \frac{1}{N}\sum_{t=1}^{N} l(\epsilon(t, \theta, Z))$$

given $Z^N = \begin{bmatrix} \boldsymbol{y}_t & \boldsymbol{u}_t \end{bmatrix}$, $t = 1, 2...N$ where Z^N is a data set of N samples of system outputs $\boldsymbol{y}$ and control inputs $\boldsymbol{u}$, $l(\cdot)$ is a positive definite function of ϵ, the error between the measured and predicted model output. Colloquially, this is a method of minimising the difference between some measured plant data and a defined model. More detail is available in [104] and the references therein.

Grey Box Identification

In system identification theory, identification of a totally unknown plant is referred to as black box identification. This is usually the case when no data or information is available for the internal plant whatsoever. If this were true, for the model in (4.32), the A matrix alone would require the identification of 25 separate variables; this would prove difficult and it is unlikely that a good model would be found. With such complex minimisation problems, it is expected that a large number of local minima would exist, trapping the solution.

For a partially known model, we can perform a grey box identification. By applying knowledge of the system, some parameters can be hard coded. In (4.32) for example, all terms with a value of 1 or 0 can be fixed as these are known mathematical relations. This reduces the number of estimated parameters to 14. Applying additional constraints, such as assuming $p^* = q^* = r^* = 0$ and knowing $g = 9.81 m/s^2$, the number of estimated parameters again is reduced, down to 9; this has resulted in a substantial reduction in the solution space by applying known relationships. Of course, the reductions to be made depend on the operating point of the aircraft about which the identification is conducted. Further reduction is possible.

By applying some basic knowledge of aircraft dynamics, the solution space can be further reduced. For example L_p, which relates rolling moment due to roll rate, will be negative for all standard aircraft configurations as it is the roll damping term. Similar logic can be applied to the remaining coefficients. Further improvements can be made by supplying parameters to initialise the search. These can be found by using known values of similar aircraft. This can also be done by calculation, using the SimGen supplied variables and calculation of the derivatives such as (4.31). Using the parameters in this way minimises the effect of any inaccuracies resulting from SimGen outputs, as the variables are only used to initialise the search. The final restriction applied is to limit the range of the variables around the supplied initialisation. This can ensure that the resulting variables are within a sensible range of values as well as reducing the computation time.

Using Approximate Model Decompositions

Even with the improvements offered by grey box identification, due to the strong coupling between many aircraft states, it can be difficult to reach the true model structure with a single estimation routine. This can be addressed by decomposing the full model into reduced order approximations. Then, specific manoeuvres for these models can be designed

to excite their dynamics. For example, the longitudinal dynamics of an aircraft decompose into a fast Short Period Pitching Oscillation (SPPO) and a slow phugoid mode. The SPPO can be excited with short sharp elevator doublets, while the phugoid is best excited with a single elevator impulse; the resulting phugoid mode develops naturally thereafter.

Once the two individual models have been identified, they can be reconstituted into the full model. A final manoeuvre can then be used to fine tune the two modes in a single run with the initial approximations as starting points. First, the SPPO approximation is given by

$$\begin{aligned} x_{sp} &= \begin{bmatrix} w \\ q \end{bmatrix}, & A_{sp} &= \begin{bmatrix} Z_w & Z_q \\ M_w & M_q \end{bmatrix}, \\ u_{sp} &= \delta_e, & B_{sp} &= \begin{bmatrix} Z_{\delta_e} \\ M_{\delta_e} \end{bmatrix}, \end{aligned} \tag{4.33}$$

which is based on the assumption that $\dot{u} = 0$, and that the SPPO varies mainly in w and q. The remaining phugoid mode, which assumes $\dot{w} = 0$, is given by

$$\begin{aligned} x_{ph} &= \begin{bmatrix} u \\ q \\ \theta \end{bmatrix}, & A_{ph} &= \begin{bmatrix} X_u & X_q & X_\theta \\ M_u & M_q & M_\theta \\ 0 & 1 & 0 \end{bmatrix}, \\ u_{ph} &= \delta_e, & B_{ph} &= \begin{bmatrix} 0 \\ M_{\delta_e} \\ 0 \end{bmatrix}. \end{aligned} \tag{4.34}$$

This model is more complex than the SPPO, and also relies on some of its parameters. Therefore, the SPPO model should be identified first, followed by the phugoid mode. Subsequently, the full model from (4.30) would be identified and then validated.

For the lateral dynamics, the two reduced order modes are the roll mode

$$\dot{p} = L_p p + L_{\delta_a} \delta_a \tag{4.35}$$

and the Dutch Roll, given by

$$\begin{aligned} x_{dr} &= \begin{bmatrix} \beta \\ r \end{bmatrix}, & A_{dr} &= \begin{bmatrix} Y_v & Y_r \\ N_v & N_r \end{bmatrix}, \\ u_{sp} &= \delta_e, & B_{sp} &= \begin{bmatrix} Y_{\delta_r} \\ N_{\delta_r} \end{bmatrix}, \end{aligned}$$

For the X8, the Dutch Roll is not a suitable reduced model due to the lack of rudder. This makes exciting the mode somewhat difficult in this case. The processes is detailed in the following section.

4.3.4 System Identification Example

Within this section, the system identification process to determine the longitudinal linear state space model of an example aircraft is detailed. The aircraft used is the Skywalker 1780, which is used in Chapter 8 to study the effects of Direct Lift Control (DLC). The X-Plane model of the aircraft is shown in Fig. 4.9. More details on the aircraft are provided in Chapter 8. The methodology detailed herein is the same used for all other identified models used in this work.

The model to be identified is in the form shown in (4.3.4), which also includes the additional height state, h. This state will be necessary for the full simulation of DLC related flights. In theory, the associated h parameters can be calculated exactly based

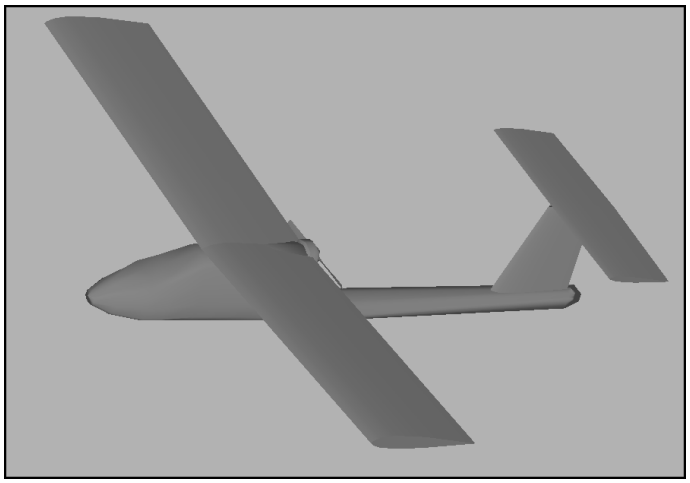

Figure 4.9: The model of the Skywalker 1780 used in X-Plane

on kinematic relationships. However, by identifying the parameters from flight data instead, the resulting model produces a better output of the height by implicitly including additional effects.

$$\boldsymbol{A} = \begin{bmatrix} X_u & X_w & X_q & -g\cos\theta^* & 0 \\ Z_u & Z_w & Z_q & -g\sin\theta^* & 0 \\ M_u & M_w & M_q & 0 & 0 \\ 0 & 0 & 1 & 0 & 0 \\ h_u & h_w & 0 & h_\theta & 0 \end{bmatrix}, \qquad \boldsymbol{x} = \begin{bmatrix} u \\ w \\ q \\ \theta \\ h \end{bmatrix},$$

$$\boldsymbol{B} = \begin{bmatrix} 0 & X_{\delta_t} & X_{\delta_d} \\ Z_{\delta_e} & 0 & Z_{\delta_d} \\ M_{\delta_e} & 0 & M_{\delta_d} \\ 0 & 0 & 0 \\ 0 & 0 & 0 \end{bmatrix}, \qquad \boldsymbol{u} = \begin{bmatrix} \delta_e \\ \delta_t \\ \delta_d \end{bmatrix},$$

The initial aircraft model parameters are taken from literature of a similarly configured aircraft [105].

Model Identification Process

The SPPO is dominated by w and q. An initial identification on the associated parameters was done after a step elevator input to excite the dynamics. The result is shown in Fig. 4.10, with $x = \begin{bmatrix} u & w \end{bmatrix}$ and no control input considered. Shown in this data is *data* and *th_ss*, where data is recorded flight response and th_ss represents the response of the proposed model to the recorded inputs. The accompanying percentage is the Normalised Root Mean Square (NRMSE) of the th_ss model compared to the recorded data. This index is calculated as

$$NRMSE = 1 - \frac{||x_d - x_m||}{||x_d - mean(x_d)||},$$

where x_d is the vector of recorded data and x_m is the vector of model output. An NRMSE of 100% (i.e. NRMSE=1) therefore represents a perfect match. The value cannot be taken at face value for model quality however, and should be used only to aid interpretation of the responses. Overall the model matches the recorded data very well in the initial state, with some error as the aircraft settles back to the trim condition. This is expected as the model is limited and will not be able to capture all the effects.

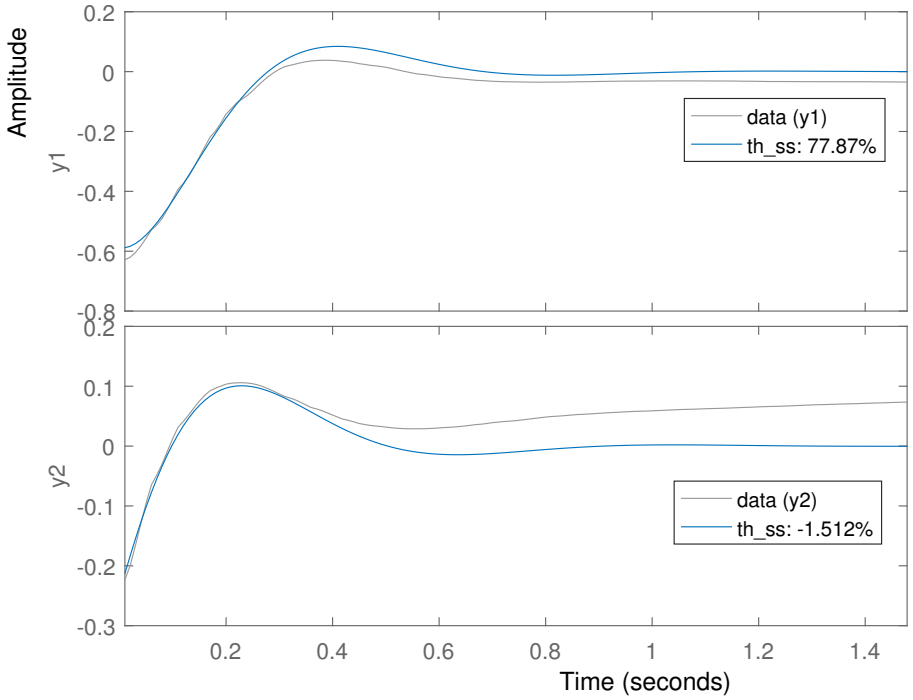

Figure 4.10: The recorded and identified model response for the SPPO of the 1780, where $y1 = w$ and $y2 = q$.

To identify the elevator coefficients, a pair of elevator doublets were used as the input, so $u = [\delta_e]$. The resulting response is shown in Fig. 4.11. Here a much better match is seen, aided by the fact that the inputs maintain the aircraft close to straight and level, minimising any changes in u which is as yet not considered in the model.

We can also do an initial identification of the δ_d coefficients with $x = \begin{bmatrix} u & w \end{bmatrix}$ and $u = [\delta_d]$. For this assessment, step inputs were not sufficient as this resulted in large changes in u, which is not yet included in the model. A chirp signal was used instead, which maintained the aircraft close to the trim u while exciting the required dynamics. The results are shown in Fig. 4.12. We see some offset in q, again due to changes in u. However, due to the nature of the chirp input a good model match is still found.

Next, we expand the model to now include all states, so $x = \begin{bmatrix} u & w & q & \theta & h \end{bmatrix}$, with $u = \begin{bmatrix} \delta_e & \delta_t & \delta_d \end{bmatrix}$. With the crucial SPPO coefficients fixed, we are able to design a manoeuvre to acquire the throttle model, as well as the associated u and h parameters. This was achieved with throttle steps and DLC flap chirps to excite all relevant dynamics. The result is given in Fig. 4.13. Here we see that overall, the resulting model matches the data very well even with a complex set of input manoeuvres over an extended period.

Finally, a verification test is performed. This test is crucial in that it must not be a repeat of data used to identify the model; this ensures that the resulting comparison is a fair representation of the model quality. For this simulation, both a δ_d doublet and δ_e doublet were employed, to ensure sufficient excitation. Again, the full model is used so that $x = \begin{bmatrix} u & w & q & \theta & h \end{bmatrix}$, with $u = \begin{bmatrix} \delta_e & \delta_d \end{bmatrix}$ used for inputs. The result is given in Fig. 4.14. The final result is an excellent model match. We see a better match than with the previous phugoid excitation. This is likely due to less aggressive control inputs giving more time for a natural model response. The verification data shows clearly that the resulting model, given below, is a good representation of the aircraft's dynamics

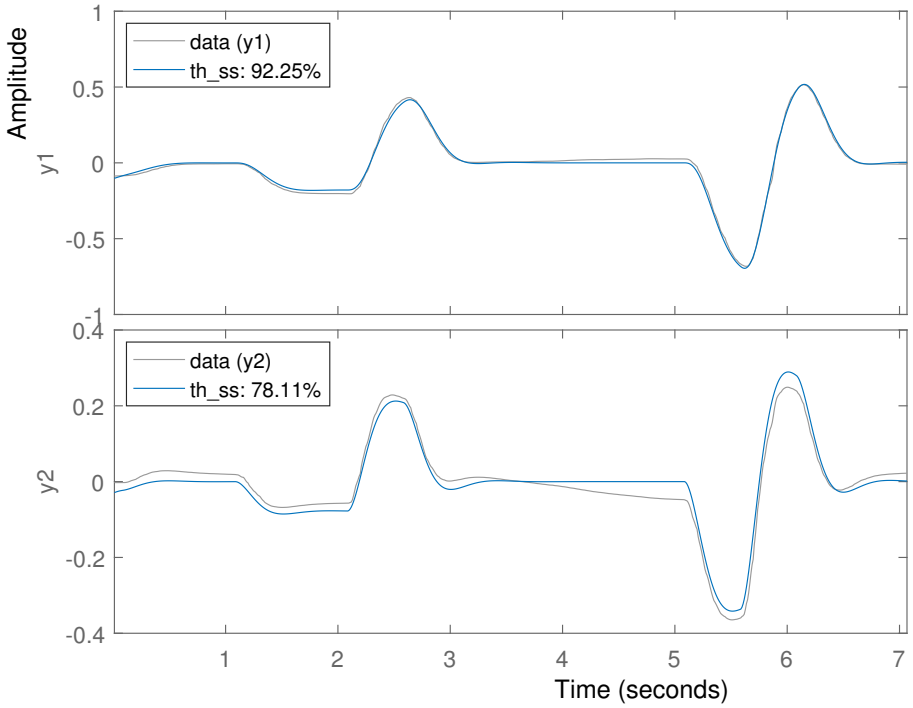

Figure 4.11: The recorded and identified model response for the a pair of elevator doublets for the 1780, where $y1 = w$ and $y2 = q$.

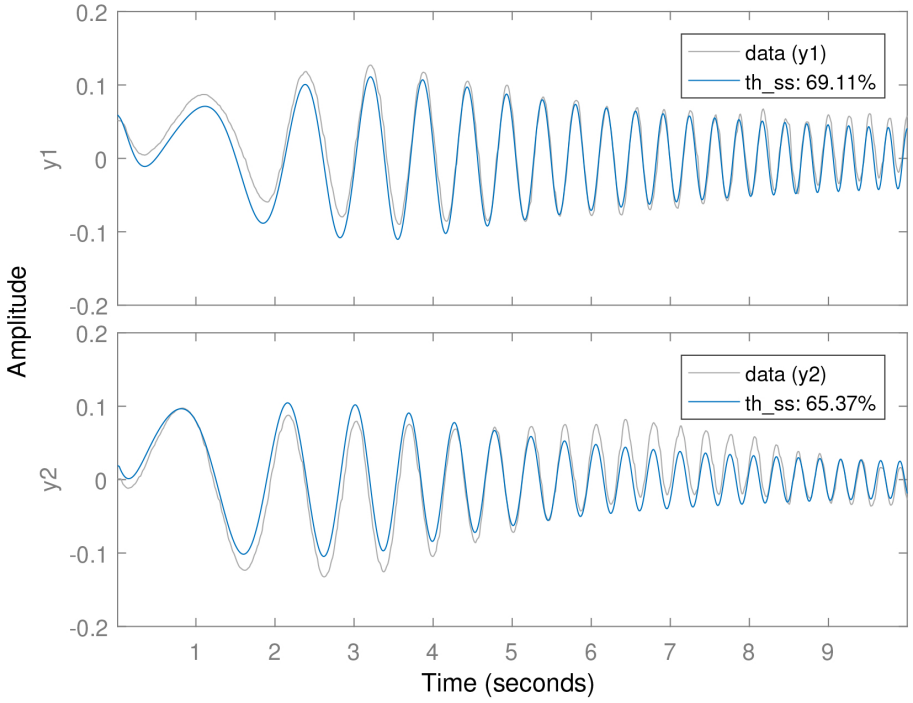

Figure 4.12: The recorded and identified model response for the a DLC flap chirp input for the 1780, where $y1 = w$ and $y2 = q$.

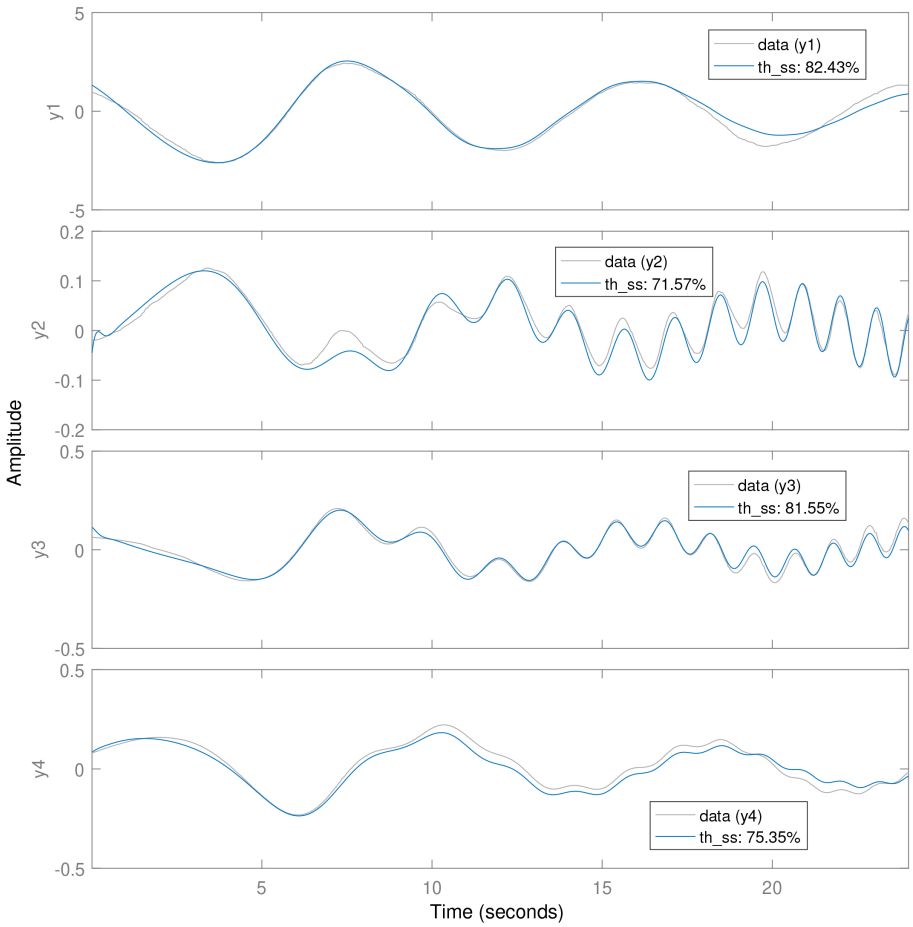

Figure 4.13: The recorded and identified model response for the a slow DLC flap chirp for phugoid excitation input for the 1780, where $y1 = u$, $y2 = w$, $y3 = q$ and $y4 = \theta$.

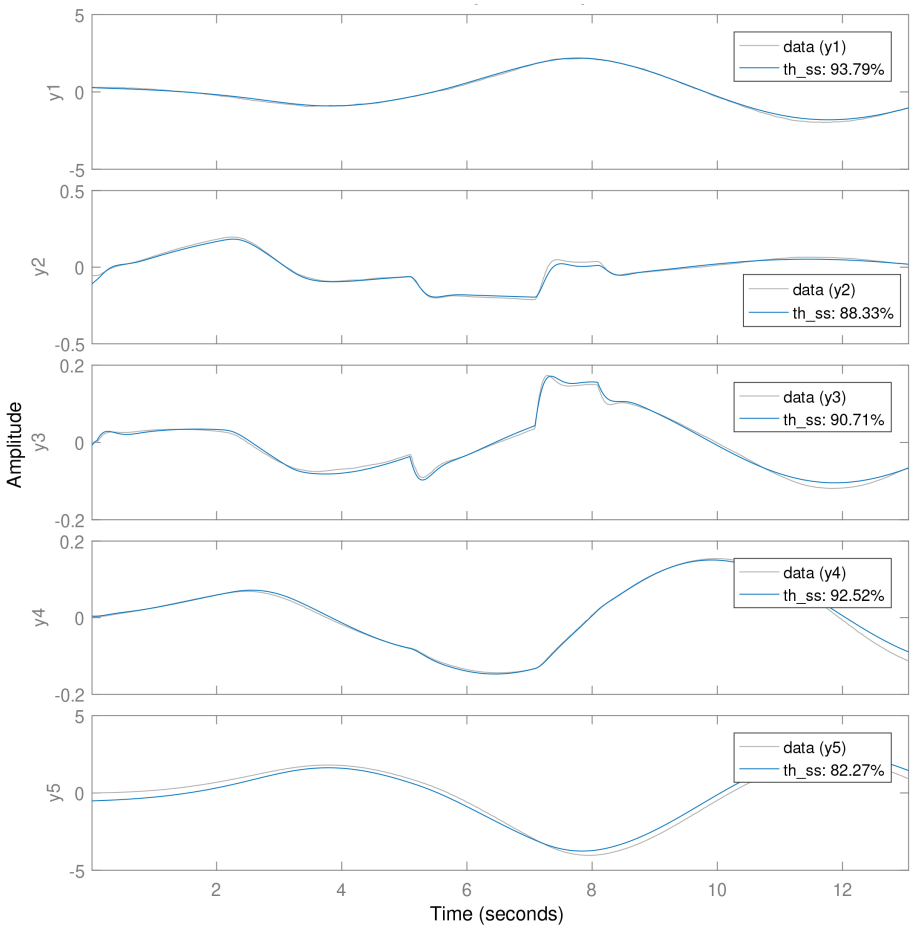

Figure 4.14: The verification data for the final state space model of the 1780.

$$\boldsymbol{A}_{1780} = \begin{bmatrix} -0.116 & 0.992 & -0.352 & -10.26 & 0 \\ -1.05 & -6.74 & 14.99 & 0 & 0 \\ 0.114 & -3.87 & -3.8 & 0 & 0 \\ 0 & 0 & 1 & 0 & 0 \\ 0.144 & -0.65 & 0 & 15.99 & 0 \end{bmatrix}, \quad \boldsymbol{B}_{1780} = \begin{bmatrix} 0 & 2.72 & -1.71 \\ -5.46 & 0 & -19.54 \\ -113.8 & 0 & 10.71 \\ 0 & 0 & 0 \\ 0 & 0 & 0 \end{bmatrix}. \tag{4.36}$$

4.4 Motor Modelling

Another key component to the fixed wing UAV is the motor. The motor is essential to aircraft flight and is responsible for the production of a significant portion of the forces acting on the aircraft. It is therefore very important to model correctly to capture the aircraft dynamics. Within the engine model, two key components must be considered: dynamic response and forces. The dynamic response describes how quickly the motor responds to input commands and is key in proper modelling of disturbance rejection capabilities. The forces and moments for a given thrust command are a separate but crucial component.

4.4.1 Thrust and Torque

Characterising the motor forces and moments requires additional test equipment. It is also essential to capture the response using the system in a state as close to what would be the flight configuration. For this test, the RC Benchmark Series 1580 Thrust Stand and Dynamometer[2] was used to capture the thrust and torque of the motor. As shown in Fig. 4.15, the motor was attached to the test bench in the aircraft flight condition. This meant that the motor was driven by the ESC, receiving commands from a ROS controller running aboard the RPi. This configuration therefore allowed mapping of throttle input to thrust output which would be utilised by any controller running aboard the aircraft. Although a similar response may have been obtained by manual input on the RC transmitter, there was no guarantee.

The thrust stand uses load cells attached to the supporting structure to measure deflections of the stand. From this, the thrust and torque can be calculated with a high degree of precision. The data output is somewhat slow to respond, meaning the motor forces must be measured at steady state throttle conditions. Multiple step inputs were manually entered into the ROS controller, allowing settling time at each instance before measurement was taken. The resulting data is shown in Fig. 4.16. For this test, throttle was incremented in 10% steps with data recorded at each step. The second order polynomial lines of best fit for thrust and torque are given by

$$F_m^p = 16.153\delta_t^2 + 14.478\delta_t,$$
$$L_m^p = 0.2811\delta_t^2 + 0.2638\delta_t,$$

where F_m^p is the polynomial model of motor force due to throttle command and L_m^p is the polynomial model of motor torque due to throttle command, with the input δ_t being throttle in the range of $0 \leq \delta_t \leq 1$. It is assumed herein that the motor force acts positively directly along and motor torque negatively purely about the x^b axis. In addition, the motor Rotations Per Minute (RPM) was also recorded. This is given in Fig. 4.17, with the polynomial best fit line defined as

[2] https://www.rcbenchmark.com/dynamometer-series-1580/

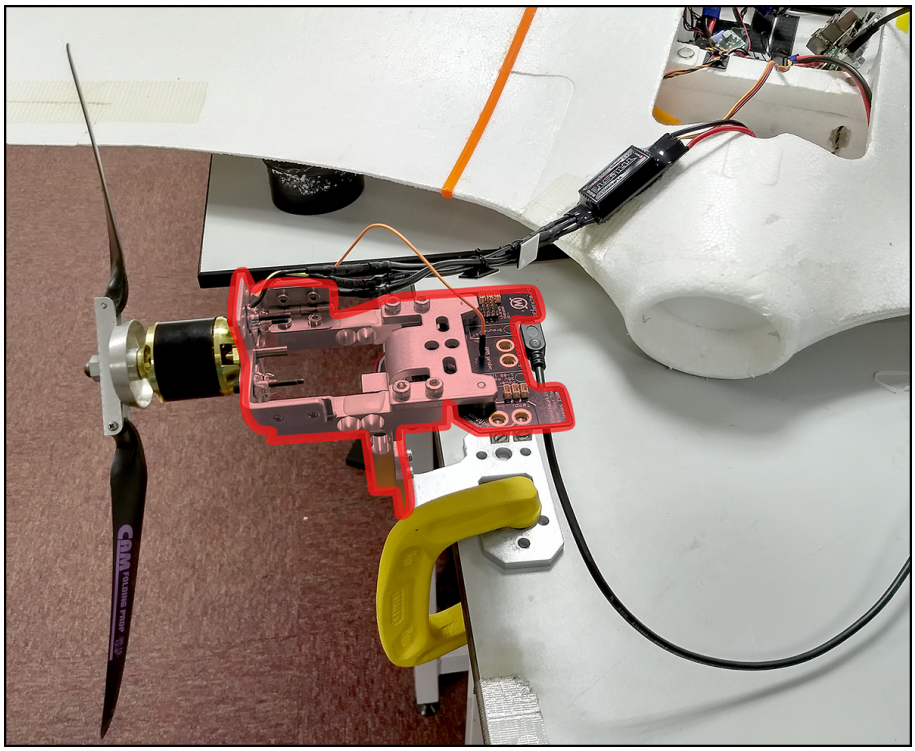

Figure 4.15: The Scorpion 3020-890kV with CAM 12x6 folding prop attached to the RC Benchmark apparatus (highlighted in red).

$$N^p = -7521.1\delta_t^2 + 16872\delta_t,$$

where N^p is the polynomial best fit of motor RPM.

4.4.2 Dynamics Modelling

With the forces and moments characterised, it remained to determine how quickly the motor output could be changed. The RC Benchmark motor stand offers the ability to record loads with time. However, there are significant delays and relatively slow responses; an example is given in Fig. 4.18. The data recorded is from a smaller motor and prop combination, used for quadrotor flight control. Such motors have generally very fast transient responses, necessary for quadrotor control. However, from the data we see both a delay and slow transient response. This suggests that there is some inherent delay in the system, as well as filtering of the load cell data. This means the test bench was not suitable for recording the dynamic responses accurately. For this, a different test methodology was needed.

Due to the significant thrust from the motor attached to the X8, the physical deflection of the thrust stand was clearly visible to the eye. Furthermore, the sound emitted by the motor was directly associated with the motor speed. It was decided that by combining these two factors, a more accurate assessment of the dynamic response could be obtained. Shown in Fig. 4.19 is the test setup used to collect the data.

The thrust stand deflection could now be tracked within the VICON system. The limitation of this method was that the deflection would only be clearly detectable as the motor approached maximum thrust. However, by recording both the throttle command and measured deflection, it would be trivial to determine the time taken to reach full thrust from a throttle input. This was easily achievable within the ROS framework, and could be done with the aircraft in flight configuration (i.e. controller running aboard the

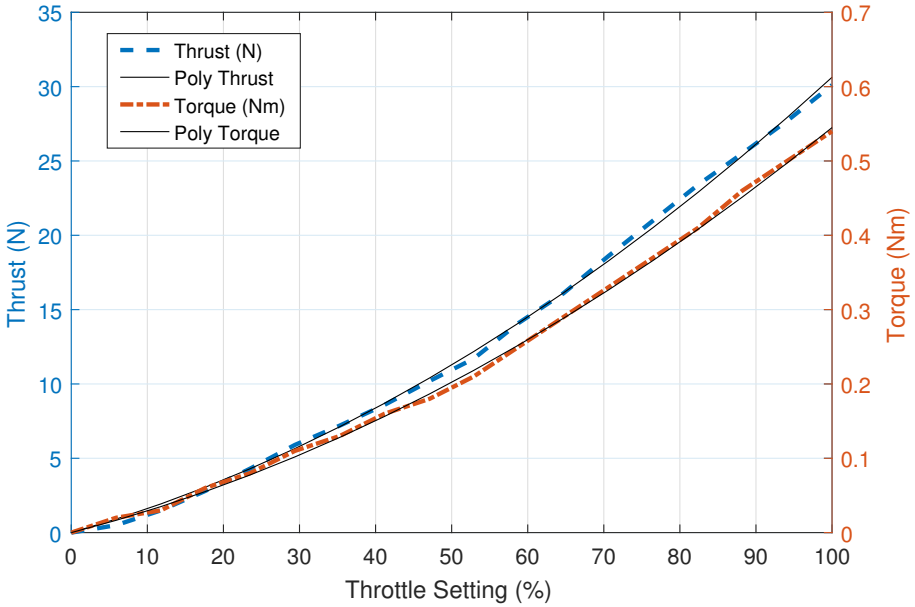

Figure 4.16: The recorded motor thrust and torque for the Scorpion 3020-890kV motor with CAM 12x6 folding prop obtained from the RC Benchmark Series 1580. Second order polynomial best fit lines are overlain for each.

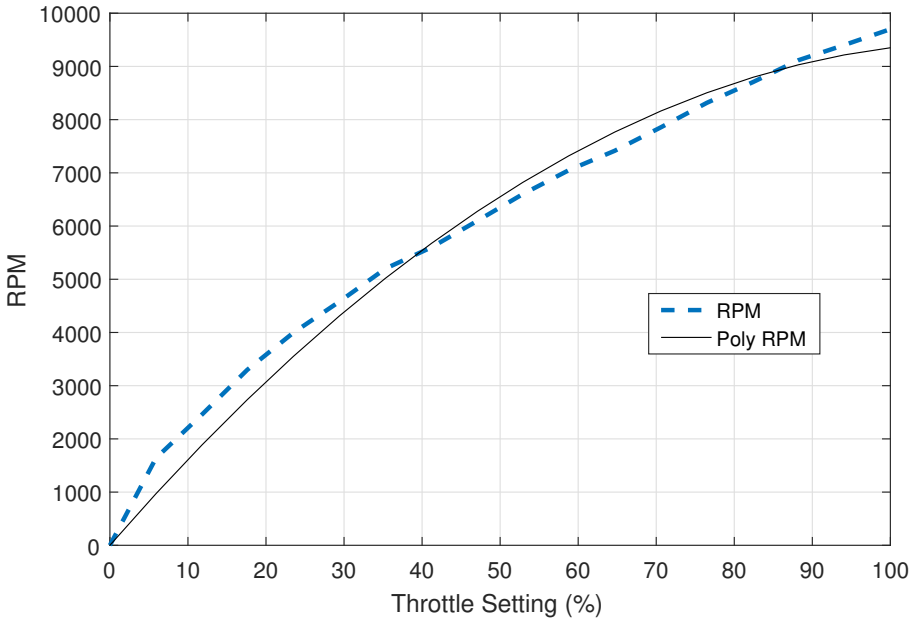

Figure 4.17: The recorded motor RPM with input throttle command. A second order polynomial line of best fit is also included.

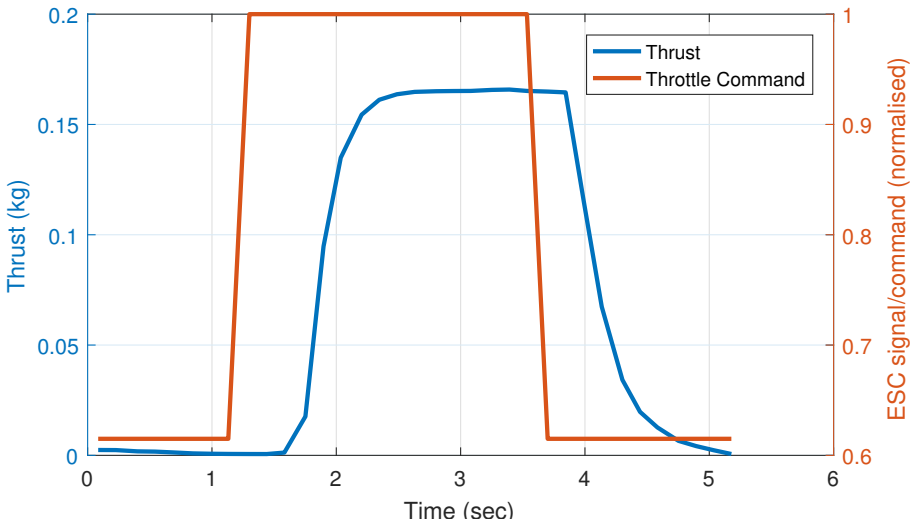

Figure 4.18: An example of recorded thrust data for a different motor/prop combination, using the RC Benchmark Series 1580 thrust stand.

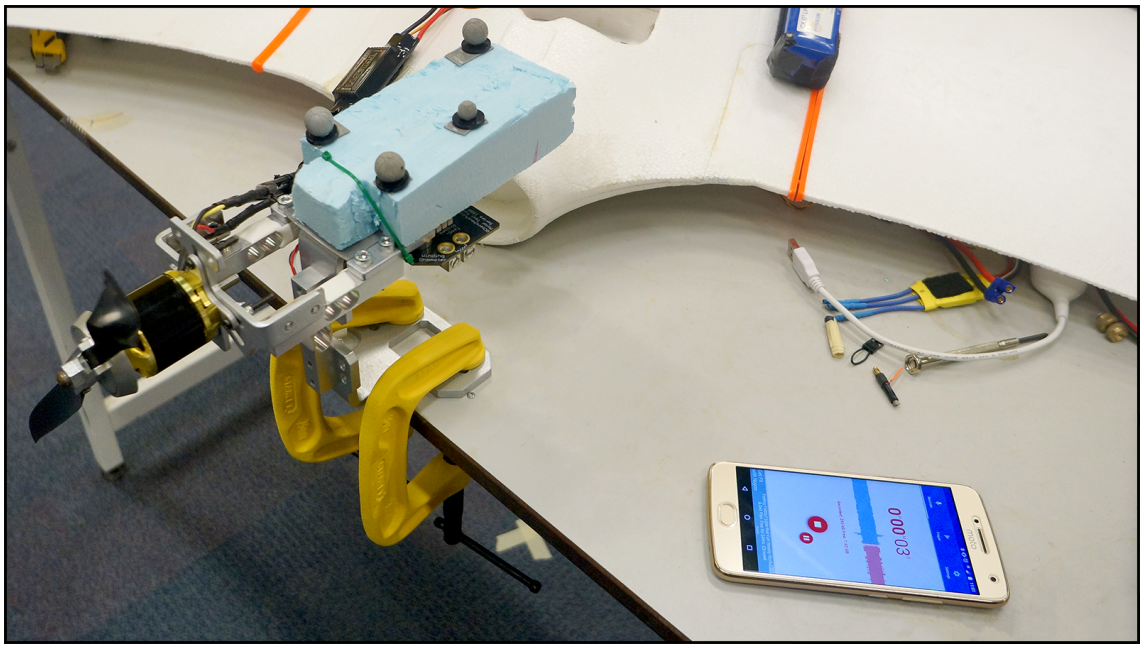

Figure 4.19: The test configuration used to determine the transient response of the Scorpion motor on the Skywalker X8.

aircraft) to capture the response in the most realistic scenario.

To validate these results, audio analysis was also performed. This data would mainly be used to verify the result from the VICON deflection for thrust stepping. However, it would also allow capture for another crucial piece of information; the rate of *deceleration* of the motor. It is unlikely that the rate at which the motor can increase RPM is identical to the rate at which it reduces. First, we define the equation of motion for the motor as

$$I_p\ddot{\theta}_p = T_m - T_f - T_D, \tag{4.37}$$

where I_p is the moment of inertia for the propulsion system (motor, prop and spinner assembly), $\ddot{\theta}_p$ is the rotational acceleration of the propulsion system, T_m is the torque exerted by the motor, T_f is the mechanical friction torque and T_D is the torque from aerodynamic drag. T_m and T_f are features of the propulsion system and as such will be consistent. However, T_m is directly proportional to the control input. Further, $T_m \gg T_f, T_D$, which allows for the acceleration of the motor. When slowing the propulsion system however, $T_m = 0$ in (4.37). We can make an approximation that

$$\ddot{\theta}_p^a \approx \frac{T_m}{I_p},$$
$$\ddot{\theta}_p^d = \frac{-T_f - T_D}{I_p},$$

where $\ddot{\theta}_p^a$ is motor acceleration and $\ddot{\theta}_p^d$ is motor deceleration. Remembering that $T_m \gg T_f, T_D$, we can say that $|\ddot{\theta}_p^a| \gg |\ddot{\theta}_p^d|$; colloquially, the propulsion system accelerates much more quickly than it decelerates. This will need consideration not only in the data analysis but the eventual motor model design. This will also be difficult to quantify with the VICON deflection test, as the deflection will only be useful for detecting when the motor is close to maximum thrust.

The audio analysis method employed could be used to

1. Verify VICON deflection testing,
2. Estimate deceleration time constant.

Using the audio analysis to confirm any measurements from the deflection data will give some additional verification to the results, as well as demonstrating that audio analysis is a viable method. This can then be used to estimate the motor slow down time constant. Using Audacity[3], a free open source audio analysis software package, the audio data collected alongside VICON deflection data was processed.

VICON Deflection Results

First, we analyse the results from the VICON deflection test. During the testing, it was noted that at full throttle a deflection of 1° was typical. This is well within the measurement resolution of the VICON system. In Fig. 4.20, the test data for the multiple inputs are presented. The data shows a clear and repeating pattern, with VICON detecting a deflection at each throttle input.

To improve the data quality, the five inputs were combined and averaged to give a mean response. This data is shown in Fig. 4.21. The data was normalised, as the magnitude of the deflection was not of concern. From this data, we see clearly that the motor requires around $0.75s$ to reach full thrust from a throttle input. The lack of recorded responses in the initial $0.5s$ is due to the minimal deflection resulting from lower motor

[3] http://www.audacityteam.org/

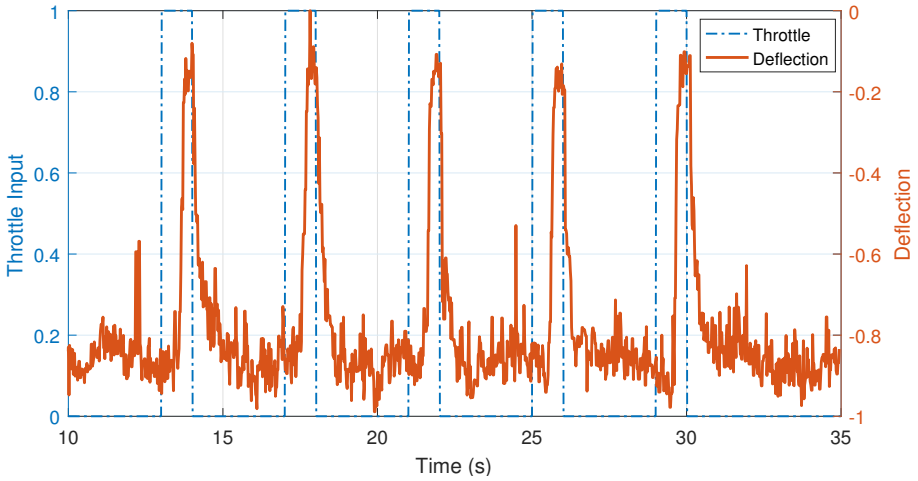

Figure 4.20: The five VICON recorded deflections of the thrust test rig when subjected to full throttle bursts.

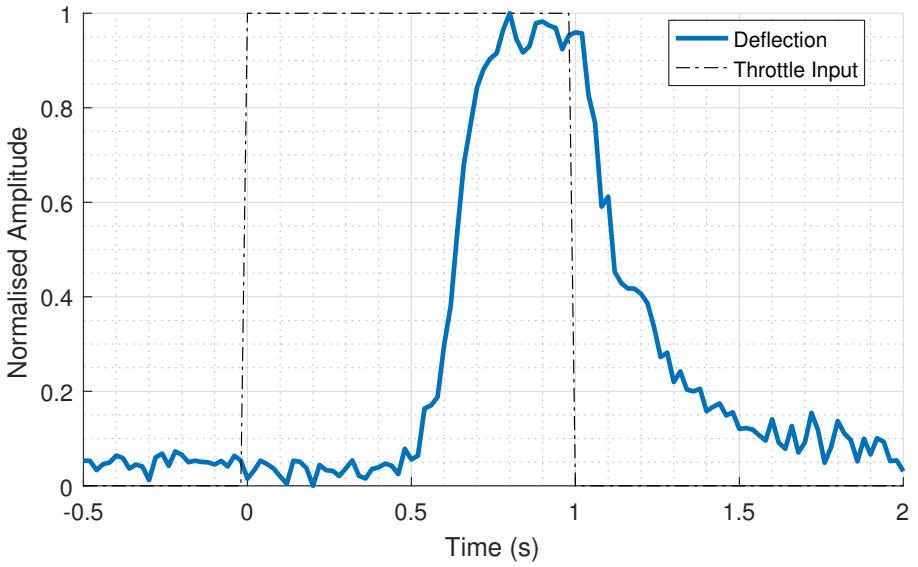

Figure 4.21: The normalised mean recorded deflection of the throttle test bench in response to a full throttle step input.

thrusts. Further, we notice that the rate of decline to the neutral deflection condition has a significantly shallower profile. The mean response indicates it takes roughly $0.25s$ from the first detection of deflection to the maximum. Conversely, it takes approximately $1s$ for the motor to return to the neutral deflection state. This affirms the discussion in Section 4.4.2 in that the rate of acceleration and deceleration are not the same.

Audio Data Results

Shown in Fig. 4.22 is the audio data recorded during the VICON deflection test. This was captured at high quality on a mobile phone, with a sampling rate of 44.1kHz, providing sufficient resolution. This data was manually processed to determine the time taken to reach full motor speed and to settle back to a stop. Fig. 4.23 shows an enlarged portion of the data. We see a clear point at which noise is detected, followed by a ramp up to a peak, followed by a steady value. On the deceleration, we once again see a peak followed by a slower decline to ambient. If we assume that the peak in noise is found at a motor speed somewhere just below maximum (as it is seen on both acceleration and deceleration), it is simple to determine the time constants by assuming the "valley" between the two

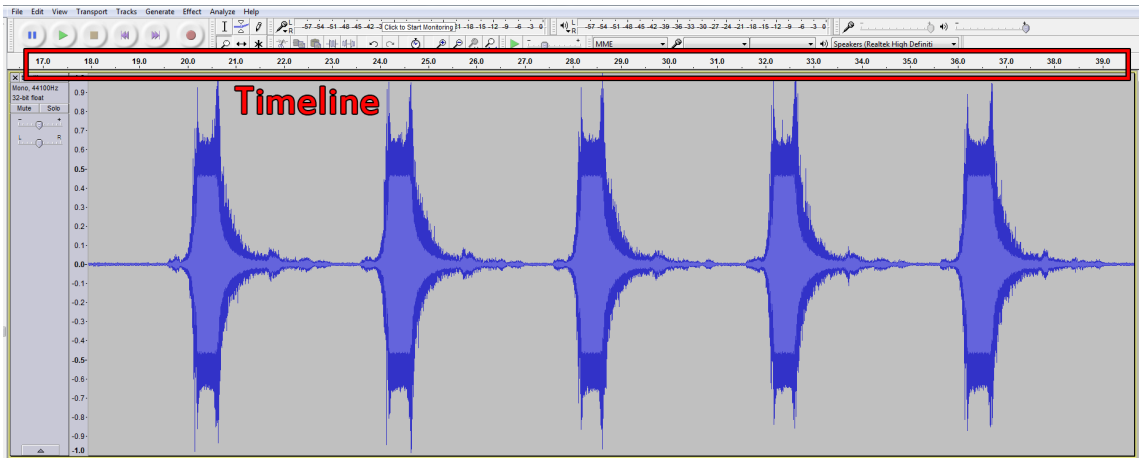

Figure 4.22: The sound recorded which accompanied the VICON deflection test.

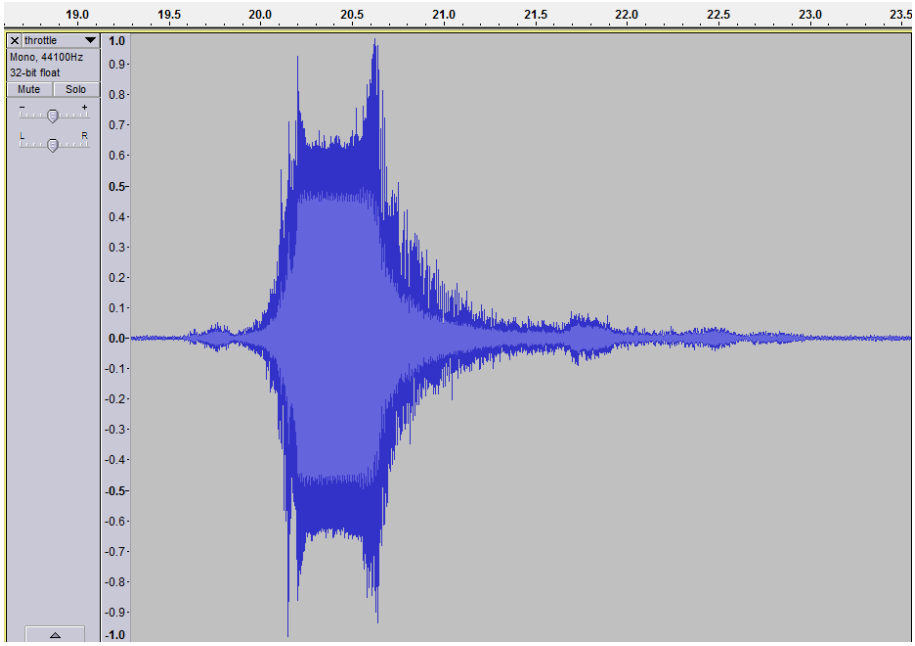

Figure 4.23: An enlarged portion of the audio data which shows a single throttle burst input with the associated time.

peaks represents steady state maximum thrust. It is clear to see that it takes $0.8s$ from the first detection of increased volume to steady state. This matches very well with the $0.75s$ identified from VICON data. On deceleration, we see that the peak lasts longer, the first indication that deceleration is also slower with audio analysis. Measuring the time between the end of steady state and ambient gives $2.5s$ as the average time for the motor to return to rest. This is *significantly* longer than the ramp up time, and further supports all previous discussion on this topic.

4.4.3 Motor Model

Using the data collected, a good measurement of the motor thrust torque has been identified. Furthermore, the dynamic model, which is much more difficult to obtain, was also found. It was shown that there is a large disparity between motor response to an increase and decrease in throttle. This requires careful consideration.

It is possible to capture these dynamics in simulation using an appropriate model. However, inclusion of these dynamics in control design is not trivial. Transfer functions

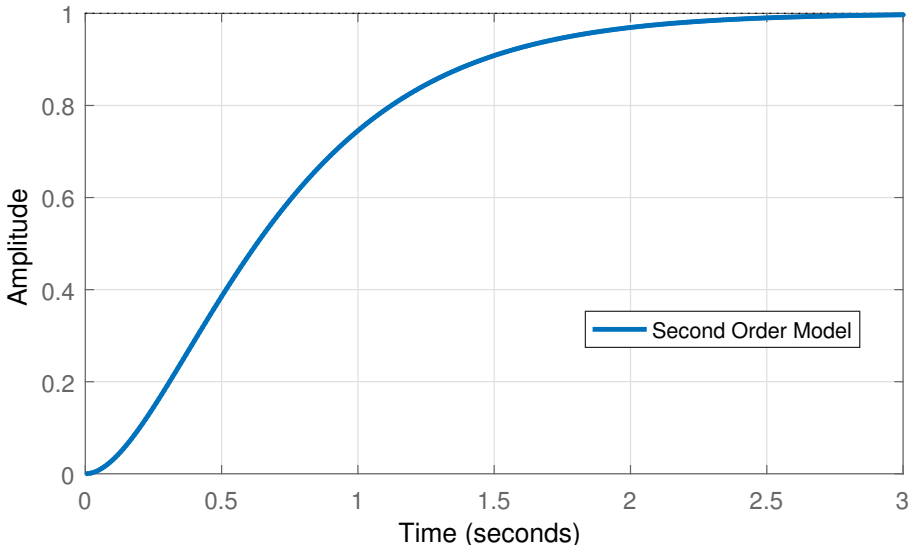

Figure 4.24: A step response of the second order model of the motor given in (4.38).

are the most common method for modelling actuator dynamics in control design. Transfer functions produce the same rate of change, regardless of directionality. A compromise was made by using a single transfer function which averaged the motor response. The model is slower in acceleration than the physical motor, but faster in deceleration. These actions are expected to be used in equal amounts in simulation. Any benefit gained in modelled motor deceleration will therefore be cancelled by drawbacks in acceleration. This model can also be used directly in control design. The loss in accuracy is deemed acceptable by the lack of overall benefit and compatibility with control design methods.

A second order model was chosen, as the included inertia was essential in properly representing the motor dynamics. The motor model given in (4.38) was chosen, as it offered a good average of the two responses. The resulting step response of this model is given in Fig. 4.24.

$$G_m(s) = \frac{2.56}{s^2 + 3.2s + 2.56} \tag{4.38}$$

4.5 X-Plane Simulation

For some of the work in this thesis, flight tests could not be safely carried out as the nature of the topic being investigated placed the aircraft at risk. Instead, a suitable simulation environment was needed. X-Plane is a commercially available and recognised flight simulation package [106]. X-Plane computes aircraft models based on a given 3D geometry model, along with the associated physical parameters e.g. mass, moments of inertia etc. The benefit is that for a given aircraft, accurate simulation can be conducted if a good geometric model is used. The X8 model used in the simulations is shown in Fig. 4.25, which was developed as part of this work. The limitation of X-Plane environment is that it operates outside of the MATLAB/Simulink ecosystem, therefore requiring an interface method for sending and receiving data.

Time was invested during this work to significantly improve the previous implementation of X-Plane/Simulink communication developed within the LUCAS lab. The previous method relies on requesting Uniform Resource Locator (URL) connections from an X-Plane plugin which was developed previously within LUCAS. Although this method allowed for both the sending and receiving of control commands and simulation data respectively, it had a significant and fundamental limitation: the available data rate was

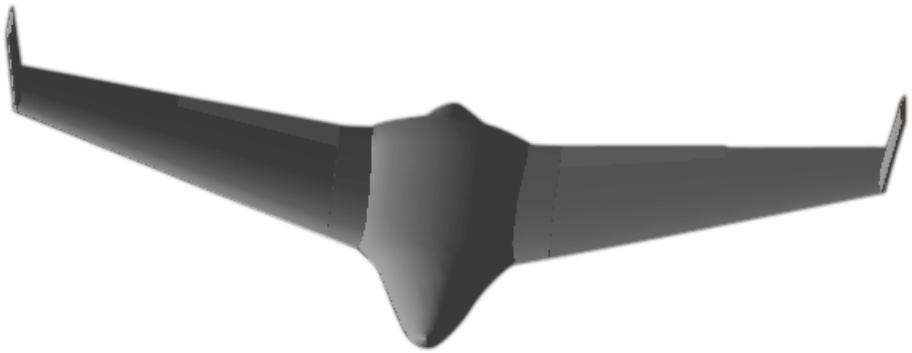

Figure 4.25: The X8 model which was used in X-Plane Simulations

proportional to the number of data sources requested, found experimentally to be approximated by

$$rate \approx \frac{200}{N_d} Hz,$$

where N_d is the number of data elements being sent or received. This relationship was determined empirically. The formula is approximate as the data rate depends on the amount of network activity and the performance of both the simulation and control computers (if run on separate machines). For a standard simulation, the rate was generally limited to $\approx$ 12Hz. Although such a low rate is sufficient for high level control simulations, for which this environment was used previously, it is too slow for low level control simulations and needed improvement. Initially, focus was applied on improving the rate at which MATLAB was able to process data requests with the aim of reaching at least a 50Hz data rate. Although significant gains were made, the URL method could not be pushed beyond 30Hz for a standard, representative simulation. An alternative method was needed.

X-Plane features an inbuilt User Datagram Protocol (UDP) communication method, which is more suitable to the timely transmission of data than URL requests. Internal settings allows this rate to be set in the range of 1-100Hz. Although this limit is lower than the approximate $200Hz$ of the previous method, it was not directly proportional to the number of data elements requested. The result being that the data refresh rate remained almost unchanged for $N = 1$ or, for example, $N = 30$.

Even with the much faster UDP method, some overhead exists, so it is not possible to achieve 100Hz data rate. However, while running in real time, it is possible to achieve a stable 80Hz. This is a substantial improvement over the previous method and is more than suitable for low level control simulations.

An additional improvement available through this method is the ability to apply arbitrary forces and moments to the aircraft axes. This has several uses, such as applying known disturbances to the aircraft, or modelling thrust. With X-Plane, aircraft engine modelling must be done when the aircraft model is designed. The engine model is limited to the variables which are available in the aircraft design program. By applying forces directly, any engine used in the non-linear or state space simulations can also be modelled for the X-Plane aircraft. This removes a source of uncontrollable uncertainty in the model, improving results.

A further improvement over the previous implementation is the ability to set the initial aircraft position and state (e.g. body velocities, control surface positions etc.) at the beginning of each simulation. This allows the subsequent simulation to be identical to the previous, allowing for highly repeatable simulations. Functions were developed to create files which can be saved/loaded while storing initialisation data as well. Using this method, the X-Plane environment was now capable of high data rate simulations, as

required by this work. The benefits of the X-Plane control method developed during this work can be summarised as

1. Data rate of up to 80Hz, suitable for low level control,
2. Applying user defined external forces and moments,
3. Saving/resetting of aircraft initial position and states,
4. Modelling of engine(s) in MATLAB/Simulink.

This is achieved with no loss of functionality from the original URL method.

4.6 Comparison of Simulation Environments

The multiple simulation environments and models which have been produced each have their own strengths and weaknesses. It is important to be aware of these and consider them when conducting simulations either for development of concepts or publication. These considerations are briefly collected in Table 4.3.

Table 4.3: Comparison of the strengths and weakness of the linear state space, non-linear Simulink and X-Plane simulation environments.

	Strengths	**Weaknesses**
State Space	Simple, fast to run, suitable for direct control design, verified parameters	Linear dynamics only
Simulink	Captures non-linear dynamics, fast to run	Reliance on SimGen parameters, unverified
X-Plane	Academically recognised, geometry based model input	No direct insight, limited control, slow to run (real time only)

Chapter 5

Anti-Windup Disturbance Observer Design for Actuator Saturation

In control design, it is common to assume that actuator positions track the demanded control action sufficiently such that the dynamics can be ignored. In practice, no actuator is ideal, and is usually limited by one of two factors: dynamics or saturation. Dynamics describe how an actuator position changes in comparison to an input. For example, a gas turbine engine takes several seconds to reach a demanded thrust setting. Saturation describes the minimum and maximum outputs of an actuator. A gas turbine has a maximum thrust which it cannot exceed, no matter what is demanded of it. Similarly, it has a minimum thrust. In this section, the effect of actuator saturation is considered.

Small UAVs are more prone to actuator saturation when compared to their full sized counterparts as the magnitude of disturbances relative to the aircraft state are much higher, requiring significantly more control deflection for rejection. Under actuator saturation, control performance degradation can occur and result in the system suffering from overshoot, limit cycles or even instability. These behaviours generally result from windup in the controller; internal controller states continue to grow in magnitude, leading to the afore described issues. Some approaches consider saturation directly in control design [107]. In such cases, the controller is designed conservatively to avoid control saturation. This is achieved at the loss of nominal performance. Additionally, in the presence of large disturbances, saturation can still occur. With a disturbance observer present this will still result in windup of the observer and degraded performance. An alternative and preferable method is to design the control scheme in a way which directly counteracts the effect of saturation, without the need for conservative control design. This is often referred to as an anti-windup compensator [90].

Due to the preferable performance characteristics, an anti-windup compensator is designed herein to alleviate the effects within a disturbance observer. The method utilised in this chapter uses classical static anti-windup techniques [108].

To study the benefits of the proposed method, performance will be demonstrated in an aircraft landing simulation. This is a dangerous phase of flight, where rapid disturbance rejection is key. Further, temporary loss of control due to windup can lead to loss of the aircraft due to close operational proximity to both the stall speed and landing surface. Comparisons will be made between three control schemes. First, LQR control will provide a reference baseline to be improved upon by either Linear Quadratic Integral (LQI) or DOBC augmentation. Within the DOBC augmentation, comparisons will also be made with the anti-windup scheme active and disabled.

Within this section, control design methodology is presented first. An augmentation of

the classical LQR with integral action and reference tracking ability is presented, referred to as the LQI. The baseline LQR design with reference tracking but no integral action is presented afterwards, as it follows a simplified version of the LQI design. Design of the DOBC scheme is then presented, after which anti-windup modification is detailed. Finally, results are presented showcasing the performance in both simulation and flight testing. This Chapter expands upon the work published in [109].

5.1 Baseline Control Design

Disturbance observer augmentation is intended to enhance the disturbance rejection properties of a baseline controller, therefore such a controller must be designed. For the work in this thesis, the Linear Quadratic Regulator (LQR) was selected for baseline control. These controllers are popular in flight control [110]. Additionally, they are well integrated with linear state space modelling methods which are therefore compatible with the chosen linear state space disturbance observer to be designed. Two baseline controllers will be designed; and LQR and an Linear Quadratic Integral (LQI). Both will be augmented to allow for reference command tracking.

5.1.1 Linear Quadratic Integral Control with Reference Command

The general problem statement for Linear Quadratic (LQ) optimal control is given as choosing $u(t)$ to minimise

$$J = \psi(x(t_f)) + \int_{t_0}^{t_f} L(x(t)), u(t), t)dt$$

Subject to

$$\dot{x} = f\left(x(t), u(t), t\right)$$
$$x(t_0) = x_0$$

Here, $\psi(x(t_f))$ represents the terminal cost, which penalises steady state error at the final time step t_f. L is the general cost function for the system as it moves from the initial condition at t_0 to the final condition. To avoid local minima in the optimisation problem, we require that L is non-negative, and must be defined accordingly. We now augment the cost using a costate vector $\lambda(t)$

$$J = \psi(x(t_f)) + \int_{0}^{\infty} \left(L + \lambda^T(f - \dot{x})\right).$$

We are free to choose $\lambda(t)$ as we wish, as it is multiplied by $f - \dot{x} = 0$. For this reason, it will be selected later as required. Also, in this case we are only considering the continous time regulator which defines $t_0 = 0$ and $t_f = \infty$. We further assume that the later designed controller is sufficient to achieve

$$\lim_{t\to\infty} (x_d - x) \to 0,$$

where x_d is the demanded value of the state x. This assumption allows for the removal of the terminal cost term. The new cost function is then given by

$$J = \int_{0}^{\infty} \left(L + \lambda^T(f - \dot{x})\right). \tag{5.1}$$

For the general LQR case, it is usual to choose

$$L = x^T Q x + u^T R u,$$

which would yield

$$J_L = \frac{1}{2}\int_0^\infty (x^T Q x + u^T R u) dt \tag{5.2}$$

as the cost function. Note that the inclusion of a factor of $\frac{1}{2}$ is taken from the standard solution to the LQR problem for state space systems [111]. It is included as it simplifies the derivation of the Algebraic Riccati Equation (ARE) solution. As it is a constant factor applied to the entire performance index of the optimisation routine, it does not affect the final result. To include integral action and reference tracking, some further modifications are required. First, we define an additional state

$$e_s = r - Cx,$$

where e_s is a state of the error between r, which is a vector of reference commands to be tracked, and the system output defined by Cx. We define a new system state as the integral of this error with time

$$x_{ie} = \int_0^\infty e_s(t) dt,$$

with which the system can be expanded to include the new states

$$\begin{bmatrix} \dot{x} \\ \dot{x}_{ie} \end{bmatrix} = \underbrace{\begin{bmatrix} A & 0 \\ -C & 0 \end{bmatrix}}_{A_i} \underbrace{\begin{bmatrix} x \\ x_{ie} \end{bmatrix}}_{x_i} + \underbrace{\begin{bmatrix} B \\ 0 \end{bmatrix}}_{B_i} u + \underbrace{\begin{bmatrix} 0 \\ I \end{bmatrix}}_{G} r. \tag{5.3}$$

With x_i being the composite of the original system state and the reference tracking error, we define a new system

$$\dot{x}_i = \underbrace{A_i x_i + B_i u + G r}_{\mathrm{f}}. \tag{5.4}$$

Now the total system error can be defined as

$$e_i = \begin{bmatrix} r - Cx \\ x_{ie} \end{bmatrix} = Mr + Hx_i, \tag{5.5}$$

where

$$M = \begin{bmatrix} I \\ 0 \end{bmatrix}, \qquad H = \begin{bmatrix} -C & 0 \\ 0 & I \end{bmatrix}.$$

Now, by replacing the system state x in (5.2) by the augmented system error state e_i, the cost function becomes

$$\bar{J} = \frac{1}{2}\int_0^\infty (e_i^T Q_i e_i + u^T R u) dt \tag{5.6}$$

Through this modification, the reference tracking with integral action problem has been cast into a general LQ *regulator* problem. This allows the application of standard LQR solutions to produce an optimal controller. It is important to note also that this modification results in Q_i weighting the error states, rather than the system states directly. By tuning the error dynamics, the state regulation gains are provided internally by the system.

By substitution of (5.5) into (5.6), the cost function becomes

$$\bar{J} = \frac{1}{2}\int_0^\infty (x_i^T H^T Q_i H x_i + 2r^T M^T Q_i H x_i + r^T M^T Q_i M r + u^T R u) dt,$$

which when compared to (5.1) allows the definition of

$$L = \frac{1}{2}\left(x_i^T H^T Q_i H x_i + 2r^T M^T Q_i H x_i + r^T M^T Q_i M r + u^T R u\right).$$

As $f - \dot{x} = 0$, we are free to choose λ in a convenient form. When following the optimum trajectory, no variation should exist in J, and therefore in $\bar{J}$. This holds as as we choose J to be continuous in x_i, u, r and t. This variation is defined by the partial derivatives of all elements of $\bar{J}$, given as

$$\Delta\bar{J} = \int_0^\infty (L_{x_i}\delta x_i + L_r \delta r + L_u \delta u + \lambda^T f_{x_i}\delta x_i + \lambda^T f_r \delta r + \lambda^T f_u \delta u - \lambda^T \delta\dot{x_i}) dt, \tag{5.7}$$

where subscripts denote the appropriate partial derivative. Using integration by parts we can define

$$-\int_0^\infty \lambda^T \delta\dot{x_i} dt = -\lambda^T(\infty)\delta x_i(\infty) + \lambda^T(0)\delta x_i(0) + \int_0^\infty \dot{\lambda}^T \delta x_i dt.$$

The initial and final states are fixed and do not vary with time, so this can be further reduced to

$$-\int_0^\infty \lambda^T \delta\dot{x_i} dt = \int_0^\infty \dot{\lambda}^T \delta x_i dt. \tag{5.8}$$

Combining (5.8) and (5.7) and grouping terms allows the expression of the variation as

$$\Delta\bar{J} = \int_0^\infty (L_{x_i} + \lambda^T f_{x_i} + \dot{\lambda}^T)\delta x_i dt + \int_0^\infty (L_r + \lambda^T f_r)\delta r dt + \int_0^\infty (L_u + \lambda^T f_u)\delta u dt.$$

Knowing that $\Delta\bar{J}$ must equal 0, we can now define three conditions which must be satisfied,

$$\begin{aligned} &L_{x_i} + \lambda^T f_{x_i} + \dot{\lambda}^T = 0, \\ &L_r + \lambda^T f_r = 0, \\ &L_u + \lambda^T f_u = 0. \end{aligned} \tag{5.9}$$

The three partial derivatives of L are given as

$$\begin{aligned} L_{x_i} &= x_i^T H^T Q_i H + r^T M^T Q_i H, \\ L_r &= r^T M^T Q_i H x_i + r^T M^T Q_i M, \\ L_u &= u^T R. \end{aligned} \tag{5.10}$$

Also, with f defined in (5.4), we have

$$\begin{aligned} f_{x_i} &= A_i, \\ f_u &= B_i, \\ f_r &= G. \end{aligned} \tag{5.11}$$

Now, using the identities from (5.9), (5.10) and (5.11) we can define

$$\begin{aligned} u^T R + \lambda^T B_i &= 0, \\ u &= -R^{-1} B_i^T \lambda \end{aligned} \tag{5.12}$$

Similarly for the state equation we define

$$x_i^T H^T Q_i H + r^T M^T Q_i H + \lambda^T A_i + \dot{\lambda}^T = 0,$$

which, when transposed, gives

$$H^T Q_i H x_i + H^T Q_i M r + A_i^T \lambda + \dot{\lambda} = 0. \tag{5.13}$$

A standard definition for this method is to set $\lambda = P x_i$, however this does not consider a reference command. To achieve this, we define

$$\lambda = P x_i + g, \tag{5.14}$$

which, when differentiated and with $\dot{x_i}$ substituted from (5.4) defines

$$\dot{\lambda} = \dot{P} x_i + P(A_i x_i + B_i u + G r) + \dot{g}. \tag{5.15}$$

By substitution of (5.14) and (5.15) into (5.13) we get

$$H^T Q_i H x_i + H^T Q_i M r + A_i^T P x_i + A_i^T g + \dot{P} x_i + P A_i x_i + P B_i u + P G r + \dot{g} = 0. \tag{5.16}$$

Next, we consider the effect of substituting (5.14) into (5.12):

$$u = -R^{-1} B_i^T P x_i - R^{-1} B_i^T g. \tag{5.17}$$

Now, combining this with (5.16) and considering the x_i terms we have

$$H^T Q_i H x_i + A_i^T P x_i + P A_i x_i - P B_i R^{-1} B_i^T P x_i = -\dot{P} x_i.$$

Crucially therefore, for all x_i the following must hold

$$\dot{P} = -P A_i - A_i^T P - H^T Q_i H + P B_i R^{-1} B_i^T P. \tag{5.18}$$

Similarly, by considering the r components which result from combining (5.17) with (5.16), we get

$$H^T Q_i M + A_i^T g + P G r + \dot{g} - P B_i R^{-1} B_i^T g = 0,$$

which means for all r, we can say

$$\dot{g} = (P B_i R^{-1} B_i^T - A_i^T) g - (H^T Q_i M + P G) r. \tag{5.19}$$

At this point we have reached the standard ARE with (5.18) as well as an auxiliary equation (5.19) which identifies the feedforward gain for a reference command. A unique steady state solution exists ($\dot{P} = 0$) for (5.18), which will be called P_{ss}. Further, by assuming that the reference input we are tracking has a constant steady state value (r_{ss}), we can find the steady state solution g_{ss} as

$$g_{ss} = (P_{ss} B_i R^{-1} B_i^T - A_i^T)^{-1} (H^T Q_i M + P_{ss} G) r_{ss}. \tag{5.20}$$

If we now write the control law as

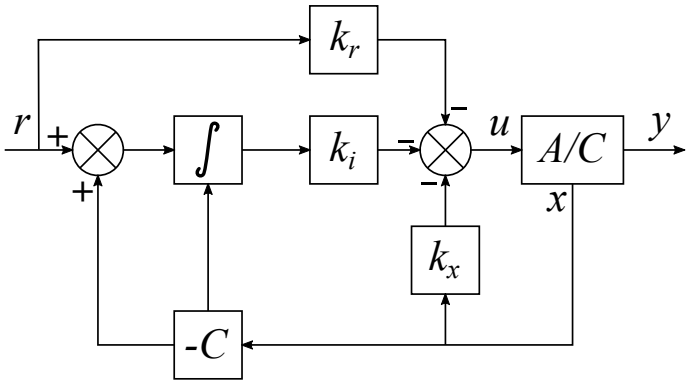

Figure 5.1: Control form for the Linear Quadratic Integral controller with reference command tracking.

$$u = -K_{x_i} x_i - K_r r, \tag{5.21}$$

by inspection of (5.21) and (5.17), we can then define

$$\begin{aligned} K_{x_i} &= -R^{-1} B_i^T P_{ss}, \\ K_r = R^{-1} B_i^T g_{ss} &= R^{-1} B_i^T (P_{ss} B_i R^{-1} B_i^T - A_i^T)^{-1} (H^T Q_i M + P_{ss} G). \end{aligned} \tag{5.22}$$

The result is clearly that once (5.18) and (5.20) have been solved, the resulting optimal state regulation and reference feedforward gains can be computed. Note that K_{x_i} contains both the state feedback gain k_x and the error integral gain k_i, in the form of (5.23). The resulting controller layout is shown in Fig 5.1.

$$K_{x_i} = \begin{bmatrix} k_x & k_i \end{bmatrix} \tag{5.23}$$

It is interesting to note that calculation of the reference gain K_r is independent of the reference command value, and such is correct for any input. Caution must applied however, as this linear model is only valid in a small flight regime and departing too far from this state will lead to errors. The addition of integral augmentation is able to deal with such errors, as well as external disturbances. The trade-off being that the integral gain cannot be too high, as it induces undesirable behaviours such as overshoot or oscillation. This consequently also limits the disturbance rejection performance. The result is that high integral gain is not always a suitable solution to disturbance rejection [51].

5.1.2 LQR Control with Reference Tracking

This section details the development of an LQR controller with reference tracking. The main purpose of this controller is to serve as a baseline for comparison between the LQI and later developed DOBC, which will use the LQR as it's baseline controller to augment.

When solving for an LQR as a regulator, the cost function would comprise the system state and control inputs, as

$$J = \frac{1}{2} \int_0^\infty (x^T Q_r x + u^T R u) dt, \tag{5.24}$$

where the selection of Q_r would allow for tuning the weights placed on individual states by the optimisation routine. However, to aid fairer comparison in simulations, we use the state regulation gain k_x from (5.23) as the LQR gains. This will allow clearer study in

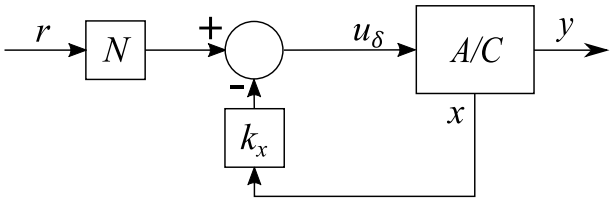

Figure 5.2: Controller layout under state regulation and with reference command tracking.

the simulation of the improvement resulting from adding integral or DOBC augmentation using the same baseline LQR. For later flight tests, the LQI is not tested, so the LQR is designed using (5.24). In either case, the control law is given by

$$u = -k_x x. \tag{5.25}$$

To include reference tracking, we define a new variable N as part of the control law,

$$u = -k_x x + Nr, \tag{5.26}$$

where N is the DC gain of the system. This is the value at which the transfer function from reference command to system output is equal to 1, in steady state. The transfer function for a closed loop system governed by the control law in (5.25) is given by

$$G_{ry} = C(sI - (A - Bk_x))^{-1}BN. \tag{5.27}$$

Again, we assume a steady state solution, so as $t \to \infty$ also $s \to 0$, which simplifies the calculation of (5.27). Setting $G_{ry} = 1$ we now have

$$N = \left[C(-(A - Bk_x))^{-1}B\right]^{-1}. \tag{5.28}$$

The resulting N will drive the system to a step reference command, in the absence of system uncertainty or disturbances. The controller layout is given in Figure 5.2. This figure highlights one of the main issues with this technique: no feedback of the error between reference and output exists. This causes two problems. First, it relies on A, B and C being known exactly. If there is any error in these matrices (as compared to the actual system), there will be steady state error for a given reference. Second, as there is no reference error feedback, there is no robustness to external disturbances, meaning this will also result in steady state error. These issues are the motivation behind adding integral augmentation as in the previous section. However, as discussed, this also has drawbacks. A better solution is DOBC augmentation, the design of which is discussed next.

5.2 Disturbance Observer Augmentation

The design of the disturbance observer and associated disturbance rejection gain is presented in this section. This follows the method described by Yang [87].

5.2.1 Observer Design

In this work, a state space LTI DOBC method is used, as it compliments the chosen modelling and control techniques. We begin with a derivation of a lumped mismatched disturbance observer [87], followed by the definition of the gain needed for disturbance rejection.

For this derivation, we use the state space model with disturbances present,

$$\begin{aligned} \dot{\boldsymbol{x}} &= \boldsymbol{A}\boldsymbol{x} + \boldsymbol{B}\boldsymbol{u} + \boldsymbol{B}_d\boldsymbol{d}, \\ \boldsymbol{y} &= \boldsymbol{C}\boldsymbol{x}, \end{aligned} \tag{5.29}$$

where the matrices have their usual meanings as defined earlier in this work. In this formulation, the disturbances $\boldsymbol{d}$ are only the external ones. To also account for modelling errors, we define the lumped disturbances as

$$\boldsymbol{d}_{lx} = \boldsymbol{B}_d\boldsymbol{d} + (\boldsymbol{A}_t - \boldsymbol{A})\boldsymbol{x} + (\boldsymbol{B}_t - \boldsymbol{B})\boldsymbol{u}, \tag{5.30}$$

where $\boldsymbol{A}_t$ and $\boldsymbol{B}_t$ are the true, unknown matrices which would perfectly describe the system and $\boldsymbol{d}_{lx}$ are the lumped disturbances. The modelled system then becomes

$$\dot{\boldsymbol{x}} = \boldsymbol{A}\boldsymbol{x} + \boldsymbol{B}\boldsymbol{u} + \boldsymbol{B}_{ld}\boldsymbol{d}_{lx} \tag{5.31}$$

First, we define our disturbance estimate dynamics as

$$\dot{\hat{\boldsymbol{d}}}_{lx} = \boldsymbol{L}(\boldsymbol{B}_{ld}\boldsymbol{d}_{lx} - \boldsymbol{B}_{ld}\hat{\boldsymbol{d}}_{lx}).$$

The disturbance measurement is taken from the system model (5.31)

$$\boldsymbol{B}_{ld}\boldsymbol{d}_{lx} = \dot{\boldsymbol{x}} - \boldsymbol{A}\boldsymbol{x} - \boldsymbol{B}\boldsymbol{u},$$

which results in

$$\dot{\hat{\boldsymbol{d}}}_{lx} = \boldsymbol{L}(\dot{\boldsymbol{x}} - \boldsymbol{A}\boldsymbol{x} - \boldsymbol{B}\boldsymbol{u} - \boldsymbol{B}_{ld}\hat{\boldsymbol{d}}_{lx}). \tag{5.32}$$

Here, $\dot{\boldsymbol{x}}$ is not available as a measurement. An auxiliary vector is defined

$$\hat{\boldsymbol{d}}_{lx} = \boldsymbol{z} + \boldsymbol{L}\boldsymbol{x},$$

with its derivative

$$\dot{\hat{\boldsymbol{d}}}_{lx} = \dot{\boldsymbol{z}} + \boldsymbol{L}\dot{\boldsymbol{x}}. \tag{5.33}$$

By substituting (5.33) into (5.32), the disturbance estimation dynamics become

$$\dot{\boldsymbol{z}} + \boldsymbol{L}\dot{\boldsymbol{x}} = \boldsymbol{L}(\dot{\boldsymbol{x}} - \boldsymbol{A}\boldsymbol{x} - \boldsymbol{B}\boldsymbol{u} - \boldsymbol{B}_{ld}\hat{\boldsymbol{d}}_{lx}),$$

which allows for cancellation of $\dot{\boldsymbol{x}}$, leading to the observer

$$\begin{cases} \dot{\boldsymbol{z}} = -\boldsymbol{L}\boldsymbol{B}_{ld}(\boldsymbol{z} + \boldsymbol{L}\boldsymbol{x}) - \boldsymbol{L}(\boldsymbol{A}\boldsymbol{x} + \boldsymbol{B}\boldsymbol{u}), \\ \hat{\boldsymbol{d}}_{lx} = \boldsymbol{z} + \boldsymbol{L}\boldsymbol{x}, \end{cases} \tag{5.34}$$

which is comprised fully of available measurements, inputs and model parameters, thus being realisable. For the stability of the disturbance observer, 3 assumptions are needed:

Assumption 1. The lumped disturbances d_{lx} and their derivatives $\dot{d}_{lx}$ are bounded.

Assumption 2. The lumped disturbances are constant in steady state ($\lim_{t\to\infty} \dot{d}_{lx}(t) = 0$).

Assumption 3. The pair $(\boldsymbol{A}, \boldsymbol{B})$ is controllable.

We can conclude the asymptotic stability of the disturbance observer with the following theorem.

Theorem 1. Suppose assumptions 1 and 2 are satisfied for the system in (5.31). The disturbance estimate can be proven to asymptotically track the lumped disturbance if the observer gain $\boldsymbol{L}$ is chosen such that $-\boldsymbol{L}\boldsymbol{B}_{ld}$ is Hurwitz.

Proof. First, define the estimation error $\boldsymbol{e}_d$ as the difference between the disturbance estimate and true value

$$\boldsymbol{e}_d = \hat{\boldsymbol{d}}_{lx} - \boldsymbol{d}_{lx},$$

which then gives the estimation error dynamics as

$$\begin{aligned}\dot{\boldsymbol{e}}_d &= \dot{\hat{\boldsymbol{d}}}_{lx} - \dot{\boldsymbol{d}}_{lx},\\ &= \dot{\boldsymbol{z}} + \boldsymbol{L}\dot{\boldsymbol{x}} - \dot{\boldsymbol{d}}_{lx},\\ &= -\boldsymbol{L}\boldsymbol{B}_{ld}\hat{\boldsymbol{d}}_{lx} - \boldsymbol{L}\left(\boldsymbol{A}\boldsymbol{x} + \boldsymbol{B}\boldsymbol{u}\right) + \boldsymbol{L}\left(\boldsymbol{A}\boldsymbol{x} + \boldsymbol{B}\boldsymbol{u} + \boldsymbol{B}_{ld}\boldsymbol{d}_{lx}\right) - \dot{\boldsymbol{d}}_{lx},\\ \dot{\boldsymbol{e}}_d &= -\boldsymbol{L}\boldsymbol{B}_{ld}\boldsymbol{e}_d - \dot{\boldsymbol{d}}_{lx}.\end{aligned} \tag{5.35}$$

These error dynamics are asymptotically stable if $-\boldsymbol{L}\boldsymbol{B}_{ld}$ is Hurwitz, $\dot{\boldsymbol{d}}_{lx}$ is bounded and satisfies $\lim_{t\to\infty}\dot{\boldsymbol{d}}_{lx}(t) = 0$. This implies that the disturbance observer estimate can asymptotically track the disturbances. □

An additional result of this the effect of L can be seen more clearly; it shows that a larger value of L will result in a more rapid convergence of the error estimation. This suggests that L should always be chosen to be as large as possible. In reality, there is always a practical limit to the maximum gain. At very high gains, sensor noise can be detected as disturbances on the states, which will lead to poor performance.

Theorem 2. Suppose assumptions 1 and 2 are satisfied, and that the system is controlled by a law of the form shown in (5.36).

$$\boldsymbol{u} = -\boldsymbol{k}_x\boldsymbol{x} + \boldsymbol{k}_{dx}\hat{\boldsymbol{d}}_{lx}, \tag{5.36}$$

The Bounded Input Bounded Output (BIBO) stability of the system under this control law is guaranteed if both $-\boldsymbol{L}\boldsymbol{B}_{ld}$ and $\boldsymbol{A} - \boldsymbol{B}\boldsymbol{k}_x$ are Hurwitz.

Proof. By combining the system (5.29) and control law (5.36) with the error system (5.35) allows the closed loop system to be written as

$$\begin{bmatrix}\dot{\boldsymbol{x}}\\ \dot{\boldsymbol{e}}_d\end{bmatrix} = \underbrace{\begin{bmatrix}\boldsymbol{A} - \boldsymbol{B}\boldsymbol{k}_x & \boldsymbol{B}\boldsymbol{k}_d\\ 0 & -\boldsymbol{L}\boldsymbol{B}_{ld}\end{bmatrix}}_{\boldsymbol{E}}\begin{bmatrix}\boldsymbol{x}\\ \boldsymbol{e}_d\end{bmatrix} + \begin{bmatrix}\boldsymbol{B}\boldsymbol{k}_d + \boldsymbol{B}_l d & 0\\ 0 & -1\end{bmatrix}\begin{bmatrix}\boldsymbol{d}_{lx}\\ \dot{\boldsymbol{d}}_{lx}\end{bmatrix}. \tag{5.37}$$

Since $-\boldsymbol{L}\boldsymbol{B}_{ld}$ is selected to be Hurwitz and $\boldsymbol{A} - \boldsymbol{B}\boldsymbol{k}_x$ is Hurwitz as a result of the LQR design routine, it can be said that the matrix $\boldsymbol{E}$ is also Hurwitz. Therefore it can be concluded that the closed loop system (5.37) is BIBO stable for any bounded $\boldsymbol{d}_{lx}$ and $\dot{\boldsymbol{d}}_{lx}$ if $\boldsymbol{L}$ and $\boldsymbol{k}_x$ are properly selected. □

Together, these two theorems demonstrate that the observer estimation is stable, and as such the closed loop dynamics of the system under the control law (5.36) is also stable. Further details can be found in many of the published works on this observer design [51,87].

In this work, the DOBC method is applied to flight control, which is subject to non-steady disturbances. This means that the assumption $\dot{\boldsymbol{d}}_{lx} \approx 0$ does not hold. However, it can still be said that if $|\dot{\boldsymbol{d}}_{lx}|$ is bounded, the estimation error is still also bounded [51]. It has been demonstrated [59] that if the observer dynamics are sufficiently faster than the disturbance dynamics, good disturbance rejection is still possible. This is investigated in later sections with flight test data.

5.2.2 Disturbance Compensation Gain

With an estimate of the disturbances obtained, it remains to define the gain which would remove the effect of these disturbances on the system output. First, we consider the general system subjected to lumped disturbances given by

$$\dot{\boldsymbol{x}} = \boldsymbol{A}\boldsymbol{x} + \boldsymbol{B}\boldsymbol{u} + \boldsymbol{B}_{ld}\boldsymbol{d}_{lx},$$

under both feedback and DOBC control defined as

$$\boldsymbol{u} = -\boldsymbol{k}_x\boldsymbol{x} + \boldsymbol{k}_{dx}\hat{\boldsymbol{d}}_{lx},$$

resulting in a closed loop response given by

$$\dot{\boldsymbol{x}} = (\boldsymbol{A} - \boldsymbol{B}\boldsymbol{k}_x)\boldsymbol{x} + \boldsymbol{B}\boldsymbol{k}_{dx}\hat{\boldsymbol{d}}_{lx} + \boldsymbol{B}_{ld}\boldsymbol{d}_{lx}.$$

Disturbances can only be removed from as many states as there are control inputs. Therefore, we aim to remove the influence of the disturbances from the system output, $\boldsymbol{y} = \boldsymbol{C}\boldsymbol{x}$, rather than the state

$$\boldsymbol{y} = \underbrace{\boldsymbol{C}\left(\boldsymbol{A} - \boldsymbol{B}\boldsymbol{k}_x\right)^{-1}}_{\boldsymbol{S}}\left[\dot{\boldsymbol{x}} - \boldsymbol{B}\boldsymbol{k}_{dx}\hat{\boldsymbol{d}}_{lx} - \boldsymbol{B}_{ld}\boldsymbol{d}_{lx}\right].$$

Now, we assume that the disturbance is constant and we aim to remove its effect from the output as $t \to \infty$. This means that $\boldsymbol{y} = 0$, giving

$$\boldsymbol{S}\boldsymbol{B}\boldsymbol{k}_{dx}\hat{\boldsymbol{d}} = \boldsymbol{S}\boldsymbol{B}_{ld}\boldsymbol{d},$$

as we have a stable observer, we can say that $\lim_{t\to\infty}(\hat{\boldsymbol{d}} - \boldsymbol{d}) = 0$, which therefore defines

$$\begin{aligned}\boldsymbol{k}_{dx} &= (\boldsymbol{S}\boldsymbol{B})^{-1}\boldsymbol{S}\boldsymbol{B}_{ld},\\ &= \left[\boldsymbol{C}(\boldsymbol{A} - \boldsymbol{B}\boldsymbol{k}_x)^{-1}\boldsymbol{B}\right]^{-1}\left[\boldsymbol{C}(\boldsymbol{A} - \boldsymbol{B}\boldsymbol{k}_x)^{-1}\boldsymbol{B}_{ld}\right].\end{aligned}$$

This gain defines the control input which will remove the effect of a disturbance from the output as long as the disturbance estimate is accurate. However, in this current state, the observer is susceptible to windup due to control saturation. The novel anti-windup modification is presented next, which aims to mitigate this issue.

5.2.3 Anti-Wind Up Modification

To understand how saturation affects the disturbance observer, we must first study how it enters the system. The previously designed observer relies on the system model in (5.29). When saturation exists for the physical system, it is modelled instead by

$$\dot{\boldsymbol{x}} = \boldsymbol{A}\boldsymbol{x} + \boldsymbol{B}\bar{\boldsymbol{u}} + \boldsymbol{B}_{ld}\boldsymbol{d}_{lx}, \tag{5.38}$$

where $\bar{\boldsymbol{u}}$ is defined by

$$\bar{\boldsymbol{u}} = \begin{cases} \boldsymbol{u}_{max}, & \text{for } \boldsymbol{u} \geq \boldsymbol{u}_{max},\\ \boldsymbol{u}, & \text{for } \boldsymbol{u}_{min} < \boldsymbol{u} < \boldsymbol{u}_{max},\\ \boldsymbol{u}_{min}, & \text{for } \boldsymbol{u} \leq \boldsymbol{u}_{min},\end{cases}$$

where $\boldsymbol{u}_{min}$ and $\boldsymbol{u}_{max}$ are the minimum and maximum amplitudes for a given control input. A mismatch is clearly present between the observer and the plant. To understand the effects, we look again at the error dynamics of the observer. As in (5.35), the dynamics are modelled by

$$\begin{aligned}\dot{\boldsymbol{e}}_d &= \dot{\hat{\boldsymbol{d}}}_{lx} - \dot{\boldsymbol{d}}_{lx},\\ &= \dot{\boldsymbol{z}} + \boldsymbol{L}\dot{\boldsymbol{x}} - \dot{\boldsymbol{d}}_{lx}.\end{aligned}$$

It is here that the error appears. The internal state of the observer, $\dot{\boldsymbol{z}}$, depends on the system model which does not include saturation. The state dynamics of the plant, $\dot{\boldsymbol{x}}$, are subject to control saturation as described in (5.38), which gives

$$\dot{\boldsymbol{e}}_d = \underbrace{\boldsymbol{L}\boldsymbol{B}_{ld}(\boldsymbol{z}+\boldsymbol{L}\boldsymbol{x}) - \boldsymbol{L}(\boldsymbol{A}\boldsymbol{x}+\boldsymbol{B}\boldsymbol{u})}_{\dot{\boldsymbol{z}}} + \underbrace{\boldsymbol{L}(\boldsymbol{A}\boldsymbol{x}+\boldsymbol{B}\bar{\boldsymbol{u}}+\boldsymbol{d}_{lx})}_{\boldsymbol{L}\dot{\boldsymbol{x}}} + \dot{\boldsymbol{d}}_{lx},$$

after collecting terms we get

$$\dot{\boldsymbol{e}}_d = -\boldsymbol{L}\boldsymbol{B}_{ld}\boldsymbol{e}_d + \boldsymbol{L}\boldsymbol{B}(\bar{\boldsymbol{u}}-\boldsymbol{u}) + \dot{\boldsymbol{d}}_{lx}.$$

Comparing this to the error dynamics in (5.35), an additional term is present which describes the effect of unmodelled saturation on the disturbance observer. To understand how this error results in windup, we look to the closed loop dynamics of the system. Under the control law (5.36), the closed loop dynamics of (5.38) are

$$\begin{aligned}
\dot{\boldsymbol{x}} &= \boldsymbol{A}\boldsymbol{x} + \boldsymbol{B}\bar{\boldsymbol{u}} + \boldsymbol{B}_{ld}\boldsymbol{d}_{lx}, \\
&= \boldsymbol{A}\boldsymbol{x} + \boldsymbol{B}\boldsymbol{u} + \boldsymbol{B}_{ld}\boldsymbol{d}_{lx} + \boldsymbol{B}\underbrace{(\bar{\boldsymbol{u}}-\boldsymbol{u})}_{\boldsymbol{S}_u}, \\
&= (\boldsymbol{A}+\boldsymbol{B}\boldsymbol{k}_x)\boldsymbol{x} + (\boldsymbol{B}\boldsymbol{k}_{dx}+\boldsymbol{B}_{ld})\boldsymbol{d}_{lx} - \underbrace{\boldsymbol{B}\boldsymbol{k}_{dx}\boldsymbol{e}_d + \boldsymbol{B}\boldsymbol{S}_u}_{\textit{saturation effect}},
\end{aligned}$$

since $\boldsymbol{e}_d$ itself is a term of $\boldsymbol{S}_u$, the *saturation effect* denotes the total effect of saturation on the dynamics. To ease analysis, we make the assumption that $\boldsymbol{B} = \boldsymbol{B}_{ld}$. This is done without loss of generality, but in this case results in $\boldsymbol{k}_{dx} = -\boldsymbol{I}$, which makes for more intuitive analysis. Recalling that the disturbance estimate dynamics defined as

$$\dot{\hat{\boldsymbol{d}}}_{lx} = -\boldsymbol{L}\boldsymbol{B}_{ld}(\hat{\boldsymbol{d}}_{lx} - \boldsymbol{d}_{lx}) + \boldsymbol{L}\boldsymbol{B}\boldsymbol{S}_u,$$

an intuitive understanding of the disturbance observer behaviour can be obtained. Considering the case where $\bar{\boldsymbol{u}} - \boldsymbol{u} \leq 0$, in the absence of other factors we can say this positive control saturation must be the result of a negative disturbance. The dynamics of the disturbance estimate in this case indicates that the estimate will have a negative rate, meaning the estimate becomes more negative than the true value. As the estimate grows larger, the control saturation exacerbates, leading to an even larger estimate of the disturbance. It is clear to see that this is how windup enters the disturbance observer dynamics, and translates to the dynamics of the physical system.

Theorem. By applying theory of the classical anti-windup modification [108], an additional term $\boldsymbol{k}_a\boldsymbol{S}_u$ can be added to the observer as

$$\begin{cases} \dot{\boldsymbol{z}} = -\boldsymbol{L}\boldsymbol{B}_{ld}(\boldsymbol{z}+\boldsymbol{L}\boldsymbol{x}) - \boldsymbol{L}(\boldsymbol{A}\boldsymbol{x}+\boldsymbol{B}\boldsymbol{u}) + \boldsymbol{k}_a\boldsymbol{S}_u \\ \hat{\boldsymbol{d}}_{lx} = \boldsymbol{z} + \boldsymbol{L}\boldsymbol{x}, \end{cases} \tag{5.39}$$

where $\boldsymbol{k}_a$ is an anti-windup gain matrix to be designed to alleviate the windup effect.

Proof. Following the same procedure to define the estimation dynamics for this observer, we arrive at

$$\dot{\boldsymbol{e}}_d = -\boldsymbol{L}\boldsymbol{B}_{ld}\boldsymbol{e}_d + (\boldsymbol{L}\boldsymbol{B}+\boldsymbol{k}_a)\boldsymbol{S}_u + \dot{\boldsymbol{d}}_{lx}.$$

It is clear that by defining

$$\boldsymbol{k}_a = -\boldsymbol{L}\boldsymbol{B}, \tag{5.40}$$

then the estimation dynamics revert to

$$\dot{\boldsymbol{e}}_d = -\boldsymbol{L}\boldsymbol{B}_{ld}\boldsymbol{e}_d + \dot{\boldsymbol{d}}_{lx},$$

which is equivalent to the dynamics in (5.35) for the observer with no saturation. □

By applying the gain term from (5.40) to the modified observer (5.39), we find that

$$\begin{cases} \dot{\boldsymbol{z}} = -\boldsymbol{L}\boldsymbol{B}_{ld}(\boldsymbol{z} + \boldsymbol{L}\boldsymbol{x}) - \boldsymbol{L}(\boldsymbol{A}\boldsymbol{x} + \boldsymbol{B}\bar{\boldsymbol{u}}), \\ \hat{\boldsymbol{d}}_{lx} = \boldsymbol{z} + \boldsymbol{L}\boldsymbol{x}, \end{cases}$$

is equivalent. Including the saturated control input directly in the observer reduces complexity of implementation, thus reducing the risk of errors. Crucially, it has been proven that this form is stable. In the following section, the performance of the proposed anti-windup scheme is studied with both simulation results and flight testing.

To demonstrate the effect of the anti-windup modification, a simulation was conducted to purposefully induce windup. Figs. 5.3 and 5.4 show the applied disturbance and associated observer estimates, the demanded throttle (i.e. controller output) and the resulting height profile for the same DOBC configuration without and with anti-windup (aw) modification. The initial disturbance on u, $u_d = -0.5$, does not lead to saturation of the throttle, and as such no windup occurs. When u_d is increased to -0.75, however, we see that the demanded throttle exceeds 100%, which leads to control saturation. Subsequently, we see clearly that the estimate for the unmodified DOBC enters the windup phase. Due to the unmodelled saturation, the observer estimates that the disturbance must be larger in magnitude which leads to the application of more throttle. No additional response is seen in h, meaning the observer continues to increase its estimate and the demanded throttle. This is windup due to control saturation. The modified observer correctly estimates the disturbance and suffers no windup. When the disturbance is removed, both estimates begin to adjust at the same time. However, due to the windup of the unmodified observer, a significant lag is in place and it takes much longer to approach the true disturbance value. This leads to a large overshoot in height.

This simple and highly controlled example demonstrates clearly how windup is caused, as well as the effect it has on the system. In the following section, more representative simulations are conducted to further demonstrate windup, with comparison to additional controllers, followed by flight testing.

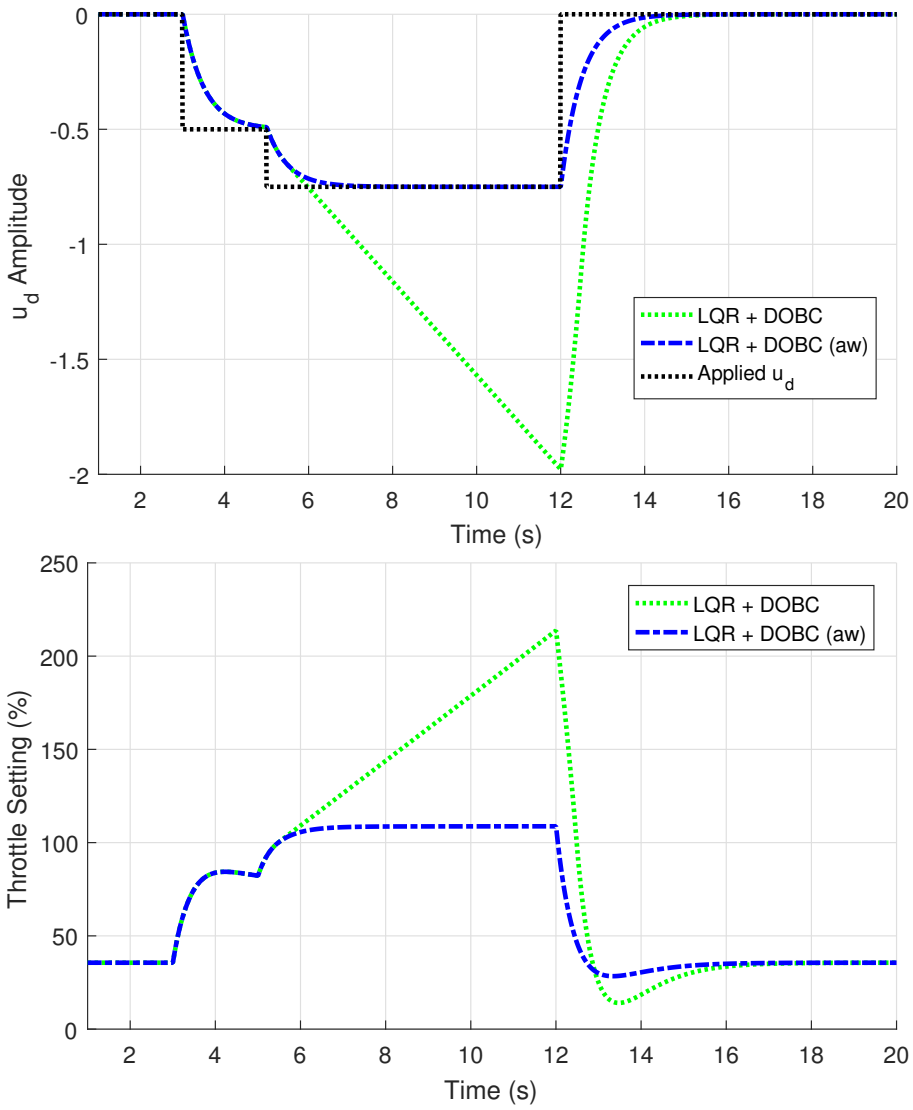

Figure 5.3: A comparison of the applied and estimated disturbance (top) and the demanded throttle (bottom) without and with anti-windup (aw) modification.

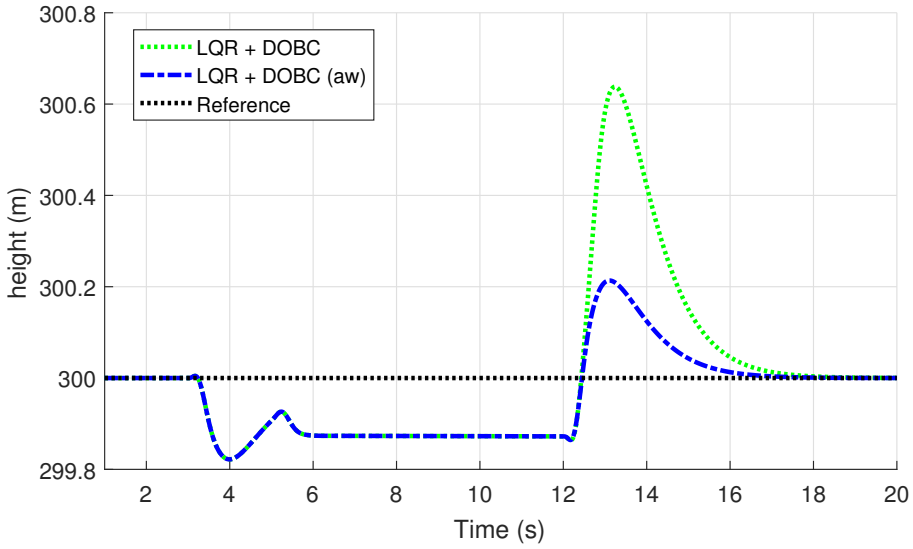

Figure 5.4: Demanded throttle for the simulation in Fig. 5.3 without and with anti-windup (aw) modification.

5.3 Simulation Study

For the performance analysis of the proposed method, a simulation study was conducted using a state space simulation of the longitudinal X8 dynamics. For these simulations, the longitudinal dynamics of the Skywalker X8 were used. The original state space model (4.30) is modified to also include the kinematic height of the aircraft, given below as h,

$$\dot{\boldsymbol{x}} = \underbrace{\begin{bmatrix} X_u & X_w & X_q & -g\cos\theta^* & 0 \\ Z_u & Z_w & Z_q & -g\sin\theta^* & 0 \\ M_u & M_w & M_q & 0 & 0 \\ 0 & 0 & 1 & 0 & 0 \\ \sin\theta^* & -\cos\theta^* & 0 & u^*\cos\theta^* + w^*\sin\theta^* & 0 \end{bmatrix}}_{\boldsymbol{A}} \underbrace{\begin{bmatrix} u \\ w \\ q \\ \theta \\ h \end{bmatrix}}_{\boldsymbol{x}} + \underbrace{\begin{bmatrix} 0 & X_{\delta t} \\ Z_{\delta\epsilon} & 0 \\ M_{\delta\epsilon} & 0 \\ 0 & 0 \\ 0 & 0 \end{bmatrix}}_{\boldsymbol{B}} \underbrace{\begin{bmatrix} \delta_e \\ \delta_t \end{bmatrix}}_{\boldsymbol{u}},$$
$$\boldsymbol{y} = \underbrace{\begin{bmatrix} 1 & 0 & 0 & 0 & 0 \\ 0 & 0 & 0 & 0 & 1 \end{bmatrix}}_{\boldsymbol{C}} \boldsymbol{x}, \tag{5.41}$$

with u and h being the controlled outputs. For this model, the state disturbances and disturbance mapping matrix are given as

$$\boldsymbol{d}_x = \begin{bmatrix} u_d \\ w_d \\ q_d \\ 0 \\ h_d \end{bmatrix}, \qquad \boldsymbol{B}_{ld} = I^{5\times 5},$$

as θ is a kinematic relationship to q, disturbances are not considered on this state. For comparison, a total of 4 control schemes will be used. The baseliine LQR given by (5.26), the LQI given by (5.21) and the DOBC given by

$$\boldsymbol{u} = -\boldsymbol{k}_x\boldsymbol{x} + \boldsymbol{N}\boldsymbol{r} + \boldsymbol{k}_{dx}\hat{\boldsymbol{d}}_{lx}, \tag{5.42}$$

where $\hat{\boldsymbol{d}}_{lx}$ is given by the nominal disturbance observer (5.34) and the anti-windup modified observer (5.39). The addition of feedforward reference gain in (5.42) has no effect on the observer dynamics other than contributing to possible actuator saturation and subsequent observer windup. The tuning matrices for the LQI, along with the resulting gains for all controllers are given as

$$Q_i = \begin{bmatrix} 1 & 0 & 0 & 0 \\ 0 & 0.05 & 0 & 0 \\ 0 & 0 & 1 & 0 \\ 0 & 0 & 0 & 0.05 \end{bmatrix}, \qquad R = \begin{bmatrix} 1 & 0 \\ 0 & 1 \end{bmatrix},$$

$$k_r = \begin{bmatrix} -0.435 & 0.337 \\ -1.50 & -0.232 \end{bmatrix}, \qquad k_i = \begin{bmatrix} -0.440 & 0.201 \\ -0.898 & -0.098 \end{bmatrix},$$

$$k_x = \begin{bmatrix} 0.385 & 0.109 & -0.199 & -2.48 & -0.337 \\ 0.663 & -0.015 & -0.027 & -0.106 & 0.232 \end{bmatrix},$$

$$k_{dx} = \begin{bmatrix} 0 & -0.016 & 0.016 & 0.397 & 0.165 \\ -0.407 & 0.019 & 0.008 & -0.203 & -0.259 \end{bmatrix},$$

Table 5.1: Summary of disturbances applied during the state space mixed disturbance simulation.

Disturbance	Magnitude	Time Active (s)
w_d	10	5→60
q_d	2	20→60
h_d	-1	30→32

$$L = \begin{bmatrix} 10 & 0 & 0 & 0 & 0 \\ 0 & 10 & 0 & 0 & 0 \\ 0 & 0 & 10 & 0 & 0 \\ 0 & 0 & 0 & 10 & 0 \\ 0 & 0 & 0 & 0 & 10 \end{bmatrix}.$$

For these simulations, the LQR feedback gains are taken from the LQI output, as per the relationship given in (5.23) which allows for the assessment of windup responses with minimal external factors.

5.3.1 Purpose of Comparison Controller Designs

Several control configurations are compared in these simulations. The LQR is included as a comparison baseline of a control method which is not susceptible to windup. The LQI is included to demonstrate the effect of windup on classical methods. Many methods for anti-windup of classical integral methods exist [95, 112], which could be used to alleviate the effect on the LQI. These are not considered in these simulations, as the unmodified LQI is only included to provide context of the windup problem when studying the DOBC method. These simulations are focused on studying the function of the proposed anti-windup method only.

5.3.2 Numerical Linear State Space Simulations

Numerical simulations are first produced. These allow study with no external disturbances and full control of modelling errors, if any are desired.

Step Disturbances

We begin with a series of step disturbances and constant reference commands. The disturbances applied are summarised in Table 5.1, with results in Figs. 5.5 and 5.6. Prior to $t = 30s$, no windup is seen for any controllers, although the DOBC schemes are outperforming the baseline LQR and augmented LQI substantially. For the third disturbance, the magnitude is above what the system is able to reject, resulting in control saturation. This is evident from $t = 32s$, where both the LQI and unmodified DOBC give significant overshoot. The LQR controller has no means to suffer from windup and as such, returns to its previous state with no overshoot. The modified DOBC scheme shows the same behaviour, which demonstrates clearly that the anti-windup modification works in this instance.

Reference Tracking with a Step Disturbance

In this simulation, a high rate 15m descent reference command is issued. Furthermore, a disturbance of $q_d = -22$ added to the simulation at $t = 20s$. The results are shown in

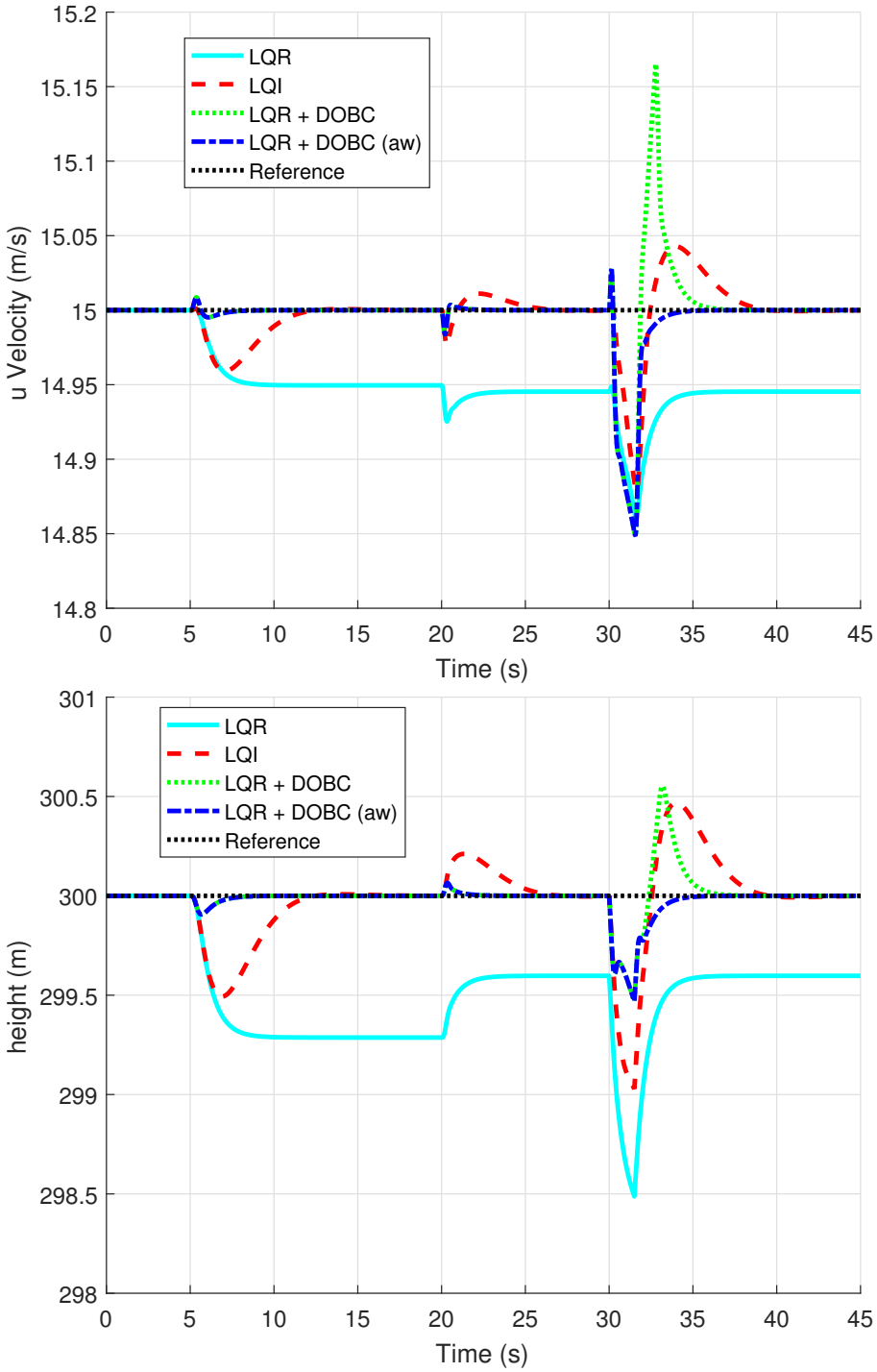

Figure 5.5: Aircraft u and h response when subject to w_d, q_d and h_d disturbances.

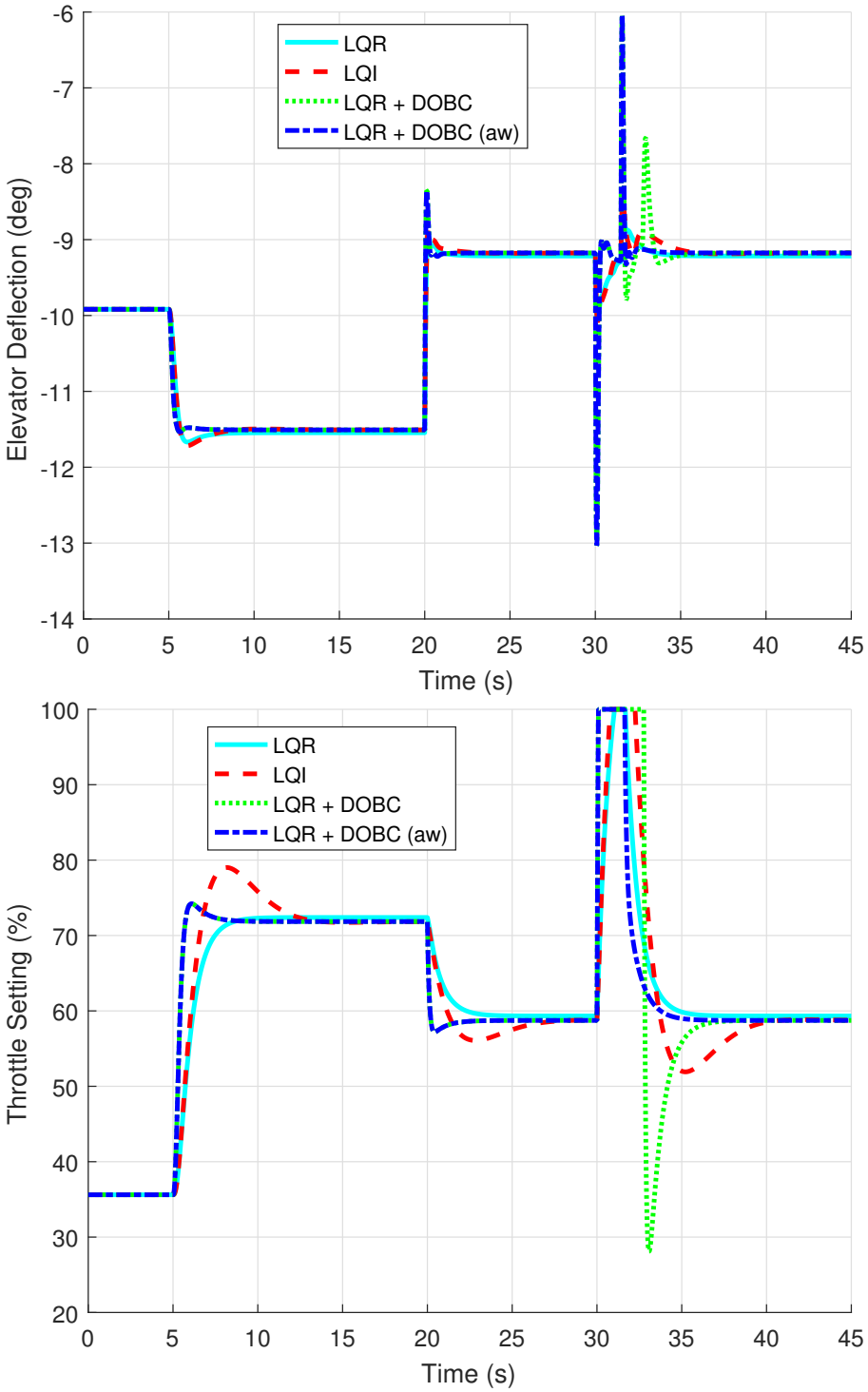

Figure 5.6: Elevator and throttle setting when subject to w_d, q_d and h_d disturbances.

Figs. 5.7 and 5.8. The rate is sufficiently high that the aircraft cannot track it without violating the u reference command, which results in saturation of the throttle during the descent. The differences in disturbance rejection are vast. Due to the induced windup during the descent, both the LQI and unmodified DOBC are completely unable to reject the disturbance, with the DOBC showing worse performance. However, the LQR and modified DOBC both show much better performance, with the latter being the best by some margin. If this were a landing scenario (with a runway at 285m above sea level, for example), all controllers but the anti-windup modified DOBC would have crashed as they descended below the runway. This simulation therefore also highlights the potential safety advantages of the designed anti-windup method.

It is also interesting to note that, despite the system being able to reject the disturbances (as demonstrated by the LQR and DOBC), due to the windup the other two controllers overshoot the reference by too much, and then suffer windup in the opposite direction. In this case, the systems have both become unstable with the aircraft continuing to loose altitude and velocity. This further supports the argument for not only improved disturbance rejection but better robustness with an anti-windup method.

Non-Continuous Disturbances

Next, we study the effect of changing disturbances and the effect of windup on the ability of the controller to reject them. Figures 5.9 and 5.10 show the results from 3 different q_d disturbances acting on the aircraft, from $t = 7s$ to $t = 28s$ in $7s$ steps.

In the initial $7s < t < 14s$ period, no saturation is present and we see that both DOBC controllers have the same performance. Between $14s < t < 21s$, saturation does occur. Here we see no difference in the performance of the two observer based schemes; simply, there is insufficient control authority to alter the response. However, as the disturbance reduces between $21s < t < 28s$, we see a significant difference. Both the LQI and unmodified DOBC schemes suffer from significant overshoot - this is a direct result of the windup during the previous disturbance. The modified observer does not suffer any windup and quickly returns to the reference command. It is in this response that we see a further difference between the observer responses. Fig. 5.10 shows the throttle response; here we can see that, due to the windup, the unmodified observer suffers a lag in response time. Both the anti-windup modified observer and the LQR, which is not susceptible to windup, reduce their throttle inputs at almost exactly 21s, when the disturbance changes. Due to the windup however, both the LQI and unmodified DOBC take until $t = 23s$ before any throttle action is taken. This is a significant delay in the response, and highlights a second benefit of the anti-windup scheme beyond eliminating overshoot in the response: removing delays in response brought about by windup.

Stochastic Disturbances

The stability of the disturbance observer is only guaranteed in the case where the rate of change of the disturbance is 0. However, as discussed in Section 5.2.1, if the observer dynamics are sufficiently fast, a non continuous disturbance can also be rejected. This performance is achieved with high observer gains, which can be applied in simulation. More care will be required when selecting high gains in flight testing, as the observer may become sensitive enough to detect sensor noise.

As discussed in the varying disturbance simulation study, it has been shown that when windup has occurred, subsequent responses by that observer become delayed until the effect of the windup is removed. To study this further, Figs. 5.11 and 5.12 show a simulation response to a Dryden generated stochastic disturbance added to the u_d channel of the model. The disturbance is active for $5s < t < 30s$.

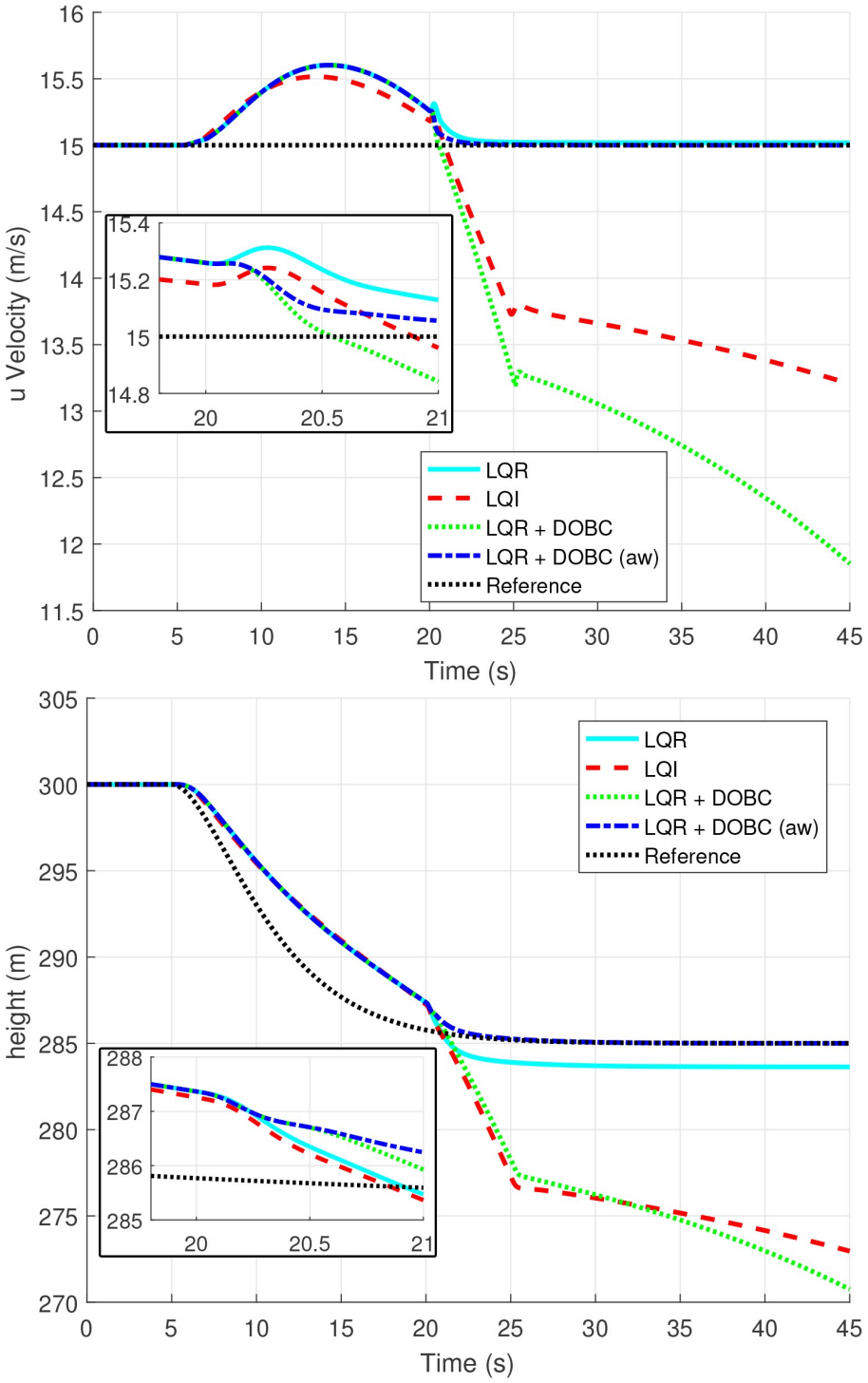

Figure 5.7: Aircraft u and h during a height reference tracking manoeuvre. A disturbance is added at $t = 20s$.

First, we notice that both the DOBC methods offer far better disturbance rejection performance than the integral controller. This further substantiates the claims that sufficiently fast observer dynamics allows for the rejection of non-continuous disturbances. At $t = 16s$, throttle saturation occurs once again and we notice that there is a similar lag in the throttle response for the unmodified DOBC controller. Further, a larger elevator deflection is seen at the same time. In this case, it appears that the controller was able to use the remaining control surfaces to attempt to maintain the reference command. However, the output responses show that the LQI and unmodified DOBC both suffer from

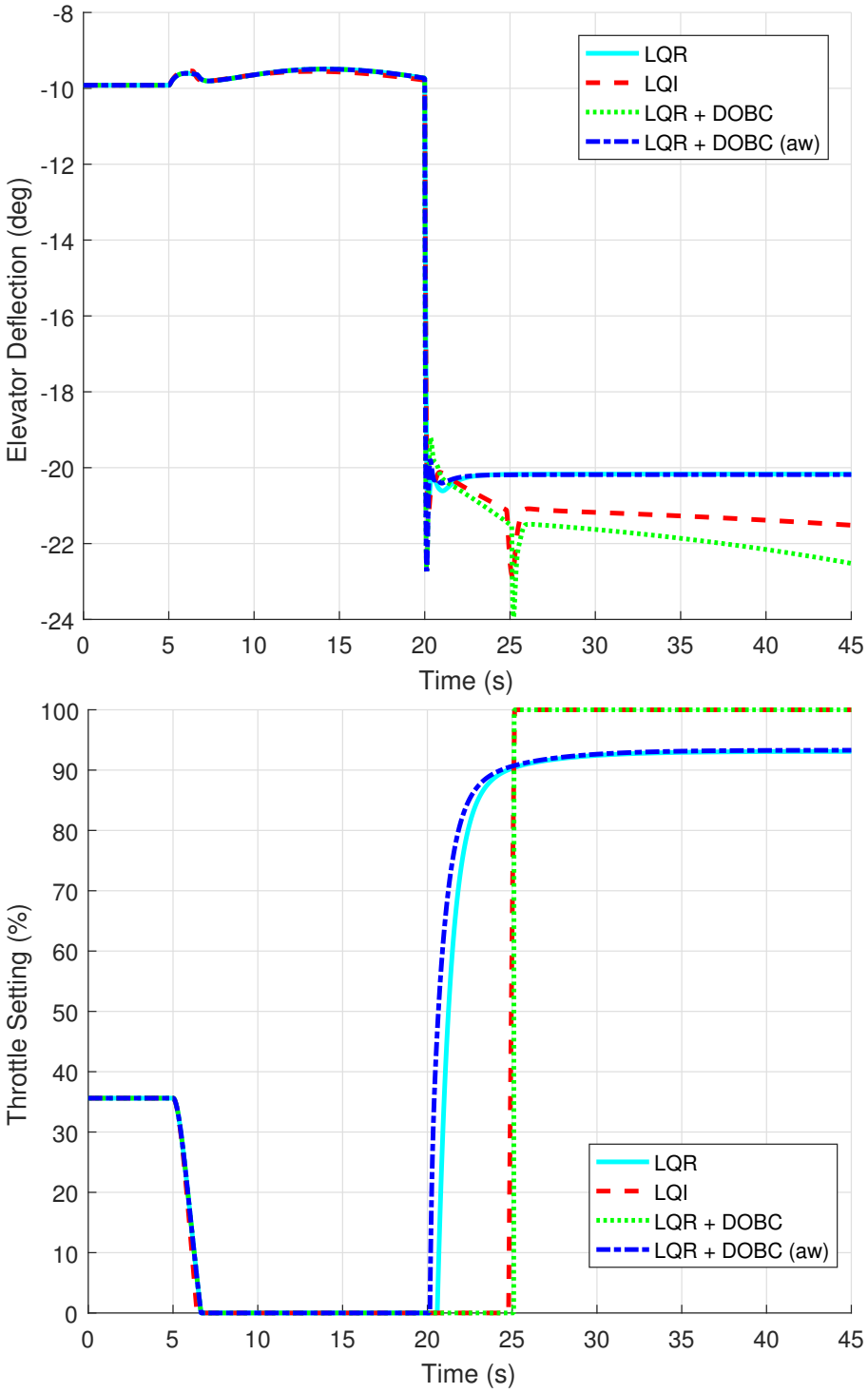

Figure 5.8: Elevator and throttle setting during a height reference tracking manoeuvre. A disturbance is added at $t = 20s$.

significant overshoot still. The error in height is however reduced for the DOBC controller, due to the larger elevator deflection over the LQI.

Although it has not clearly been shown that the controller windup reduces response rate in the output graphs, it is once again clear in the control input that a lag in response is present.

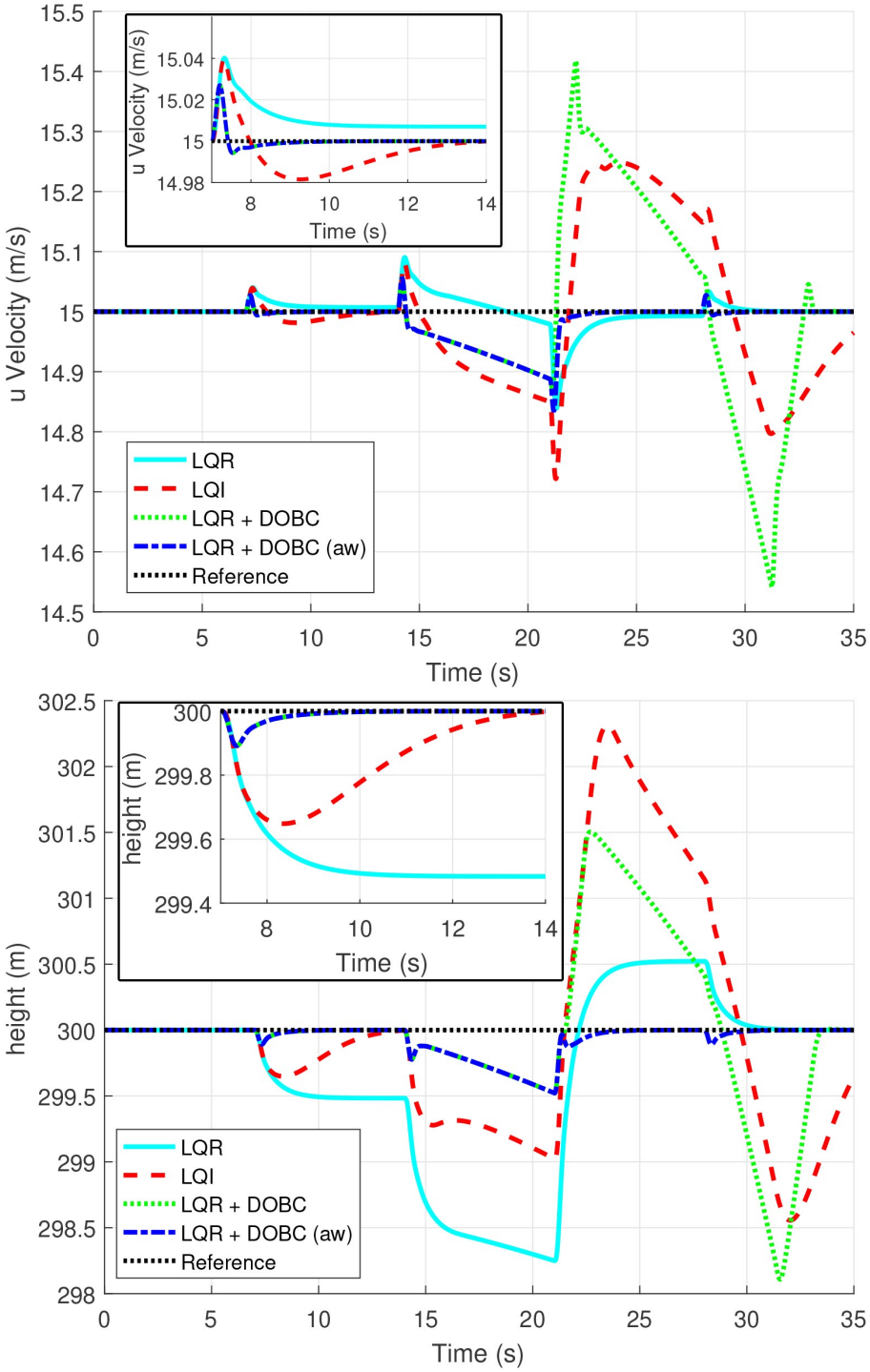

Figure 5.9: Aircraft u and h tracking with varying q_d disturbances.

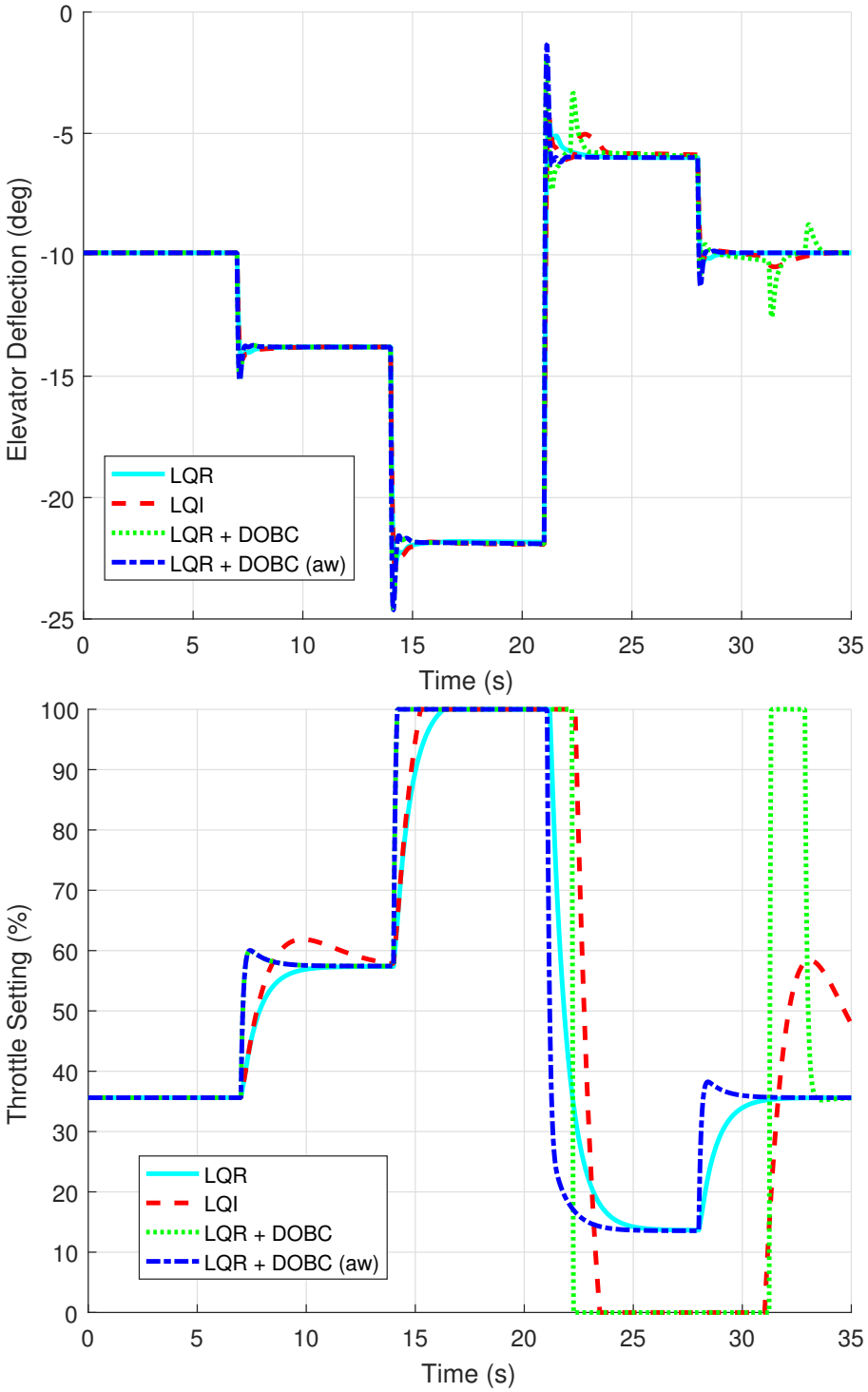

Figure 5.10: Elevator and throttle setting with varying q_d disturbances.

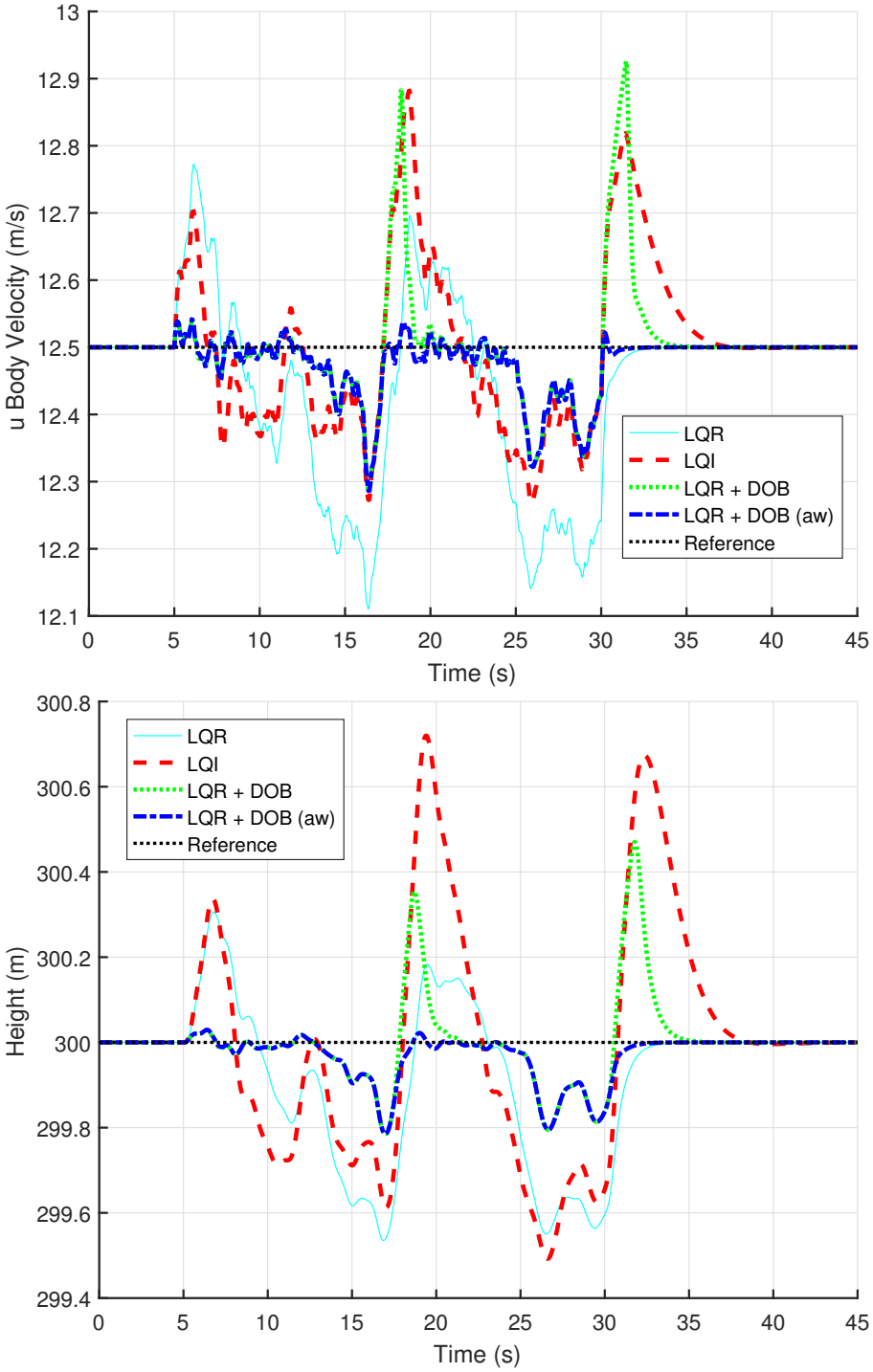

Figure 5.11: Aircraft u and h tracking with a Dryden u_d disturbance.

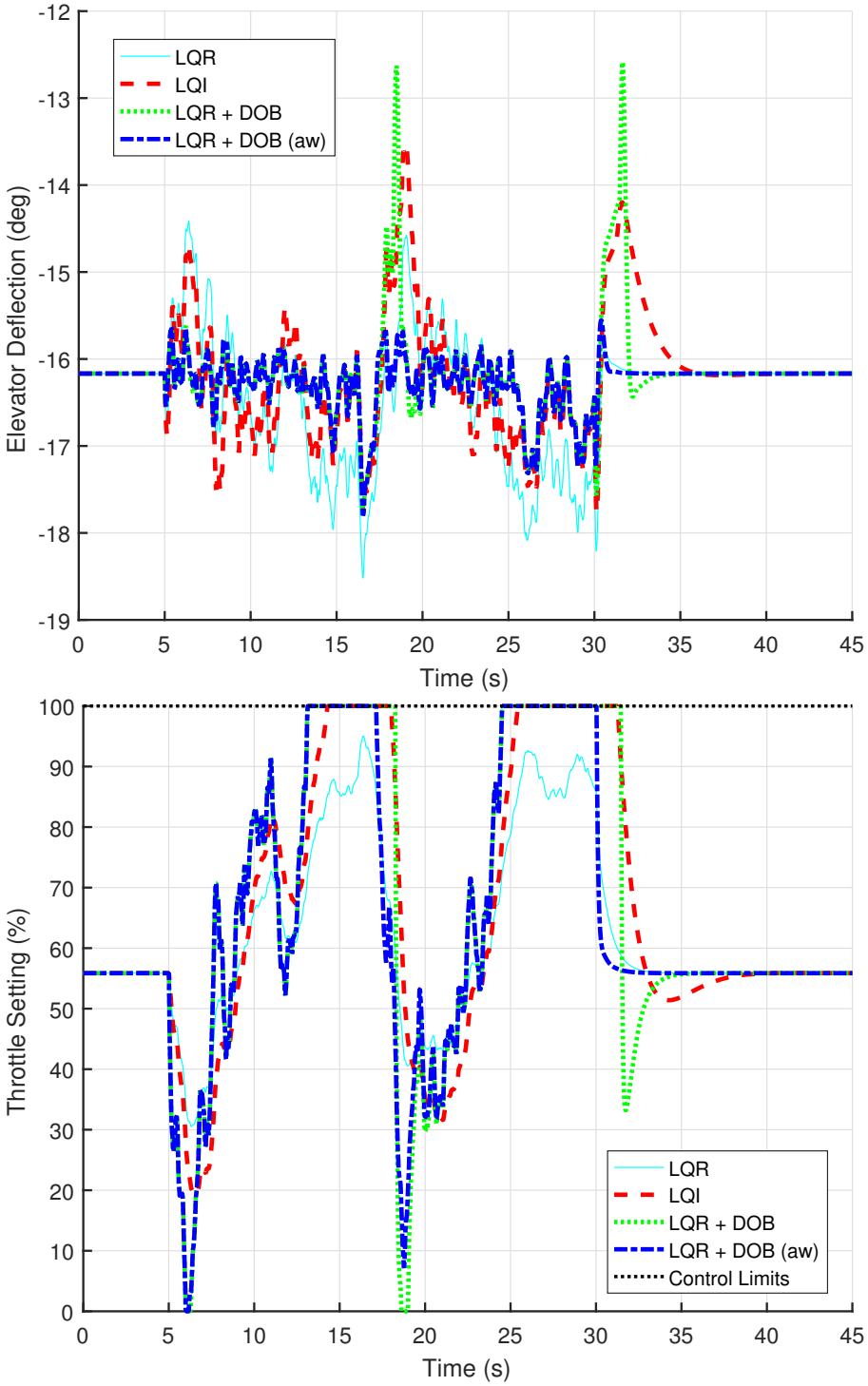

Figure 5.12: Elevator and throttle setting with a Dryden u_d disturbance.

Table 5.2: Summary of disturbances applied during the X-Plane mixed disturbance simulation.

Disturbance	Magnitude	Time Active (s)
u_d	-1	35→75
w_d	22	22→75
q_d	-1.5	35→75

5.3.3 X-Plane Simulations

The numerical simulations provided an unclouded insight into the behaviour of the controllers in an uncluttered simulation environment. Next, the verified X-Plane simulation will be used to verify the responses. With X-Plane, not only will the imposed disturbances be acting, but other, uncontrolled disturbances such as modelling errors will inevitably exist. For these simulations, $\boldsymbol{R}$ and $\boldsymbol{L}$ gains were tuned to reduce the controller aggression. This was done to ensure stability of the controllers during their assessment. All adjustments were made equally so comparisons between responses in these simulations remain valid.

For these simulations, the references are chosen once more to represent a landing scenario. First, velocity is reduced before a descent is commanded. This serves two purposes. Firstly, it is representative of the a landing sequence. Secondly, this intentionally brings the aircraft away from the trim condition around which the model, and subsequently the controllers, were obtained. This allows for study of the off-model performance of the various controllers. Good performance here indicates suitability for flight testing.

Figs. 5.13 and 5.14 give the results with the applied disturbances summarised in Table 5.2. The first key point of this simulation is, despite the forced modelling errors, the anti-windup modified DOBC still offers a significant improvement over the alternative methods. During the initial $35s$, the reference commands cannot be tracked perfectly so there is a common level of error between the various controllers. However, after the initial period we can see once again that the LQI and unmodified DOBC both suffer from windup and subsequently poor performance. The anti-windup modified DOBC shows no such effects and is able to settle to the final reference commands easily. We note also that once again the windup has led to a significant undershoot of the reference height command, which could represent very dangerous circumstances for the aircraft if this were a landing.

In this simulation, we can clearly see that windup induced prior to the disturbance at $35s$ has impaired recovery of the LQI and unmodified DOBC. The modified DOBC show that the system is able to fully reject the disturbance and maintain the reference command. The controllers suffering from windup are not able to respond in time and show a significant undershoot, which then leads to a large overshoot. The reason is clear when studying the commanded throttle inputs. During the long descent, a significant windup term would have acrued within both the LQI and unmodified DOBC. This causes a severe lag in the response with the unmodified DOBC responding at around 38s, and the LQI at around 39s. The anti-windup DOBC was able to respond immediately to the disturbance. This very clearly highlights the function and benefit of the anti-windup modification.

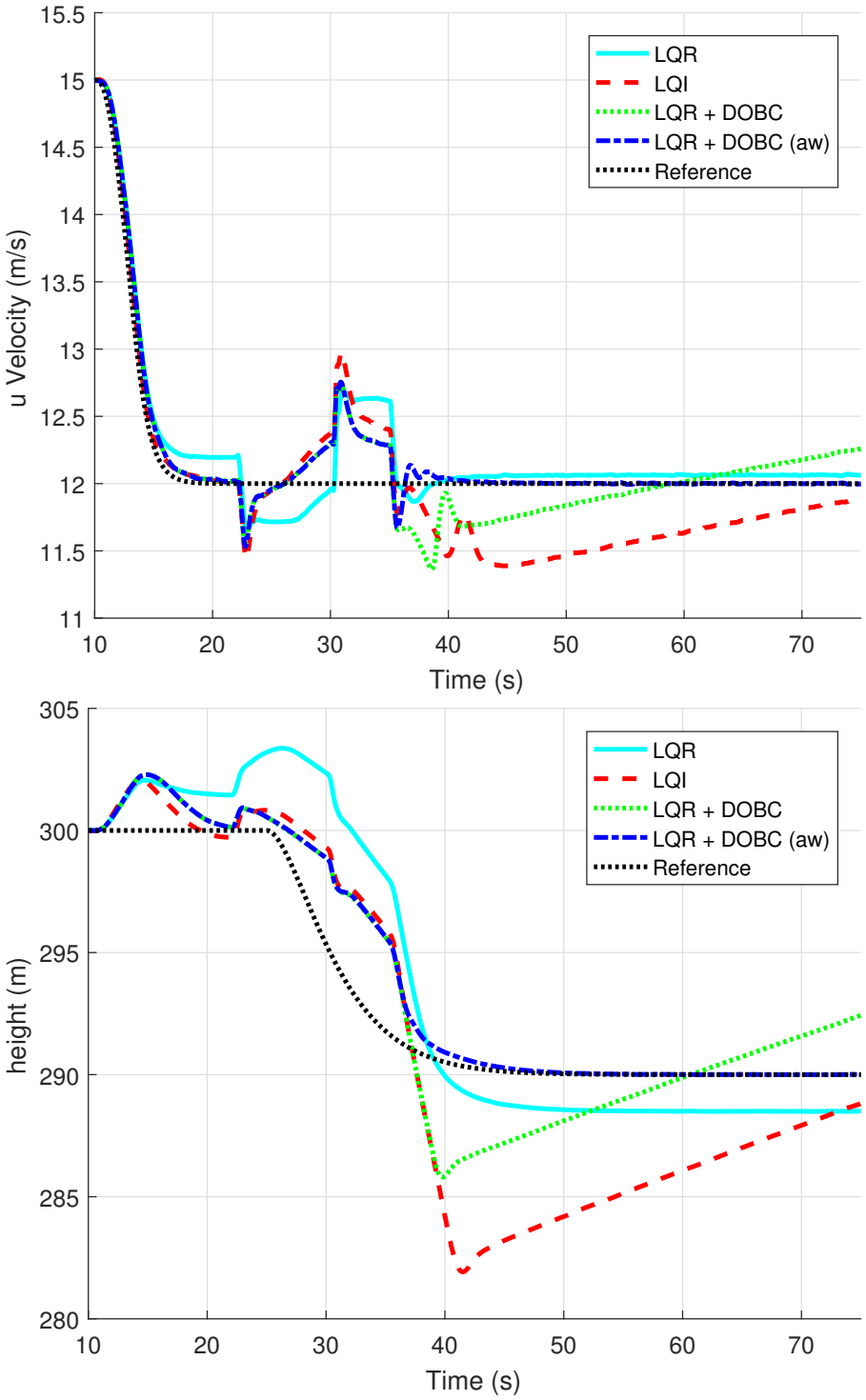

Figure 5.13: Aircraft u and h tracking in an X-Plane landing simulation.

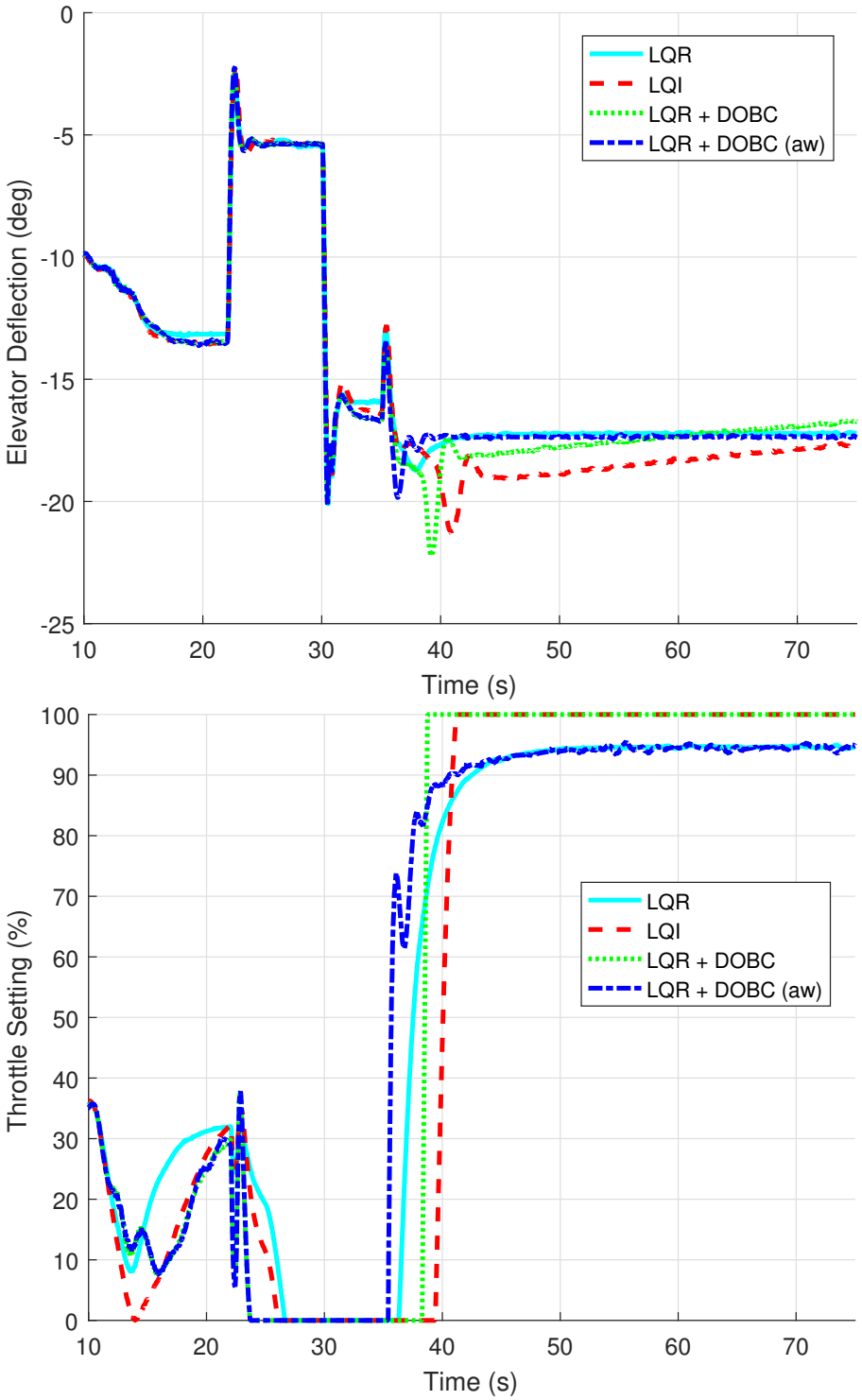

Figure 5.14: Elevator and throttle setting in an X-Plane landing simulation.

5.4 Flight Testing

Within the simulation section, the function and performance benefit of the anti-windup modification was clearly shown. For validation, flight tests were conducted to demonstrate the transferability of the method to a physical platform. This is a key test, as this technique is entirely based on the difference between theoretical models and real world systems. As the numerical simulations had shown, caution was required. Conducting these experiments on a flying platform could have very real and dangerous consequences. For this reason, some changes were imposed.

First, performance is studied in the lateral channel for flight testing. Saturation in the longitudinal channel could very easily lead to aircraft stall, making it very difficult or impossible to safely recover the aircraft. In the lateral channel, risk was limited to aircraft inversion. The X8 is capable of brief periods of inverted flight, and this would allow time for manual pilot recovery if necessary.

Second, the integral controller would not be tested in flight. The main reason for this was to further limit risk by reducing the number of test flights needed. Furthermore, the aim of this chapter is to demonstrate the performance benefit to the DOBC scheme of the anti-windup method rather than as a comparison to LQI control. The information gathered by applying LQI in flight would be very limited over what has been shown in simulations previously.

Finally, to enable saturation to appear under safe circumstances, the available control authority would be limited. In standard configuration, $\pm 30^\circ$ of deflection is available as a roll input. However, the roll rates produced by such deflections are extreme, and would put the aircraft at risk very quickly. It would also limit recoverability. For this reason, the control limits were artificially reduced to $\pm 0.15 rad$ ($\sim 8.5^\circ$). This would allow for saturation to occur at more reasonable roll rates, allowing for safe flight testing.

5.4.1 Control Design

For flight testing, a simple model of the aircraft lateral dynamics will be used. The model is given as

$$\underbrace{\begin{bmatrix}\dot{p}\\ \dot{\phi}\end{bmatrix}}_{\dot{\boldsymbol{x}}} = \underbrace{\begin{bmatrix}-27.5 & 0\\ 1 & 0\end{bmatrix}}_{\boldsymbol{A}_{lat}} \underbrace{\begin{bmatrix}p\\ \phi\end{bmatrix}}_{\boldsymbol{x}} + \underbrace{\begin{bmatrix}224\\ 0\end{bmatrix}}_{\boldsymbol{B}_{lat}} \underbrace{\delta_e}_{u}, \tag{5.43}$$

here p and ϕ are the roll rate and roll angle, respectively and δ_e is the elevon roll deflection. This simple model is easy to implement and allows for the demonstration of DOBC performance in flight testing with a limited model. The design of the feedback control is identical to the method outlined earlier in this chapter other than the system matrices used, which are replaced by those detailed in (6.2) and the roll angle output defined as $y = \begin{bmatrix}0 & 1\end{bmatrix}\boldsymbol{x}$. The LQR weighting matrices are taken as

$$\boldsymbol{Q}_{lat} = \begin{bmatrix}0.1 & 0\\ 0 & 2\end{bmatrix} \qquad \boldsymbol{R}_{lat} = \begin{bmatrix}3.6\end{bmatrix},$$

which gives the feedback control gain as

$$\boldsymbol{k}_{lat} = \begin{bmatrix}0.1083 & 0.7906\end{bmatrix}.$$

The DOBC design also follows the method outlined previously, with $\boldsymbol{L} = diag\begin{bmatrix}1.5 & 0.75\end{bmatrix}$.

5.4.2 Automatic Input Generation

To allow for comparison of performance between flights, manual control inputs would not be acceptable as this would incur too much variance. For this reason, a method for automatic control input generation was required. There were four main considerations for these manoeuvres:

1. Demonstrate steady disturbance rejection ability
2. Demonstrate reference tracking performance
3. Allow for precise repeatability for fair comparison
4. Be routinely feasible in the available space constraints

1 - To allow for rejection of steady (constant) disturbance, such as modelling errors, the manoeuvre would require a period of zero reference command. This period would need to be long enough to allow the disturbance observers time to estimate the disturbance and demonstrate its removal from the output.

2 - For reference tracking, two key features need to be investigated. Firstly, the ability of the disturbance observer to estimate and remove a disturbance with the aircraft at a non-reference condition. This is expected to require some time for accurate disturbance estimation. Secondly, it is important that the disturbance observers does not significantly reduce the tracking performance of the baseline controller. To satisfy both of these conditions, a pair of roll doublets will be used; one of lower angle, with a longer duration, followed by a larger angle command with short duration. This combination allows for assessment of both criteria. Furthermore, for some flight testing the manoeuvres magnitude may need to be increased or decreased, depending on the test. The designed reference command can be multiplied easily by a scalar to control the test magnitude, while still maintaining some comparability.

3 - Repeatability of the reference command is essential; the main reason for using an automatic command over manual input is to allow for consistent repetition each time a test is conducted. This allows for maximum data comparability and performance comparison of controllers on various flights or testing days.

4 - Finally, it is important that the manoeuvre is short enough that it can be run within the flight testing area repeatedly. This means it must be short enough that the aircraft cannot exceed the flight area, regardless of the weather conditions. This essentially means that even on a day with no headwind (to reduce the ground speed of the aircraft), the manoeuvre must be short enough to be conducted in the operational area.

The designed manoeuvre is shown in Fig 5.15. The initial 5s settling time satisfies objective 1, while the roll doublets satisfy objective 2. Furthermore, a small pause between the two doublets is added to study the return to zero reference following a reference command step; this is to demonstrate that reference commands do not bring about a disturbance estimate which affects the aircraft at zero reference.

Objective 4 is satisfied with the overall time of 18s for the manoeuvre. With no wind, the ground distance covered is 270m, which is within the operational area requirements. The larger turns were placed later in the manoeuvre for two reasons. Firstly, it allows assessment of performance with a small initial input; this means the run can be abandoned before the more aggressive inputs if the initial rolls show an undesirable response. Secondly, the larger turns will be more clearly visible to the pilot, meaning it will be possible to distinguish the end of the manoeuvre clearly form the ground. This will aid avoiding premature termination of the automatic reference command.

Finally, to satisfy objective 3, these roll commands can be embedded in the flight control software. The automatic reference command was programmed as a module, the

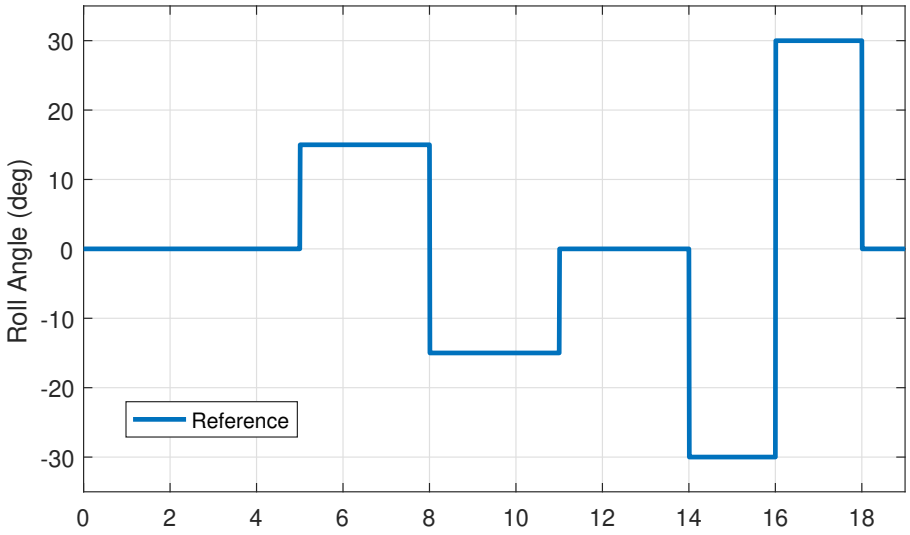

Figure 5.15: The chosen automatic reference input for flight testing of the lateral flight controllers.

only inputs being trigger and reset conditions. For example, activation of the module may require a switch on the transmitter to be in a particular position. Once in this position, an internal clock runs and triggers the turns at the specified time. This makes it very easy to detect the time at which the mode was activated in the data processing stage, allowing for easy plotting. Furthermore, by setting the reset condition appropriately (for example, a change in the offboard activation switch can reset the timer) the timer can be reset for repeated runs easily.

The designed manoeuvre, along with the method by which it was programmed into the flight control software, have satisfied all the requirements.

5.4.3 Results

To study the function of the anti-windup augmentation, two flight tests were conducted. The aim of this test was to demonstrate that, in the absence of saturation, the anti-windup modification has no effect on the overall controller performance. Fig. 5.16 presents the first flight test result. Here, we give the baseline DOBC performance (designated *DOBC*) to the same scheme with anti-windup active (designated *DOBC (aw)*). For this flight, each controller performed two passes of the reference input. This allows for differentiation between response characteristics and external disturbance.

Prior to point *a* in Fig. 5.16, there was no significant saturation. This results in a broadly similar result for all four passes. Point *a2* is the first point of significant saturation, as this is the largest reference step during the test. The resulting response at point *b1* shows a clear and consistent difference between the two controllers. The anti-windup schemes respond much more quickly to this reference command. The control responses at *b2* indicate that the anti-windup controllers are able to utilise the full deflection available, explaining the improved response. The unmodified controllers show a slow creep of the aileron deflection. This is the effect of the feedback input being overridden by the DOBC windup signal, which is slowly disappearing.

Although this result only briefly demonstrates the anti-windup function, an additional important point is that performance between the observers is consistent when saturation has not occured. This is important, as the anti-windup method should not degrade controller function when no saturation is present.

Rapid Step Input Anti-Windup Flight

The next flight test aimed to induce saturation more, to further highlight the effect of windup and the anti-windup augmentation. Fig. 5.17 gives the result. A series of large reference step commands are used in this test.

The first feature for discussion occurs at point *a1*. It appears that the LQR controller has outperformed both observers in this reference step, as it is closer to the commanded reference before the next change. However, point *a2* shows that all three controllers are commanding maximum deflection. The difference in response is therefore attributed to different external disturbances during this reference command. Crucially, it can be seen that the roll rate (gradient of the roll angle line) is the same for all three controllers, which confirms that the same control action is being taken.

At point *a2*, all three controllers have saturated the output; it can be reasonably be expected therefore that a difference should be seen in the subsequent response, indicated by point *b1*. The LQR and DOBC (aw) perform very similarly, reaching the demanded reference before the next step change. It should be noted that the LQR achieved this with an initial roll angle of $-19.7°$, which is a larger initial error than the DOBC (aw) which had an initial roll angle of $-7.6°$. The DOBC scheme is not able to achieve this in time, despite a middling initial error of $11.1°$. This error is bounded by the response of the other two controllers, both of which were able to reach the reference. The DOBC response cannot be attributed to limited control authority. Indeed, point *b2* shows once again the lagging slow creep of aileron position seen in the previous test which demonstrates windup.

Performance between points *b* and *c* are similar for all three controllers, a result of the equally saturated outputs. At points *c1* and *c2* the windup effect is seen once more, although to a lesser degree. Line *d1* is an additional feature of the windup. It was shown from the other responses that for this set of reference commands, the windup limits response rate in the positive roll direction, while not affecting the negative direction (due to saturation). Line *d1* shows that the DOBC scheme has an increasingly negative response. This response is not shared by the anti-windup modified DOBC. Crucially, it is also not shared by the baseline LQR. This indicates that this is a result of windup, which therefore also demonstrates that the anti-windup function is working correctly in this test also.

5.4.4 Flight Test Conclusions

The two presented flight tests have shown that the anti-windup scheme has been successfully implemented on the physical aircraft. The first test indicated that in the absence of saturation, the DOBC and DOBC (aw) schemes have the same performance characteristics which shows that the anti-windup method does not have a detrimental impact on performance. When saturation did occur, windup resulted in a slowed roll response from the DOBC controller compared to the DOBC (aw) controller. Repeating the test for each controller shows that the consistent performance difference is not a result of external disturbances.

The second flight test now included an LQR controller, which is not susceptible to windup. Here it was shown that the DOBC (aw) performance matched that of the LQR under control saturation. It is pertinent to remember that due to the heavily constrained control authority, no improvement is expected in disturbance rejection by either DOBC scheme in this flight. This is a crucial result, as it shows the anti-windup scheme is working as intended. Again, the degraded performance of the DOBC without anti-windup was presented which differed significantly from the other results. The anti-windup method has been successfully implemented on a flying platform.

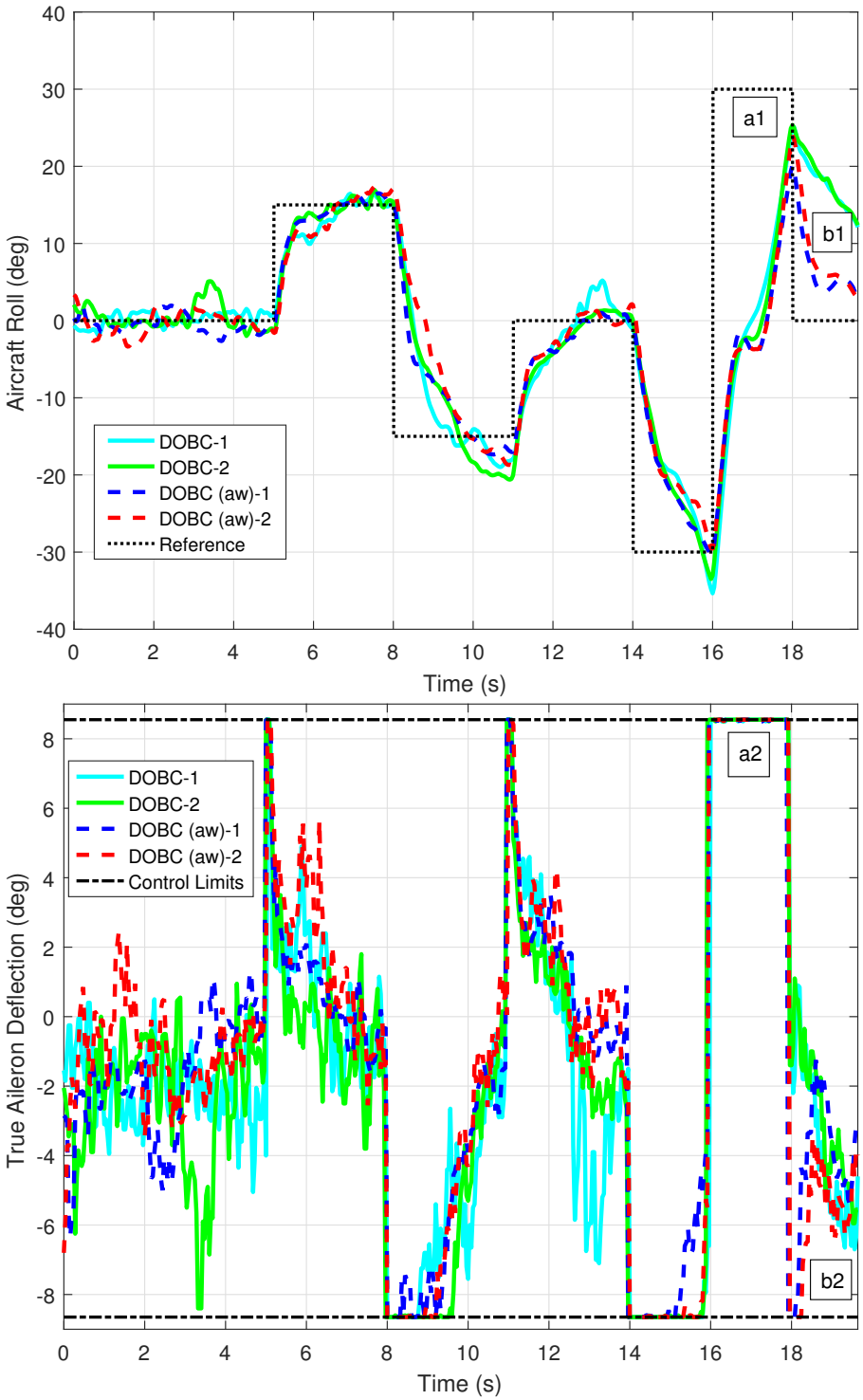

Figure 5.16: Flight data for DOBC without and with anti-windup (aw) and artificially limited control deflection.

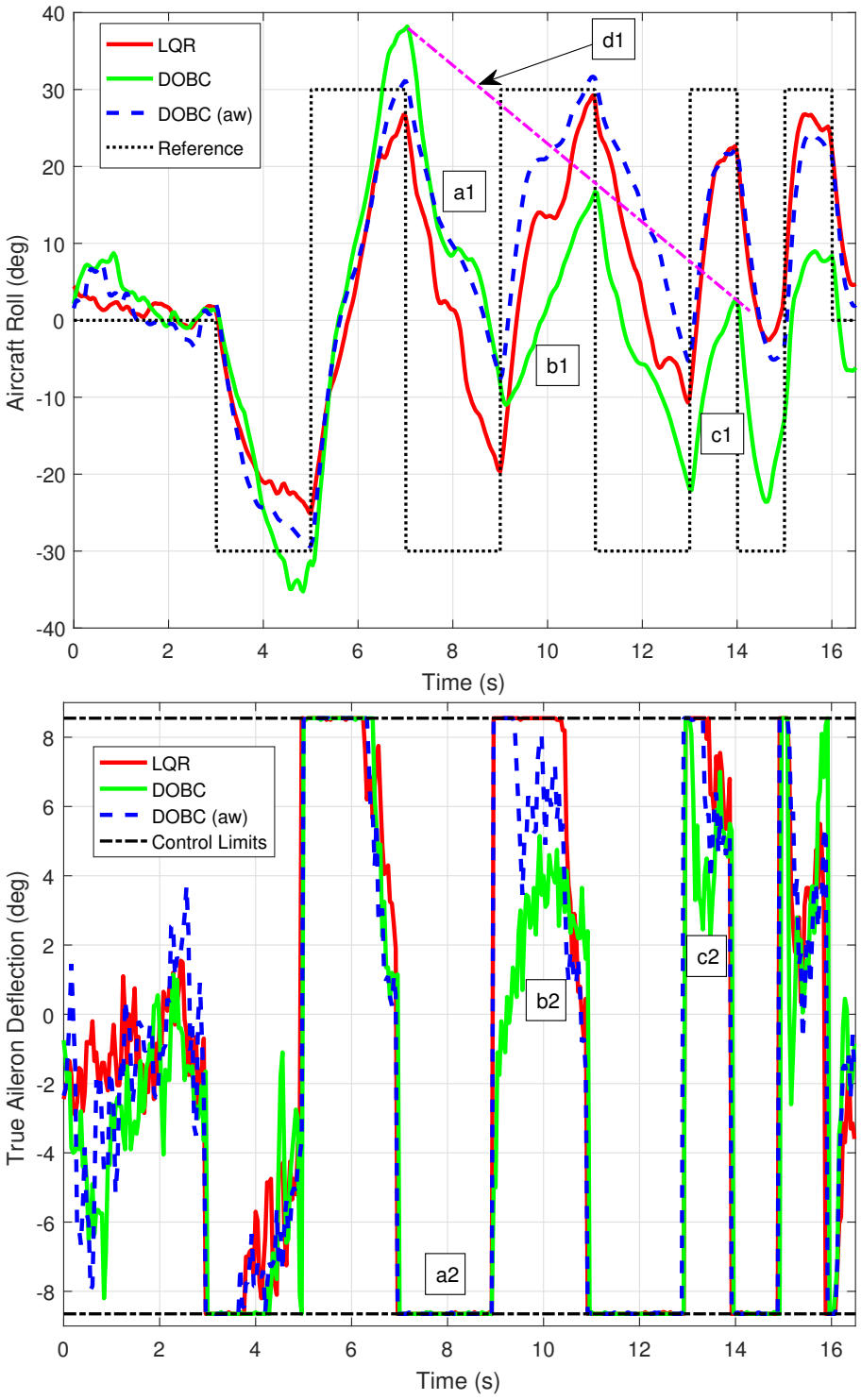

Figure 5.17: Flight response for DOBC without and with anti-windup (aw) and artificially limited control deflection using a modified reference input.

5.5 Conclusions

Within this section, the need for an anti-windup augmentation of the DOBC was discussed. The design process was conducted based on well known and proven anti-windup methods with proven stability. The dangers to the aircraft under the effects of windup due to control saturation were clearly demonstrated.

Performance of the proposed method was demonstrated with a range of simulations. It was shown that without the anti-windup method, DOBC methods are susceptible to windup in the same way as traditional integral augmentation. The effect of windup was demonstrated to result in significant overshoot of the reference command as well as delayed response to changes in disturbances. It was shown that with the anti-windup modification, the DOBC method is completely alleviated of the effects of windup due to control saturation. It was also demonstrated that the resulting overshoot of reference commands could lead to dangerous situations for the aircraft. A landing example was presented where, without the anti-windup modification, the aircraft would have crashed into the runway, as it was pushed well below the reference height. Further, with the modification, the DOBC is able to respond rapidly to varying disturbances, offering better response to Dryden disturbances.

The numerical simulations were further validated by X-Plane simulation. It was demonstrated that the modified DOBC method is able to maintain its performance advantage with a non-linear plant. This was achieved by intentionally forcing the aircraft away from the linearisation point, introducing significant modelling errors.

With performance well validated in simulation, a flight test was conducted. This flight test was tightly controlled for safety factors, as the simulations demonstrated clearly that windup could lead to dangerous flight conditions. Regardless of the limitations, it was demonstrated that the anti-windup modification translated to a physical plant and the performance advantages demonstrated in simulation were proven in flight testing.

Overall, this section demonstrated clearly the performance issues which control saturation induced windup can lead to. Further, the developed anti-windup method was shown to alleviate the affect of windup fully, with no performance degradation. A very clear performance and safety advantage was demonstrated with a number of simulations. Finally, the results were then validated with flight tests.

Chapter 6

Enhancing the Disturbance Observer with Actuator Dynamics

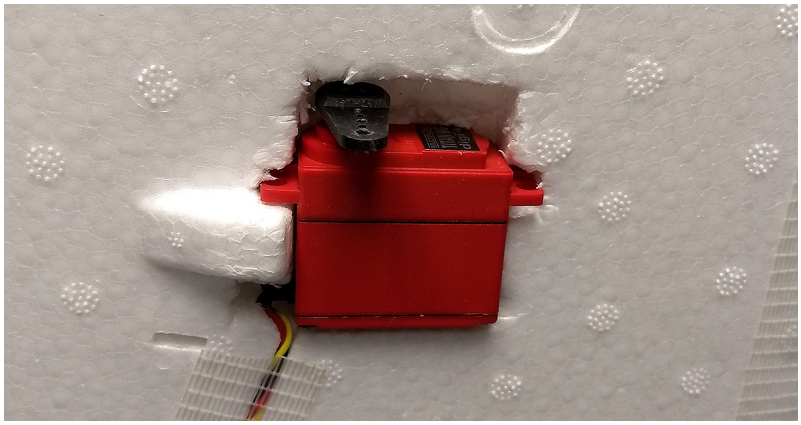

Figure 6.1: A Titan MG Digital servo Skywalker X8 in this thesis.

In the previous chapter it was shown that unmodelled actuator saturation can lead to windup within a disturbance observer, resulting in degraded performance. In this chapter we continue to consider the effect of actuator dynamics on the observer. It will be demonstrated that these dynamics produce a second source of error: the mismatch between *demanded* and *applied* actuator action. Within this chapter, we introduce ϵ to denote the true actuator position, such as the deflection of an elevon on the aircraft. Often in control design, it is assumed that $u \approx \epsilon$. The assumption is valid when the actuator dynamics are faster than the dynamics of the controller. This is a valid and reasonable assumption in most cases, which simplifies the control design. The controller dynamics for small UAVs are faster compared to that of full sized aircraft. This is necessary as the dynamics of small UAVs are also faster. This introduces a problem, as the above assumption may become invalid. In some instances, it is no longer reasonable to ignore the actuator dynamics.

Small UAVs typically utilise small electronic servos for the actuation of control surfaces, an example is shown in Fig. 6.1. These servos used on the Skywalker X8 in this thesis have actuation speeds of around $400°/s$. Connections to the control surfaces are typically configured such that the actuated surface moves with the same speed. The resulting actuation speed is substantially larger than what is common on large aircraft with hydraulic actuators. For example, Wang studied control surface requirements for a large Unmanned Combat Aerial Vehicle (UCAV) [113], where the minimum requirement for sweep rate is given as $60°/s$. A UCAV is a high performance aircraft, so it is reasonable to assume this requirement is typical of a fast hydraulic actuator. The difference in actuator

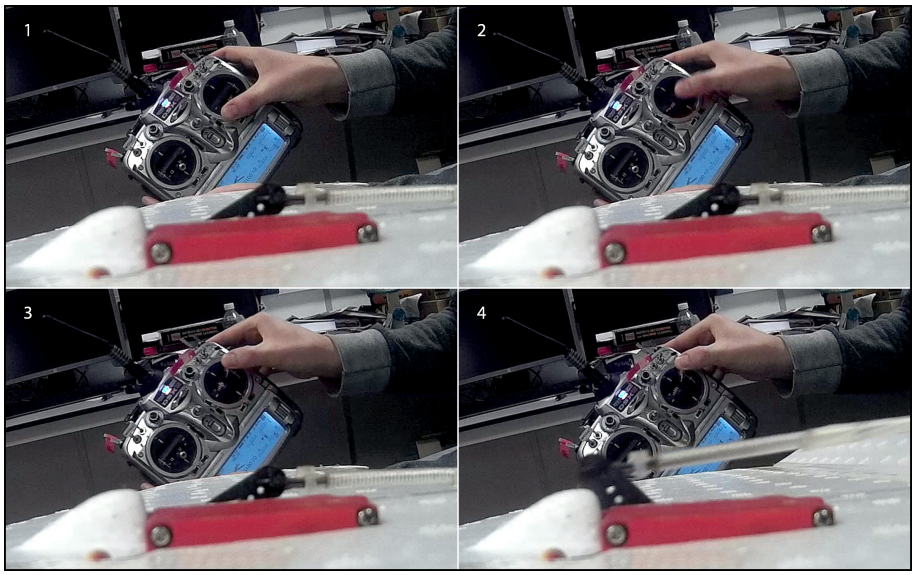

Figure 6.2: High frame rate recording of a manual control input demonstrating the response delay. Red item is the servo-actuator with black armature under the left wing of the X8.

performance for small UAVs and large aircraft is undeniably substantial.

Simulations in the previous chapter did not include actuator dynamics, thus no effect was seen. In the previous flight tests however, actuator dynamics were present, yet no performance degradation was noticed. This raises a question; is it necessary to include actuator dynamics in the observer? Within this chapter it will be demonstrated that while not necessary, inclusion of actuator dynamics allows for increased DOBC performance. The performance benefit is realised even with the very high bandwidth actuators on the studied small UAV.

The servos used on the X8 are designed for high performance. Cheaper, slower servos are also commonly used for small UAVs. In such cases, the benefits demonstrated herein would be even greater. A conventional aircraft with slow hydraulic actuators would benefit further. This Chapter expands upon the work published in [114]. As was done in this publication, here the term Actuator Augmented Disturbance Observer Based Control (ADOBC) is used to refer to the actuator augmented disturbance observer, to allow for clarity of discussion only.

6.1 Actuator Modelling

In order to conduct accurate analysis and simulations, further understanding of the actuator dynamics was required. Accurate identification of an actuator model would yield simulations which accurately represent the true system.

Initial analysis of the actuator response to manual control input was conducted using high speed video capture. This was intended as an initial study of the actuator time response. With a maximum available frame rate of 60 Frames Per Second (FPS), the accuracy was limited to approximately 0.017s $\left(\frac{1}{60}s\right)$. In addition to the actuator dynamic response, an unexpected initial response delay was discovered. Fig 6.2 gives a sample of the video recording of the delay between control input and response; the manual control input is fully completed before any motion of the actuator is observed.

This is defined herein as *response delay*, further defined in Fig 6.3. The video analysis indicated a response delay of 0.217s and a 0.15s time constant for the actuator response. It was highly unexpected for the response delay to be of greater magnitude than the actuator time constant.

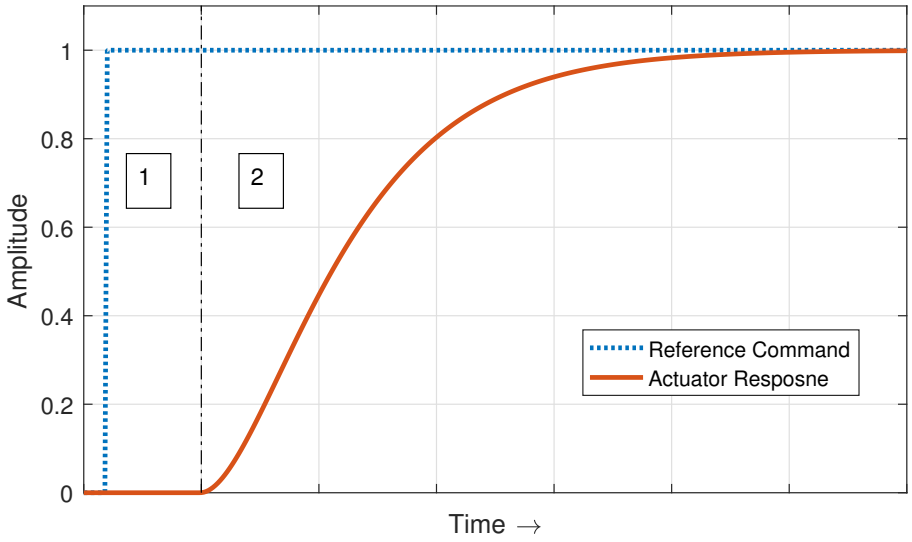

Figure 6.3: Definition of the two considered time delay components.
1: Response delay - lag between action demand and initial motion
2: Actuator dynamics - physical actuator response rate

However, it is also not truly representative of the delay which will be present when the aircraft is in offboard mode. Manual input, as shown in Fig 3.1, enters the system through a different path than any ROS control scheme. Furthermore, the frame rate limitation and non-precise measurements given by the video analysis limited the usable data produced; a better test methodology was required.

6.1.1 Test Methodology

To allow for accurate measurement of the response delay, it was critical that good synchronisation between recorded control input and actuator response was obtained. Using the Run on Target Hardware (ROTH) method described in Chapter 3, it was possible to record the actuator demand in the same environment (and time scale) as it was generated. However, the actuator systems aboard the aircraft provide no means by which to record their position, so an alternative method of tracking was required.

A VICON motion tracking[1] area is available in LUCAS, which offers very high precision tracking at 100Hz. This would be ideal for actuator measurements if the data could be synchronised with the demanded input. This is non-trivial as the VICON software is run on a ground station PC, separate to the Raspberry Pi running aboard the X8. By using a local area network, it was possible to publish the VICON data to the ROS network using the UDP protocol. The network latency has been measured to be of an order less than 1ms, meaning it would not affect actuator measurements. With VICON data now available on the ROS network, it was possible to generate a model to run aboard the X8 which recorded precisely the moment of a control demand along with the VICON measured actuator response. This ensures that the measurements are fully synchronised. Fig. 6.4 shows how the X8 actuator was tracked within the VICON area.

The aircraft was secured in the tracking area such that only the actuator surfaces were free to move. The orientation was selected such that the tracked surface would rotate purely around the VICON x axis, to simplify analysis. This meant that during data analysis, any recorded motion could be attributed to actuation of the control surface only. A model was designed to run in offboard mode which demanded three doublets of control input with three different step times. An example recorded response is shown in Fig. 6.5.

[1]Further detail available at https://www.vicon.com/motion-capture/engineering

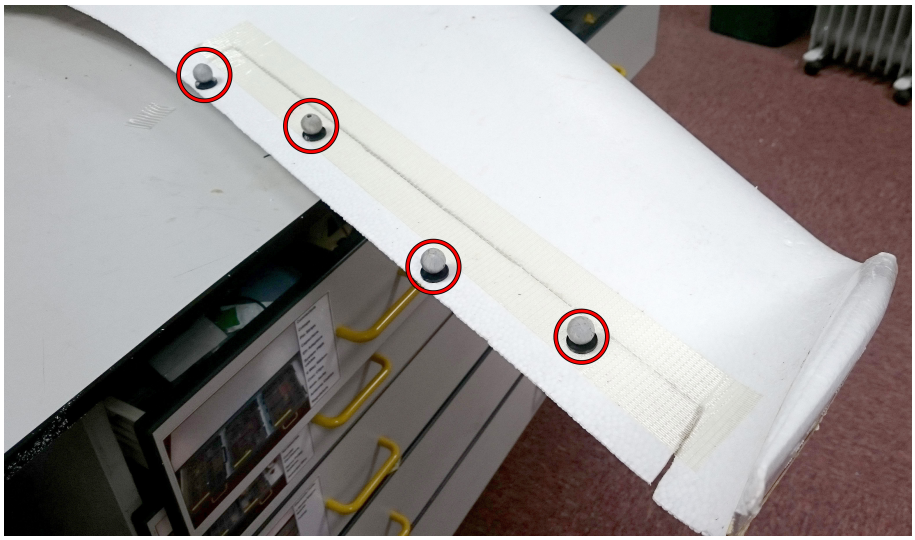

Figure 6.4: The four highlighted VICON tracker balls attached to the X8 control surface.

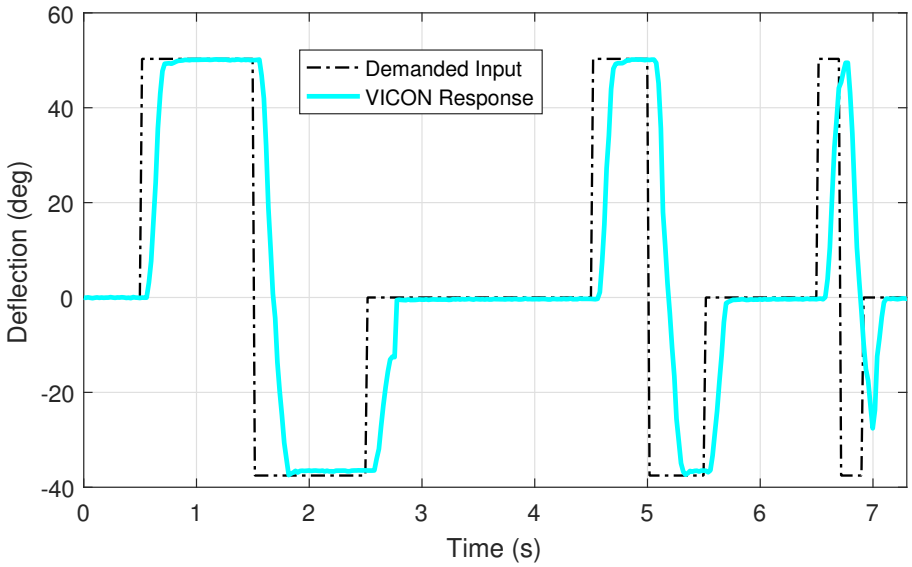

Figure 6.5: A sample of the recorded actuator response to demanded control input.

There are several points worthy of discussion. Firstly, the response delay can be seen clearly in any change in input demand. It shows a delay of around 0.1s, as opposed to the 0.217s from the video footage. This indicates that the path from manual transmitter input to Pixhawk output is partially responsible for the 0.217s response delay measured by video analysis. Secondly, upon closer inspection the actuator response has distinct acceleration and deceleration phases, with a constant velocity between them. This is an expected result as the servo has an internal control scheme. This data shows the actuator to have a maximum deflection rate of $450°/s$. The third point is that at some points (e.g. $t \approx 2.8s$), the data shows signs of inconsistencies. This may have been a result of VICON struggling to track the reflectors on the foam X8 body. During the tracking setup, the bright white, highly reflective surface of the X8 required significant camera calibration to mitigate measurement noise. For this reason, it would be pertinent to run the test multiple times and obtain an averaged result.

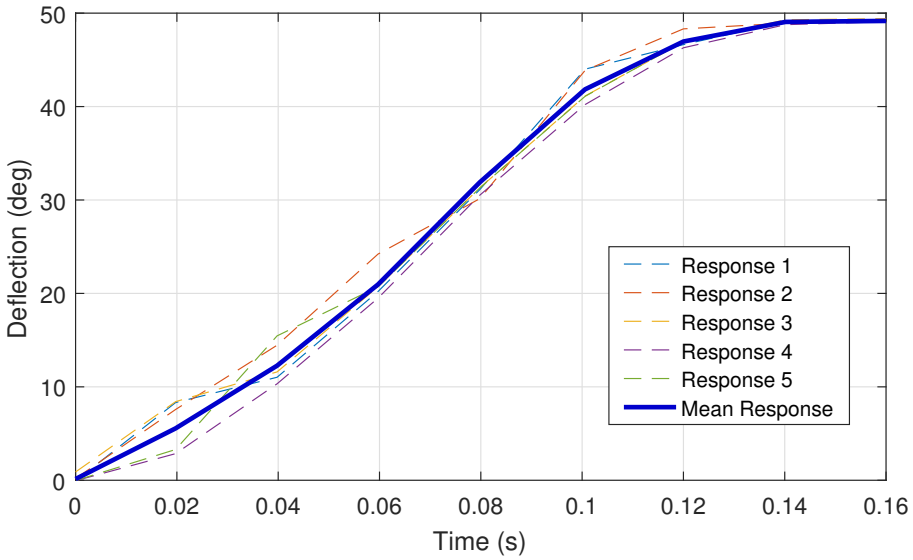

Figure 6.6: The five recorded responses and resulting mean response, to a step input with response delay removed.

6.1.2 Actuator Model

The data acquisition model was run and repeated a full deflection command five times and the resulting responses were averaged to reduce measurement noise. The response, ignoring response delay, is shown in Fig. 6.6.

Using the averaged response, the response delay was also identified as 0.08s. This is much less than the manual mode delay of 0.217s. Due to the test methodology it can be said that this response delay is representative of the delay present for any ROS offboard controller. On the other hand, the response time of 0.14s from the VICON data is very close to the 0.15s estimated from the video data.

This actuator response can be modelled by a simple first order model, or a second order model, given as

$$G(s)_f = \frac{1}{\tau s + 1}, \qquad G(s)_s = \frac{\omega_n^2}{s^2 + 2\zeta\omega_n s + \omega_n^2}, \tag{6.1}$$

where $G(s)_f$ and $G(s)_s$ are the first and second order actuator transfer functions respectively, τ is the time constant, ω_n is the natural frequency and ζ is the damping ratio. A comparison of the best matches for the two models is shown in Fig. 6.7. It can be seen that the second order model matches more closely than the first order, as expected. For this reason, the second order model is used in the numerical simulation of aircraft dynamics. For control design, a decision was made to use the less accurate first order model. Using the first order model in the observer means that some modelling error will exist, which the method is expected to account for and remove from the output. This also demonstrates performance in the absence of an ideal actuator model, which is unlikely to exist in many applications. This makes the result more applicable to low cost UAVs.

6.1.3 Actuator Response Under Load

VICON motion data was acquired with the actuator under no load other than that of the surface inertia and attachment friction, which can be assumed as negligible. To confirm the validity of ground data for application to flight control, the case of actuator response under load was also considered. First, a calculation of the approximate force on the surface

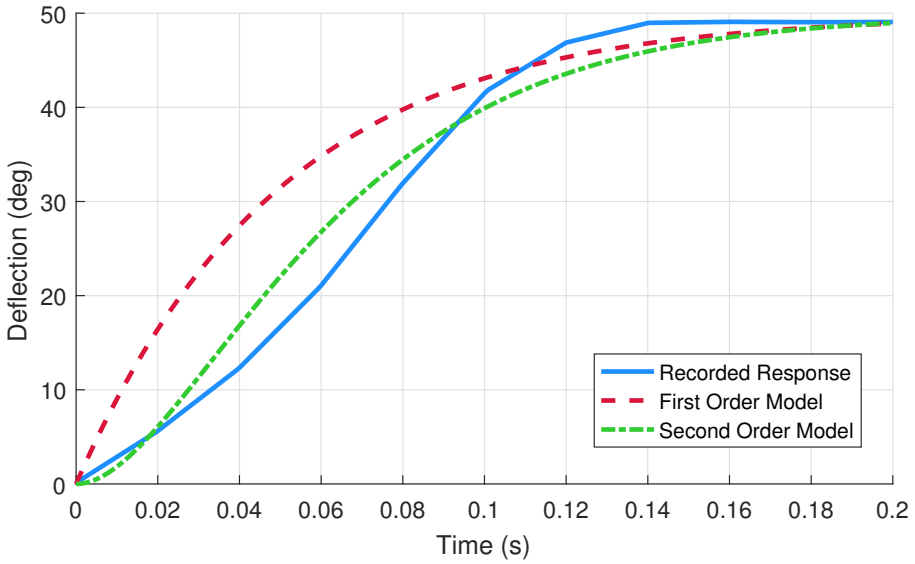

Figure 6.7: A comparison of the best matching first and second order models for the actuator response without consideration of response delay.

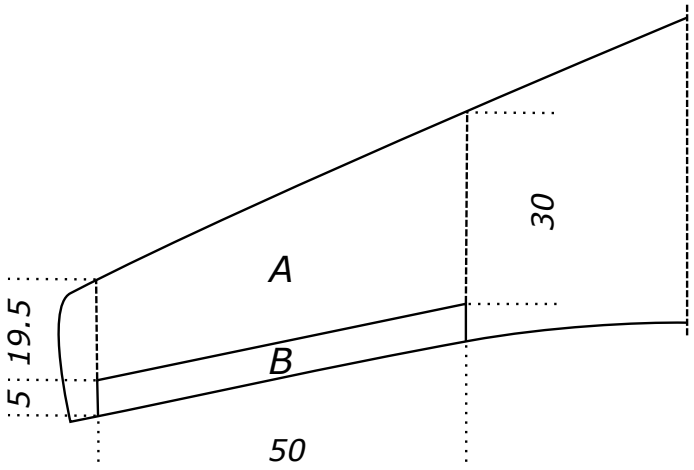

Figure 6.8: A top down schematic of the left wing of the Skywalker X8. All dimensions in cm.

under aerodynamic manoeuvre load was conducted. A schematic of the layout is shown in Fig. 6.8.

Flight data was collected for maximum roll rate acceleration resulting from a maximum control deflection during straight and level flight. For flight at $15m/s$, the general trim flight condition, it was found that $\dot{p}_{max} = 45rad/s^2$. The aircraft roll moment of inertia is known from ground measurements to be $I_{xx} = 0.3653kgm^2$. From this, the rolling moment required for $\dot{p}_{max}$ can be calculated as

$$L_{\dot{p}_{max}} = I_{xx}\dot{p}_{max} = 16.4Nm.$$

The centroid of the wing section indicated in Fig. 6.8 is $0.7m$ from the aircraft centre-line. Assuming that each of the two control surfaces produced an equal force for the roll manoeuvre, the force on one wing section required to generate $L_{\dot{p}_{max}}$ can be calculated as

$$L_{\dot{p}_{max}} = 2 \times 0.7 \times F_{\dot{p}_{max}},$$
$$F_{\dot{p}_{max}} = 11.7N,$$

which is rounded to $12N$ for an upper limit estimate. This $12N$ results from a pressure

difference over the whole area of $A + B$. The portion of this force acting on the control surface could be approximated from the ratio of areas as

$$F_B = F_{\dot{p}_{max}} \frac{B}{A+B} = 12 \frac{0.025}{0.1238} = 2.42N.$$

This represents a upper bound estimate on the force expected, accounting for the approximations made during the calculation. In particular, the assumption that the pressure difference is equal across the wing is the most far reaching; As demonstrated in [115], the majority of the pressure change occurs toward the front of the wing. However, in this case, it serves to increase the load on the control surface above what is expected. This only acts to increase the valid range of the results. To study actuator performance under this load, an equivalent $250g$ weight was attached to the control surface directly. Using the same filming method as in the initial study, no change in actuation time could be detected; the internal control scheme of the servo-actuator is able to account for the added load. This means that, at most, the weight adds $1/60s$ of actuation time, as this is the limit of the camera's capture rate. The resulting error is small enough to be considered insignificant, thus the actuator model identified in ground testing can be deemed sufficient for modelling the actuator under flight loads.

6.2 Augmenting a Disturbance Observer with Actuator Dynamics

6.2.1 Aircraft Model

This chapter uses the same lateral aircraft model used used in Chapter 5, reproduced here for clarity as

$$\underbrace{\begin{bmatrix} \dot{p} \\ \dot{\phi} \end{bmatrix}}_{\dot{\boldsymbol{x}}} = \underbrace{\begin{bmatrix} -27.5 & 0 \\ 1 & 0 \end{bmatrix}}_{\boldsymbol{A}} \underbrace{\begin{bmatrix} p \\ \phi \end{bmatrix}}_{\boldsymbol{x}} + \underbrace{\begin{bmatrix} 224 \\ 0 \end{bmatrix}}_{\boldsymbol{B}} \underbrace{\delta_e}_{u}, \tag{6.2}$$

where p and ϕ are the roll rate and roll angle, respectively and δ_e is the elevon deflection. The simplicity of the model has no bearing on the validity of the results produced herein, as it is the effect of actuator dynamics which is being investigated. The simple model will however induce modelling inaccuracies during the flight test. This aims to further demonstrate the ability of the DOBC to perform successfully with a limited model.

6.2.2 Actuator Augmented DOBC

The DOBC scheme used previously must be modified and expanded to include actuator dynamics. The previous DOBC design used a state space model in the form

$$\dot{\boldsymbol{x}} = \boldsymbol{A}\boldsymbol{x} + \boldsymbol{B}u + \boldsymbol{d}_{lx}, \tag{6.3}$$

based on the aircraft model given in (6.2), where $\boldsymbol{A}$ and $\boldsymbol{B}$ are the matrices for aircraft dynamics and control effectiveness, $\boldsymbol{x}$ is the system state vector, u is the input command and $\boldsymbol{d}_{lx}$ are the lumped disturbances acting on the system. In this Chapter, the same feedback control method is used as was in Chapter 5. The control law is given as

$$u = -\boldsymbol{k}_x\boldsymbol{x} + \boldsymbol{N}\boldsymbol{r} + \boldsymbol{k}_{dx}\hat{\boldsymbol{d}}_{lx}.$$

This model does not account for any actuator dynamics, assuming that the demanded control u is similar to the applied control. This is reasonable for systems which have observer dynamics which are slower than the actuator dynamics. However, for good DOBC

function when a non-steady disturbance is considered, it is required that the observer dynamics are faster than that of the disturbance. For flight control, wind gust disturbances have fast dynamics, meaning a faster observer is needed. Consequently, the observer dynamics can approach the point where any difference between the demanded control and true actuator positions can be detected as a disturbance on the system. In an attempt to address this, a previous nonlinear DOBC design for estimation of helicopter flapping angles [89] is adapted to include a model of the actuator dynamics in the observer. The new model then becomes the cascaded system shown below

$$\begin{aligned} \dot{\boldsymbol{x}} &= \boldsymbol{A}_1\boldsymbol{x} + \boldsymbol{B}_1\epsilon + \boldsymbol{d}_{lx}, \\ \dot{\epsilon} &= A_2\epsilon + B_2 u, \end{aligned} \tag{6.4}$$

where $\boldsymbol{A}_1 = \boldsymbol{A}$, $\boldsymbol{B}_1 = \boldsymbol{B}$, as defined in (6.2), ϵ is the actuator deflection based on the demanded control input u, and A_2 and B_2 are the state space representations of the first order actuator model in (6.1). By moving the control input u to be an input to the actuator position model rather than directly in the system state, it is possible to include the actuator modelling into the system. This model is however limited. As shown in Fig. 6.7, neither the first or second order actuator model are able to represent the actuator dynamics with true accuracy. By using the DOBC technique, the modelled actuator deflection ϵ can be improved by including an estimation term based on state measurements.

6.2.3 Actuator Augmented Disturbance Observer Design

First, the actuator model from (6.4) is utilised to define the dynamics component of our observer

$$\dot{\epsilon} = A_2\epsilon + B_2 u, \tag{6.5}$$

the measurement term for the actuator position is found by rearranging the system state equation from (6.4) as

$$\boldsymbol{B}_1\epsilon = \dot{\boldsymbol{x}} - \boldsymbol{A}_1\boldsymbol{x} - \hat{\boldsymbol{d}}_{lx}, \tag{6.6}$$

where $\boldsymbol{d}_{lx}$ has been replaced with its estimate $\hat{\boldsymbol{d}}_{lx}$. This is done as we assume a suitable observer for this term will be designed later. Next, an estimator for the actuator position is defined as

$$\dot{\hat{\epsilon}} = A_2\hat{\epsilon} + B_2 u + \boldsymbol{L}_\epsilon(\dot{\boldsymbol{x}} - \boldsymbol{A}_1\boldsymbol{x} - \hat{\boldsymbol{d}}_{lx} - \boldsymbol{B}_1\hat{\epsilon}), \tag{6.7}$$

where $\hat{\epsilon}$ is the estimated actuator position and $\boldsymbol{L}_\epsilon$ is the observer gain parameter. However, in the current form, this estimator features a measurement which is unavailable in $\dot{\boldsymbol{x}}$. Continuing with the standard DOBC method of defining an auxiliary equation to remove $\dot{\boldsymbol{x}}$. First, define

$$\hat{\epsilon} = z_2 + \boldsymbol{L}_\epsilon\boldsymbol{x}, \tag{6.8}$$

where z_2 is an auxiliary vector representing an internal state of the observer. From this we can also define

$$\dot{\hat{\epsilon}} = \dot{z}_2 + L_\epsilon\dot{\boldsymbol{x}}. \tag{6.9}$$

By substituting $\dot{\hat{\epsilon}}$ from (6.9) into (6.7), we get

$$\dot{z}_2 + \boldsymbol{L}_\epsilon\dot{x} = A_2\hat{\epsilon} + B_2 u + \boldsymbol{L}_\epsilon(\dot{\boldsymbol{x}} - \boldsymbol{A}_1\boldsymbol{x} - \hat{\boldsymbol{d}}_{lx} - \boldsymbol{B}_1\hat{\epsilon}), \tag{6.10}$$

which allows for removal of the $\boldsymbol{L}_\epsilon\dot{\boldsymbol{x}}$ term which appears in both sides of the equation. Finally, the disturbance observer with actuator dynamics by is defined by combining (6.10) and (6.8) into

$$\begin{cases} \dot{z}_2 = A_2\hat{\epsilon} + B_2 u + \boldsymbol{L}_\epsilon(-\boldsymbol{A}_1\boldsymbol{x} - \boldsymbol{B}_1\hat{\epsilon} - \hat{\boldsymbol{d}}_{lx}) \\ \hat{\epsilon} = z_2 + \boldsymbol{L}_\epsilon\boldsymbol{x}. \end{cases} \tag{6.11}$$

This has a similar form to the basic disturbance observer designed previously, except for featuring *dynamics* as well as a measurement component. This does mean that the process of tuning the observer gain $\boldsymbol{L}_\epsilon$ is more complex than for the basic observer. For the basic observer, the $\boldsymbol{L}$ gain in essence controls the convergence rate of the estimate to the true disturbance; generally, a high observer gain is desirable. For the actuator observer, the $\boldsymbol{L}_\epsilon$ gain changes how $\hat{\epsilon}$ is generated. This is discussed in detail in Section 6.2.4.

The disturbance observer design for lumped disturbances on the UAV states is similar to the observer designed in Chapter 5. Here, the previously used u is replaced by $\hat{\epsilon}$ generated by (6.11) for disturbance observer design. The new disturbance observer is then designed as

$$\begin{cases} \dot{\boldsymbol{z}}_1 = -\boldsymbol{L}(\boldsymbol{z}_1 + \boldsymbol{L}\boldsymbol{x}) + \boldsymbol{L}(-\boldsymbol{A}_1\boldsymbol{x} - \boldsymbol{B}_1\hat{\epsilon}) \\ \hat{\boldsymbol{d}}_{lx} = \boldsymbol{z}_1 + \boldsymbol{L}\boldsymbol{x}. \end{cases} \tag{6.12}$$

Define the observation errors as $e_\epsilon = \epsilon - \hat{\epsilon}$ and $\boldsymbol{e}_d = \boldsymbol{d}_{lx} - \hat{\boldsymbol{d}}_{lx}$. Combining the system dynamics (6.4) and the observers (6.11) and (6.12), the error dynamics of the observers are governed by

$$\begin{bmatrix} \dot{e}_\epsilon \\ \dot{\boldsymbol{e}}_d \end{bmatrix} = \begin{bmatrix} A_2 - \boldsymbol{L}_\epsilon\boldsymbol{B}_1 & -\boldsymbol{L}_\epsilon \\ -\boldsymbol{L}\boldsymbol{B}_1 & -\boldsymbol{L} \end{bmatrix} \begin{bmatrix} e_\epsilon \\ \boldsymbol{e}_d \end{bmatrix} + \begin{bmatrix} 0 \\ \dot{\boldsymbol{d}}_{lx} \end{bmatrix} \tag{6.13}$$

The exponential stability of the observer error dynamics is guaranteed with appropriate design of observer gains $\boldsymbol{L}$ and $\boldsymbol{L}_\epsilon$ such that the matrix

$$\tilde{\boldsymbol{A}} = \begin{bmatrix} A_2 - \boldsymbol{L}_\epsilon\boldsymbol{B}_1 & -\boldsymbol{L}_\epsilon \\ -\boldsymbol{L}\boldsymbol{B}_1 & -\boldsymbol{L} \end{bmatrix}$$

is chosen to be Hurwitz stable, and 3 further assumptions are made [87]:

1. Both the lumped disturbances d_{lx} and their derivatives $\dot{d}_{lx}$ are bounded
2. The lumped disturbances are constant in steady state ($\lim_{t\to\infty} \dot{d}_{lx}(t) = 0$)
3. The pair $(\boldsymbol{A}_1, \boldsymbol{B}_1)$ is controllable.

As the estimation error for the observers converge to zero regardless of the control signal, the overall closed loop stability can be proven as in [89].

As the neither the feedback control scheme or the lumped disturbances being estimated have been changed, the disturbance rejection gain calculation follows the same method as outlined in Chapter 5. The same control method is also used, with the control defined as

6.2.4 Disturbance Observer Gain Selection

The disturbance observer gain is defined as

$$\boldsymbol{L}_t = \begin{bmatrix} \boldsymbol{L} \\ \boldsymbol{L}_\epsilon \end{bmatrix} \tag{6.14}$$

where $\boldsymbol{L}_t \in \mathbb{R}^{3\times 2}$, $\boldsymbol{L} \in \mathbb{R}^{2\times 2}$ and $\boldsymbol{L}_\epsilon \in \mathbb{R}^{1\times 2}$ are the total, state and actuator observer gains. For design of the state observer gain $\boldsymbol{L}$, which is common to both the DOBC and ADOBC, it was tuned for best acceptable performance based on DOBC simulations. The same gain was then also set as the baseline $\boldsymbol{L}$ gain for the ADOBC controller. As will be shown in the results, a high $\boldsymbol{L}$ gain which performs well with the DOBC scheme will typically also perform well for the ADOBC scheme; the reverse is not true. This means it is more reasonable to tune the baseline $\boldsymbol{L}$ gain for good DOBC performance. In the

results section, this base gain will be multiplied by scalars to show the effect of increasing gains for the two schemes. This is done as shown

$$\boldsymbol{L}_t = L_k \boldsymbol{L}_t^B, \tag{6.15}$$

where $L_k \in \mathbb{R}$ is the scalar used to tune the gain based on $\boldsymbol{L}_t^B$, the baseline gain. This is given as

$$\boldsymbol{L}_t^B = \begin{bmatrix} 1.5 & 0 \\ 0 & 0.75 \\ 0.01 & 0 \end{bmatrix}. \tag{6.16}$$

The selection of $\boldsymbol{L}_\epsilon$ warrants some discussion. The first point to note is that $\hat{\epsilon}$ is updated only on measurements of the roll rate, p. This is intuitive as the control surfaces only affect the roll rate of the aircraft, as seen in the model (6.2). Secondly, it is clear that the gain is comparatively small compared to the state observer gains. This is a more subtle point to consider. In essence, the balance between $||\boldsymbol{L}||$ and $||\boldsymbol{L}_\epsilon||$ dictates how much the overall system attributes an external disturbance to either *a*) an actuator deflection or *b*) an external disturbance. For example, as $\boldsymbol{L}_\epsilon \to 0$, the estimate of ϵ will tend towards the dynamic model. Conversely, as $\boldsymbol{L}_\epsilon \to \infty$, the estimate of ϵ will tend toward the measurement from the aircraft state. The issue arises when a disturbance is also acting on the system. In this case, the balance of observer gains can lead to the disturbance being falsely attributed to an actuator deflection; this causes a degradation of performance. An example of this situation is shown in Figs 6.9 and 6.10.

For these demonstration simulations, the first order actuator model used in the ADOBC scheme is intentionally slowed to exacerbate the effect for visual clarity. Two gains are compared, $\boldsymbol{L}_\epsilon = \begin{bmatrix} 0.5 & 0 \end{bmatrix}$ and $\boldsymbol{L}_\epsilon = \begin{bmatrix} 0 & 0 \end{bmatrix}$; these are labelled as $L_\epsilon = 0.5$ and $L_\epsilon = 0$ on the figures respectively. First, a large reference step is introduced at $t = 0.5s$. By comparing the actuator estimation plots, the higher $\boldsymbol{L}_\epsilon$ can be seen to give a more accurate actuator position estimate, accounting for the modelling errors. This also leads to slightly better reference tracking performance. A disturbance is then added at $t = 3s$. Here, the converse effect is seen. The higher $\boldsymbol{L}_\epsilon$ gain attributes a significant amount of this disturbance to a false actuator position estimation, while the other assumes it is entirely external. Now, despite the small error in actuator position for $\boldsymbol{L}_\epsilon = 0$, the disturbance rejection performance is significantly improved.

This parameter requires some manual tuning for best performance and it is expected that the ideal balance will shift depending on the system and nature of the disturbances. In this case, the improved disturbance rejection means $L_\epsilon = 0$ offers better performance. The gains given in (6.16) represent a good middle ground between the two, offering accurate updates of the actuator state estimates while being able to separate actuator position errors and external disturbances. Further, by maintaining the ratio between $||\boldsymbol{L}||$ and $||\boldsymbol{L}_\epsilon||$, as achieved by (6.15), the characteristic performance of the ADOBC scheme with respect to this estimation error behaviour is maintained, while the overall observer gain is altered. This allows for accurate and fair comparison of performance differences resulting from these changes.

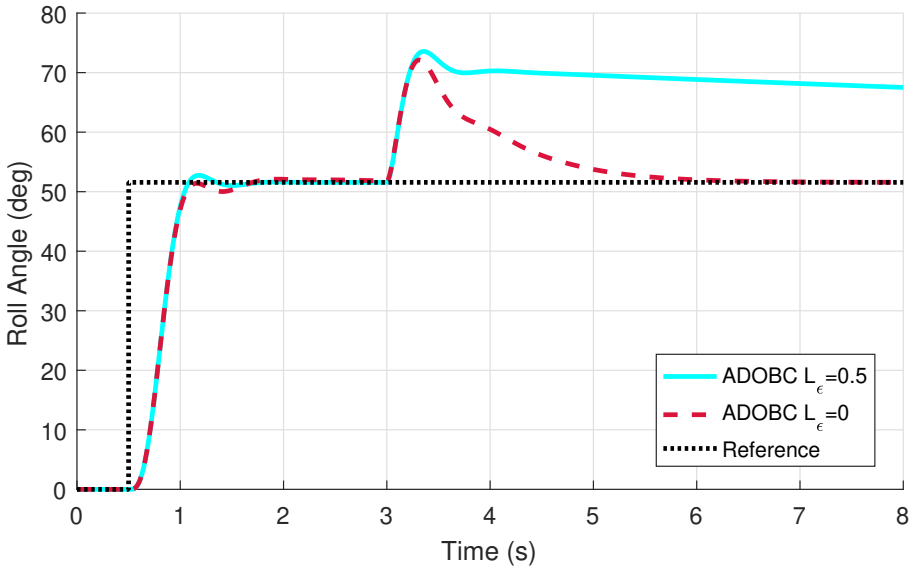

Figure 6.9: ADOBC responses with varying $\boldsymbol{L}_\epsilon$ gains to a reference step. A disturbance is added at $t = 3s$.

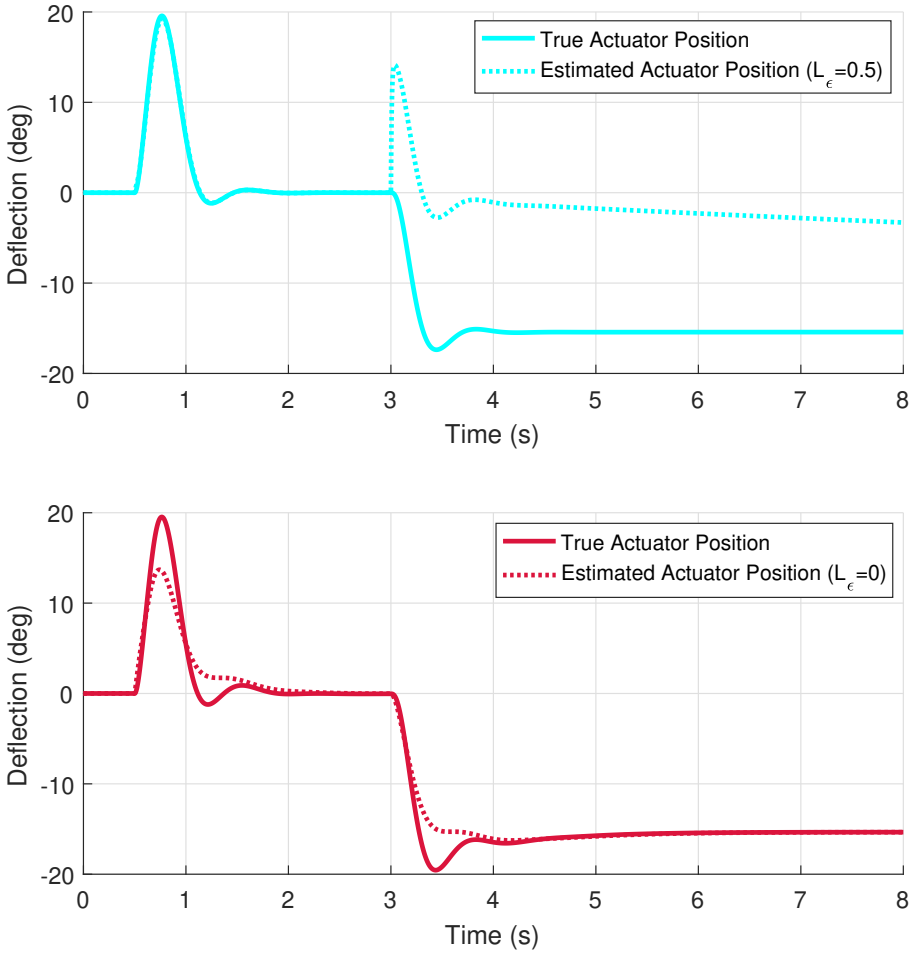

Figure 6.10: True and estimated actuator positions for the ADOBC responses with varying $\boldsymbol{L}_\epsilon$ gains.

6.3 Results

The results intend to demonstrate the performance advantages of the actuator augmented DOBC design. As the performance advantages depend on the difference between com-

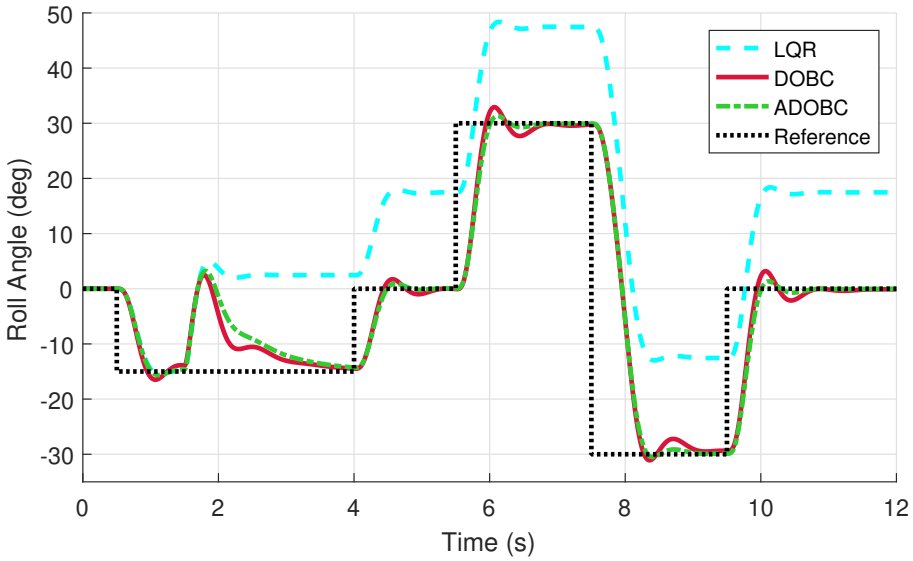

Figure 6.11: Comparison of the baseline LQR, DOBC and ADOBC responses to reference commands. A disturbance is added at $t = 1.5s$.

manded and applied control, it is expected that the differences for the X8 will be quite small. As the small electronic servo actuators are very fast (especially compared to full size aircraft which use hydraulic systems), tight experimental control is required. Numerical simulations are used initially to demonstrate the distinct advantages of the proposed solution. Under fully controlled simulation, subtle differences can be noticed easily in the absence of external noise and disturbance. However, to prove the function is viable for application to aircraft, all findings of the numerical simulations are then validated with flight test results.

6.3.1 Numerical Simulation of DOBC and ADOBC Performance

An initial comparison is drawn between the baseline LQR with the DOBC and ADOBC observers. Unless otherwise stated, the L_k observer scalar is maintained at 1 and the two observers use the same $\boldsymbol{L}$ gain. First, in Fig. 6.11 a performance comparison of the three controllers to a series of reference steps is given.

With the initial reference step command, it is interesting to see all three controllers perform very similarly; the ADOBC shows slightly less oscillation and overshoot than the DOBC. At $t = 1.5s$, a disturbance is added. First, the LQR suffers significant offset from the reference command due to the disturbance. Both the DOBC and ADOBC perform far better. In this case, the DOBC offers slightly faster initial disturbance rejection. In the subsequent reference commands it can be seen that the DOBC has induced some additional overshoot and oscillation when tracking reference commands.

Overall, it is not possible to determine which of the disturbance observer methods is preferable in this result. The basic DOBC offers better disturbance rejection, but slightly worse reference tracking. However, it is important to remember that the intention of the augmentation proposed here is to allow for faster observer dynamics through higher observer gains. In the initial discussion, it was mentioned that as the DOBC dynamics become faster, small errors between demanded and applied control could lead to problems. To investigate if this is the case, the L_k observer gain will be studied next. Two topics of interest are to be studied. First, does increasing the observer gain introduce issues from unmodelled actuator dynamics? Second, does augmenting the observer with actuator dynamics improve performance in this regard?

To study these issues, the following simulation was conducted. In Fig. 6.12 the two

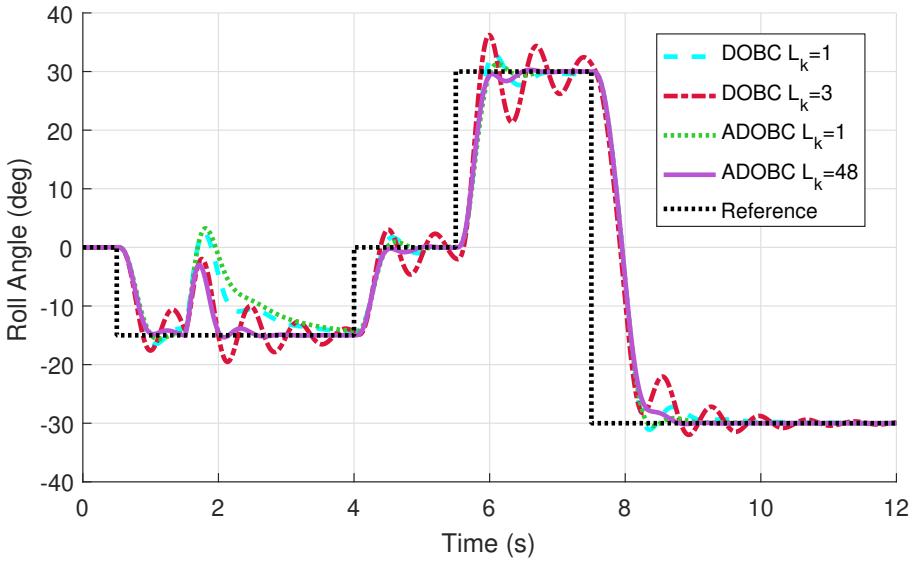

Figure 6.12: The effect of increasing observer gains for the DOBC and proposed ADOBC schemes.

schemes are compared with increasing gains. Here, it is demonstrated that a modest increase in the DOBC observer gain results in degraded performance. Conversely, a substantial increase for the ADOBC scheme results in no such issue. This shows that even with modest observer gains, the basic DOBC scheme begins to observe disturbances due to the difference between u and ϵ. This is confirmed by noticing that the oscillations begin at the initial reference command, prior to the addition of external disturbances at $t = 1.5s$. When the disturbance is added, the oscillations return. This clearly indicates it is the result of actuator deflections, not external disturbances. For the ADOBC, despite using a simplified model of the actuator dynamics, substantial increases in observer gain are possible with no noticeable disadvantage. The high observer gain ADOBC gives substantially improved disturbance rejection performance as well as no induced penalty for reference tracking.

The result is clear; inclusion of actuator dynamics within the observer allow for a substantial increase in the observer gain. The result is improvement in both reference tracking and a substantial improvement in disturbance rejection performance. This result is obtained even in the presence of non-trivial actuator modelling error. With appropriately tuned gains for the actuator position estimate, the ADOBC method is able to accurately estimate the actuator positions while also being able to separate external disturbances from actuator model errors.

The final step remaining in the process is to demonstrate that this performance translates to real world performance.

6.3.2 Flight Testing

A flight testing program was initiated to study the performance of the ADOBC scheme as compared to the baseline DOBC and LQR controllers. The main points of interest are confirming no loss of performance compared to the DOBC in normal flight and demonstrating the higher stable observer gain enabled by the actuator augmentation. The automatic reference command system detailed in Section 5.4.2 was also implemented in these tests.

Initial Disturbance Rejection Performance Study

In preparation for later test flights with forced physical disturbance, an initial test flight was planned which made use of an artificial disturbance. The generalised control scheme

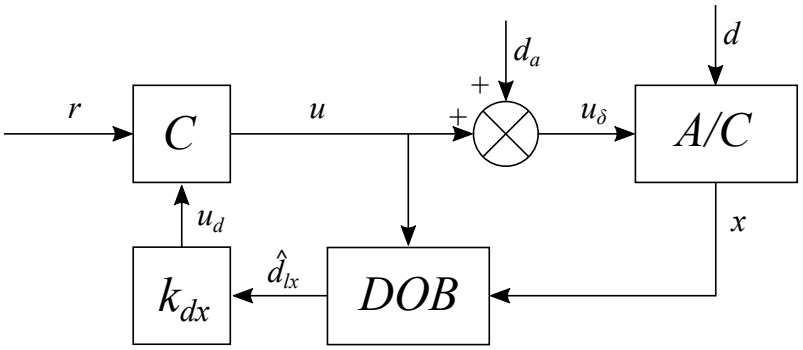

Figure 6.13: Generalised control scheme for flight testing of artificial disturbance injection, d_a.

for this test is shown in Fig. 6.13. Here, the artificial disturbance d_a is added to the control demand from the general controller C, r is the reference command, u_δ is the total control demand sent to the aircraft denoted by A/C, d is the general unknown disturbance, x is the aircraft state and DOB represents the generalised disturbance observer generating the lumped disturbance estimate $\hat{d}_{lx}$. With this path of entry, d_a will be estimated by the disturbance observer as a component of the disturbances acting on the aircraft, while allowing the operator full control of its application. Repeatable and controlled disturbance application is difficult to achieve in flight testing. Using this artificial method, a reliable and repeatable disturbance is available for testing.

This method of artificial disturbance represented the safest means of initially testing control performance to a forced disturbance, as the disturbance could be removed at any time. Furthermore, this offers a unique opportunity for data analysis in flight testing which is usually reserved for simulation; as the disturbance is controlled by the operator, the exact moment at which it is activated is known and available when data processing. This allows for good insight into controller performance in flight testing with a *known disturbance*. For all flights herein, unless otherwise stated, the total observer gain matrix used was

$$\boldsymbol{L}_t = \begin{bmatrix} 1.5 & 0 \\ 0 & 0.75 \\ 0.014 & 0 \end{bmatrix},$$

where $\boldsymbol{L}_t(3,1) = 0.014 = L_\epsilon$, is the actuator observer gain used. This value was found from some initial flight testing to give better results than the $L_\epsilon = 0.01$ used in simulation.

Baseline Flight Test

Prior to the activation of any external disturbances, a baseline test was conducted to compare the performance of the three controllers. The result is shown in Fig. 6.14. Here it can be seen clearly that the aircraft has some steady state error which the LQR is not able to remove, in the form of a constant positive roll bias of around 5°. This results in overshoot of positive roll commands and undershoot of negative roll commands. The two disturbance observer based schemes perform well, removing the bias from the aircraft in both steady state and reference commands; any difference between the DOBC and ADOBC schemes is not significant enough to be discernible from external disturbances. This is very similar to what was seen from numerical simulation.

Next, the baseline disturbance rejection performance with the artificial disturbance is studied. For the disturbance, a 6° roll command was chosen as d_a. This was expected to produce a visible result without creating an overly significant disturbance which could endanger the aircraft. The results are shown in Fig. 6.15. Due to flight constraints, the disturbance could not be maintained for equal time for the three passes; the plotted

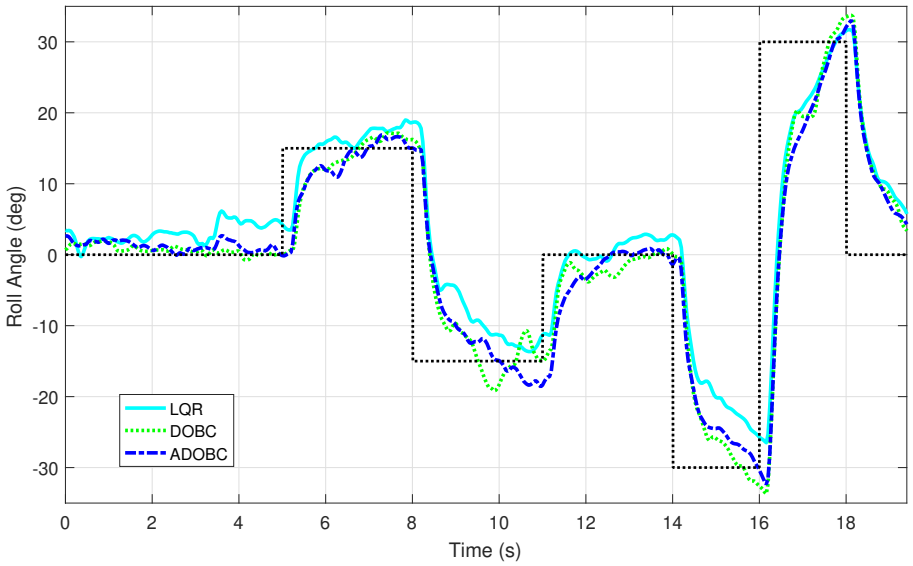

Figure 6.14: The baseline pass using the automatic reference input with no artificial disturbance active.

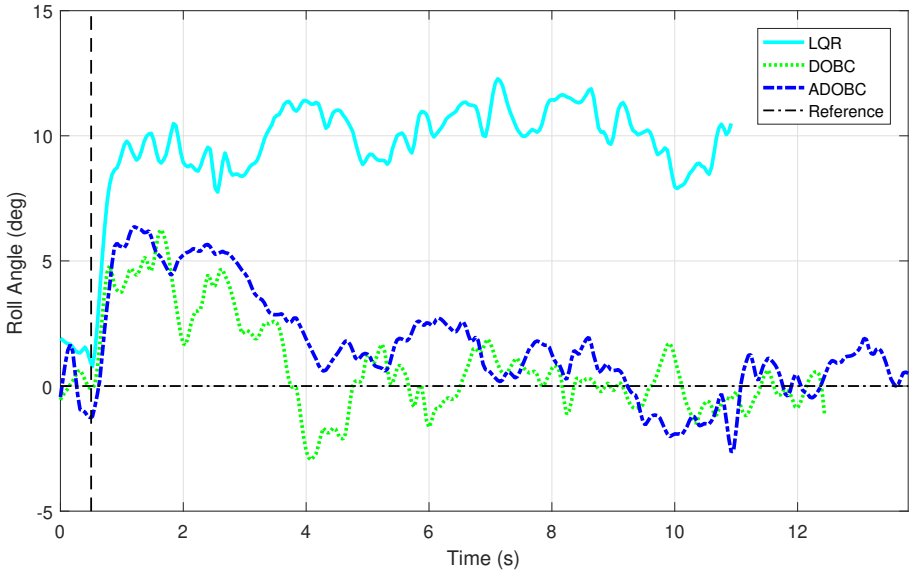

Figure 6.15: The result for artificial disturbance activation in flight. The activation occurs 0.5s, denoted by the vertical dotted line. Variations exist in the length of data due to flight constraints.

data ends when the disturbance was removed. The effect of the disturbance can be seen very quickly as the aircraft begins to roll. With the LQR scheme, the aircraft settles at around $\phi = 10°$. Due to the lack of reference feedback this scheme is expected to have this steady state error. Both DOBC schemes reduce the initial roll magnitude and restore the aircraft to the reference condition quickly. However, the same behaviour as demonstrated in the initial numerical simulations can be seen again. With equivalent observer gains, the DOBC scheme is able to reject the disturbance more quickly than the ADOBC scheme, settling back to the reference command significantly more quickly. This further validates the numerical simulations.

With this encouraging flight result, the aircraft was prepared with the first physical disturbance. To achieve a repeatable disturbance, a known weight was attached to the aircraft wing tip as shown in Fig. 6.16. This weight would provide a constant rolling moment disturbance to the aircraft, having a similar effect to the artificial disturbance

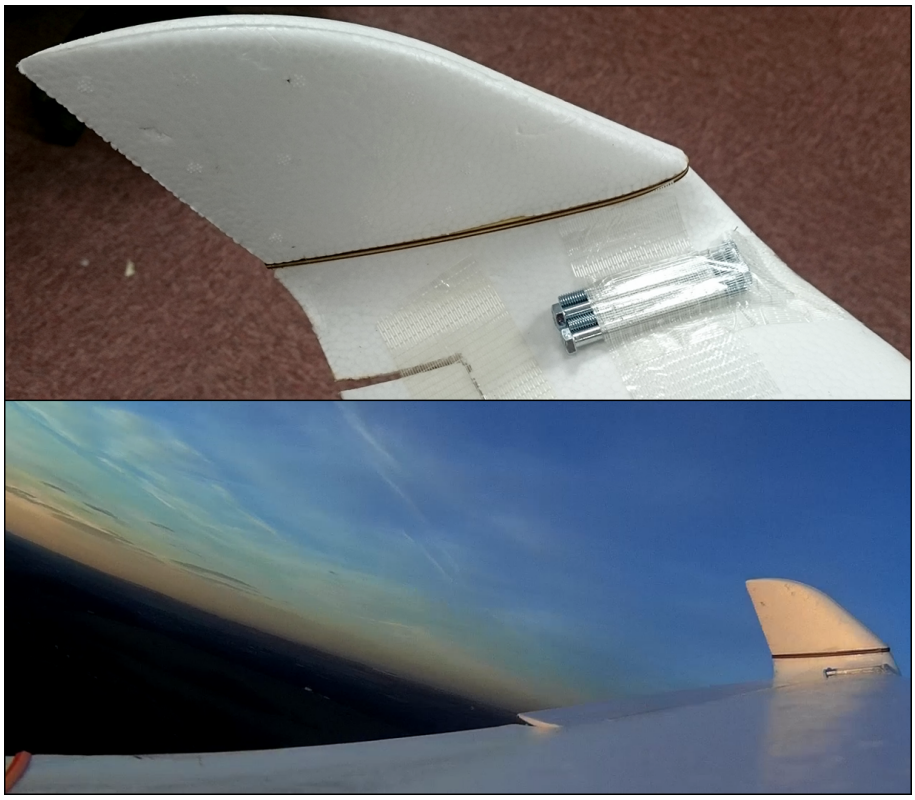

Figure 6.16: The physical disturbance weight attached to the wing tip both on the ground and in flight.

injected previously. To test this, the weight was first attached to the left wing tip, which would produce a negative rolling moment. In the initial flight test, a permanent positive roll disturbance was seen in the LQR response. It is therefore expected that this weight will reduce the steady state error somewhat, with the system approaching nominal conditions.

This flight was conducted separately to the initial flight, so the external disturbance levels are expected to vary. Fig. 6.17 shows the flight test result for the same automatic input. First, it is immediately clear that the addition of the weight has removed the majority of the previously seen external disturbance, as the LQR controller now remains very close to the reference command. Secondly, the overall magnitude of the external disturbances is noticeably less during this flight, as the responses are generally smoother. This allows some additional insight, as with three out of four reference roll commands the DOBC controller has a consistent overshoot, which is not seen for the other two controllers. This suggests further that the behaviour seen from the DOBC in numerical simulations has translated to flight testing - actuator errors appear to lead to small overshoots of the reference commands.

Unbalanced External Disturbance

With good performance shown with both the artificial disturbance and balanced external disturbance, the next flight would be conducted with the weight placed on the right wing tip, which is expected to exacerbate the performance degradation, particularly for the LQR. The results are shown in Fig. 6.18. The LQR is significantly affected by this additional disturbance, as the steady state error is now much more pronounced. The two DOBC schemes are perform well, compensating for the effect of the weight and offering excellent reference tracking. This test does not show any additional difference between the two observer schemes, even with the larger disturbance. This is expected, as it can

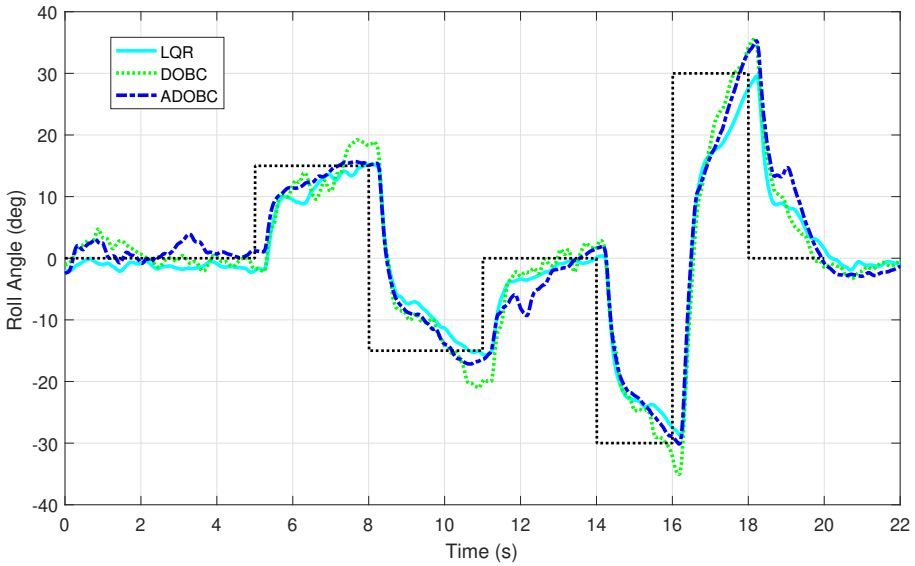

Figure 6.17: Flight data for automatic input response with balancing external weight disturbance applied.

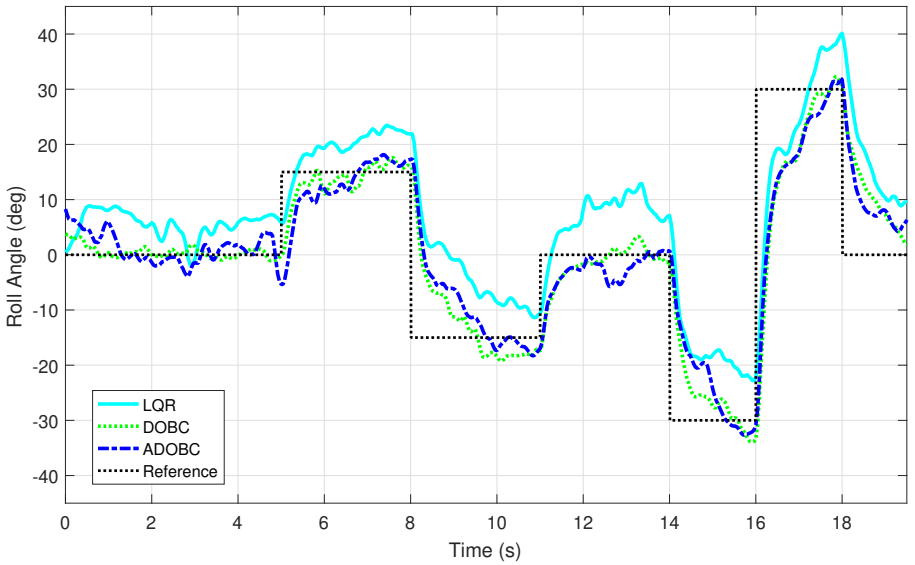

Figure 6.18: The results for the three control schemes for the aircraft response to automatic reference commands with the unbalanced weight applied to the right wing tip.

be seen in the initial $3s$ that both observers have correctly estimated the disturbance and removed it from the output. It is clear from this data that the DOBC controllers offer significant benefits over the LQR.

Actuator Observer Gains

As discussed in Section 6.2, the effect of the gain L_ϵ is more intricate with the ADOBC than L for the DOBC. To investigate the effect of this in flight, a test was planned which used three different L_ϵ gains. The nominal L_ϵ gain of 0.014 was compared with $L_\epsilon = 0$ and $L_\epsilon = 0.14$. The artificial roll disturbance was used in this flight test, as the dynamic response to a disturbance was to be investigated. The result is given in Fig. 6.19. Here, it is clearly evident that the $L_\epsilon = 0.14$ setting has resulted in detrimental performance. The aircraft reaches the reference command 12.1s after the artificial disturbance injection; this is substantially slower than the other gains. It can be seen that both $L_\epsilon = 0$ and

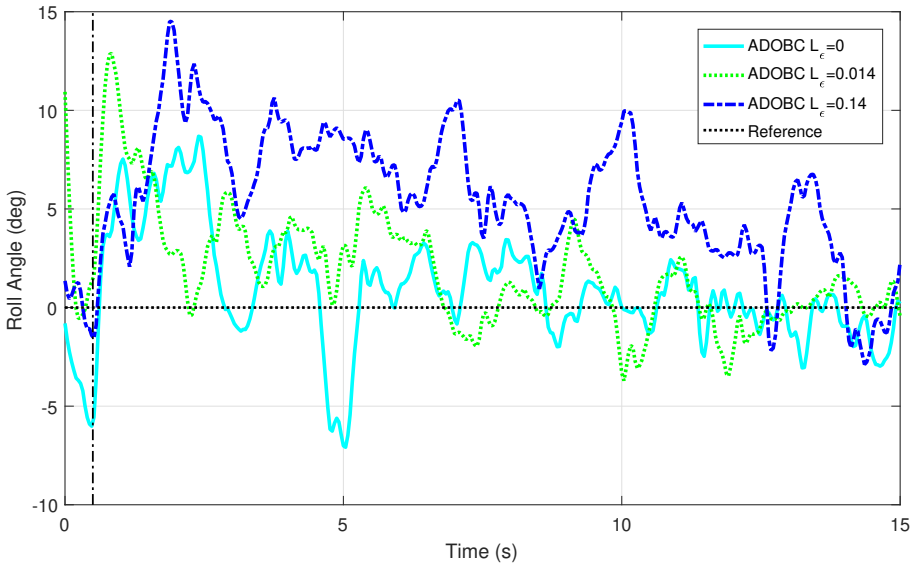

Figure 6.19: Comparison of aircraft performance during zero reference passes with various L_ϵ actuator observer gains. An artificial disturbance is injected at 0.5s, denoted by the dash-dot line.

0.014 perform much better, seeming to reach the reference command at similar times. However, more detailed inspection reveals that $L_\epsilon = 0.014$ maintains a slight bias toward the disturbance for slightly longer than $L_\epsilon = 0$; this also corresponds with the numerical simulations.

The next test was a run of the automatic reference command with the various gains. The artificial disturbance result showed that $L_\epsilon = 0$ had faster disturbance rejection. It was important to establish if there were any drawbacks to this, as this result relies entirely on the actuator model with no updated estimate from the aircraft's response. The results are demonstrated in Fig. 6.20. With this data, it is the $L_\epsilon = 0$ gain which exhibits reduced performance. Both the initial disturbance rejection performance and reference tracking commands show worse performance than the other gains. Although the high L_ϵ gain shows reasonable performance, it does exhibit the characteristics of the LQR controller in as much as a steady, positive roll offset appears present in some of the data. The initial 5s has a generally constant offset akin to the LQR performance in previous flights. Furthermore, overshoot is present in turn 1 and undershoot in turn 3, which both closely resemble the LQR response. A more subtle point of the data is the comparatively more stable performance of the $L_\epsilon = 0.014$ flight. Throughout the manoeuvre, and particularly in the initial 5s, it can be seen that for this gain setting the aircraft exhibits overall much smoother behaviour, with less oscillations present. This suggests that the inclusion of a reasonable L_ϵ gain is favourable over no L_ϵ at all. Overall, the L_ϵ of 0.014 exhibits the most consistent behaviour with good disturbance rejection properties. This is also in line with the numerical simulation results.

An additional manoeuvre was carried out during this flight test; a manual input full roll command to complete a full 360° turn. The result is given in Fig. 6.21. The data is noisy as the wind had increased in this portion of the flight. However, this noise offers some interesting insight into controller performance. Both the high and mid gain controllers undergo a significant disturbance of similar magnitude (at 4s and 10s, respectively). The response from the high gain observer is once again very slow to return to the reference command, whereas the mid gain observer returns to the reference much more quickly. Furthermore, the 0 estimator gain observer provides very good reference tracking and appears to offer better disturbance rejection. Based on this data, it would be suggested that L_ϵ be reduced from the current default of 0.014, for a better balance of characteristics.

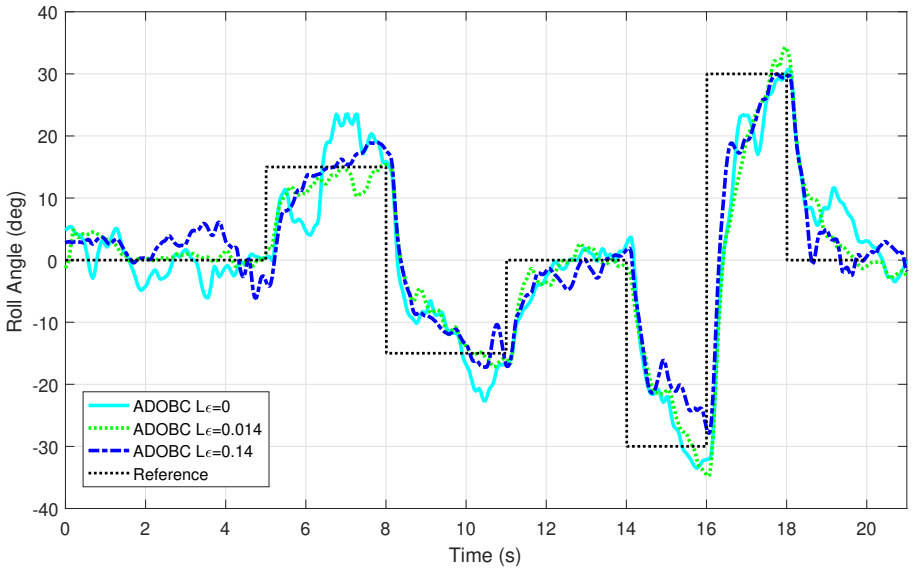

Figure 6.20: Comparison of aircraft performance with automatic reference command using various L_ϵ actuator observer gains.

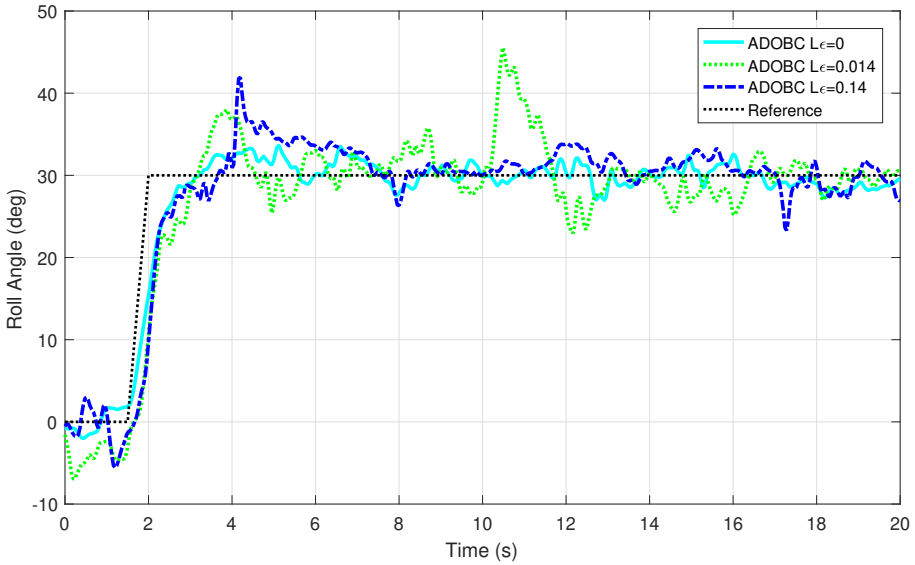

Figure 6.21: Comparison of aircraft performance during a manual maximum roll command input with various L_ϵ actuator observer gains.

For the remaining flights, $L_\epsilon = 0.01$ was used.

The Effect of Increasing L on the ADOBC

The flight test results up this point have indicated that the results from numerical simulations have translated to the physical plant. The final point to investigate is if the inclusion of actuator dynamics allows for an increased ADOBC observer gain over the baseline DOBC, giving better disturbance rejection. To investigate this point, a final test was conducted to compare the baseline LQR, DOBC and ADOBC. An artificial step disturbance would be used once again. For this test, the DOBC gain was increased by an $L_k = 2$ over the nominal value. This is compared with the ADOBC at the same $L_k = 2$, in addition to the $L_k = 8$ result. This final result represents an additional increase over what was demonstrated in the previous flight test, and a substantial increase over that of the DOBC. The result is given in Fig. 6.22.

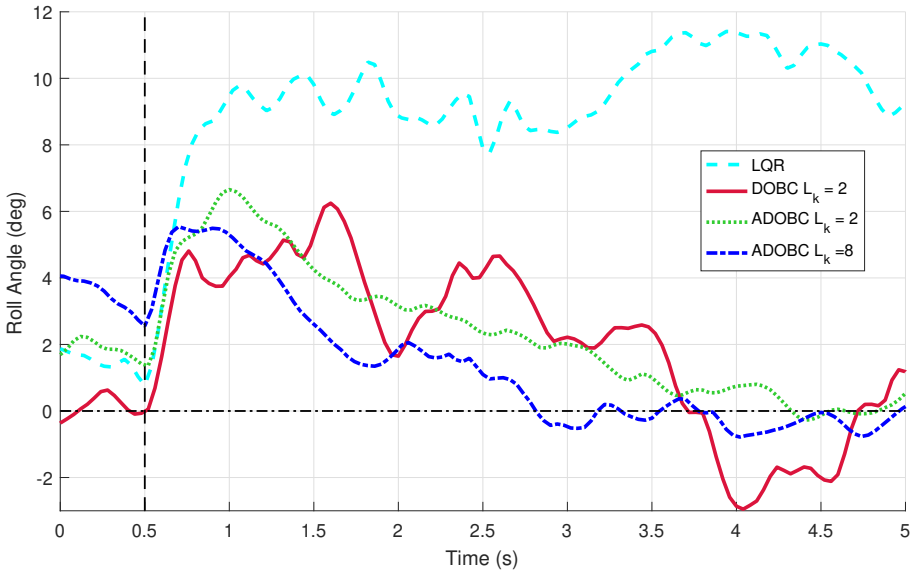

Figure 6.22: A flight test comparison of the LQR, DOBC and ADOBC to an artificial disturbance with varying L_k gains.

The results are clear. First, all the observer based schemes have resulted in better disturbance rejection performance as compared to the LQR, as expected. Next, it is noted that the behaviour of the DOBC controller has become oscillatory, corresponding with expectations from the numerical simulations. The ADOBC controller with the same L_k gain performs very similarly, with much less oscillation. This further confirms the numerical simulation results. Finally, the ADOBC controller with $L_k = 8$, which represents a significant increase in observer gain, is free of oscillation and gives the best disturbance rejection performance by a significant margin. This final result confirms and validates the findings of numerical simulations. The ADOBC augmentation allows for an increased observer gain over the DOBC which translates to overall improved disturbance rejection performance. These responses match well with expectations when compared to the earlier numerical simulations. The results are also in line with expectations from earlier flight test data shown in Fig. 6.15, despite being conducted on different days (and as such with no guarantee of similar flight conditions).

6.4 Conclusions

Within this chapter, it was shown that linear state space disturbance observers developed in previous literature were susceptible to performance degradation in the presence of actuator dynamics. It was shown that such unmodelled dynamics restricted the magnitude of observer gain which could be applied without resulting in performance degradation. This limitation on observer gain constrained the rate at which the observer could estimate disturbances, which limits the rate at which their effects can be mitigated. An augmentation to the previous DOBC design was proposed to address this issue, dubbed as the ADOBC in this chapter. The resulting performance was studied with simulations and flight testing.

Initially, dynamics of the actuators used on the Skywalker X8 were investigated to produce suitable models. During this investigation, it was found that the response was composed of an initial time delay followed by the dynamic response of the actuator. To account for this in control design and simulation, the actuator model time constants were increased to include the effect of the time delay within the dynamics. Explicit consideration of the time delay in control design is non-trivial; this method offered a good compromise. It was also determined that under maximum expected flight load the actuator response

was essentially unchanged. This meant the modelled response would not change in flight, maintaining validity.

An augmentation of the DOBC design utilised in Chapter 5 was presented which estimated the true actuator deflections, using an actuator model, demanded control input and aircraft state measurements. The actuator model used in the observer was first order, while numerical simulation used a second order model. This allowed study of the performance with actuator modelling uncertainty. Some discussion was presented regarding the tuning of the observer gain for estimation of actuator dynamics. It was shown that with proper tuning of this gain, the proposed ADOBC method was able to accurately estimate the actuator deflections in the presence of modelling uncertainty and external disturbances.

Simulation studies revealed that using equivalent gains, the DOBC method offered slightly faster disturbance rejection than the ADOBC. However, the intention of the ADOBC augmentation was to allow for higher observer gains for a system with actuator dynamics. When this was investigated, it was discovered that the ADOBC augmentation allowed for observer gains of an order of magnitude higher than the DOBC. This resulted in much faster estimation and crucially rejection of the disturbances. A range of flight tests were conducted where the benefits of the ADOBC method found in numerical simulation were shown to translate very well to the physical aircraft.

The developed observer actuator augmentation has shown undeniable benefits when applied to a system with actuator dynamics. Actuator dynamics are an unavoidable feature of physical systems. The proposed development is therefore very beneficial in improving DOBC estimation performance in real world systems. It is pertinent to remember that the improvements shown herein were realised on a system with very high actuator bandwidth. Due to the nature of the problem, the benefits would be even larger for systems with slower actuators, such as full scale aircraft with hydraulic actuators.

Chapter 7

Modelling and Mitigation of Aircraft Structural Oscillations

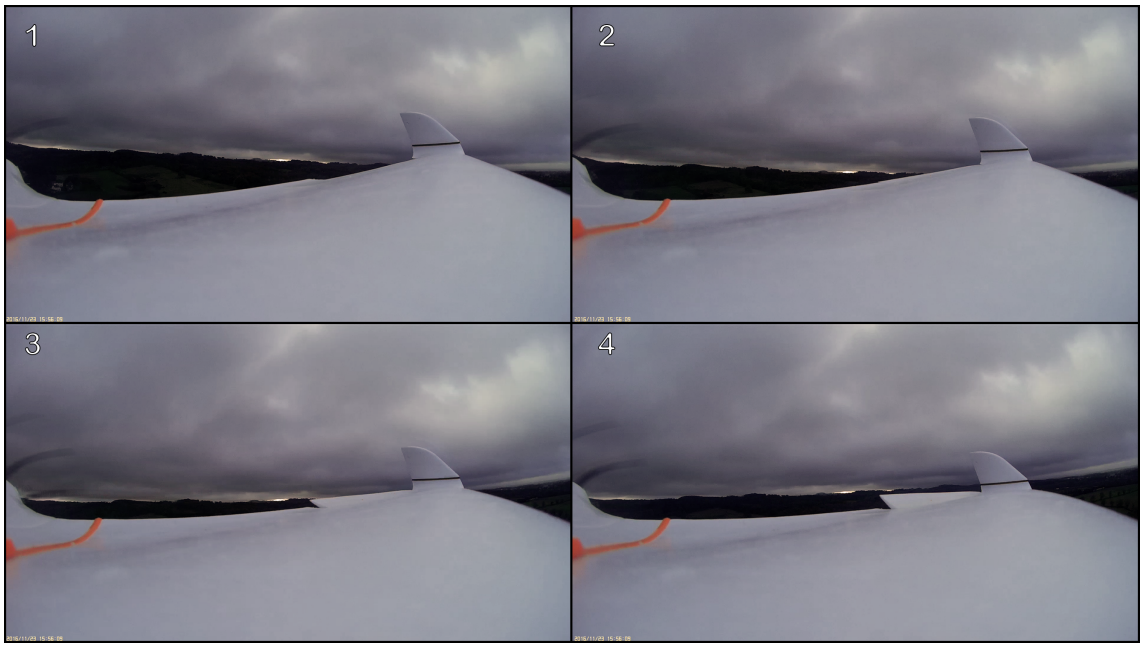

Figure 7.1: Video stills taken from the aircraft in oscillation. Each frame (1-4) represents a $\frac{1}{30}s$ progression in time. Note the opposing vertical motion of the wing tip and body.

During initial flight testing of the LQR with DOBC, severe longitudinal oscillations were noticed in the gain tuning process. These gains appeared once either the LQR or DOBC gains were increased beyond critical points. At or below these gains, the aircraft would show some signs of oscillation which would generally disappear shortly afterwards. Once past the critical point, however, the oscillation became severe and continued until the controller was disabled. This limitation was a problem, as to remain stable the gains needed to be quite low for both the LQR and disturbance observer, restricting performance. A higher gain will give the baseline controller better tracking performance and improved robustness. Higher disturbance observer gain allows for faster estimation of disturbances which therefore gives improved performance. A solution was needed to allow the gains to be increased further.

The root cause of this issue was found to be structural. As is discussed within this chapter, the unconventional construction methods used for small UAVs means this problem is unlikely to be limited only to the Skywalker X8. A solution which could be applied to any aircraft would therefore be preferable. In this chapter, the work done to identify

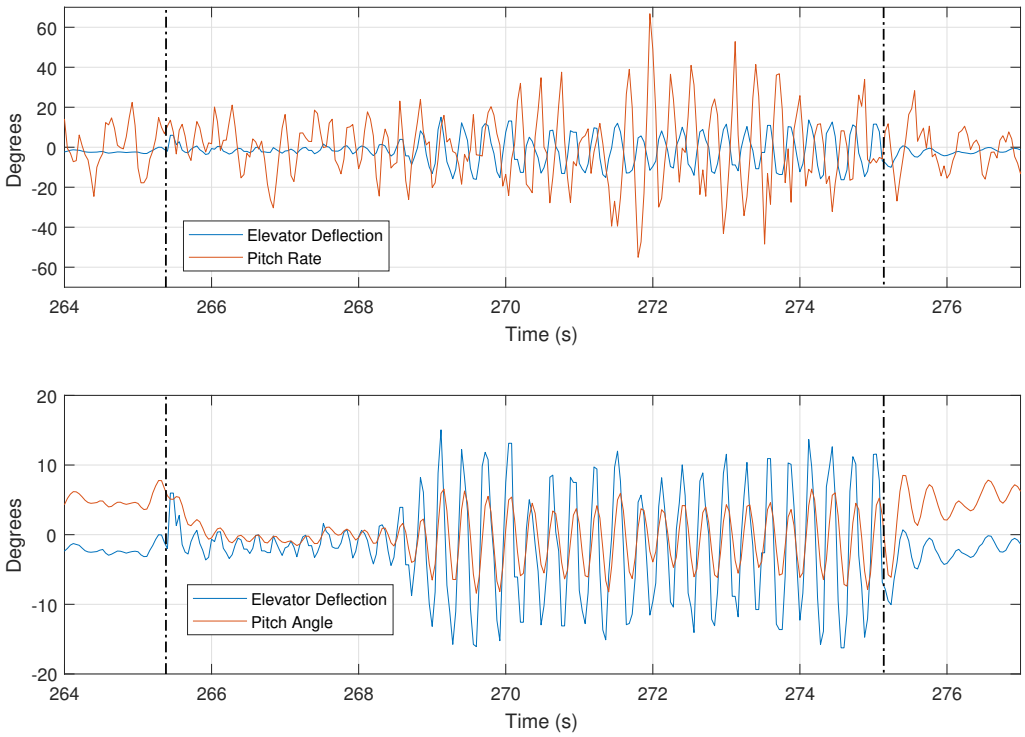

Figure 7.2: Formation of the longitudinal structural oscillation. Activation of the offboard controller is denoted by the black dashed lines.

the cause of the oscillation is presented, along with the proposed solution and data to demonstrate the resulting performance.

7.1 Introduction

The longitudinal oscillation which appeared during flight testing was severe to the point of endangering the aircraft. The longitudinal oscillation is demonstrated with in flight footage in Fig. 7.1. The camera was placed close to the neutral point of the opposing wing tip and body oscillations, resulting in clear footage showing both aircraft parts oscillating.

This motion was seen previously in initial testing of the X8 when the Pixhawk flight controller was first installed. This appeared to be a result of excessively high control gains, which excited this mode. Reducing the Pixhawk gains removed the issue. At a later time, the oscillations returned, this time while the aircraft was under offboard control. Fig. 7.2 demonstrates the formation of this mode as the controller is activated. Here we notice that the behaviour is absent until offboard activation. A slow build up is seen, after which the oscillation continues with its maximum oscillation amplitude until the controller is disabled. It can be seen that elevator deflection and pitch angle are very close in phase, while pitch rate and elevator deflection appear to be out of phase. This phenomenon is quite different to traditional aeroelastic flutter. Traditional flutter is a result of an interaction between structural modes and airflow [116]. In the witnessed response, we see that control action is directly related to this mode. Later discussion will also show that unstable oscillations do not occur below key feedback gains, further differing from traditional flutter. It was also considered that this oscillation may arise from the natural modes of the aircraft. However, investigations of the short period pitching oscillation for the X8 determined this to be in the range of 8Hz, which is out of range for the witnessed motion.

Further investigation was required to identify the source of the oscillation. There are

two possible causes:

1. Internal controller behaviour
2. Aircraft structural/aerodynamic interaction

If the controller is the source, this will be an internal property related to control design which excited a structural interaction in the aircraft. If the aircraft is the source, then a structural response of the aircraft is exciting a response within the controller. This was the initial point to be investigated, as the answer would direct the next phase of the investigation.

Frequency Identification Methodology

To reliably analyse the effect of various controller adjustments on the aircraft response, a suitable metric is required. For this, the Fast Fourier Transform (FFT) was used. This process analyses data recorded in the time domain and returns the components in the frequency domain. As the flight data is digital and discretely sampled, the Discrete Fourier Transform (DFT) was used. The DFT of a signal vector $\boldsymbol{x}$ is defined by

$$\boldsymbol{y}_k = \sum_{j=0}^{n-1} \omega^{jk} \boldsymbol{x}_j,$$

where the result $\boldsymbol{y}$ is a vector of complex numbers, $\boldsymbol{x}$ is a vector containing n uniformly sampled points, j and k are indices running from 0 to $n-1$, $\omega = e^{-2\pi i/n}$ where i is the imaginary unit. Once $\boldsymbol{y}$ has been calculated, some further processing is required to determine the frequency components. First, we compute the two sided spectrum $\boldsymbol{P_2}$ as

$$\boldsymbol{P_2} = \left|\frac{\boldsymbol{y}}{n}\right|,$$

from which we can compute the single sided spectrum $\boldsymbol{P_1}$. First, we extract the first half of $\boldsymbol{P_2}$ by

$$\boldsymbol{P_1} = \boldsymbol{P_2}(1:h),$$

where h is an index defined as

$$h = \left[\frac{n}{2} + 1\right],$$

which is rounded to the nearest integer for an index. The final operation to calculate $\boldsymbol{P_1}$ is applied

$$\boldsymbol{P_1}(2:[h-1]) = 2 \times \boldsymbol{P_1}(2:[h-1])$$

Finally, we can plot $\boldsymbol{P_1}$ across the frequency range, aiming to identify a peak frequency. Fig 7.3 shows the result for the data shown in Fig. 7.2; note that $\boldsymbol{P_1}$ values below 1Hz have been multiplied by their frequency, creating a linear filter between 1 and 0Hz. As the analysed data has a non-zero mean, the $\boldsymbol{P_1}$ response produces high signal strength as $f \to 0$; filtering out this data clarifies the range of interest. The result is easily interpreted, with the peak magnitude identified in the legend. We can see low level noise for the majority of the frequency range with a clearly defined peak at 3.41Hz. Using this technique, we can quickly assess the resulting differences in performance from any subsequent changes.

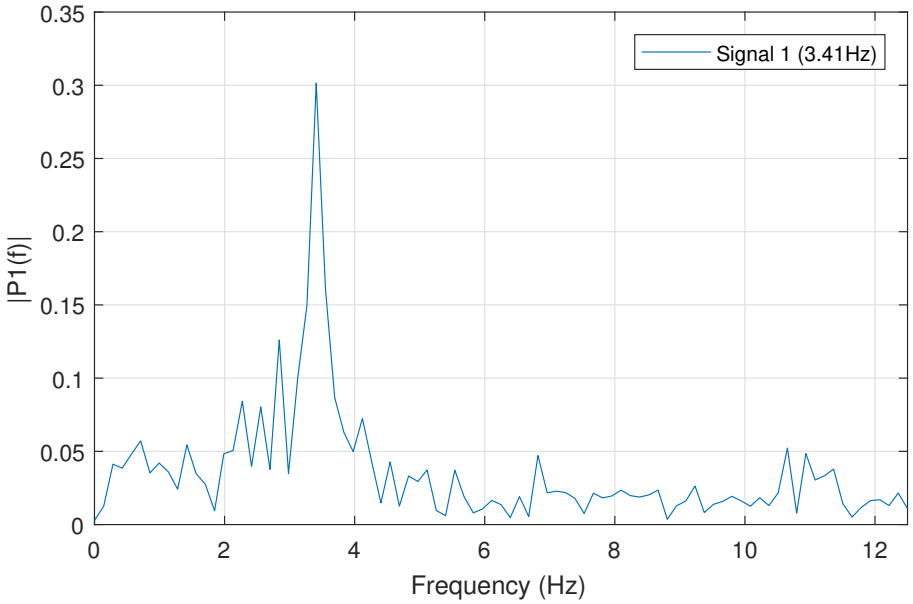

Figure 7.3: The frequency decomposition of the pitch angle data supplied in Fig. 7.2.

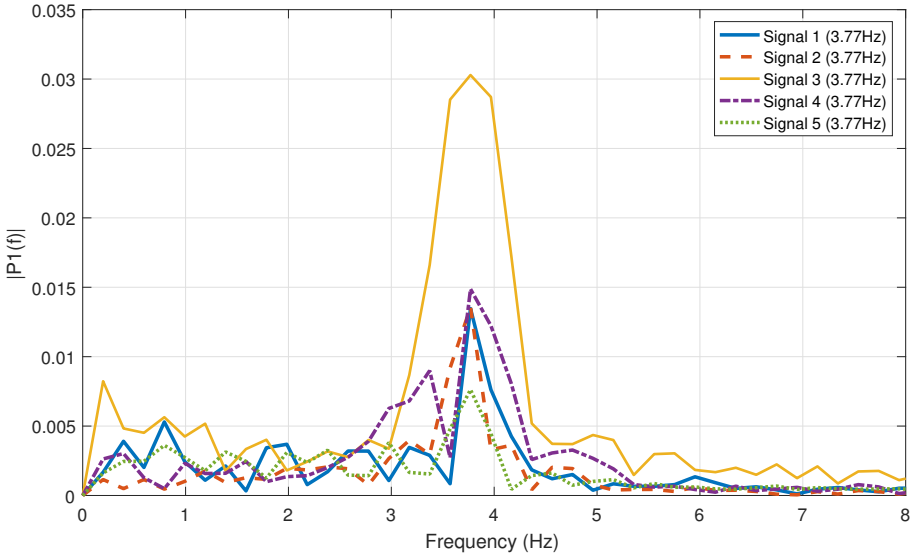

Figure 7.4: The dominant frequencies from 5 periods of various controller gains of a single flight test. The x axis was limited to 8Hz when plotting for clarity.

Oscillation Cause Identification

As it is far simpler to adjust controller gains than it is to carry out any meaningful structural modifications, this source was investigated first. Initially, only the LQR controller was active in the longitudinal control scheme and a series of gain values were tested in flight. Then, with the LQR gain fixed, the DOBC scheme was activated with a range of gains tested again. As all the data was collected in the same flight, changes in external factors such as aircraft balance (due to battery placement etc.) and air density could be assumed to be equal across tests. The gains were purposefully chosen to ensure mode excitation.

Fig. 7.4 shows the resulting analysis from 5 periods in the flight, with the dominant frequency for each signal. Table 7.1 shows a comparison of the gain scalars for signals 1-5, demonstrating the range of test conditions. Scalars were applied as a multiple to the preset controller gains used in flight.

Table 7.1: The various LQR and DOBC controller gain scalars used during controller architecture frequency flight testing.

Signal	Controller	LQR Kp Scalar	DOBC L Scaler
1	LQR	0.9	0
2	LQR	0.81	0
3	LQR	0.61	0
4	LQR + DOBC	0.61	0.61
5	LQR + DOBC	0.61	0.46

The results are quite clear in that all 5 signals present the same dominant frequency for the oscillations, despite the significantly differing gains. Even the addition of the DOBC scheme has no effect on the frequency.

The resolution of the result is limited by the amount of samples provided in each input vector. In this case, all samples were chosen to have the same length and therefore have the same resolution of 0.198Hz. The length of the input vector is mainly limited by the amount of time that the pilot is willing to let the aircraft maintain the oscillation, as the motion is rather violent. This data strongly suggests that the oscillation frequency is independent of controller gain. Furthermore, it has been demonstrated that it is not a feature of either the LQR or combination of LQR + DOBC schemes, as alterations of neither affected the frequency. To fully rule out the control scheme, we next focus on adjustments to the aircraft structure. If this results in a notable change in peak frequency, we can be very certain that the root cause of the oscillation is the airframe.

For this test, a constant structural modification was implemented. As in Chapter 6, weight was attached to both wing tips (as shown in Fig. 6.16). The hypothesis for this test was that an oscillation of structural should alter the frequency of any recorded oscillation. To further rule out controller features, the DOBC gain was modified during this flight to determine its effect on the oscillation.

Structural stiffening was considered as a possible modification to the aircraft for this flight. However, despite many efforts, no suitable stiffening method could be produced due to the location of the axis around which oscillation took place. The X8 already features dual carbon spars which extend beyond the central axis of the structural flexing, as shown in Fig. 7.6. For these reasons, it was deemed infeasible to perform this test using structural stiffening.

The result of 3 different portions of oscillation are shown in Fig. 7.5. Each of these flights also used a different L scalar gain. A clear and significant reduction in the oscillation frequency is seen (3.8Hz $\rightarrow$ 2.7Hz), demonstrating that the weight has had a significant effect on the response.

The 3 peak frequencies are within 1 resolutions' width of each other, representing a very tight group. Furthermore, the independence of frequency to controller gain has been demonstrated once more. At this point it was decided that the root cause of the longitudinal oscillations was most certainly structural.

7.1.1 Aeroservoelastic Oscillation

Aeroservoelastic oscillation (or flutter), in aeronautical terms, refers to an oscillation of the aircraft caused by, in some part, an interaction between the aerodynamic forces, servo (or actuator) dynamics and the elastic (flexible) aircraft structure. This is a long-standing common problem in aeronautical engineering, with some early textbooks on the topic being published as early as 1951 [117]. Structural oscillation especially is a feature for large aircraft such as the B-52 [116], C5-A Galaxy and Boeing 747 [118]. This is due to their size coupled with light weight, flexible structures. Modern small UAVs are of course

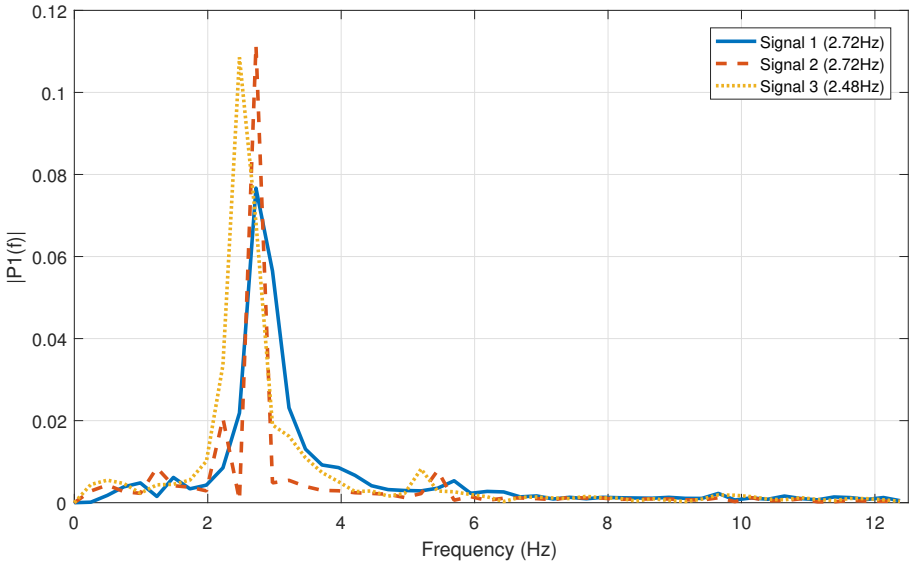

Figure 7.5: Frequency response of flight controller with 3 different DOBC gains during the weighted wing flight tests.

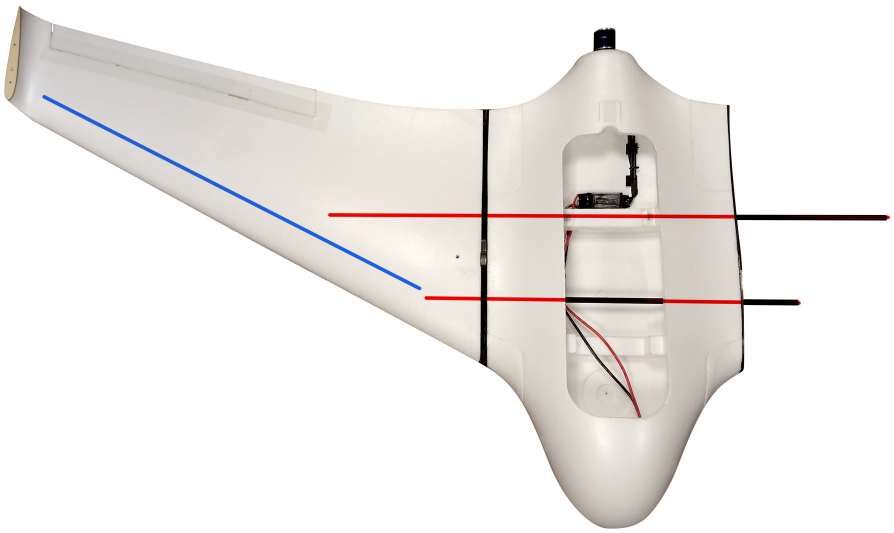

Figure 7.6: The X8 aircraft with a wing removed showing the carbon structural components. Red: Two main spars. Blue: Wing leading edge spar.

significantly smaller than these aircraft. However, due to their design and construction materials, they are still relatively flexible, as is the case with the Skywalker X8. The X8 is made of Expanded Polypropylene (EPP) foam, which is relatively soft and flexible. Two carbon rods are used as spars to add some structural rigidity, with a third used in the leading edge of the wing. Fig. 7.6 shows these components on the aircraft. Despite featuring multiple carbon spars, they are connected to each other only through EPP, allowing plenty of scope for flexing. This is clearly very different to typical structures on full sized aircraft. Further, this structure is typical of modern small UAVs, meaning it is unlikely this issue is limited to the X8.

In literature, a range of active methods of addressing flutter have been studied including classical root locus methods [119], energy based control [120], adaptive control [121] and Linear Quadratic Gaussian (LQG) control [122] with observers [123,124]. A recent survey [125] demonstrates clearly that the vast majority of research in this area is on active control of flutter. The issue with application of active methods to the X8, or small UAVs in general, are the additional requirements. First, most methods rely on additional sensors

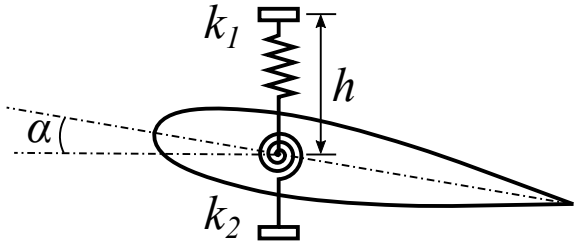

Figure 7.7: A generic model of flexible wing dynamics as part of a flexible airframe model.

placed along the wing, such as accelerometers or gyroscopes. This would add both cost and complexity to small UAVs, which is undesirable. Additionally, many of these methods require models of the wing for the design of active control laws for suppression of the flutter. Acquisition of these models is a non-trivial task which is well beyond the scope of what is feasible for the majority of small UAV operators. This would require a significant amount of time to develop and implement. Active methods were therefore disregarded for this work.

Some literature on passive methods can be found which include structural optimisation [126] and notch filters [127]. Structural modifications were considered during initial flight testing and deemed not applicable in this case. Further, this would limit the application of the technique to this particular airframe. A passive solution such as the notch filter offered a far better alternative. The filter is easier to develop and implement than active methods as it only has two tuning parameters: frequency and damping ratio. The frequency is fixed to that of the oscillation which is being addressed, leaving only the damping ratio as a tuning parameter. This process is simpler than any active method, while also being shown to be highly successful [127]. As the notch filter is simply a transfer function, it could easily be discretised and applied to the aircraft control scheme using the ROS framework. The drawback of notch filtering is that, by design, it reduces control authority in the frequency region of interest. To determine if the notch filter was suitable for the application, an extensive range of simulations was required, coupled with a flight test to validate the results. Two issues were investigated:

- Suppression of the oscillation
- Effect on overall controller performance

Ideally, a notch filter which can completely suppress the effect of the oscillation, allowing for higher control gains would also cause no reduction in controller performance to both reference commands and disturbance rejection.

7.2 Oscillation Modelling & Control Design

To investigate the notch filter performance, the aircraft simulation models would need to be updated to include flexible body dynamics. Many such models exist in the previously discussed literature for active methods. These models generally take the form shown in Fig. 7.7, where h is the wing plunge (deflection of spring k_1) and α is the pitch change of the wing (torsion of spring k_2). This, combined with aerodynamic information about the wing is used to produce a model of the wing flutter in flight, around which a control law is designed. This is a complex model, which then requires further integration with the aircraft structural model to fully implement. Such models are clearly more suited to advanced active controllers, being well above the fidelity requirements for the notch filter simulations.

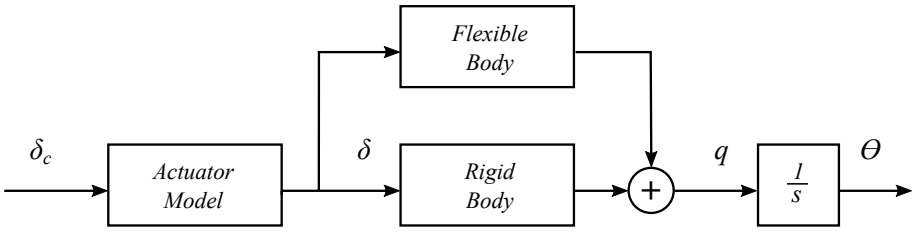

Figure 7.8: The system layout with transfer functions for the notch filter, actuator model, pitch rate and pitch angle.

For the purposes of this work, a simpler model was needed which could easily be integrated into the current aircraft models.

7.2.1 Oscillation & Actuator Modelling

An entirely separate section of literature is dedicated to a similar problem in the control of missiles [128–130]. Missiles tend to have long, slender bodies coupled with high speed control surfaces which tend to excite flexible body modes. In these works, the flexible body dynamics are typically modelled by a transfer function such as

$$\frac{q(s)}{\delta(s)} = G^q_{fb}(s) = \frac{\omega^2 K_b K_\delta s}{s^2 + 2\zeta\omega s + \omega^2}, \tag{7.1}$$

where q is pitch rate, δ is the actuator deflection, ω is the natural frequency of the oscillation mode, K_b is the mode gain, K_δ is the control surface effectiveness and ζ is the mode damping. This model is far better suited to the requirements of this work, as it is simple and easily implementable. Further, the parameters are either already known, or can be tuned to produce responses which are similar to what has been seen in flight. The model can easily be integrated into either frequency domain or state space models. Fig. 7.8 outlines how this model was incorporated into the frequency domain models used in this study.

Here, the actuator model transforms control demand δ_c to actuator deflection δ, the rigid body model is the transfer function which transforms actuator position into a pitch rate. The flexible body model also takes in the true actuator position and adds additional pitch rate depending on the actuator position. The output to the system, θ is the resulting total pitch angle. All these models exist in the frequency domain, meaning the total simulation model is easily produced, once the flexible body model was tuned.

This model is derived for an $3.6Hz$ oscillation, which lies in the middle of the two frequencies identified in the initial flight testing. Further, K_δ was obtained from the aircraft model. The remaining parameters to be tuned are ζ and K_b. Tuning the parameters for the model to represent the flight characteristics is a very challenging subject. It was decided that the best method was to tune the model to produce as similar a response as that recorded in Fig. 7.2, using a simulation with the same control gains and actuator models. The resulting response is shown in Fig. 7.9. The pitch response magnitude is slightly larger than what was recorded in flight. However, this means that any solution developed in the theoretical environment should be more than sufficient to account for the physical response. The theoretical solution developed should therefore also be more robust to modelling errors when applied to the physical aircraft.

The remaining characteristics of the simulation match the flight data; a delayed build up and in phase elevator deflections and pitch angles. Fortunately, all numerical simulations in this section will be validated by flight test data, so the small error in pitch angle magnitude is not significant. This response was achieved with $\zeta = 0.05$ and $K_b = 1200$.

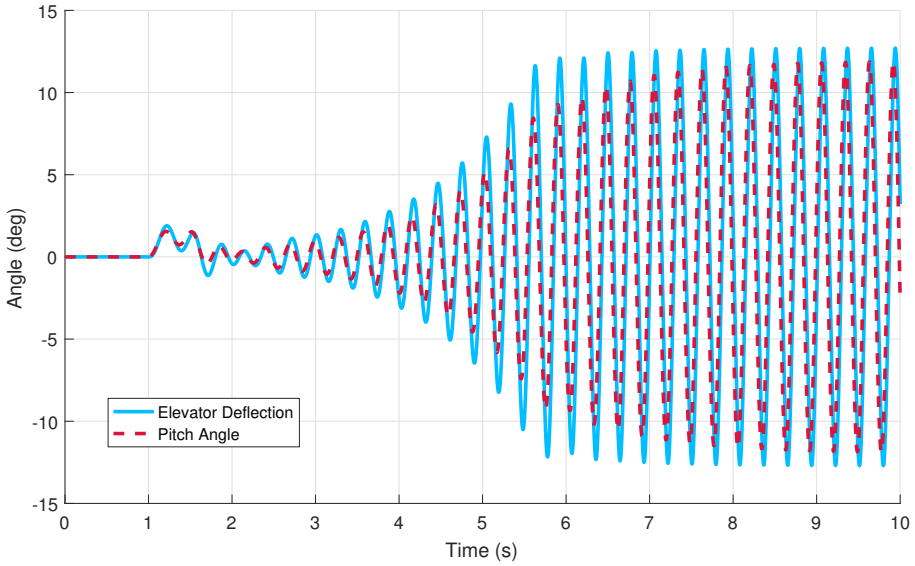

Figure 7.9: The aircraft response to a disturbance under LQR control with flexible body modelling included.

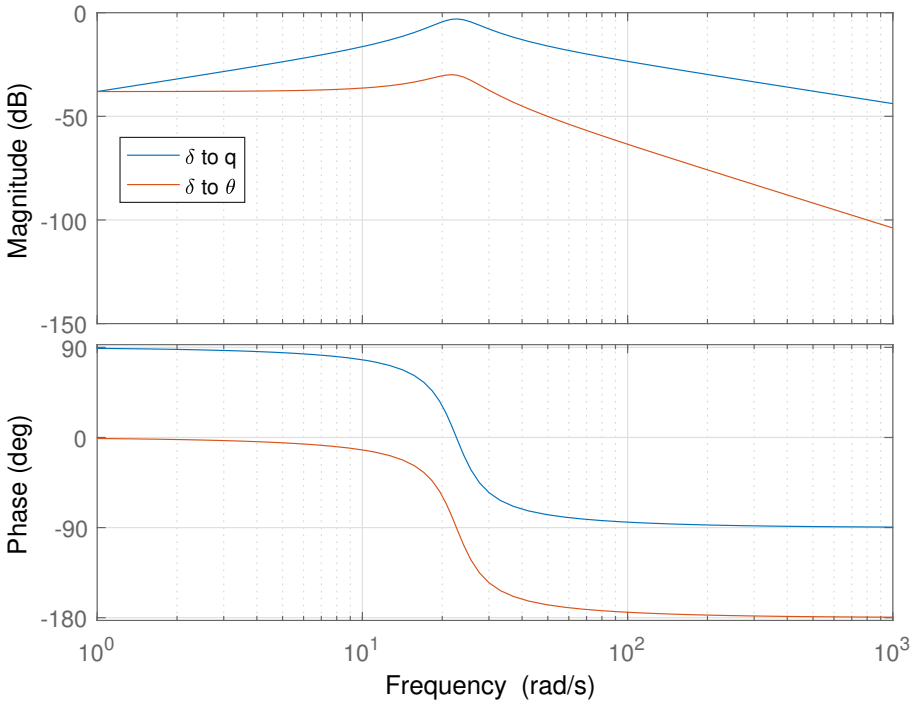

Figure 7.10: The bode plot for the flexible body model to pitch rate (q) and pitch angle (θ).

The bode plot for $G^q_{fb}(s)$ and $G^\theta_{fb}(s)$ are given in Fig. 7.10. The transfer function $G^\theta_{fb}(s)$ represents the transfer function from input to pitch angle, and is given by

$$G^\theta_{fb}(s) = \frac{1}{s} G^q_{fb}(s).$$

Clearly, the flexible body itself is stable, so any instability which emerges in the simulations is the result of interaction between the controller and the flexible body. Further, the bode plot for θ shows that the model has no noticeable influence at the lower frequencies, as expected. A peak occurs at the critical frequency, with a sustained drop off thereafter. This fits with the intuitive understanding of the effect of such a flexible body model.

As demonstrated in Fig. 7.8, the flexible body model uses the actuator position as

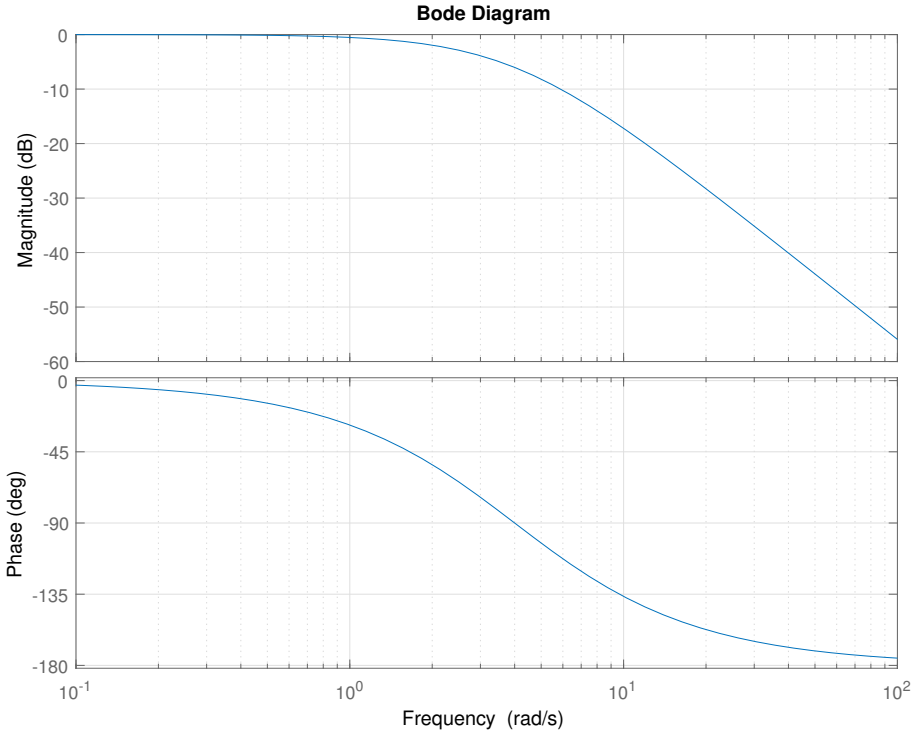

Figure 7.11: The bode plot for the employed second order actuator model.

its input as opposed to the demanded control. The actuator model employed for this study is the second order actuator model described in Fig. 6.7. The second order model was chosen for two reasons. Firstly, it is the same form of model predominantly used in the relevant literature. This is likely due to the second reason, which is that the inclusion of the actuator inertia has a significant effect in this application. As the output of the flexible body model is directly dependant on the actuator position, using the more accurate model is favourable. For control design, the first order model will still be used for its ease of implementation. Presented in Fig. 7.11 is the Bode plot for the second order actuator model. We see that the magnitude begins to drop off from around 1rad/s, with the associated phase change.

7.2.2 Notch Filter Design

Two aspects needed to be considered in the addition of the notch filter; filter design and performance impact. This was studied using bode diagrams generated from the state space model of the aircraft. The general formula for a second order notch filter, $G_n(s)$, is given by (7.2)

$$G_n(s) = \frac{s^2 + \omega_n^2}{s^2 + 2\zeta_n\omega_n s + \omega_n^2}, \tag{7.2}$$

where ζ_n and ω_n are the corresponding damping ratio and natural frequency of the filter to be designed. As the frequency is that of the oscillation mode we want to control, it is only the damping ratio which can be tuned for performance. To visualise the effect of this parameter, several values were plotted with a bode diagram shown in Fig. 7.12. The effect of ζ_n is very clear; as $\zeta_n \to 0$, the filter effect becomes more significant as the gain profile becomes more pronounced. The phase shift also becomes more pronounced.

Ideally, the filter which offers the most gain reduction at the target frequency would be used as it is most likely to suppress the oscillations. However, this will also limit the intentional control action at that frequency and introduce additional phase lag. In the

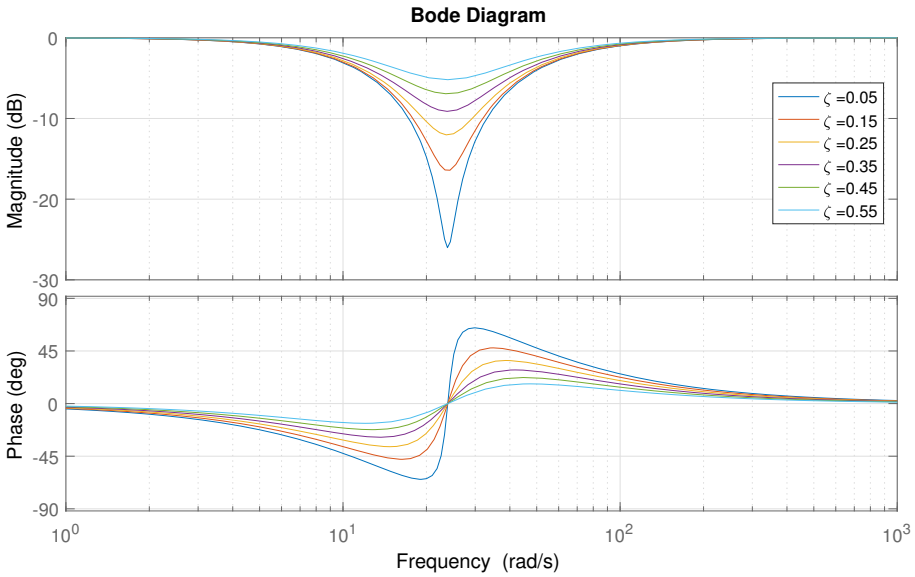

Figure 7.12: A comparison of the effect of ζ in a notch filtered centred at 3.8Hz (23.9rad/s).

following simulations, the notch filter will be designed using a $\zeta_n = 0.025$, which represents a very strong notch filter. This was chosen as it represents a worst-case scenario for the performance impact of the notch filter, making assessment easier.

7.3 Frequency Domain Analysis

To better understand the effect of controller gain, flexible body dynamics, actuator dynamics and notch filters, an investigation was conducted in the frequency domain. The intention of this analysis was to better understand how the various components affect the overall system. Furthermore, we aim to demonstrate analytically that the inclusion of a notch filter, in the presence of aircraft oscillation, allows for higher gains without loss of stability. This will first be studied analytically with bode plot stability criteria.

For this analysis, only the baseline LQR controller is studied; the disturbance observer is not included as there is limited benefit from the additional analysis. The oscillations will appear to the observer as a disturbance, resulting in a control demand to act on the disturbance. The data in Fig. 7.2 shows that the oscillation is out of phase with control action, meaning additional action will lead to additional oscillations, repeating the cycle and leading to instability. The concern in this analysis is therefore primarily avoiding excitation of the oscillation mode by the feedback controller. Later, numerical simulations are included which demonstrate clearly the detrimental performance when DOBC augmentation is activated without a mitigation method present.

7.3.1 Open Loop Transfer Function Calculations

As discussed in [128], state variable feedback modifies the zeros of an open loop system, meaning open loop systems are suitable for stability analysis. To produce the transfer functions used in the following analysis, the system shown in Fig. 7.13 was used, with the loop broken at the designated analysis point.
In Fig. 7.13, G_N is the notch filter, G_A is the actuator model, G_q is the rigid body pitch rate, G_F is the flexible body pitch rate, and K represents the state feedback for the associated parameters. The total transfer function, G_t is calculated as

$$G_t = -G_N G_A (G_q + G_F) K_q - G_N G_A (G_q + G_F) G_i K_\theta,$$

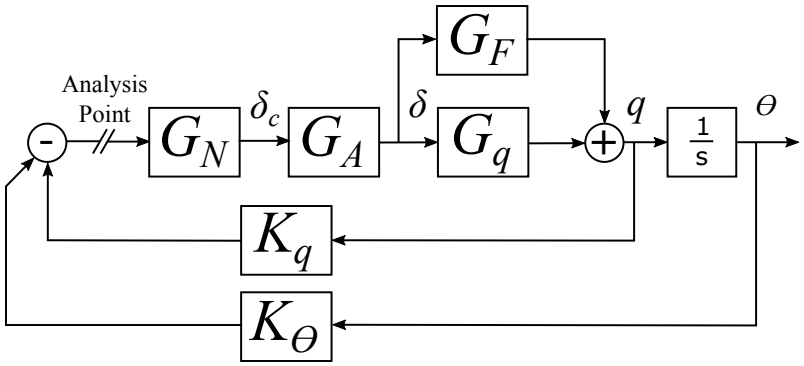

Figure 7.13: The system of transfer functions used to produce the open loop bode plots for stability analysis.

where G_i is the transfer function of the integration block. For the various different analyses where aspects of the system are enabled or disabled, their transfer functions were simply set to unity if not required. In the case of the flexible body model, the transfer function was removed entirely, as it is a parallel addition rather than series multiplication. Setting G_F to unity in this situation would be incorrect.

Bode plot analysis focuses on two features to characterise stability: gain and phase margin. In frequency analysis, a system is classed as unstable if the *gain* of the system is 0dB at the point where the *phase* of the system is $-180°$. To study the amount of margin to stability, we consider two cases separately. Phase margin being the distance, at 0dB gain, between the phase of the system and $-180°$. Gain margin is the amount of gain which can be added before the total gain reaches 0dB, at the $-180°$ phase point. The added gain can only be positive, as the system is only stable if the gain at -180° phase is less than 0dB. These criteria will be used to assess the effect of the notch filter, as well as feedback control gains, on the overall system stability.

Addition of the flexible body mode makes this analysis somewhat more complex. An example is given in Fig. 7.14. Here, the gain peak added by the flexible body has resulted in multiple crossings of the $0dB$ line. For such cases where there are multiple points to study, the most critical value will always be considered. If any of $P1$ or $P2$ were unstable, it would be said that the whole system is unstable in phase.

Region of Interest

The analysis was concentrated on a reasonably small region of interest. The key frequency was that of the flexible body mode at $22.6rad/s$. Using a frequency range of $1 \leq f \leq 100rad/s$ on the Bode plots would give sufficient information at and around the region of interest. Below 1 rad/s, the flexible body mode has no influence. Above $100rad/s$ is well above the effective bandwidth of the actuators and the flexible body mode itself, so would also not provide any useful information.

7.3.2 Overall System Bode Plot

In Fig. 7.15 we produce the bode plot from control command to pitch angle using various LQR feedback gains, produced by adjusting the R penalty for the system with flexible body and actuator modelling in place. The effect of the flexible body model is clearly visible with the magnitude spike at around 22.6rad/s (3.6Hz). We see that the model represents the results seen in flight testing very well. With $R = 3.2$, the aircraft is stable although with a small gain margin of $2.8dB$. Even the modest increase in gain with $R = 1.6$ leads to instability, with a gain margin of $-0.52dB$. This matches very well with

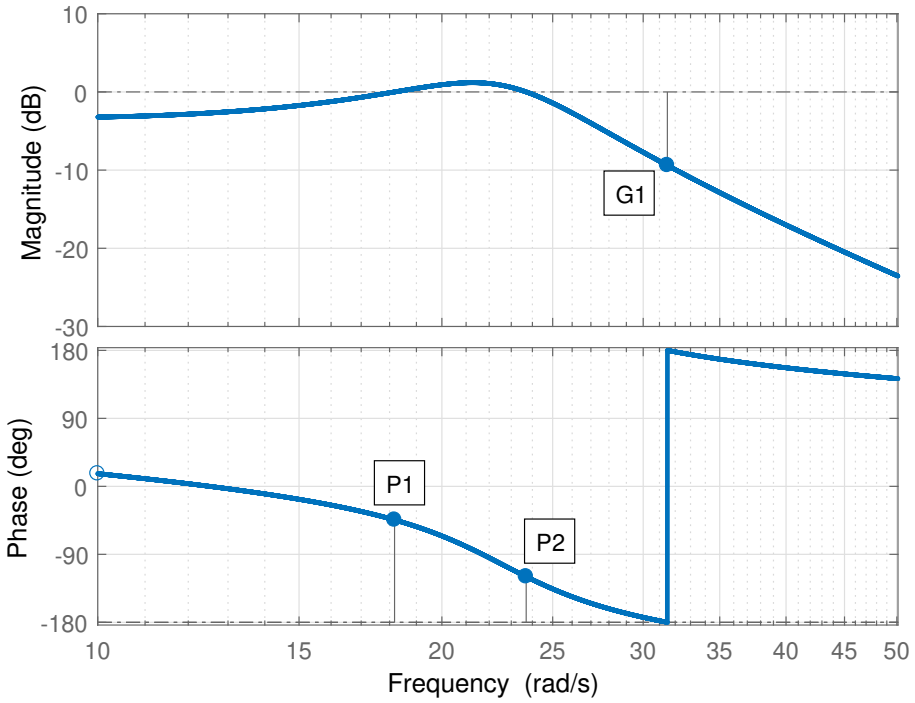

Figure 7.14: The bode plot for the system under LQR control with R=12.8 showing the resulting gain and phase margins.

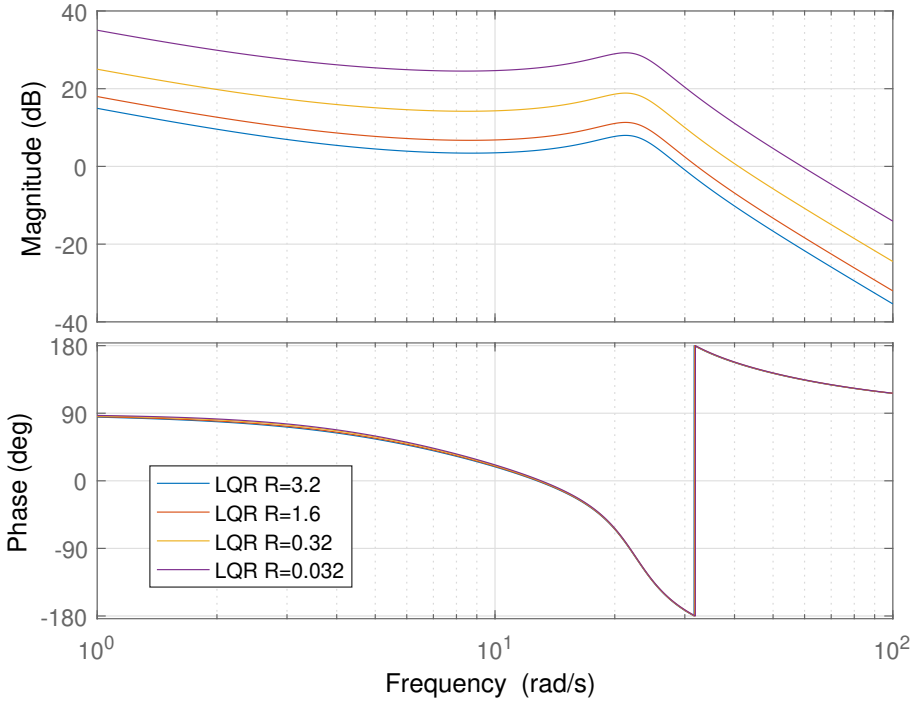

Figure 7.15: The Bode plot from reference command to pitch angle for the actuator augmented control system.

what was seen during flight testing, where the LQR with $R = 3.2$ was determined to be the maximum stable feedback gain.

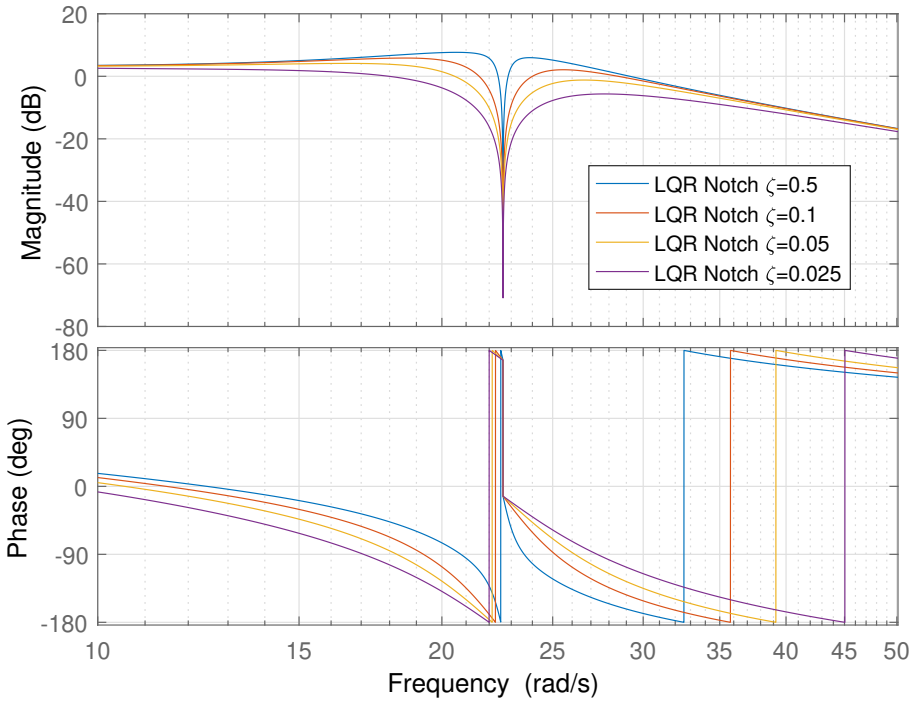

Figure 7.16: The Bode plot from reference command to pitch angle for the actuator augmented control system with flexible body modelling and various notch filters.

7.3.3 Inclusion of the Notch Filter

Now, the notch filter is included in the model, with the bode plots given in Fig. 7.16. Here, R is maintained at 3.2, with a range of notch filter damping ratios compared. The effect is immediately clear in that the inclusion of a notch filter improves the gain margin by a significant portion. For the modest damping ratio of $\zeta = 0.5$ the gain margin is increased to $6.4dB$ (over the previous margin of $2.8dB$). The phase margin is a modest $14.6°$, which is also a small improvement over the margin of $12°$ without the notch filter for the equivalent system. As the notch filter damping increases, the stability of the system follows suit. When $\zeta = 0.025$, the gain and phase margins have increased to $16.2dB$ and $76.4°$, respectively.

The apparent effect of notch filter addition is increased stability and phase margin. However, as seen in Fig. 7.12, the notch filter reduces phase margin. This is true when the notch filter is considered in isolation. However, when the structural oscillation is also present, the net effect must be considered. While the notch filter itself slightly reduces phase margin, the strong reduction in the effect of the flexible body oscillation results in greatly increased gain and phase margin. The net result is therefore that the addition of the notch filter leads to improved gain and phase margin.

7.3.4 Gain Tuning

In Fig. 7.16, it was shown that the notch filter adds stability to the system. The implication of this is that the baseline LQR gain can be increased without the system becoming unstable as it did in Fig. 7.15. This is studied in Fig. 7.17, where the same range of R values are compared.

Without the notch filter, only $R = 3.2$ was stable with a gain margin of $2.8dB$ and a phase margin of $11.3°$. Reducing to $R = 1.6$ (thereby increasing feedback gain) made the system unstable. Now, with the notch filter in place, using a significantly lower $R = 0.32$ (even higher feedback gain), the system remains stable. Furthermore, this is achieved with

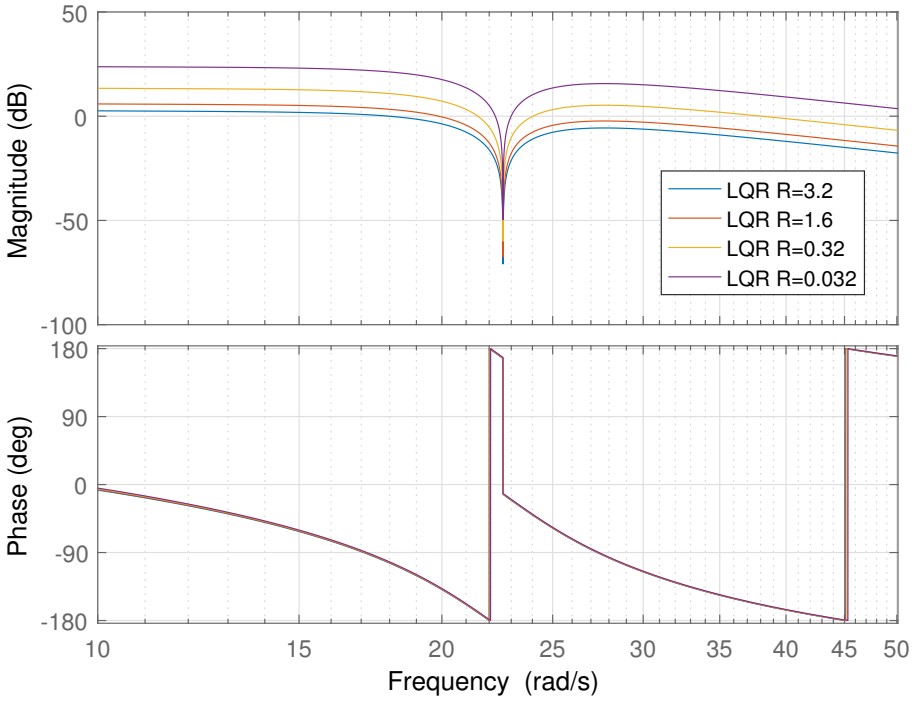

Figure 7.17: The Bode plot from command to pitch angle using with varying R weightings.

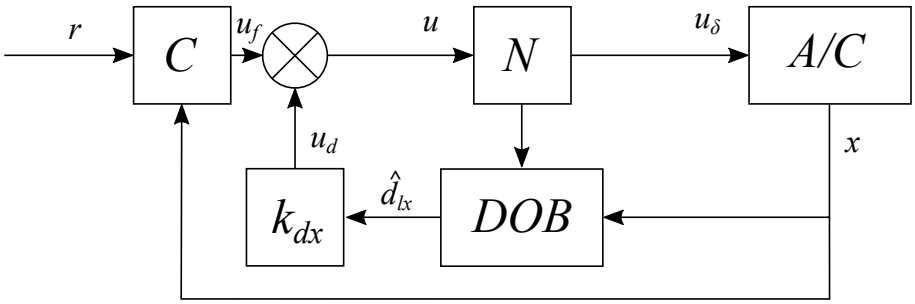

Figure 7.18: The genaral layout of the LQR ADOBC control scheme with notch filtering (denoted by N) in this section.

gain and phase margins of $5.96dB$ and $11.5°$ respectively, which are both better than the lower gain system without a notch filter.

This is a very promising result, as it indicates that the notch filter is working as intended. It remains to determine if this improvement in stability translates to better DOBC performance. This is studied next in simulation.

7.4 Numerical Simulation

The frequency domain analysis has demonstrated clearly that the addition of the notch filter yields a more stable system. It remains to determine if this allows for higher observer gains. For this section, an ADOBC scheme was designed for the longitudinal dynamics following the method outlined in Chapter 6. An overview of this controller is given in Fig. 7.18. As the notch filter is a known part of the control design, we can design the layout such that the ADOBC scheme takes the notch filtered control demand as the input. If this was not done (i.e. passing u to the DOB), the observer would detect the mismatches between demanded control and the applied control, which has been filtered.

The key points to be studied are within this section are:

- Applicability of frequency domain analysis to flight control

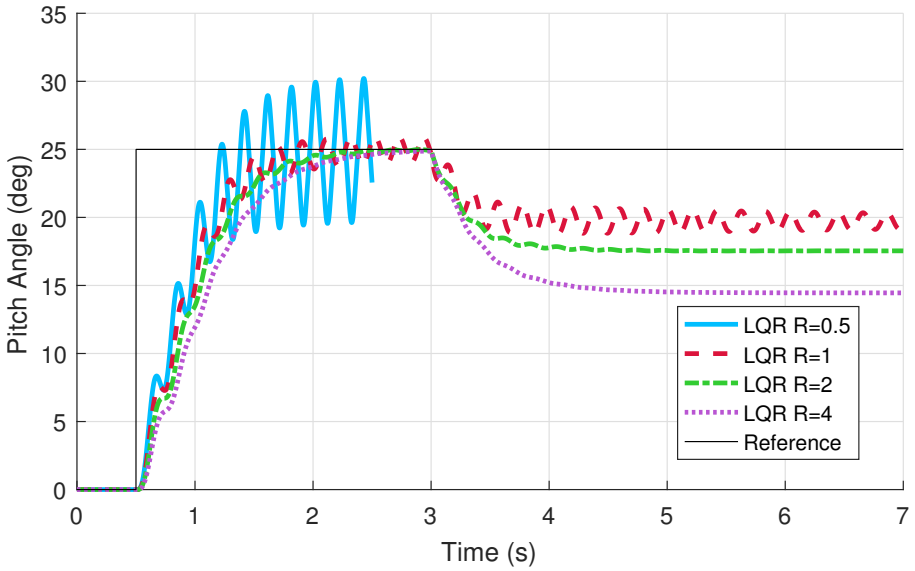

Figure 7.19: A comparison of LQR performances with flexible body modelling and no notch filter, with a range of R values. A disturbance is added at $t = 3s$.

- Improvement in available ADOBC performance
- Performance impact of the additional notch filter

As we aim to study the notch filter for performance impacts, it was decided to maintain the designed filter with $\zeta = 0.025$. Although the frequency analysis suggests that less damping ratio could be used to maintain stability, this was decided against for two reasons. First, it is intended to test this solution on the aircraft. It is likely that modelling errors exist and therefore the filter which works perfectly in theoretical analysis may not transfer to the true plant. Using a high damping ratio adds some additional robustness to the filter against these modelling errors. Secondly, a key point of this study is to determine any negative effects on control performance due to the inclusion of the notch filter. By using a strong (heavily damped) filter, any such effects will be more pronounced and as such more easily detected in the analysis.

7.4.1 LQR Simulation Results

The first simulations investigate the LQR performance. We aim to confirm the frequency domain analysis, as well as quantify the results in a more easily interpreted format.

LQR Gain without a Notch Filter

The initial simulation studies the LQR response with flexible body modelling but no notch filter. We compare a range of R values, as shown in Fig. 7.19. The results match very will with the frequency domain analysis. Increasing the feedback gain results in an unstable system, while the baseline $R = 3.2$ value is stable, although with undesirable performance. Decreasing the feedback gain results in more stable systems, although both reference tracking and disturbance rejection performance suffers.

LQR Gain with a Notch Filter

Next, we include the notch filter and study the effects. The result is shown in Fig. 7.20. Again, this result matches well with the frequency domain analysis. However, the effect of the notch filter is much clearer in this simulation. For the same gain, the response is far

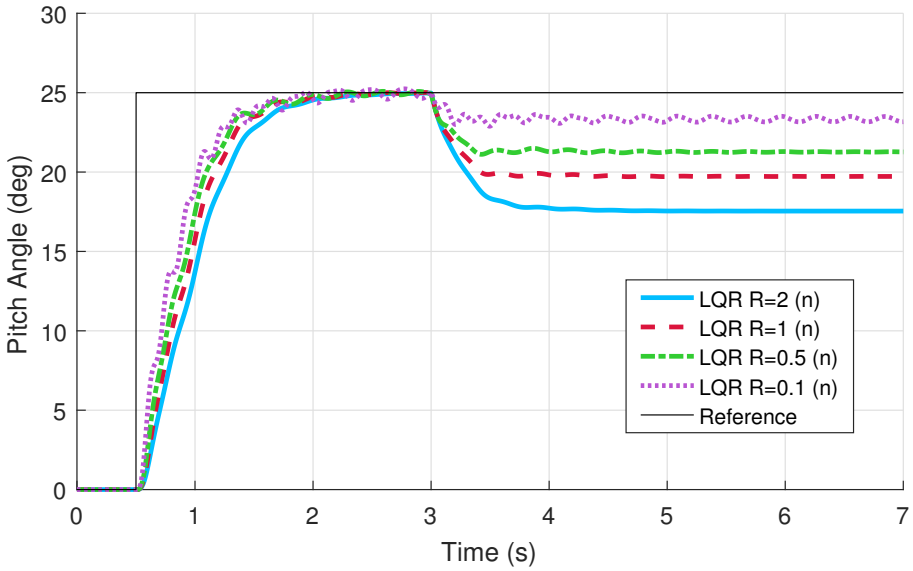

Figure 7.20: A comparison of LQR performances with flexible body modelling and a notch filter, with a range of R values. A disturbance is added at $t = 3s$.

less oscillatory. Furthermore the $R = 0.5$ response, which was previously unstable, is now stable and offers good performance. It is also demonstrated that the feedback gain can be further increased while maintaining stability. For the $R = 0.1$ response, we see that the system is beginning to once again show effects of the structural oscillation.

There is no noticeable degradation in performance in any regard due to the notch filter. On the contrary, the additional gain results in better disturbance rejection and slightly improved reference tracking, showing that the notch filter allows for better performance. This is a very good result, as it confirms two of the key points of the simulation study. First, the frequency domain analysis does translate to simulation with matching results. Second, it has been shown that for the same gain, the notch filter does not reduce performance of the system in a noticeable way. Actually the additional gain allowed by the inclusion of the notch filter results in *better* performance.

7.4.2 ADOBC Simulation Results

The effect of the notch filter on the baseline feedback control has been established. It was shown that without the notch filter the feedback gain must be reduced to avoid excitation of the flexible body mode. It is expected that with the ADOBC active, this will still be the case as excitation of the flexible body mode will be detected as a disturbance. This in turn will lead to additional control action from the ADOBC, exciting the dynamics further and leading to an unstable system. With the notch filter in place, the feedback gains could be increased without exciting the flexible body mode. This would suggest that similar performance benefits could be obtained from the ADOBC. This will be studied here in numerical simulation.

Baseline ADOBC Performance

First, we maintain the ADOBC observer gain and compare the performance with various LQR configurations. The result is given in Fig. 7.21, with a reference step and disturbance added at $t = 3s$. This result matches closely with what was seen during flight testing - activation of the ADOBC scheme leads to significant and unstable oscillation. Reducing the feedback gain, and thus reducing flexible body mode excitation, also leads to a stable observer.

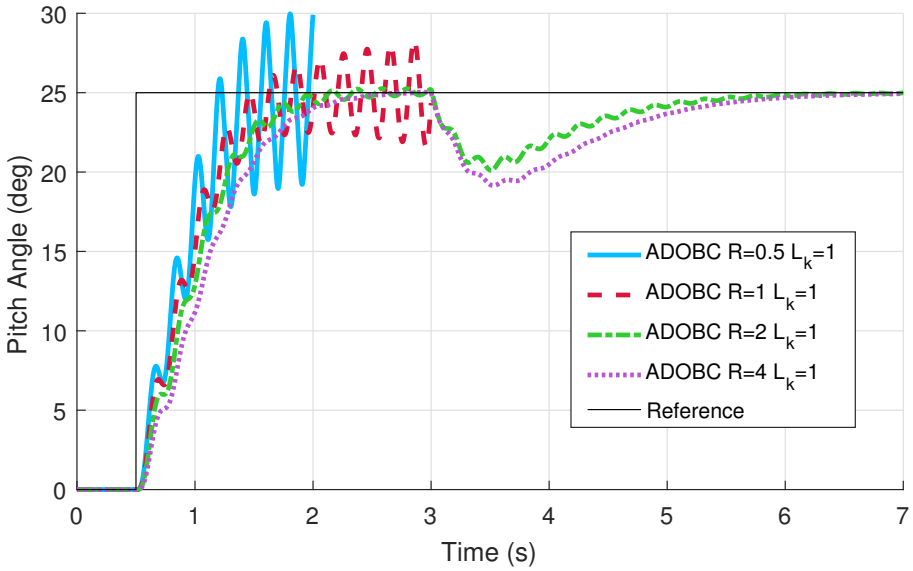

Figure 7.21: A comparison of LQR and ADOBC performances with flexible body modelling comparing a range of R values. A disturbance is added at $t = 3s$.

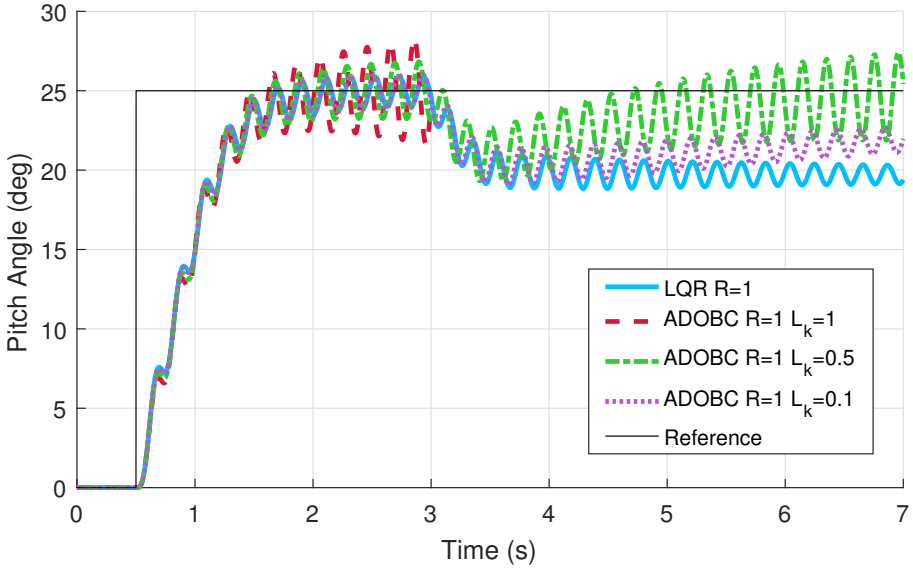

Figure 7.22: A comparison of baseline LQR performances with flexible body modelling with ADOBC observer gains. A disturbance is added at $t = 3s$.

In Fig. 7.22, we maintain the baseline LQR gain and instead reduce the ADOBC gain to reach stability. Here we see that reducing the ADOBC gain does improve stability. However, with an $L_k = 0.5$, the system has slow disturbance rejection performance as well as an unstable oscillation, which is increasing in magnitude with time. Reducing to $L_k = 0.1$ results in the oscillation magnitude being stable. However, the resulting disturbance rejection performance is very poor.

Notch Filtered ADOBC Performance

It has been shown that without the notch filter, the applicable ADOBC gain is very low, which yields poor performance. We now investigate the performance in the presence of the notch filter. First, in Fig. 7.23 we study the resulting performance with increasing feedback gain, with the ADOBC gain maintained at the default value. The result is clear in that with the notch filter in place, the higher feedback gains do not result in unstable

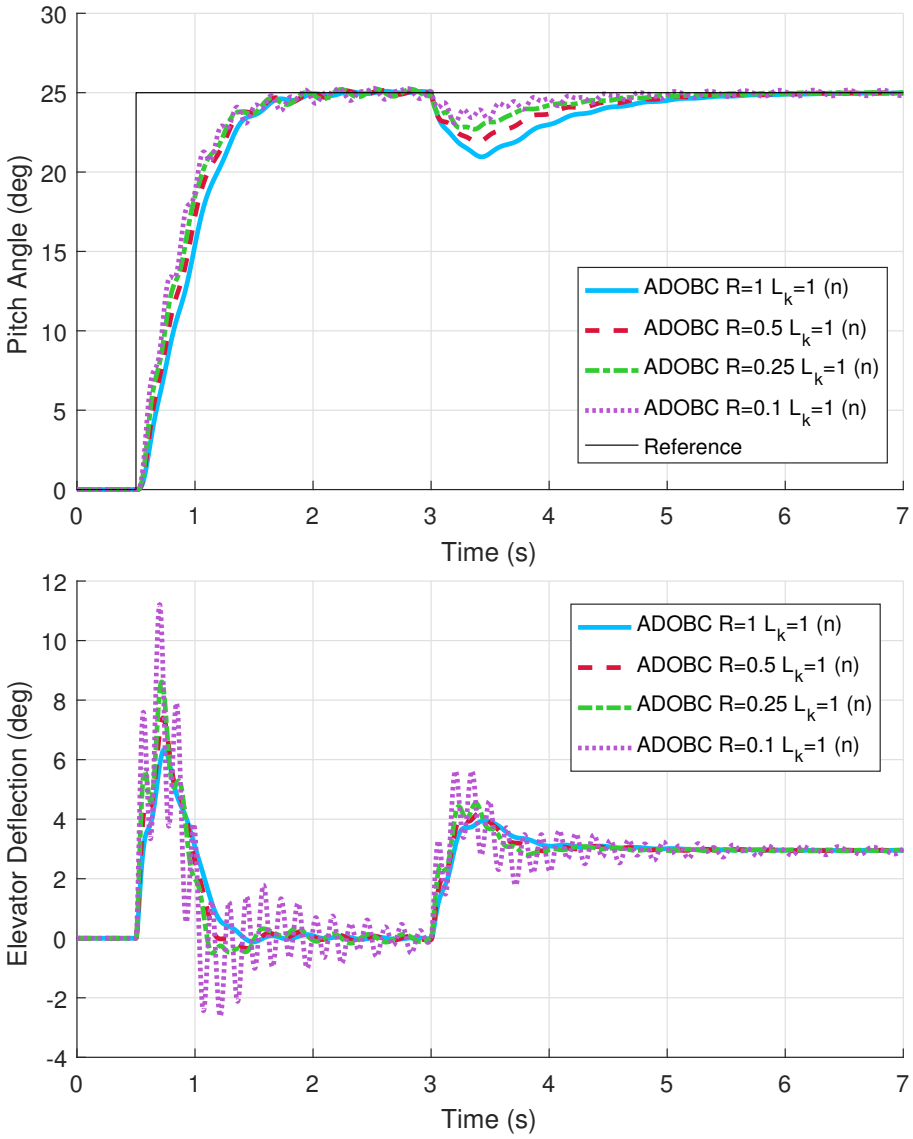

Figure 7.23: A comparison of performance of the LQR and ADOBC schemes using a range of R values with the notch filter and flexible body modelling active.

ADOBC responses. For the $R = 0.1$ response, we see the same oscillations as were present without the ADOBC (Fig. 7.20). However, the addition of the ADOBC now only provides improved disturbance rejection performance with no instability. However, when looking at the control deflection, we see that with the higher feedback gains some undesirable control action is introduced.

Next, we study the performance of the system with the baseline feedback gains, while increasing the ADOBC gain. This is shown in Fig. 7.24. For this simulation, the magnitude of the disturbance added at $t = 3s$ is increased to twice that used in the previous simulations to allow for clearer comparison of disturbance rejection performance. The results are conclusive in that adding additional ADOBC gain can be done stably. A significant increase of $L_k = 16$ is achieved. Furthermore, this is done without the additional oscillatory control action which resulted from increasing the feedback control gain. We also see that the increased ADOBC gain results in much improved disturbance rejection. For the $L_k = 16$ simulation, we see that some oscillation does begin to appear in the control output. However, with the notch filter in place this does not grow into an unstable condition as it did previously without the notch filter.

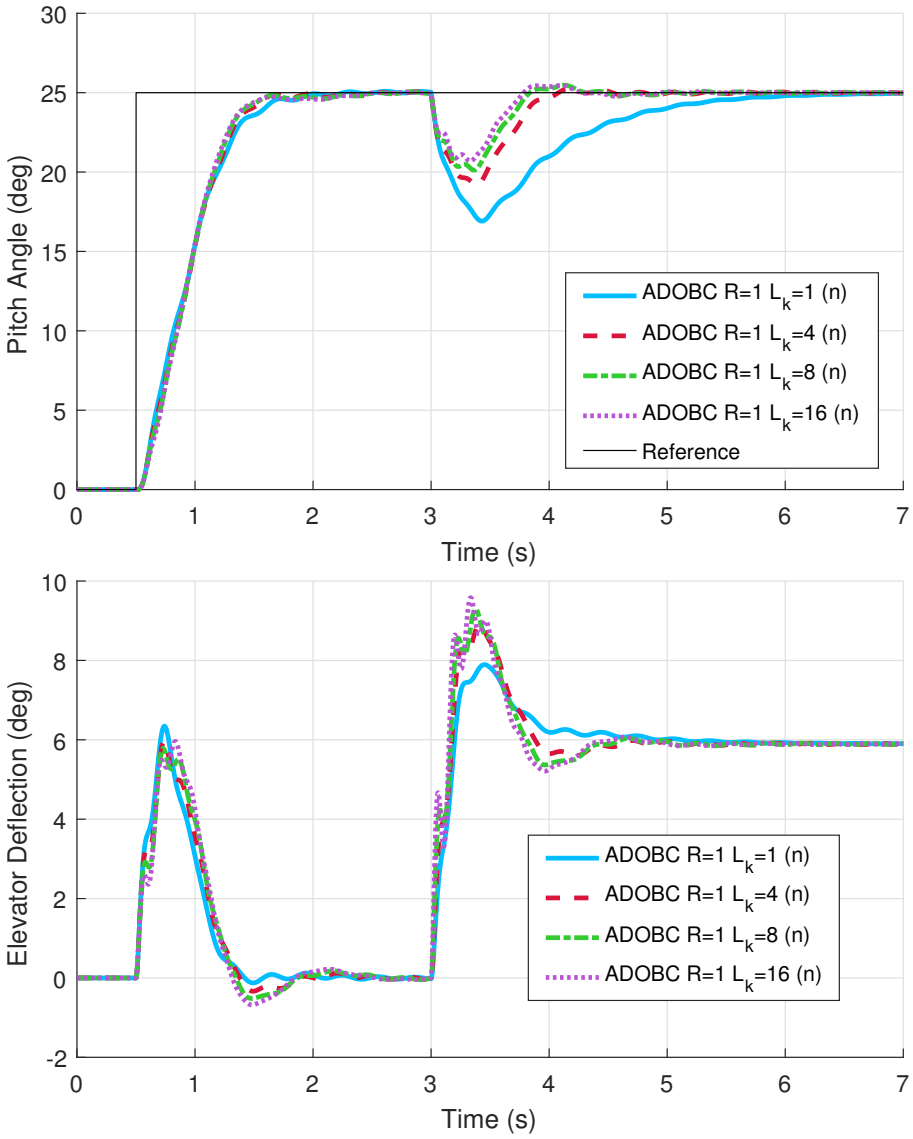

Figure 7.24: A comparison of performance of the LQR and ADOBC schemes using a range of L_k values with the notch filter and flexible body modelling active.

Overall Performance Improvement

The previous simulations have indicated that the notch filter has allowed for a small increase in feedback gain and a substantial increase in ADOBC gain in the presence of flexible body dynamics. A final simulation is now conducted to compare the resultant controllers. In Fig. 7.25 we study the performance of the baseline LQR to the LQR with ADOBC both without and with notch filter applied. Each of the controllers were manually tuned to give the best possible performance in the given configuration.

To minimise the effect of the flexible body mode, the LQR feedback gain had to be reduced slightly. This did allow for a small increase in the ADOBC gain to $L_k = 1.5$, although it can be seen from both the pitch angle and elevator deflection plots that this gain is extremely close to becoming unstable, as it exacerbates the flexible body oscillations. With the notch filter in place, however, both the feedback gain and ADOBC gain could be increased; the additional ADOBC gain is particularly noticeable, as the disturbance rejection performance at $t = 3s$ is substantially improved.

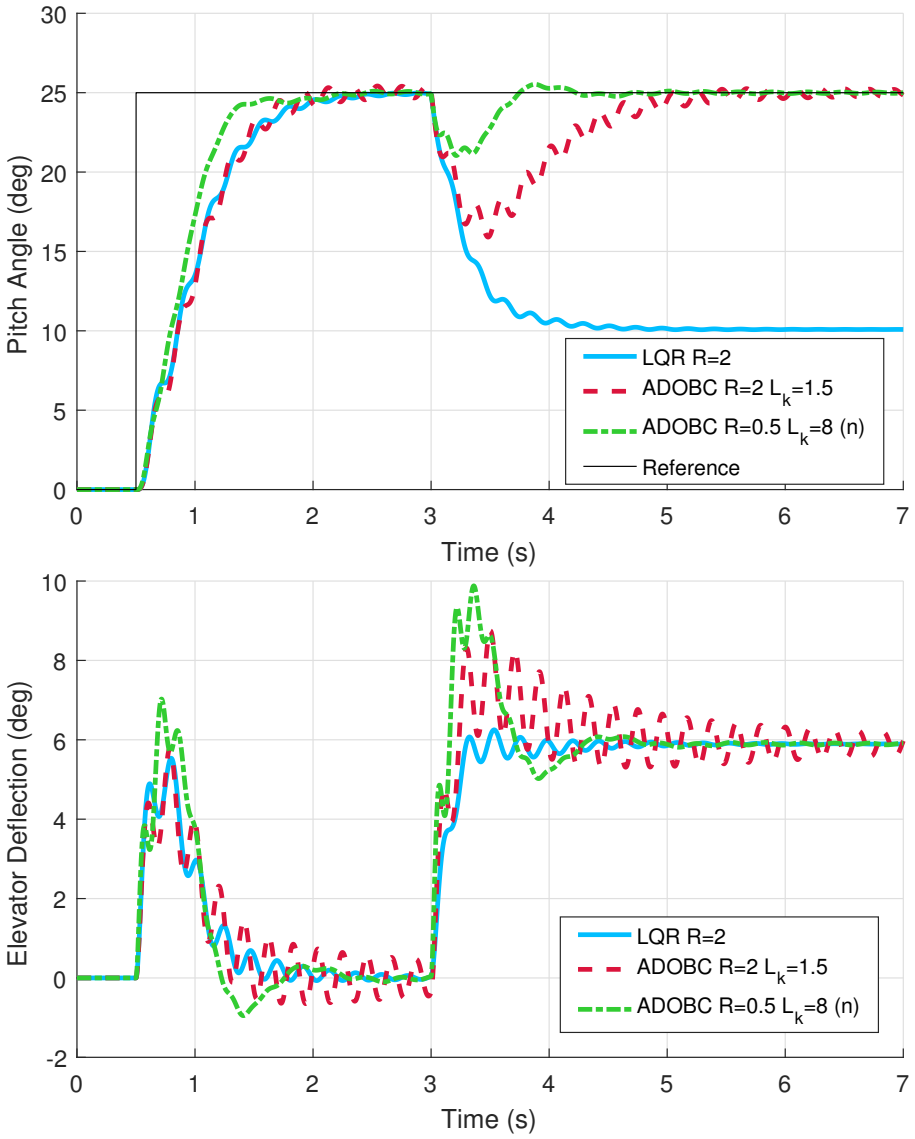

Figure 7.25: A performance comparison of simulation with flexible body modelling active, to various controller tunings with and without the notch filter active.

7.4.3 Numerical Simulation Conclusions

The numerical simulation results have given valuable insight into the problem. All the points of investigation outlined at the beginning of this section were achieved. Initial simulations of the LQR controller confirmed the results from the frequency domain analysis. Addition of the flexible body mode severely reduced the stability margins of the system, and required the feedback gain to be reduced to minimise the oscillations in the output channel. It was also demonstrated that without a notch filter the ADOBC gain had to be reduced to avoid instability. This resulted in very poor disturbance rejection performance.

With the notch filter added to the system, it was shown that the feedback gain could be increased while remaining stable. However, despite the system being stable, at high feedback gains a significant amount of oscillation was seen in the output and control inputs, which represented an undesirable system state. Still, the modest feedback gain increase was achieved and provided some improvement in performance.

With the ADOBC, the notch filter allowed for a very large increase in the observer gain. This was achieved with little to no increase in oscillation in either the input our output channels. The additional disturbance rejection performance which resulted from

this was very noticeable. In the final simulation, three controller configurations were compared. The notch filtered result provided the best performance by a clear margin. This demonstrated very well that the addition of the notch filter does not produce any noticeable degradation in control performance. Furthermore, the additional gains which could be applied in the presence of the notch filter were far more impactful and produced clear and noticeable improvement in the resulting performance.

Overall, the notch filter has been demonstrated to offer a viable solution to the flexible body problem in simulation. The additional feedback gain provided a small enhancement to reference tracking performance. However, the disturbance rejection performance resulting from the ADOBC gain was substantial and of great interest. The next step would be to demonstrate the function of this filter in flight testing. This would first be studied in the X-Plane environment to provide some validation of the numerical simulation. The system would then be studied in flight testing. As these flights place significant stress on the aircraft with added risk, it was decided that only the additional disturbance rejection from ADOBC gain increase would be studied.

7.5 X-Plane Validation

Before flight testing of the notch filter solution, some further simulations were conducted using the X-Plane simulation environment. This was intended simply to validate the state space simulations prior to flight testing. For this reason, the simulations focus purely on stability of the system rather than performance. Furthermore, the X-Plane interface does not allow for the inclusion of flexible body dynamics directly. For these simulations, the output pitch rate of the flexible body model was transformed to a disturbance moment to yield the equivalent pitch rate in X-Plane. In this way, the effect of the flexible body is introduced into the X-Plane environment in the best way possible within the constraints of the interface.

7.5.1 Notch filter performance in the X-Plane Environment

First, Fig. 7.26 shows the performance of the LQR controller with notch filtering toggled. Here it is clear that the notch filter is required for stability of the controller as it offers a significant reduction in the level of flexible body oscillation. This simulation is more sensitive to oscillation than the state space implementations. This is believed to be due to the method of implementation of the flexible body model and as such will not be investigated. The main concern for this work is the notch filter's ability to suppress the oscillation without reducing performance; both of these have been demonstrated.

Next, we compare the same performance in the presence of the ADOBC scheme. The results are shown in Fig. 7.27. Again, the flexible body model is having a more significant effect than noted in the state space simulations. However, the notch filter is sufficient to maintain stability while showing no reduction in reference tracking performance.

These results provide sufficient evidence that the notch filter is ready and safe to be flight tested. Flight test results will be the most valuable in affirming the performance of the notch filter.

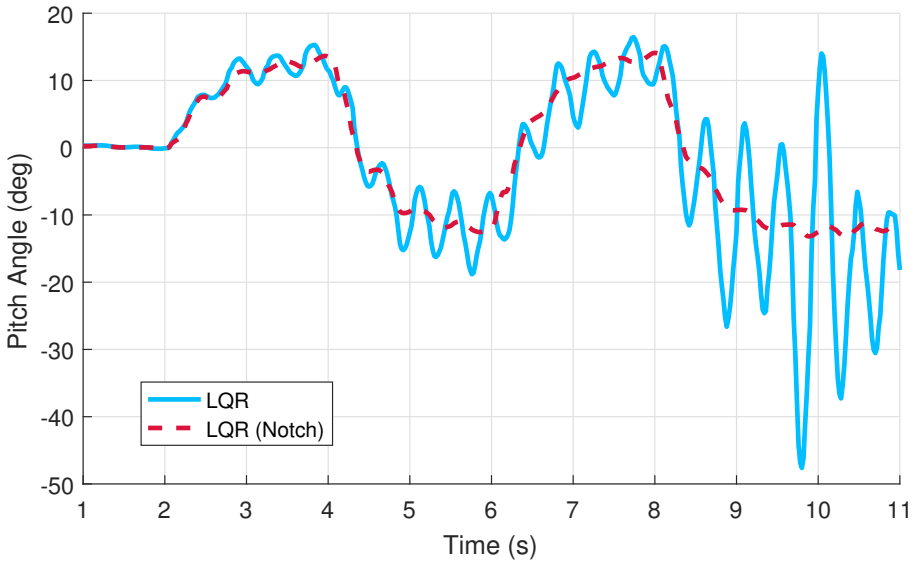

Figure 7.26: X-Plane simulation results using the LQR controller with notch filtering toggled for comparison.

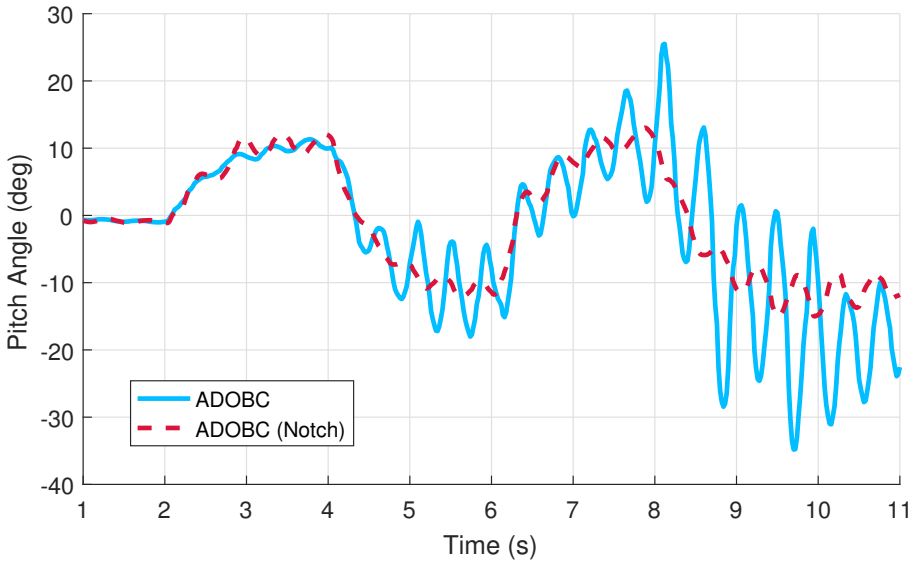

Figure 7.27: X-Plane simulation results using the ADOBC controller with notch filtering toggled for comparison.

7.6 Flight Test Validation

To demonstrate that the notch filter would function on the aircraft, a flight test was carried out. During this flight test, oscillations were deliberately initiated by increasing the L_K multiplier until it became visible in the aircraft response. Several tests would then be conducted to study the ability of the notch filter to suppress the motion.

7.6.1 Digitising the Filter

Before the filter could be transferred to the aircraft, it needed to be converted from the continuous time form to discrete time. Given in (7.3) is the continuous form of a notch filter tuned for 22.6rad/s.

$$G_n(s) = \frac{s^2 + 511.7}{s^2 + 20s + 511.7} \tag{7.3}$$

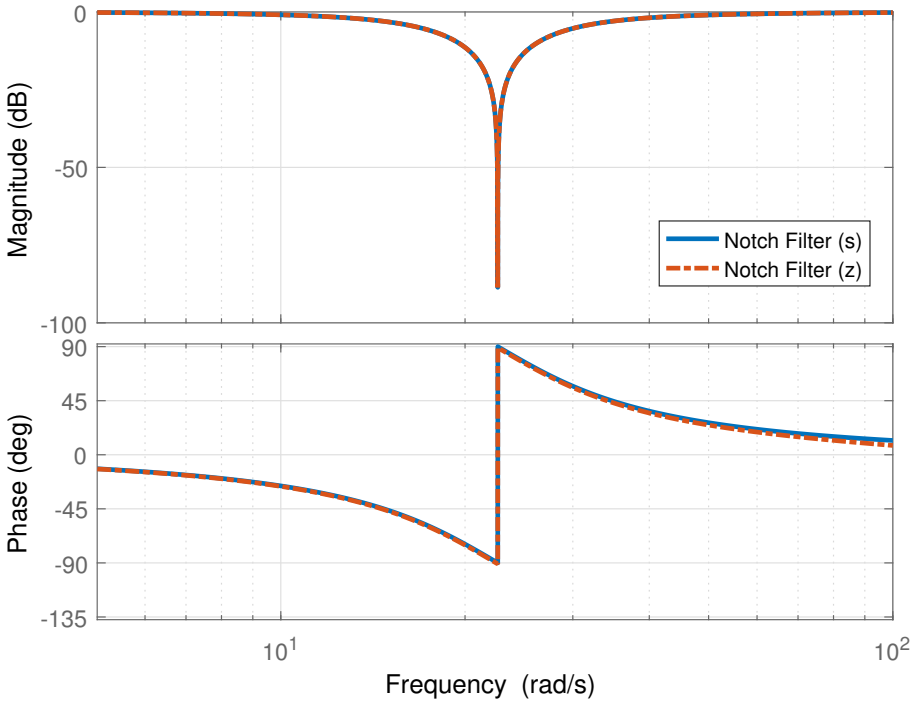

Figure 7.28: Comparison bode plot for the continuous and discrete notch filters given in (7.3) and (7.4) respectively.

When a discretisation scheme is applied for a 0.02s time step, the function in (7.3) is converted to (7.4).

$$G_n(z) = \frac{0.8242z^2 - 1.483z + 0.8242}{z^2 - 1.504z + 0.6703} \tag{7.4}$$

To compare the result of the discretisation, the bode plot of the two filters given in Fig. 7.28. Overall the two filters match very well, with only a small noticeable difference in phase as the frequency approaches $10^2 rad/s$; At $f = 10^2 rad/s$, the phase of the continuous filter, $N(s) = 11.9°$ while the discrete filter $N(z) = 7.76°$. This error is minimal and is unlikely to cause any noticeable effects. This discrete filter is sufficient for flight testing.

7.6.2 Flight Test Results

The first action to be performed in the flight testing was increasing the L_k gain until the oscillation occurred. This process is shown in Fig. 7.29. Due to the sensitivity of the longitudinal motion, the oscillation occurred quickly. However, as can be seen from the initial period where $L_k = 0$, the oscillation is not present until the gain is increased. Once the critical gain had been breached, it was impossible to discern further changes in the response during the flight test. For this reason, the L_k gain was maintained at around 0.5 in all subsequent testing, as this resulted in oscillations appearing reliably.

Next, the aircraft was flown using the Pixhawk autopilot until the beginning of a test pass, at which point control was passed to the offboard controller. Generally, it would take a few seconds for the first oscillation to appear. This was allowed to continue for several seconds to ensure the motion would continue indefinitely. Then, the notch filter was activated and the response observed. Fig. 7.30 demonstrates two of these passes.

The result shown here is very clear. Immediately after activation of the notch filter, the oscillation begins to subside and within 2 seconds it has been entirely removed from the output. This is a very positive result as it indicates very clearly that the filter is functioning as intended aboard the aircraft. This also further validates that the discretisation of the

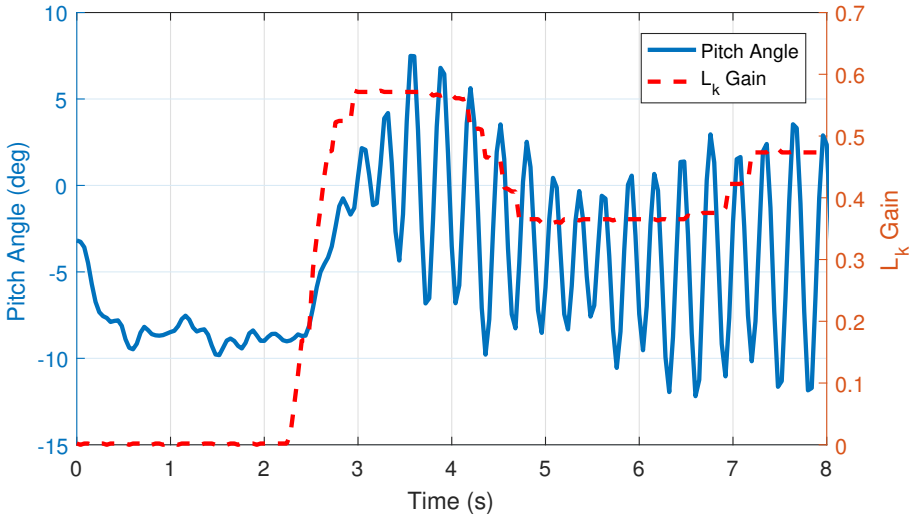

Figure 7.29: Comparison of the aircraft pitch angle with the applied L_k gain also plotted.

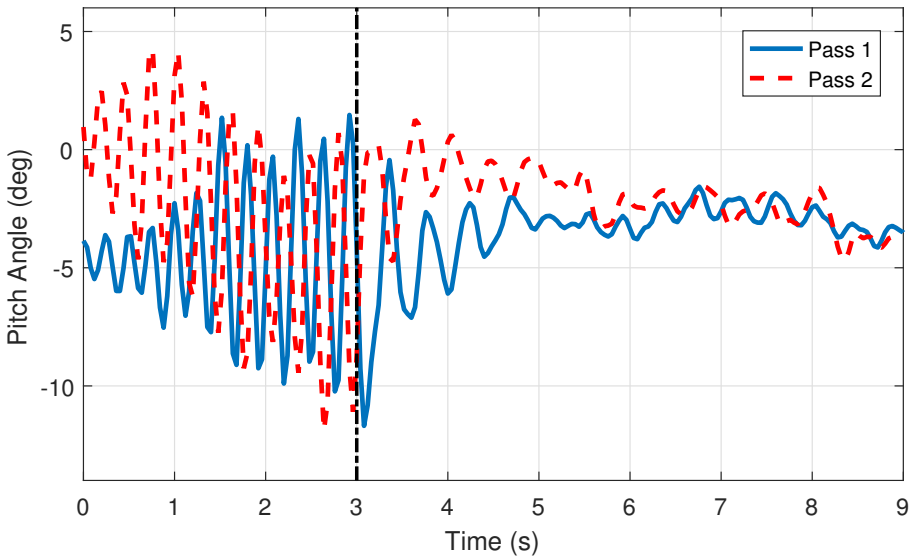

Figure 7.30: Aircraft pitch during a sustained longitudinal oscillation, with the notch filter activation denoted by the vertical line at 3 seconds.

continuous time notch filter has been successful. A final demonstration of the notch filter performance is given in Fig. 7.31.

In this test, the filter is activated, then deactivated and finally activated once more. This was all conducted in a single pass. This test demonstrates clearly that the notch filter must be active at all times to suppress the oscillation, as shortly after it is deactivated the motion can be seen to return.

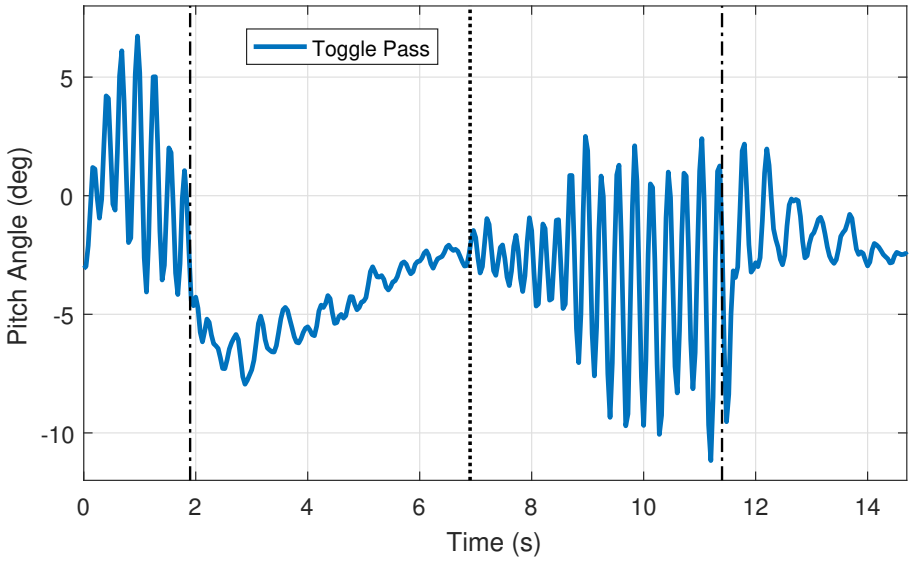

Figure 7.31: Aircraft pitch during a sustained longitudinal oscillation. In this test, the notch filter is toggled on (dash-dot lines) and off (dot-dot line) during the same pass to further demonstrate its ability to suppress the oscillation.

Finally, to demonstrate the benefit of the notch filter on performance, some reference tracking is analysed. This test was conducted in a single flight, following the following test schedule:

1. LQR reference tracking pass
2. Tune L_k to maximum with stable oscillation mode, designated *low* L_k
3. Conduct reference tracking pass
4. Enable Notch Filter
5. Tune L_k to maximum with stable oscillation mode, designated *high* L_k
6. Conduct reference tracking pass

The aim of this test is to demonstrate if the additional performance afforded by the notch filter translates to flight testing results. The reference step performance is given in Fig. 7.32. During flight, it was not possible to monitor the L_k gain being applied. However, during post processing of the data, the transmitter output could be analysed to determine the resulting gains. It was found that "low $L_k = 0.31$", and "high $L_k = 4$". $L_k = 4$ was the maximum gain programmed into the test flight program. It was chosen as this would be sufficient for demonstrating the additional gain while allowing reasonable resolution on the transmitter input to control the input L_k accurately during the tuning process. The result is given in Fig. 7.32.

The most striking difference is the significant offset from the LQR result. This is most likely a result of incorrect trim setting in the controller. The LQR is designed to operate around a trim condition, which requires trimming of both the state and control inputs. This result indicates that the trim control input for the elevator is not accurate, leading to a $-5°$ offset in steady state pitch.

The ADOBC response is quite different, with both schemes removing the steady state offset. However, upon more detailed inspection, some differences arise. First, we notice that the high L_k controller settles to the reference command much more quickly than the

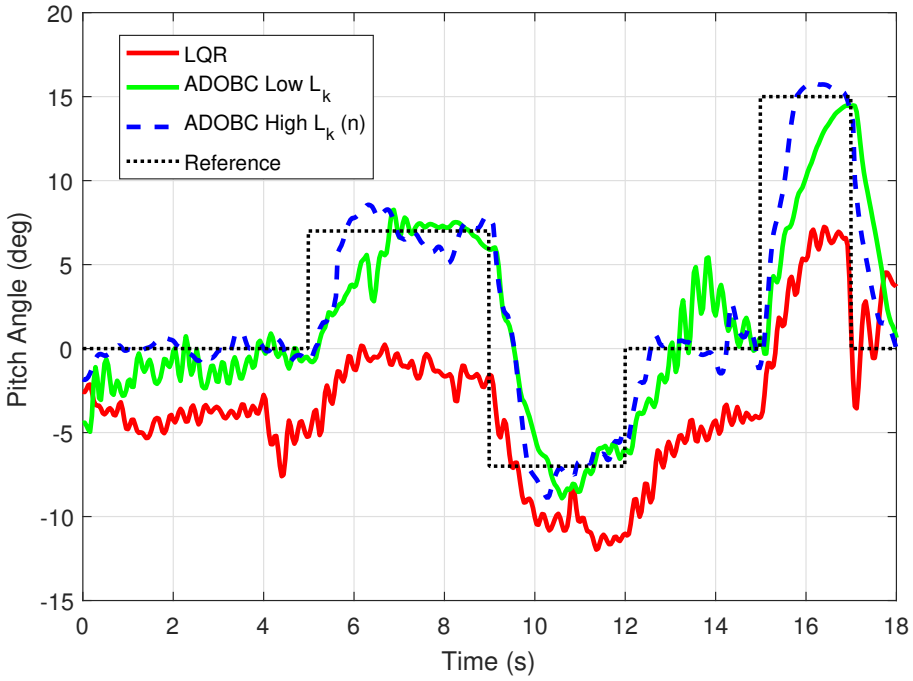

Figure 7.32: A comparison of performance between the LQR only, and the ADOBC with two observer gain settings.

low L_k; this is a direct result of the increased observer gain. Second, structural oscillations are clearly present in the unfiltered response but not in the filtered response. This further demonstrates that the notch filter is sufficiently suppressing the oscillations.

Once reference steps take place, the difference between LQR and ADOBC responses is once again clearly evident. We also see that the high L_k observer scheme is outperforming the low L_k scheme in the entire flight. The difference is most evident in the $12s \leq t \leq 18s$ period of the graph. At around 14s the oscillations for the unfiltered response briefly grow, demonstrating that the low L_k gain is close to its critical gain point. To gain a better understanding of the intricate differences, the control demands are also plotted in Fig. 7.33.

Here the oscillation problem is substantially clearer. The unfiltered control schemes have continuous oscillatory control demands, where the notch filtered ADOBC does not. We can see from Fig. 7.33 that at $t = 15s$, both ADOBC schemes apply the same initial elevator deflection and with similar magnitudes for the remainder of the manoeuvre; this raises the question of why the low L_k gain scheme produces significantly worse reference tracking. As the only data stored by the Pixhawk is the control demand, the plotted data is therefore only the demanded control action. To better represent the true dynamics, the demanded control action was passed through the second order actuator model. This results in a good approximation of the resulting true control deflection, which is given in Fig. 7.34.

Here it is immediately clear that, due to the oscillatory form of the elevator deflection, the low L_k gain scheme has a much lower average deflection during this period. Comparing the same data for the filtered scheme shows that the actuator model filter has had almost no influence on the shape of the graph, with the average deflection being much the same. So not only does the structural oscillation limit the stable gain which can be applied, but the resulting oscillatory control demands lead to a less effective control output for the system.

Furthermore, we can see more easily from Fig. 7.34 that the trim elevator command for the LQR is not accurate, as both the ADOBC schemes settle to a larger average elevator

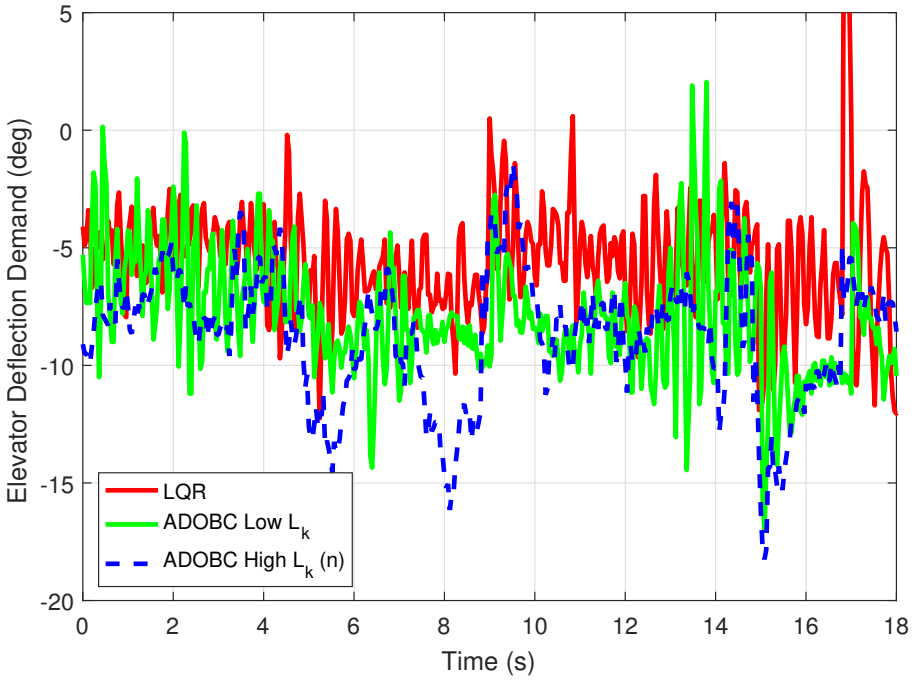

Figure 7.33: A comparison of demanded elevator deflection of the LQR only, and the ADOBC with two observer gain settings.

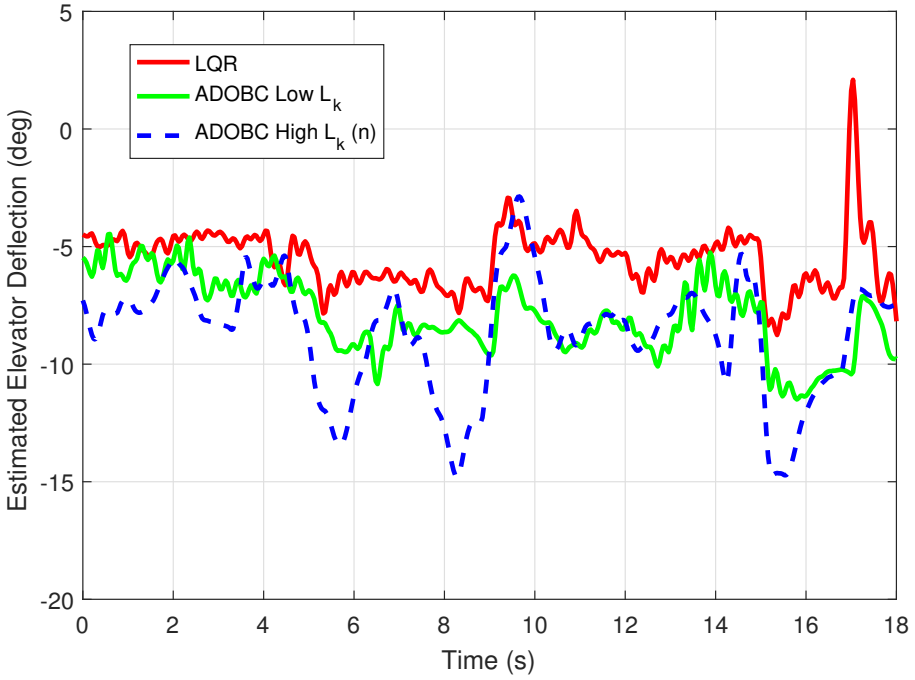

Figure 7.34: A comparison of the estimated actuator deflections resulting from the control demands.

command in the initial 5 seconds.

Shown in Fig. 7.35 is a frequency decomposition of the control demand for this period. The effect of the notch filter is immediately clear in this data, as the effect of the flexible body mode have been entirely suppressed, which further solidifies the function of the notch filter in the flight test.

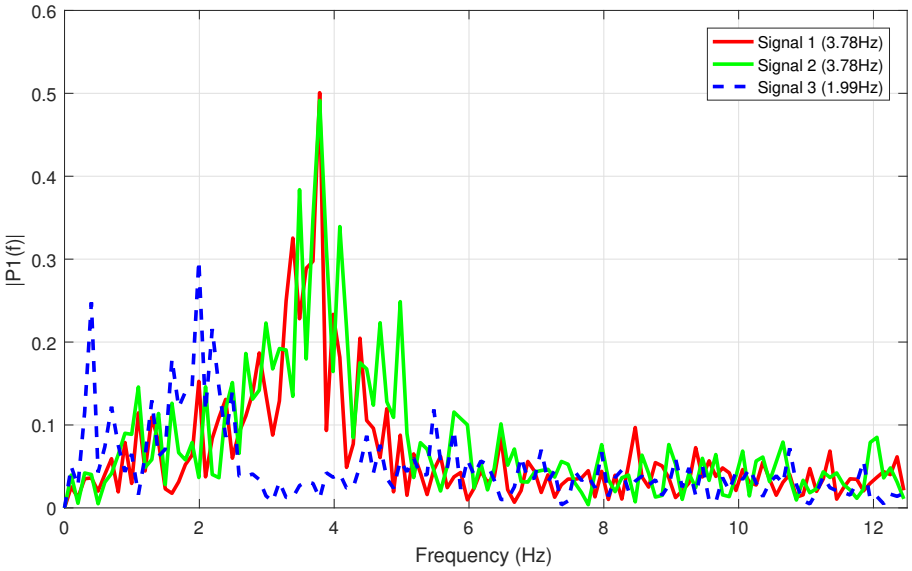

Figure 7.35: A comparison of demanded elevator deflection of the LQR only, and the ADOBC with two observer gain settings.

7.7 Conclusions

This chapter has investigated the phenomenon of controller instability due to unmodelled aircraft structural dynamics. The issue was first seen with initial trials of the Pixhawk autopilot on the Skywalker X8. At that time, it was considered only to be the result of overly aggressive control gains. Later, the issue reappeared during early stages of flight testing with various offboard controllers. It was here that the issue was deemed to warrant further investigation.

A range of tests were conducted which concluded that the source of the oscillation was the aircraft itself. The structure of the X8 is different to conventional aircraft construction. It is mainly composed of EPP foam, with some carbon spars for rigidity. This construction is very common to small UAVs, which suggests this problem may be common to other small UAV airframes too. This meant that a generic solution which could be applied to any aircraft was preferable.

An appropriate model from literature was identified from the modelling of structural dynamics of missiles. Also identified during the literature search for an appropriate model was a potential means for addressing the issue - a notch filter. Initial investigation of the problem in the frequency domain was then conducted, where the influence of the flexible body model on the feedback control scheme was very clear. Higher feedback gains reduced the stability of the system with the flexible body model present. This matched well with the behaviours seen during flight testing, where reducing the feedback control gains removed the problem. The frequency analysis also indicated that the notch filter offered the means to counteract this problem and significantly improve system stability.

To understand the effects of the oscillation on the ADOBC scheme, the frequency domain analysis was then expanded to numerical simulation. Here, it was shown that with higher feedback gains the magnitude of the oscillations would increase. As the oscillations appear to the observer as disturbances, high levels of oscillation in the simulation would result in additional control action from the ADOBC scheme, which would exacerbate the effect and render the system unstable. It was demonstrated that to mitigate this, either the feedback gain or observer gains had to be reduced substantially. In effect, the flexible body dynamics applied a limit to the maximum gains which could be applied.

Studies of the notch filter demonstrated clearly that the initial frequency domain anal-

ysis was correct. With the notch filter in place, higher feedback gains could be applied. However, the available increase was still limited as undesirable control action would appear at very high levels. However, even with this control action, the system was stable with the notch filter in place. A far more substantial increase in gain was available to the ADOBC scheme with the notch filter in place, while maintaining system stability. With the notch filter in place, a small amount of additional feedback gain coupled with much higher disturbance observer gains resulted in a system with much better overall performance than without the notch filter. The simulations therefore demonstrated that there were no noticeable drawbacks to the inclusion of the notch filter on system performance. These results were then validated with X-Plane simulations.

Finally, the notch filter was tested in flight aboard the Skywalker X8. Initial testing was conducted allowing the aircraft to enter unstable oscillations. When the notch filter was activated, the oscillations were quickly removed from the system, showing promising initial results. Toggling the notch filter off again showed that the oscillations returned very quickly. A final comprehensive flight test was conducted to compare the maximum stable observer gain without the notch filter, to a much higher stable gain with the notch filter. This flight showed clear improvements in performance for the high gain observer with notch filtering. Analysis of the control demand showed that without the notch filter, even in a stable configuration, oscillations were ever present without the filter. When the notch filter was enabled, the oscillations were completely removed. Some post processing of the demanded control action then showed that the modelled actuator deflections for the high gain observer with the notch filter were far more substantial, giving the reason for the significant improvement in flight testing.

Overall the chapter was very successful in identifying, understanding and modelling the problem of oscillation. The proposed notch filter solution was thoroughly investigated and the resulting performance improvement in flight testing was very clear. This problem is unlikely to be limited to the Skywalker X8, as it is a result of the non-conventional construction methods of the small UAVs when compared to larger aircraft. The developed solution is simple and generic enough that it could readily be applied to any similar aircraft with this issue, with no noticeable reduction in performance. It also has the benefit of being control based, so can be quickly and cheaply applied.

Chapter 8

The Application of Direct Lift Control

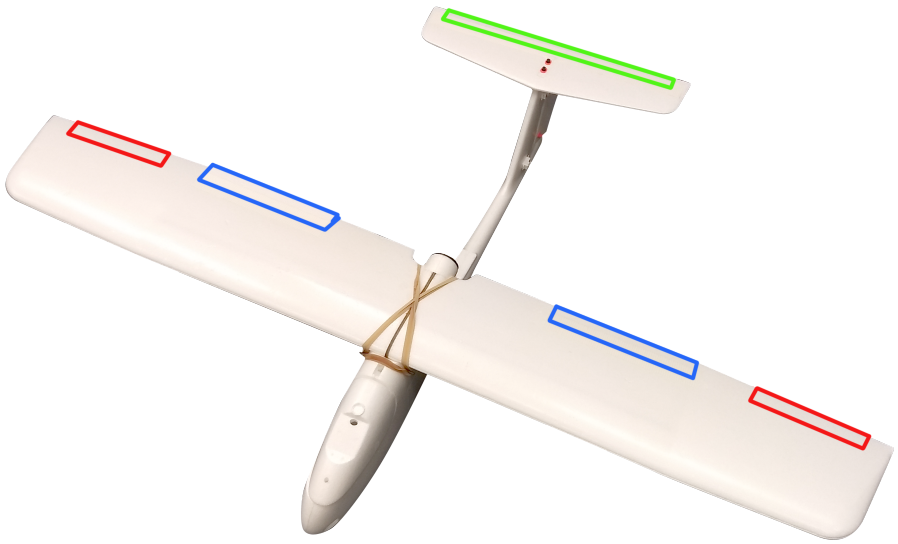

Figure 8.1: The Skywalker 1780 aircraft with control surfaces highlighted. Red: Ailerons. Blue: Flaps. Green: Elevator.

Direct Lift Control (DLC) is a means of directly controlling aircraft vertical velocity through the use of aerodynamic control surfaces, typically the flaps, to control the total lift being produced. Use of DLC may allow for improved tracking of a glide slope, especially in the presence of disturbances. This yields a design challenge for DOBC, as glide slope tracking only requires the regulation of two states. The addition of the DLC surface means the system becomes over actuated - the traditional means of disturbance rejection gain calculation are not able to deal with this problem. This issue is investigated herein.

DLC has been discussed in literature since as early as the 1960's [131]. The technique was identified as a means for improving landing accuracy of commercial aircraft which was more accurate than the conventional method. For conventional aircraft control, the attitude must be altered first to change the lift being produced which in turn results in a change in vertical velocity. DLC alters the angle of the flaps on the wing to directly alter the lift, thereby resulting in faster control of the lift. In large commercial aircraft this has a significant effect as the flap dynamics are relatively fast compared to the pitch dynamics. For small UAVs, the pitch dynamics are quite fast. However, as the actuators are electronic servos rather than hydraulic systems, their dynamics are also much faster. It may therefore be possible to improve disturbance rejection, particularly in the vertical

direction, by utilising DLC on small UAVs. Flaps are commonly found on conventional configuration aircraft.

Previous implementations of DLC in literature have focused on large scale aircraft [132] with a focus on landing safety [133]. Disturbance rejection and passenger comfort have also been studied [134, 135] and it was shown that the use of DLC offers good improvements in both areas. Some more recent work has studied modern civilian transport aircraft [136] as well as hypersonic aircraft [137]. In all cases it was shown that DLC offers good benefit, particularly in the comfort and disturbance rejection areas. It is therefore very likely that, for a small UAV with fast actuator dynamics, these benefits should also be realisable. Although comfort is not of concern for small UAVs, reduced harshness in flight may have other benefits such as being able to operate more sensitive equipment onboard.

For this section, a different aircraft is needed. As the Skywalker X8 is a flying wing, it does not have flaps and is not able to make use of DLC control. Any changes to main wing lift will result in pitching. Conventional configuration aircraft are able to account for the pitching changes with elevator deflection, leaving only the vertical velocity as the net result - this is not possible with a flying wing. For this reason, the Skywalker 1780 aircraft is used as the basis for this study; it is pictured in Fig. 8.1.

8.1 Control Design for Glide Slope Tracking

The standard LQR design used previously resulted in good performance of step reference commands. However, this design is limited in application to constant reference commands (i.e. step changes). Fig. 8.2 represents the constituent components of a landing manoeuvre, namely the approach and flare. Our interest in this section regards the approach, which involves tracking of a trajectory commonly known as the glide slope. For this, an augmentation to the previous design is needed. This design is outlined in this section.

8.1.1 Problem Definition

During the approach, the aircraft is required to maintain velocity while tracking a continuously descending reference altitude. The angle of the glide slope is defined by γ, which is relative to the flat horizon. The performance objective is therefore to track

$$\begin{aligned} u &= u_r, \\ h(t) &= h_r(t) \\ &= h_0 + \dot{h}_g t, \end{aligned}$$

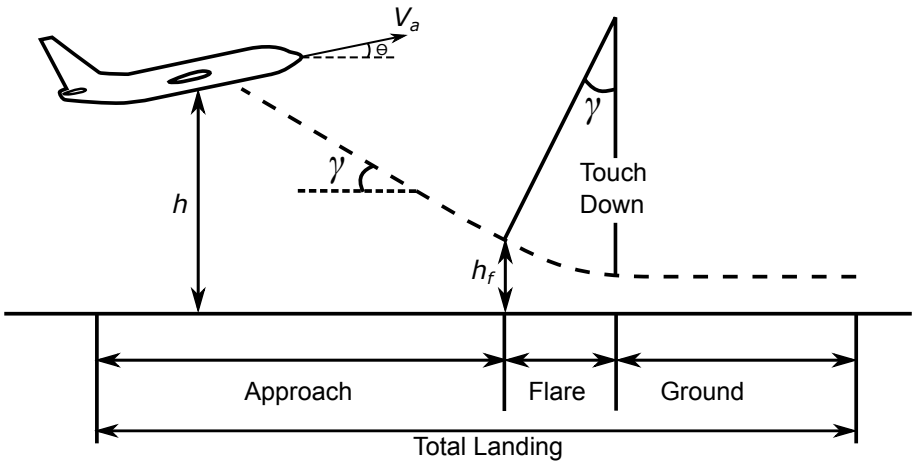

Figure 8.2: A diagram showing the general glide slope tracking problem

where u and h are the forward body velocity and kinematic height, respectively, u_r is the reference velocity to be maintained, h_0 is the height at which glide slope tracking is initiated, $\dot{h}_g$ is the descent rate and t is the time during the manoeuvre. We can determine $\dot{h}_g$ using the glide slope angle, γ. In conventional aircraft operation, $\gamma = 3^\circ$ is typical. With $u = 15m/s$, this leads to $\dot{h}_g = -0.786m/s$. However, for the Skywalker 1780, this descent rate requires a very low throttle setting to achieve, which leaves minimal available authority for disturbance rejection in the negative throttle direction. If we set $\dot{h}_g = -0.5m/s$, which yields $\gamma \approx 2^\circ$, the aircraft is able to descend with a more reasonable throttle setting. Therefore we define

$$\dot{h}_g = -0.5m/s.$$

Generally the choice of h_0 is arbitrary. For the numerical simulations, it will be taken as 0 without loss of generality. For X-Plane simulations, we take h_0 as the height at which the controller is engaged, with the descent defined from there. The starting height in X-Plane can be considered arbitrary if it is the same for all simulations, which is ensured by the simulation configuration. Further, the height changes are small enough that factors such as change in air density are small enough to be negligible. Next, we must design a baseline controller which is able to track this reference system. We assume that for the most part, u_r will be maintained at the reference value; if changes are needed, only step responses will be considered. The designed controller will therefore only consider a time varying h_r.

8.1.2 Reference Tracking Design

We begin with a linear time invariant system, following the method outlined in [138]

$$\begin{aligned} \dot{\boldsymbol{x}} &= \boldsymbol{A}\boldsymbol{x} + \boldsymbol{B}\boldsymbol{u} + \boldsymbol{E}\boldsymbol{v}, \\ \boldsymbol{e} &= \boldsymbol{C}\boldsymbol{x} + \boldsymbol{D}\boldsymbol{u} + \boldsymbol{F}\boldsymbol{v}, \\ \dot{\boldsymbol{v}} &= \boldsymbol{A}_1\boldsymbol{v}, \end{aligned} \tag{8.1}$$

where $\boldsymbol{x} \in \mathbb{R}^n$ is the system state, $\boldsymbol{u} \in \mathbb{R}^m$ is the input and $\boldsymbol{e} \in \mathbb{R}^p$ is the error between system state and reference $\boldsymbol{v} \in \mathbb{R}^q$, where $\boldsymbol{A}_1$ describes the reference dynamics. $\boldsymbol{E}$ and $\boldsymbol{F}$ are the disturbance and reference mapping matrices for $\boldsymbol{v}$, respectively. This generic formulation of the problem allows $\boldsymbol{v}$ to contain dynamic references, disturbances or both. In our case, we assume the disturbances cannot be modelled, thus meaning $\boldsymbol{v}$ only contains reference dynamics. The full derivation of the controller is not repeated here for brevity; it can be found in [138].

We assume that this system will be controlled by a law defined as

$$\boldsymbol{u} = \boldsymbol{k}_x\boldsymbol{x} + \boldsymbol{k}_v\boldsymbol{v}, \tag{8.2}$$

where $\boldsymbol{k}_x \in \mathbb{R}^{m\times n}$ and $\boldsymbol{k}_v \in \mathbb{R}^{m\times q}$ are constant gain matrices. The matrices and gains are defined in Section 8.1.5.

8.1.3 Model Definition

As the two systems being considered for DOBC augmentation are quite similar in notation and form, $\boldsymbol{S}_1$ and $\boldsymbol{S}_2$ will be defined here to refer to the aircraft with and without DLC control, respectively. This will aid clearer discussion in the remainder of this chapter. The full model definitions will be given first, with discussion on selection of modelling parameters in Section 8.1.4

First, we define the system matrices and states for the DLC aircraft as

$$\dot{\boldsymbol{x}}_1 = \underbrace{\begin{bmatrix} -0.116 & 0.992 & -0.352 & -10.26 & 0 \\ -1.05 & -6.74 & 14.99 & 0 & 0 \\ 0.114 & -3.87 & -3.8 & 0 & 0 \\ 0 & 0 & 1 & 0 & 0 \\ 0.144 & -0.65 & 0 & 15.99 & 0 \end{bmatrix}}_{\boldsymbol{A}} \boldsymbol{x}_1 + \underbrace{\begin{bmatrix} 0 & 2.72 & -0.029 \\ -0.095 & 0 & -0.34 \\ -1.99 & 0 & 0.187 \\ 0 & 0 & 0 \\ 0 & 0 & 0 \end{bmatrix}}_{\boldsymbol{B}_1} \boldsymbol{\eta}_1,$$

$$\boldsymbol{x}_1 = \begin{bmatrix} u & w & q & \theta & h \end{bmatrix}^T, \qquad \boldsymbol{\eta}_1 = \begin{bmatrix} \delta_e & \delta_t & \delta_d \end{bmatrix}^T,$$

where δ_e, δ_t and δ_d are the elevator, throttle and DLC surface deflections. The system output is given by

$$\boldsymbol{y}_1 = \underbrace{\begin{bmatrix} 1 & 0 & 0 & 0 & 0 \\ 0 & 0 & 0 & 0 & 1 \end{bmatrix}}_{\boldsymbol{C}} \boldsymbol{x}_1.$$

The actuator dynamics are given by

$$\dot{\boldsymbol{\epsilon}}_1 = \underbrace{\begin{bmatrix} -6.25 & 0 & 0 & 0 \\ 0 & 0 & 1 & 0 \\ 0 & -2.56 & -3.2 & 0 \\ 0 & 0 & 0 & -6.25 \end{bmatrix}}_{\boldsymbol{A}_1^\epsilon} \boldsymbol{\epsilon}_1 + \underbrace{\begin{bmatrix} 6.25 & 0 & 0 \\ 0 & 0 & 0 \\ 0 & 2.56 & 0 \\ 0 & 0 & 6.25 \end{bmatrix}}_{\boldsymbol{B}_1^\epsilon} \boldsymbol{u}_1,$$

$$\boldsymbol{\epsilon}_1 = \begin{bmatrix} \delta_e & \delta_t & \dot{\delta}_t & \delta_d \end{bmatrix}, \qquad \boldsymbol{u}_1 = \begin{bmatrix} u_e & u_t & u_d \end{bmatrix}^T,$$

with the actuator states then defined as

$$\boldsymbol{\eta}_1 = \underbrace{\begin{bmatrix} 1 & 0 & 0 & 0 \\ 0 & 1 & 0 & 0 \\ 0 & 0 & 0 & 1 \end{bmatrix}}_{\boldsymbol{C}_1^\epsilon} \boldsymbol{\epsilon}_1.$$

The thrust model uses the same dynamics as described in Chapter 4 for the X8, with thrust scaled down based on the motor typically used for the Skywalker 1780. The resulting DLC aircraft system, with lumped disturbances included, is then described by

$$\boldsymbol{S}_1 = \left\{ \begin{array}{c} \dot{\boldsymbol{x}}_1 = \boldsymbol{A}\boldsymbol{x}_1 + \boldsymbol{B}_1\boldsymbol{\eta}_1 + \boldsymbol{d}_{lx_1}, \\ \boldsymbol{y}_1 = \boldsymbol{C}\boldsymbol{x}_1, \\ \dot{\boldsymbol{\epsilon}}_1 = \boldsymbol{A}_1^\epsilon\boldsymbol{\epsilon}_1 + \boldsymbol{B}_1^\epsilon\boldsymbol{u}_1 \\ \boldsymbol{\eta}_1 = \boldsymbol{C}_1^\epsilon\boldsymbol{\epsilon}_1 \end{array} \right\}. \tag{8.3}$$

The aircraft *without* DLC flaps shares many common features with $\boldsymbol{S}_1$, featuring only different actuator states and dynamics. This system is defined as

$$\dot{\boldsymbol{x}}_2 = \underbrace{\begin{bmatrix} -0.116 & 0.992 & -0.352 & -10.26 & 0 \\ -1.05 & -6.74 & 14.99 & 0 & 0 \\ 0.114 & -3.87 & -3.8 & 0 & 0 \\ 0 & 0 & 1 & 0 & 0 \\ 0.144 & -0.65 & 0 & 15.99 & 0 \end{bmatrix}}_{\boldsymbol{A}} \boldsymbol{x}_2 + \underbrace{\begin{bmatrix} 0 & 2.72 \\ -0.095 & 0 \\ -1.99 & 0 \\ 0 & 0 \\ 0 & 0 \end{bmatrix}}_{\boldsymbol{B}_2} \boldsymbol{\eta}_2,$$

$$\boldsymbol{x}_2 = \begin{bmatrix} u & w & q & \theta & h \end{bmatrix}^T, \qquad \boldsymbol{\eta}_2 = \begin{bmatrix} \delta_e & \delta_t \end{bmatrix}^T,$$

and the output is given by

$$\boldsymbol{y}_2 = \underbrace{\begin{bmatrix} 1 & 0 & 0 & 0 & 0 \\ 0 & 0 & 0 & 0 & 1 \end{bmatrix}}_{\boldsymbol{C}} \boldsymbol{x}_2.$$

The actuators are modelled by

$$\dot{\boldsymbol{\epsilon}}_2 = \underbrace{\begin{bmatrix} -6.25 & 0 & 0 \\ 0 & 0 & 1 \\ 0 & -2.56 & -3.2 \end{bmatrix}}_{\boldsymbol{A}_2^{\epsilon}} \boldsymbol{\epsilon}_2 + \underbrace{\begin{bmatrix} 6.25 & 0 \\ 0 & 0 \\ 0 & 2.56 \end{bmatrix}}_{\boldsymbol{B}_2^{\epsilon}} \boldsymbol{u}_2,$$

$$\boldsymbol{\epsilon}_2 = \begin{bmatrix} \delta_e & \delta_t & \dot{\delta}_t \end{bmatrix}, \qquad \boldsymbol{u}_2 = \begin{bmatrix} u_e & u_t \end{bmatrix}^T,$$

with the actuator states then defined as

$$\boldsymbol{\eta}_2 = \underbrace{\begin{bmatrix} 1 & 0 & 0 \\ 0 & 1 & 0 \end{bmatrix}}_{\boldsymbol{C}_2^{\epsilon}} \boldsymbol{\epsilon}_2.$$

The total system of the aircraft dynamics without DLC flaps can then be defined as

$$\boldsymbol{S}_2 = \left\{ \begin{array}{c} \dot{\boldsymbol{x}}_2 = \boldsymbol{A}\boldsymbol{x}_2 + \boldsymbol{B}_2\boldsymbol{\eta}_2 + \boldsymbol{d}_{lx_2}, \\ \boldsymbol{y}_2 = \boldsymbol{C}\boldsymbol{x}_2, \\ \dot{\boldsymbol{\epsilon}}_2 = \boldsymbol{A}_2^{\epsilon}\boldsymbol{\epsilon}_2 + \boldsymbol{B}_2^{\epsilon}\boldsymbol{u}_2 \\ \boldsymbol{\eta}_2 = \boldsymbol{C}_2^{\epsilon}\boldsymbol{\epsilon}_2 \end{array} \right\}. \tag{8.4}$$

It should be noted that $\boldsymbol{S}_1$ and $\boldsymbol{S}_2$ share common $\boldsymbol{A}$ and $\boldsymbol{C}$ matrices, which result in equivalent state dynamics and system outputs; the difference between the two systems is entirely due to the inclusion of DLC flaps in $\boldsymbol{S}_1$ and the modelling requirements associated with this.

Flight Test Considerations

The model (particularly the chosen states) used to produce this controller impose some complications on flight testing. With DLC, vertical velocity w becomes very important. Standard sensor suites for most small UAV autopilots are not able to measure u and ww independently, as it requires measuring of flow angles.

Equipment is available within the facilities used during this work which can measure u and w directly and accurately in flight, making flight testing possible. This is achieved through a multi-hole pitot probe which can sense angle of attack and sideslip. Where this is not available, some other means of measuring these angles will be required. Alternatively, online estimation of these is possible for small UAVs [139], which may offer a viable alternative.

8.1.4 Actuator Modelling

The actuator models used for the control surfaces (DLC flap and elevator) are the same as the first order model defined in (6.1) and used throughout the associated chapter. As the DLC flap and elevators are driven by the same servo actuators on the aircraft, the responses will be very similar.

For the motor, the model defined in (4.38) was used as a very similar propulsion unit is used for the Skywalker 1780, which would have a similar response. The control inputs

are passed through actuator models to ensure the dynamics are appropriately considered in the simulations.

Fair comparison of the two aircraft is non-trivial. The reference tracking LQR design process outlined in this chapter is only suitable for systems where the number of inputs is equal to the number of controlled outputs. This would be the case for the aircraft without DLC. However, with the inclusion of DLC, adjustments are needed. Several options exists:

- Separate controllers with/without DLC
- Control allocation for the DLC system
- Separate feedback and disturbance rejection control

Designing two separate controllers, one with and one without DLC, makes it difficult to draw fair comparisons between the resulting systems as it may be difficult to pinpoint the source of any change in performance. This would likely require a large amount of tuning and validation simulations to ensure similar baseline performance. This was not an ideal option.

Control allocation is the process of creating a mapping from a "virtual" control input, used in control design, to true control deflections of the physical system. In the case of the DLC aircraft, a virtual control input comprising two control variables would be mapped onto the three physical controls. This would allow for the use of the outlined method for the DLC aircraft. This does require additional efforts into the control allocation methodology and ultimately still results in two separate baseline controllers being designed - without and with virtual control rather than without and with DLC. In essence, this would simply shift the problem from feedback design to allocation design.

The third option would be to utilise the DLC flap only for disturbance rejection, using the same baseline feedback control for reference tracking. Using this method, the baseline feedback control performance would be truly equal in all comparisons. This would then allow for study on the benefit of the DLC flap in terms of disturbance rejection only. This was the preferable option. This did incur an additional problem however. The previously used means for determining the disturbance rejection gain, described in Section 5.2.2, requires the inversion of a matrix $\boldsymbol{SB}$. For the case where the number of inputs is not equal to the number of outputs, this matrix is non-square and therefore not invertible - the calculation of the disturbance compensation gain cannot be completed. This is addressed in Section 8.2.2.

8.1.5 Controller Configuration

For design of the feedback controller, we use $\boldsymbol{S}_2$ in control design. To define the remainder of the required matrices in (8.1), we set $\boldsymbol{E}, \boldsymbol{D}$ to 0 matrices of the appropriate dimension,

$$\boldsymbol{F} = \begin{bmatrix} 1 & 0 & 0 \\ 0 & 0 & 1 \end{bmatrix},$$

and the reference system $\boldsymbol{v} = \begin{bmatrix} u_r & \dot{h}_g & h_r \end{bmatrix}$ defines

$$\boldsymbol{A}_1 = \begin{bmatrix} 0 & 0 & 0 \\ 0 & 0 & 0 \\ 0 & 0 & 1 \end{bmatrix}.$$

For the design of the baseline feedback gain $\boldsymbol{k}_x$, we use the weighting matrices

$$\boldsymbol{Q} = \begin{bmatrix} 1 & 0 \\ 0 & 1 \end{bmatrix}, \qquad \boldsymbol{R} = \begin{bmatrix} 0.4 & 0 \\ 0 & 4 \end{bmatrix}.$$

This $\boldsymbol{R}$ matrix was found to provide good performance in initial tuning of the feedback controller; throttle action was penalised more to account for the slower dynamics. The resulting control law is given by

$$\boldsymbol{u}_2 = -\boldsymbol{k}_{x_2}\boldsymbol{x}_2,$$

To apply the control law to $\boldsymbol{S}_1$, the control law must be adapted for compatibility with $\boldsymbol{u}_1$. This is accomplished by setting

$$\boldsymbol{u}_1 = -\boldsymbol{k}_{x_1}\boldsymbol{x}_1, \quad \textit{where} \quad \boldsymbol{k}_{x_1} = \begin{bmatrix} \boldsymbol{k}_{x_2} \\ 0^{5\times 1} \end{bmatrix}.$$

This ensures that the feedback control system designed for $\boldsymbol{S}_2$ has equivalent performance when applied to $\boldsymbol{S}_1$.

8.2 Over-Actuated DOBC Compensation Gain for DLC

The design of the disturbance observer follows the methods outlined in Chapter 6, with an observer for actuator dynamics and an observer for lumped disturbances, which utilises the actuator estimates. However due to the inclusion of second order actuator dynamics for the throttle, a small modification is required within the actuator observer, presented in the following section.

8.2.1 Disturbance Observer Design

This section will present the disturbance observer design for $\boldsymbol{S}_1$; the same process is used for $\boldsymbol{S}_2$ with the appropriate system equations and as such is not repeated herein for brevity. The method is broadly similar as that in Chapter 6, with a slight modification due to the second order actuator model.

First, the actuator model from (8.3) is taken to describe the dynamics component of the actuator position observer as

$$\dot{\boldsymbol{\epsilon}}_1 = \boldsymbol{A}_1^{\epsilon}\boldsymbol{\epsilon}_1 + \boldsymbol{B}_1^{\epsilon}\boldsymbol{u}_1,$$

however as we only require estimates of the actuator positions, we select these as the dynamics outputs by taking

$$\dot{\boldsymbol{\eta}}_1 = \boldsymbol{C}_1^{\epsilon}\left(\boldsymbol{A}_1^{\epsilon}\boldsymbol{\epsilon}_1 + \boldsymbol{B}_1^{\epsilon}\boldsymbol{u}_1\right).$$

This is necessary due to the inclusion of second order actuator dynamics in the observer. We continue as in the previous actuator observer by taking the measurement for actuator positions as

$$\boldsymbol{B}_1\boldsymbol{\eta}_1 = \dot{\boldsymbol{x}}_1 - \boldsymbol{A}\boldsymbol{x}_1 - \hat{\boldsymbol{d}}_{lx_1},$$

where the lumped disturbances have been replaced by their estimate, assuming a suitable observer will be designed for this term. The estimate for actuator position can then be given as

$$\dot{\hat{\boldsymbol{\eta}}}_1 = \boldsymbol{C}_1^{\epsilon}\left(\boldsymbol{A}_1^{\epsilon}\boldsymbol{\epsilon}_1 + \boldsymbol{B}_1^{\epsilon}\boldsymbol{u}_1\right) + \boldsymbol{L}_{\eta_1}(\dot{\boldsymbol{x}}_1 - \boldsymbol{A}\boldsymbol{x}_1 - \boldsymbol{B}_1\hat{\boldsymbol{\eta}}_1 - \hat{\boldsymbol{d}}_{lx_1}).$$

Following the standard DOBC procedure of defining an auxiliary state $\boldsymbol{z}$ to remove $\dot{\boldsymbol{x}}$ from the estimate dynamics, we arrive at the following observers for actuator position

$$\begin{cases} \dot{z}_2 = \boldsymbol{C}_1^{\epsilon}\left(\boldsymbol{A}_1^{\epsilon}\boldsymbol{\epsilon}_1 + \boldsymbol{B}_1^{\epsilon}\boldsymbol{u}_1\right) + \boldsymbol{L}_{\eta_1}(-\boldsymbol{A}\boldsymbol{x}_1 - \boldsymbol{B}_1\hat{\boldsymbol{\eta}}_1 - \hat{\boldsymbol{d}}_{lx_1}), \\ \hat{\boldsymbol{\eta}}_1 = z_2 + \boldsymbol{L}_{\eta_1}\boldsymbol{x}_1, \end{cases}$$

and lumped state disturbances

$$\begin{cases} \dot{\boldsymbol{z}}_1 = -\boldsymbol{L}_1(\boldsymbol{z}_1 + \boldsymbol{L}_1\boldsymbol{x}) + \boldsymbol{L}_1(-\boldsymbol{A}_1\boldsymbol{x}_1 - \boldsymbol{B}_1\hat{\boldsymbol{\eta}}_1), \\ \hat{\boldsymbol{d}}_{lx_1} = \boldsymbol{z}_1 + \boldsymbol{L}_1\boldsymbol{x}. \end{cases}$$

The stability proofs for this observer continue as in Chapter 6 and are not repeated for brevity. For the tuning of the observer gains, manual tuning was conducted to determine the most suitable observer gain. For fair comparison, the tuning was conducted with simulations of $\boldsymbol{S}_1$. The same observer gain was then used for $\boldsymbol{S}_2$, with the DLC flap estimation gain removed to maintain correct dimensions. As it is the performance benefit of the DLC flap and over actuated observer being examined in these simulations, no study of the observer performance with regards to disturbance estimation is conducted. It is assumed that the observers are sufficiently able to track the disturbances, as has been demonstrated in previous chapters.

8.2.2 Over-Actuated DOBC Compensation Gain for DLC

The classical method of linear DOBC design for state space systems assumes that the number of controlled outputs is equal to the number of inputs available. Then, based on the assumption that the disturbance is constant and the observer is able to estimate the disturbances accurately, a gain can be calculated which will remove the effect of the disturbance from the output. For the non-DLC aircraft, this calculation is given as

$$\boldsymbol{k}_{dx_2} = \left[\boldsymbol{C}(\boldsymbol{A} - \boldsymbol{B}_2\boldsymbol{k}_{x_2})^{-1}\boldsymbol{B}_2\right]^{-1}\left[\boldsymbol{C}(\boldsymbol{A} - \boldsymbol{B}_2\boldsymbol{k}_{x_2})^{-1}\boldsymbol{B}_d\right],$$

where $\boldsymbol{C}(\boldsymbol{A} - \boldsymbol{B}_2\boldsymbol{k}_{x_2})^{-1}\boldsymbol{B}_2 = \boldsymbol{N}_2^{2\times 2}$ is invertible, and $\boldsymbol{k}_{dx_2}$ is therefore uniquely defined. The gain is uniquely determined as for any given disturbance there exists a single, unique actuator configuration which removes the effect of the disturbance in the output.

However, in the case of $\boldsymbol{S}_1$, the DLC enabled aircraft, there are now more actuators available as inputs than outputs being controlled. Therefore the condition no longer holds that a unique actuator configuration configuration exists to remove the disturbance effect from the system output. Mathematically, this can be seen from the calculation of the disturbance compensation gain for this system

$$\boldsymbol{k}_{dx_1} = \left[\boldsymbol{C}(\boldsymbol{A} - \boldsymbol{B}_1\boldsymbol{k}_{x_1})^{-1}\boldsymbol{B}_1\right]^{-1}\left[\boldsymbol{C}(\boldsymbol{A} - \boldsymbol{B}_1\boldsymbol{k}_{x_1})^{-1}\boldsymbol{B}_d\right], \tag{8.5}$$

where $\boldsymbol{C}(\boldsymbol{A} - \boldsymbol{B}_1\boldsymbol{k}_{x_1})^{-1}\boldsymbol{B}_1 = \boldsymbol{N}_1^{2\times 3}$ is *not* invertible, meaning $\boldsymbol{k}_{dx}$ cannot be determined in this way. The compensation gain must be determined in a new way.

8.2.3 Pseudoinverse Control Allocation Theory

The over-actuated case can be thought of as a set of control configurations, all of which yield the same system output. The question then becomes how to determine the most suitable configuration - the optimal result. In the case studied herein, we aim to maximise the benefit of the additional DLC control surface for disturbance rejection. Control allocation is the research topic which deals with the over-actuated control design problem. A multitude of methods exist to solve this issue, from simple linear solutions to complex online optimisation [140]. As this work is an initial study into the feasibility of DLC control for disturbance rejection, a simple solution was desirable. One of the earliest and simplest control allocation methods is the pseudoinverse method, where the pseudoinverse of general matrix $\boldsymbol{B}$ is given by [141]

$$\boldsymbol{B}^{\#} = \boldsymbol{B}^T(\boldsymbol{B}\boldsymbol{B}^T)^{-1},$$

where $(\cdot)^{\#}$ indicates the pseudoinverse operation. This provides the minimum-norm solution, also known as the Moore-Penrose pseudoinverse. Using this operation, we can solve (8.5) for $\boldsymbol{k}_{dx_1}$ as

$$\boldsymbol{k}_{dx_1} = \boldsymbol{N}_1^{\#}\boldsymbol{C}(\boldsymbol{A} - \boldsymbol{B}_1\boldsymbol{k}_{x_1})^{-1}\boldsymbol{B}_d.$$

This has therefore solved the over-actuated problem for determination of the disturbance rejection gain. However, as initially stated this is only a single solution in a larger set of possible solutions. It may be possible to determine a more optimal solution. Generally, optimal solutions require a performance index against which to determine optimality, from a user defined criteria. The weighted pseudoinverse [142] is one way by which this can be achieved. By introducing $\boldsymbol{W}$, a weighting matrix, it is possible to control the calculation of $\boldsymbol{k}_{dx_1}$ within the set of feasible solutions. For this, we define

$$\boldsymbol{W} = \begin{bmatrix} \eta_k^e & 0 & 0 \\ 0 & \eta_k^t & 0 \\ 0 & 0 & \eta_k^d \end{bmatrix}, \tag{8.6}$$

where $\eta_k^{(\cdot)}$ is the weighting for the actuator denoted by the superscript. By introducing the weighting matrix to the pseudoinverse calculation as

$$\boldsymbol{B}^{\#} = \boldsymbol{W}(\boldsymbol{B}\boldsymbol{W})^T(\boldsymbol{B}\boldsymbol{W}(\boldsymbol{B}\boldsymbol{W})^T)^{-1},$$

the weighting on the control inputs can be applied with an effect akin to the $\boldsymbol{R}$ matrix in LQR design. This method therefore requires manual tuning to obtain best performance. This was deemed sufficient for this initial investigation.

8.2.4 The Effect of Weighting on Pseudoinverse Disturbance Rejection Gains

To demonstrate the effect of this weighting matrix, we study the effects of $\boldsymbol{S}_1$ (8.1.3) under LQR feedback control. The feedback gain for this system is given as

$$\boldsymbol{k}_{x_1} = \begin{bmatrix} 0.184 & -0.489 & 0.889 & 11.62 & 0.659 \\ -0.438 & 0.023 & -0.102 & -0.80 & -0.161 \\ 0 & 0 & 0 & 0 & 0 \end{bmatrix},$$

which was obtained using the process outlined in this section. Now, following the procedure outlined in Section 8.2.3,

$$\text{taking } \boldsymbol{W}_1 = \begin{bmatrix} 1 & 0 & 0 \\ 0 & 1 & 0 \\ 0 & 0 & 1 \end{bmatrix} \text{ gives } \boldsymbol{k}_{dx_1}^a = \begin{bmatrix} -0.002 & 0.283 & -0.498 & -7.0 & -0.697 \\ 0.367 & 0.030 & 0.001 & -0.207 & 0.289 \\ -0.008 & -0.056 & 0.098 & 1.38 & 0.131 \end{bmatrix},$$

the minimum norm solution to the given problem. Assuming we want disturbance rejection with less δ_e utilisation and more δ_t,

$$\text{setting } \boldsymbol{W}_2 = \begin{bmatrix} 5 & 0 & 0 \\ 0 & 0.2 & 0 \\ 0 & 0 & 1 \end{bmatrix} \text{ yields } \boldsymbol{k}_{dx_1}^b = \begin{bmatrix} -0.0002 & 0.246 & -0.433 & -6.09 & -0.605 \\ 0.367 & 0.026 & 0.008 & -0.106 & 0.299 \\ -0.001 & -0.243 & 0.427 & 6.0 & 0.596 \end{bmatrix}.$$

The result may appear somewhat unexpected. Studying the d_u terms (column 1 of $\boldsymbol{k}_{dx_1}^b$), we see that the elevator and DLC flap have seen reduced gains whilst the throttle is unchanged. This is unintuitive, as more throttle action was demanded from the weighting

matrix. However, it is the relative magnitudes which must be considered. For example, multiplying $\boldsymbol{W}_2$ by a factor of 5 would yield the same $\boldsymbol{k}^b_{dx_1}$ gain, with a weighting matrix

$$5\boldsymbol{W}_2 = \begin{bmatrix} 25 & 0 & 0 \\ 0 & 1 & 0 \\ 0 & 0 & 5 \end{bmatrix},$$

which heavily penalises δ_e action with some penalty on δ_d action too. The resulting changes in $\boldsymbol{k}^b_{dx_1}$ then are more intuitive, as δ_e has significantly lower gain, and δ_d has somewhat lower gain. This effect is studied in more detail in Section 8.3.3 with numerical simulations.

The stability proof for this observer follows the same process as outlined in Chapter 5 and is not reproduced here.

8.3 Simulations

To study the effect of DLC in a controlled environment, numerical state space simulations were conducted. There are several factors to be investigated in these simulations:

- Is the designed reference tracking strategy sufficient?
- Does DLC improve disturbance rejection?
- Are there drawbacks to the addition of DLC control?
- Does the weighted pseudoinverse allow control of disturbance rejection?
- Does the performance translate to more realistic environments?

First, we confirm that the addition of the DLC flap does indeed allow for better disturbance rejection and quantify the improvements. It is also important to investigate any drawbacks associated with the inclusion of DLC - after all you don't get something for nothing. For example, does the improved disturbance rejection come at the price of significantly more complex controller tuning?

Another key factor is to understand the effects of the weighted pseudoinverse gain calculation. Does it allow for control of the distribution of control effort to a satisfactory level for disturbance rejection, or is a more advanced method needed?

Finally, as with previous work, a study will be conducted to ensure the findings of numerical simulations translate to a more representative environment. In this case, X-Plane is used for verification.

8.3.1 LQR Reference Tracking Performance

First, to study the benefit of the reference tracking augmentation, glide slope tracking performance in the absence of disturbance was studied. Numerical state space simulations are conducted first. In these initial simulations, actuator modelling is disabled as their effects are not considered.

Here, we compare the original DC gain feedforward method defined in Section 5.1.2 to the newly designed controller. The DC gain feedforward method is referred to as "LQR (N)", while the newly designed method is referred to as "LQR (v)". As we are considering this controller in the context of glide slope tracking, we compare performance to a step $\dot{h}_g = -0.5m/s$ input active while $1 \leq t \leq 10s$. The outputs are given in Fig. 8.3 with the control inputs in Fig. 8.4. The difference is immediately obvious; with the LQR (v) design, no steady state error is seen during the glide slope tracking in either u or h, while

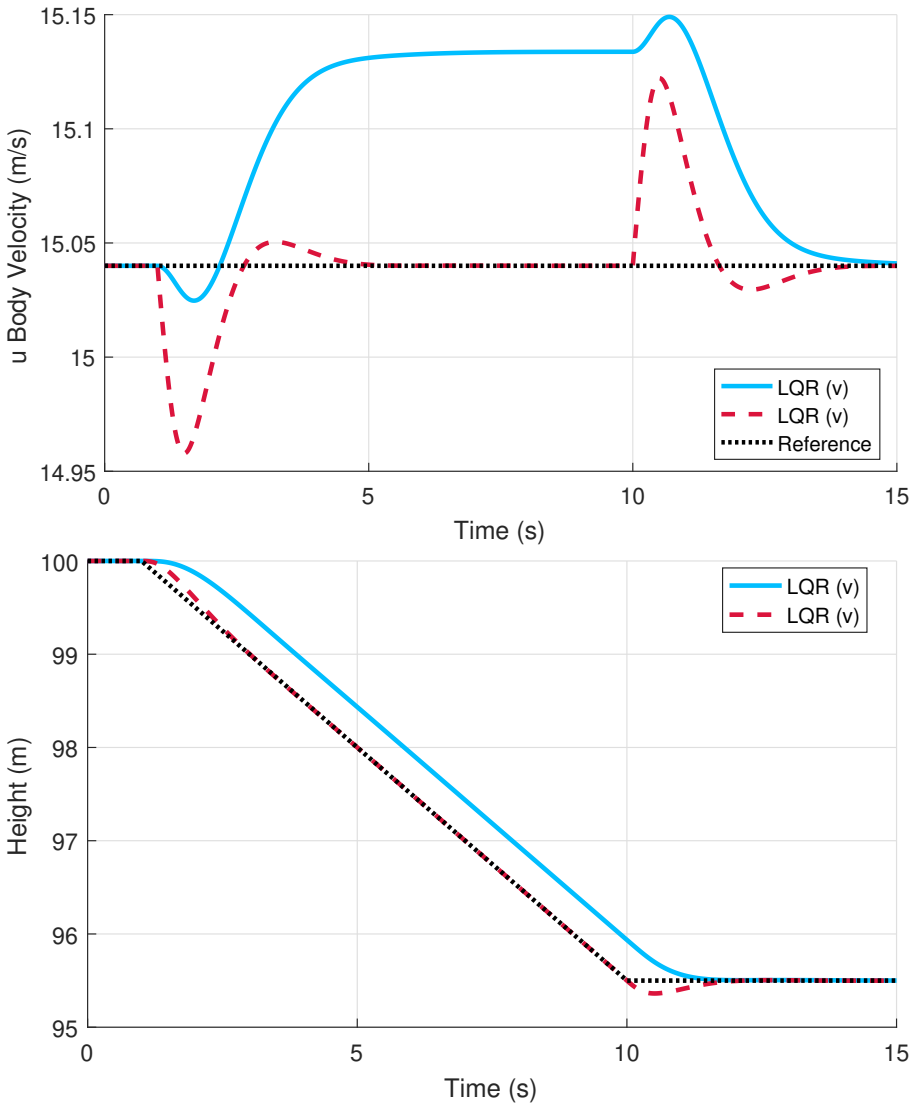

Figure 8.3: The aircraft outputs to a glide slope tracking manoeuvre comparing the two methods of LQR design.

the LQR (N) design has a constant steady state error while the reference command is changing. From the control inputs we can see that the LQR (v) system responds to the reference input more aggressively, giving less initial error.

We also see that the LQR (v) design has some undershoot at the bottom of the glide slope. This could be accounted for in the design by adjusting the reference system. However, for glide slope tracking this manoeuvre translates to the flare, rather than an abrupt change to the reference command so this overshoot is not a concern.

This simulation demonstrates clearly the benefit of this design method. For all future simulations in this chapter, the LQR (v) design will be used as the baseline controller.

8.3.2 Effect of DLC

Next, we compare the baseline LQR (v) system with the two disturbance observer systems, $\boldsymbol{S}_1$ and $\boldsymbol{S}_2$. For the initial comparison, no allocation weighting is applied in the calculation of $\boldsymbol{k}_{dx_1}$. Fig. 8.5 and 8.6 give the outputs and inputs for a glide slope tracking manoeuvre. The disturbances applied are given in Table 8.1; these disturbances are applied throughout the following simulations.

Here we see that the performance of $\boldsymbol{S}_1$ is nearly identical to $\boldsymbol{S}_2$. The data for pitch

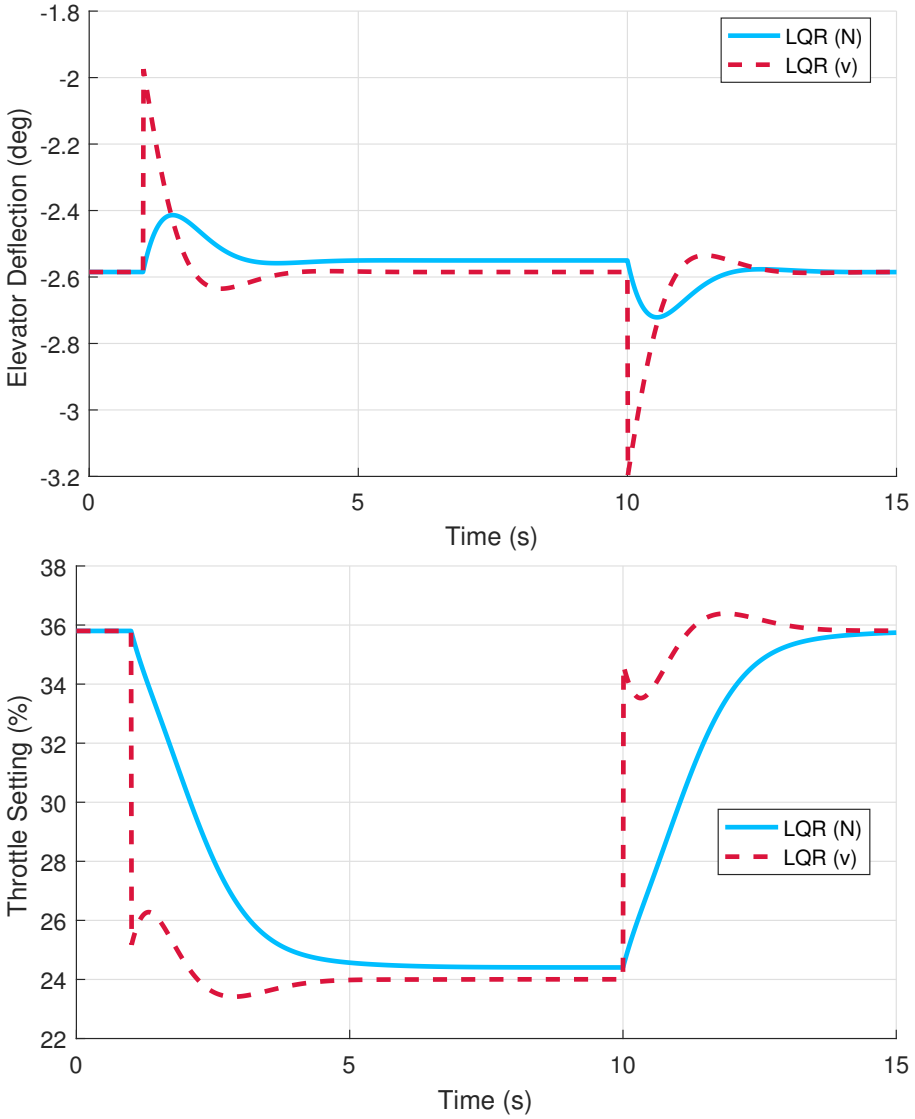

Figure 8.4: The aircraft control inputs to a glide slope tracking manoeuvre comparing the two methods of LQR design.

angle θ has also been plotted. Although it is not a controlled variable, it is still of interest in the application. During landing, the variation in θ must be regulated tightly within a range to avoid damage to the aircraft or dangerous flight conditions. One possible benefit of the DLC flap is improved θ regulation, as the aircraft does not necessarily need to be pitched to adjust height. In this case however, the response of $\boldsymbol{S}_1$ shows no benefit above $\boldsymbol{S}_2$. Small differences are present in the control inputs, but these are not enough to have noticeable effects on the outputs. This is a positive point for the initial comparison, as in the default state the addition of the DLC flap has not had much effect allowing for similar responses and therefore fair comparison. However, we also notice in Fig. 8.6 that δ_d deflections are an order of magnitude less than that of the elevator, with the throttle also seeing comparatively high usage. This suggests that, with more influence on the DLC flap for disturbance rejection, some differences might be noticeable. This is investigated next.

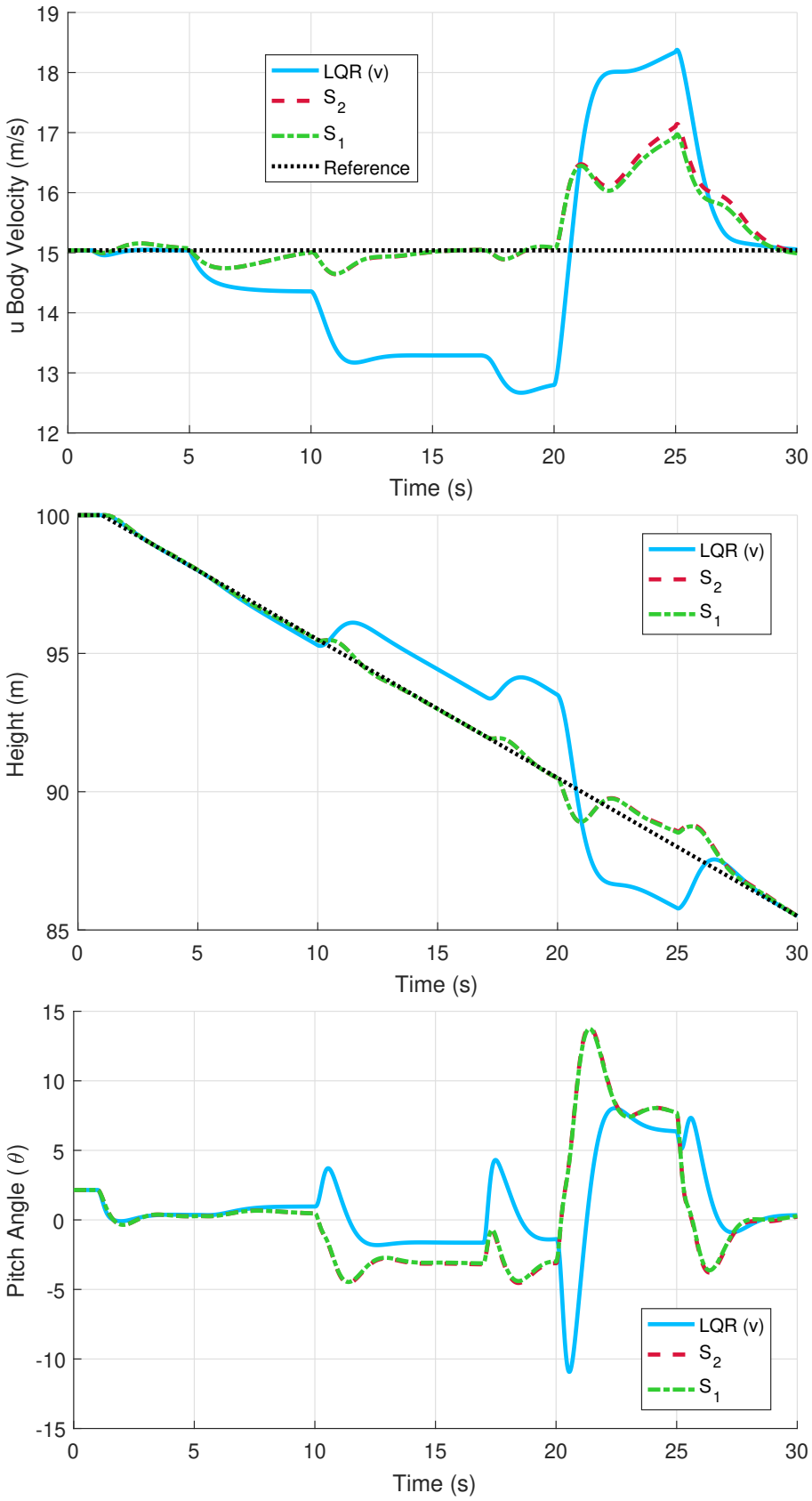

Figure 8.5: The aircraft outputs to a glide slope tracking manoeuvre with disturbances comparing the LQR, $\boldsymbol{S}_2$ (no DLC) and $\boldsymbol{S}_1$ (DLC).

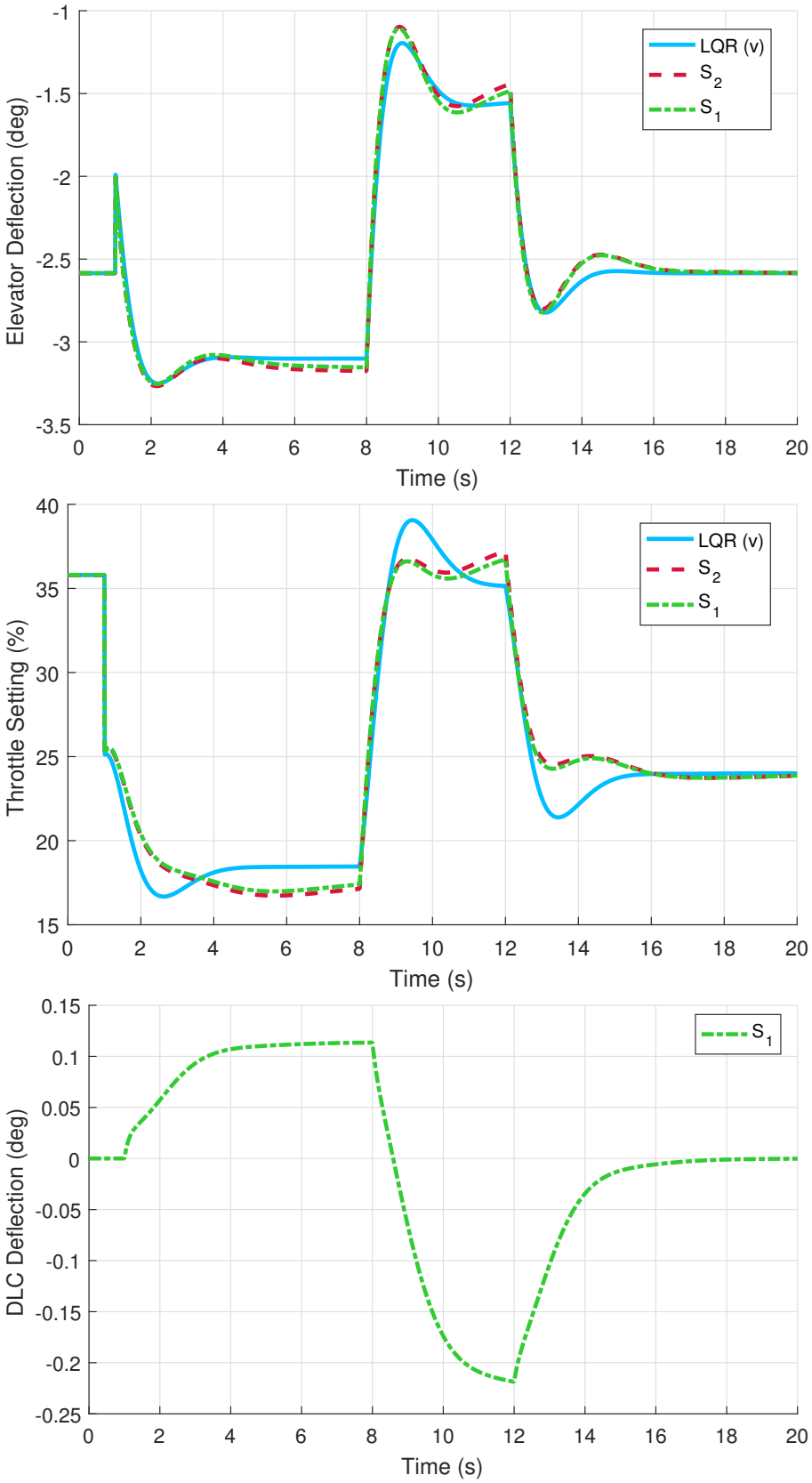

Figure 8.6: The aircraft control inputs to a glide slope tracking manoeuvre with disturbances comparing the LQR, $\boldsymbol{S}_2$ (no DLC) and $\boldsymbol{S}_1$ (DLC).

Table 8.1: The disturbances and associated time at which they were applied when studying the effect of actuator dynamics on disturbance rejection.

Disturbance	Time (s)	Values
u_d	5, 25	-1, 0
w_d	10, 20, 25	-10, 25, 0
q_d	17, 25	5, 0

8.3.3 Emphasising DLC Flap Utilisation for Disturbance Rejection

Next, we utilise the η_k^d weighting term from (8.6) to alter the emphasis on the DLC flap in the calculation of k_{dx_1}. The results, along with the weighting used, are given in Figs. 8.7 and 8.8. Several interesting points are noted. In the rejection of disturbances between $10s \leq t \leq 20s$, performance is broadly similar. Some improvement in u tracking for $\eta_k^D = 0.01$ exists. As there is no difference in actuator dynamics, this must come from the DLC flap dynamics. The disturbance during this period is in the w channel. Utilising the DLC flap more allows it to be rejected directly. With less DLC action, this disturbance must be rejected by modifying other states first, which is slower. The performance difference is quite small. At $t = 20s$, a substantial difference in performance is noticed. This is due to saturation of the elevator and throttle inputs. With more DLC action, these inputs are not saturated, allowing the disturbance to be rejected. This is a benefit of additional control authority rather than DLC dynamics.

The obvious question at this point is "Why use the DLC flap?". These simulations have shown that its inclusion results in largely similar performance (in the absence of control saturation) as the aircraft with no DLC flap, even after weighting the disturbance rejection gain to utilise the DLC flap more. The key may lie with the fact that these simulations include no actuator dynamics. Without the DLC flap, the system utilises the elevator and throttle to counteract the w_d disturbance. However, the elevator achieves this by pitching the aircraft to control u, which is able to reject w_d due to the strong coupling. The limitation here being that the aircraft state must be adjusted first, to reject the disturbance as a secondary outcome. Furthermore, using the throttle relies on the motor to produce additional thrust, which is therefore limited by the actuator dynamics of the motor which have been measured to be noticeably slower than the other actuators in Section 8.1.4. Therefore, we should include actuator dynamics to better understand the benefits of the DLC addition.

8.3.4 The Effect of Actuator Dynamics on Disturbance Rejection

We now assess the performance of the controllers with actuator dynamics present. The actuator models used in this work are discussed in Section 8.1.4. The elevator and DLC flaps are modelled with the first order servo models, and the throttle with the second order motor model. Shown in Figs. 8.9 and 8.10 are the resulting states and control inputs when tracking a glide slope with disturbances.

An immediate difference in performance is seen with the first disturbance at $t = 10s$. $\boldsymbol{S}_1$ rejects the disturbance completely and in a much more timely manner than $\boldsymbol{S}_2$. This is a clear benefit of the faster DLC actuation dynamics, as it can be seen that $\boldsymbol{S}_2$ and the LQR must make much more use of throttle action to reject the disturbance. Without the DLC flap, $\boldsymbol{S}_2$ takes 4 seconds longer to return to reference; even at this time, some overshoot exists as the aircraft is also returning to the reference height at this time. A very clear benefit of the DLC flap when actuator dynamics are present is shown. With the disturbance at $t = 20s$, it is once again shown that the addition of the DLC flap allows for larger disturbances to be totally rejected. The peak disturbance effect on u is

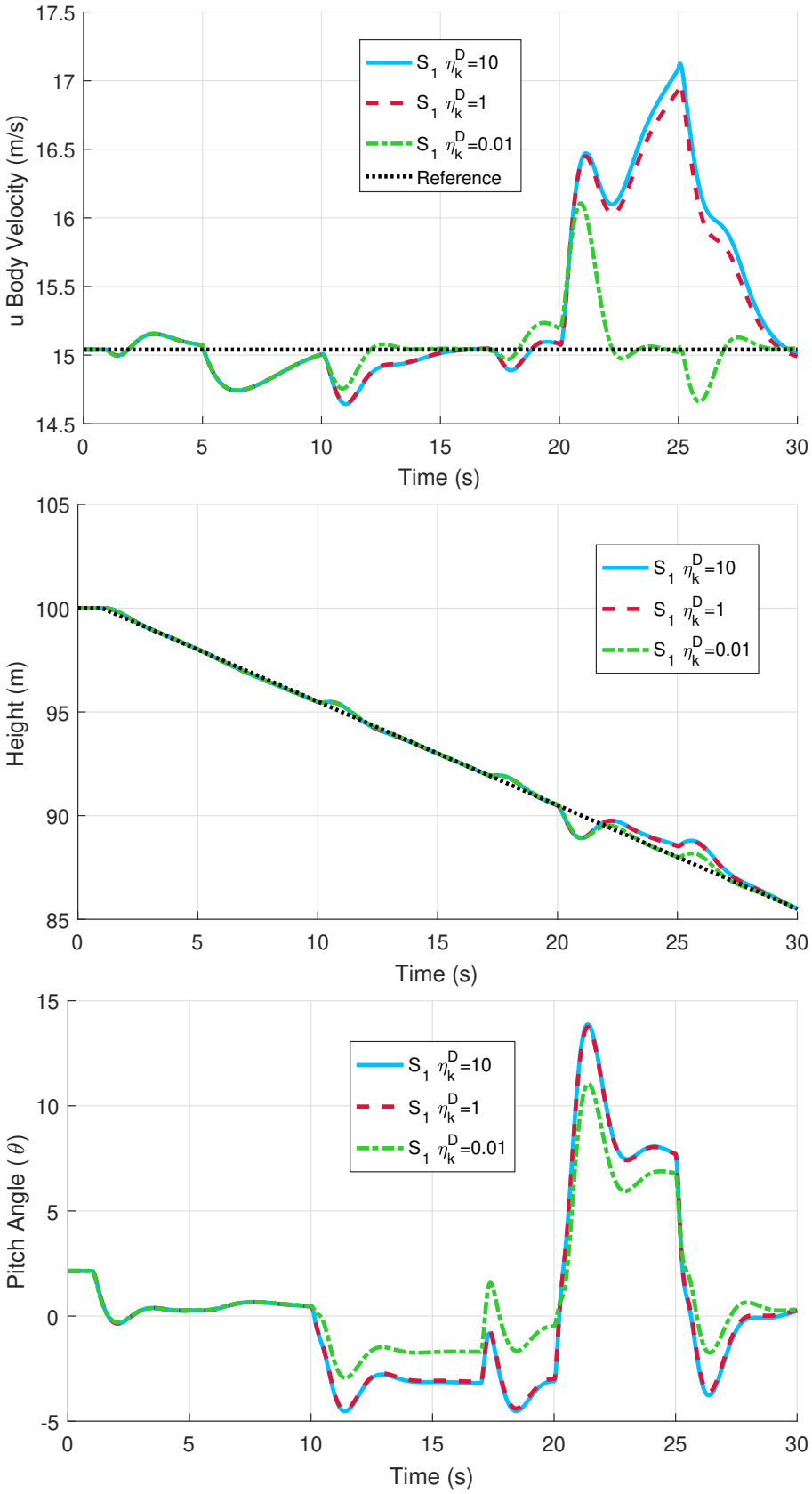

Figure 8.7: The aircraft outputs to a glide slope tracking manoeuvre with disturbances comparing varying η_k^D weightings.

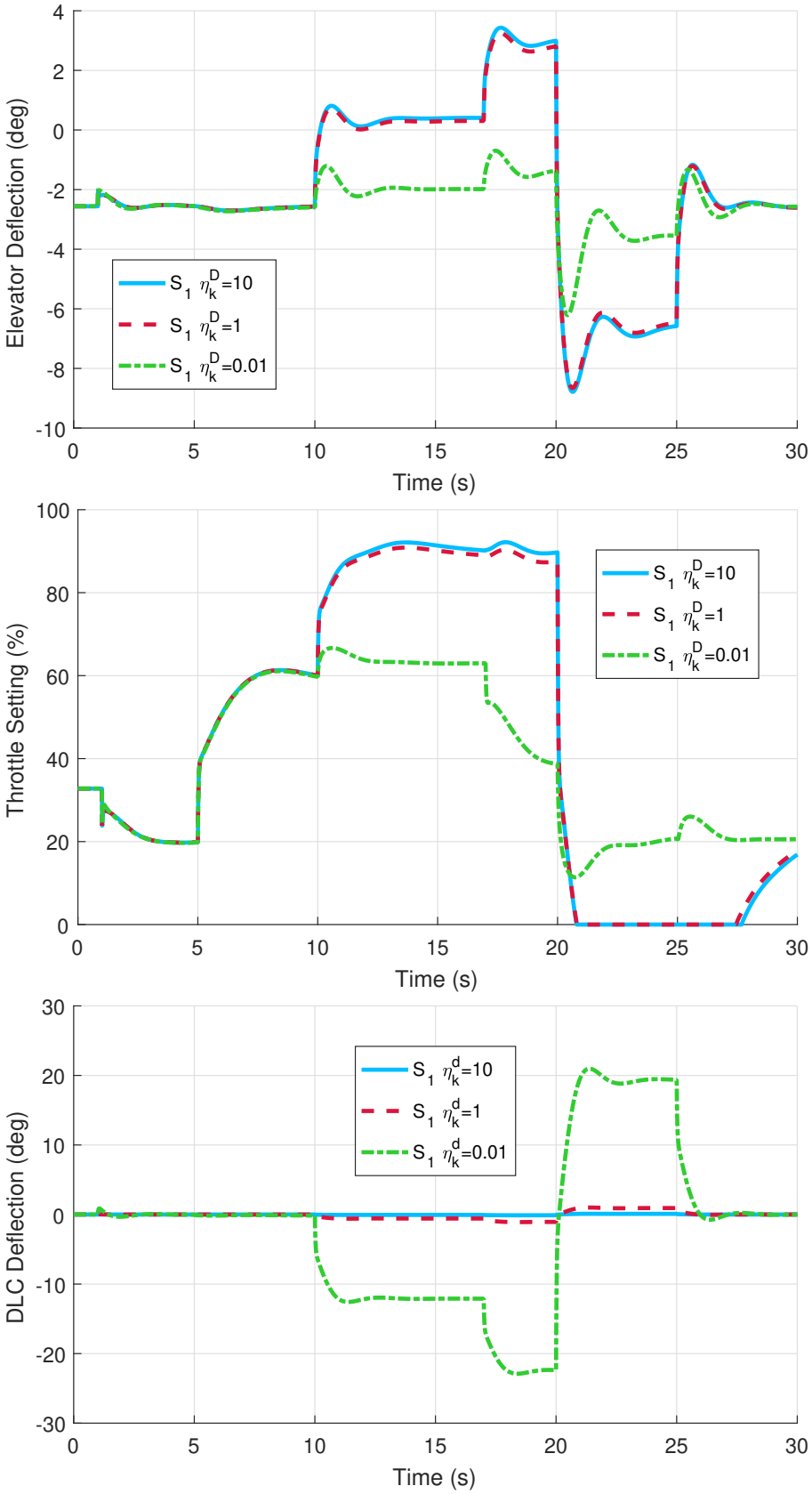

Figure 8.8: The aircraft control inputs to a glide slope tracking manoeuvre with disturbances comparing varying η_k^D weightings.

far smaller for $\boldsymbol{S}_1$, with the disturbance being completely rejected in around 1.5s. The benefits are clearly visible in both u and h. This disturbance is beyond the rejectable range for $\boldsymbol{S}_2$ (and LQR), as the throttle is completely saturated. This occurs with steady errors in both u and h. In this case the DLC adds additional control authority which is successfully leveraged to reject the disturbance in both output channels. Overall, $\boldsymbol{S}_1$ now offers significantly improved performance over $\boldsymbol{S}_2$.

An additional benefit is improved θ regulation. $\boldsymbol{S}_1$ reduces the effect of changes in θ, while maintaining the state closer to the reference in steady state. This represents far more favourable performance during glide slope tracking and implies better performance during landing also.

These simulations have demonstrated very clearly the benefit which $\boldsymbol{S}_1$ offers over $\boldsymbol{S}_2$ and particularly the baseline LQR. $\boldsymbol{S}_1$ system is able to reject a larger range of disturbances in a more timely manner than $\boldsymbol{S}_2$ while also maintaining the important pitch angle state closer to the trim condition. While it is expected that an additional control surface should improve the range of rejectable disturbances, it has been demonstrated that an improved rate of disturbance rejection also exists for $\boldsymbol{S}_1$. This was shown to be a result of the faster actuator dynamics offered by the DLC flap over the motor, as without actuator dynamics the performance difference between $\boldsymbol{S}_1$ and $\boldsymbol{S}_2$ designs was negligible. It was also shown that the weighted pseudoinverse calculation of the disturbance rejection gain functioned as intended and was wholly fit for purpose: it allows for control over the distribution of control efforts needed to reject a disturbance, while resulting in near identical output performance. This demonstrated that the weighting factor only affected how the output performance was achieved, rather than the actual performance. This is a crucial advancement in the design of over-actuated DOBC methods.

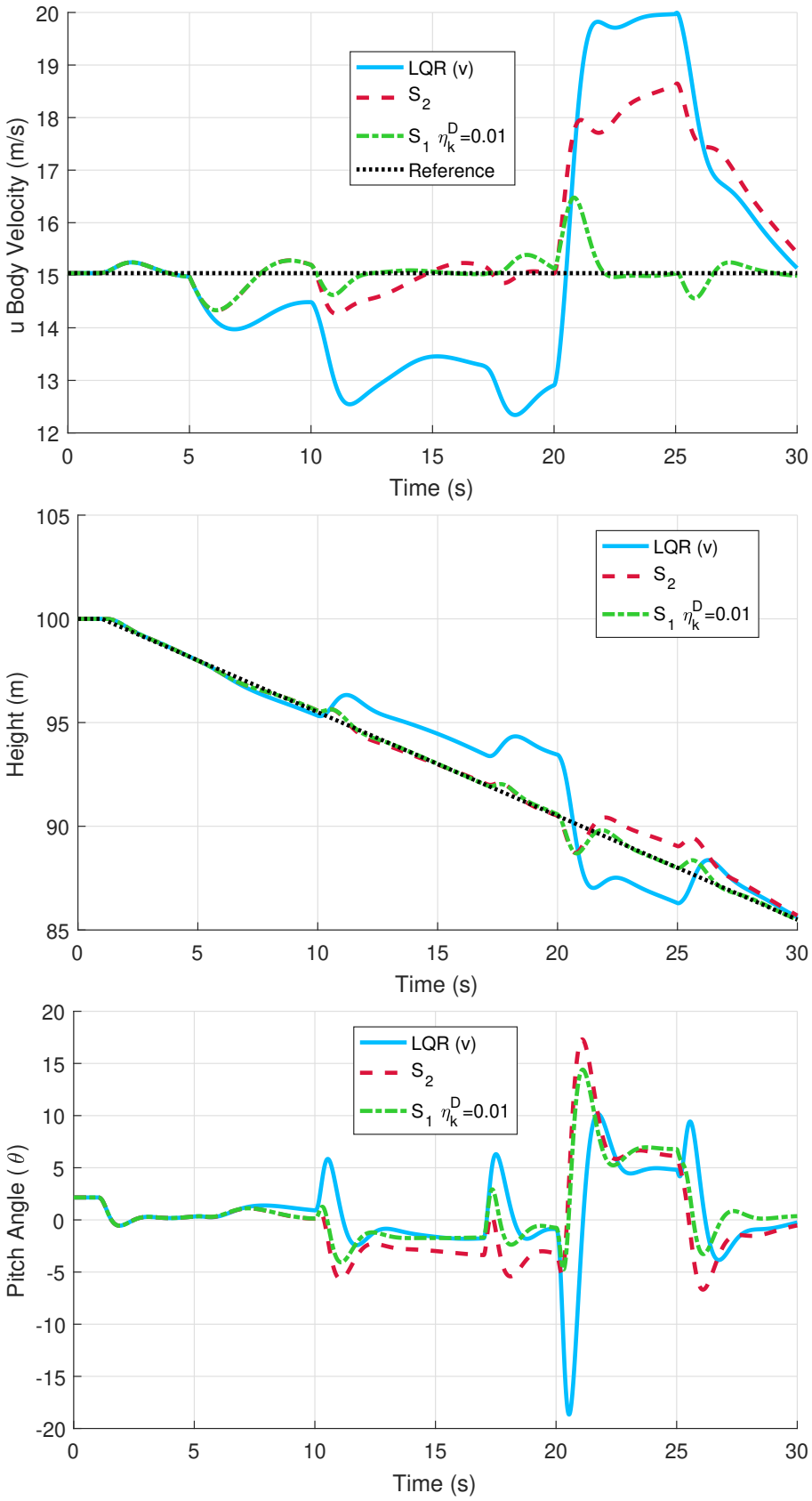

Figure 8.9: Reference tracking performance of the three controllers to a glide slope with disturbances.

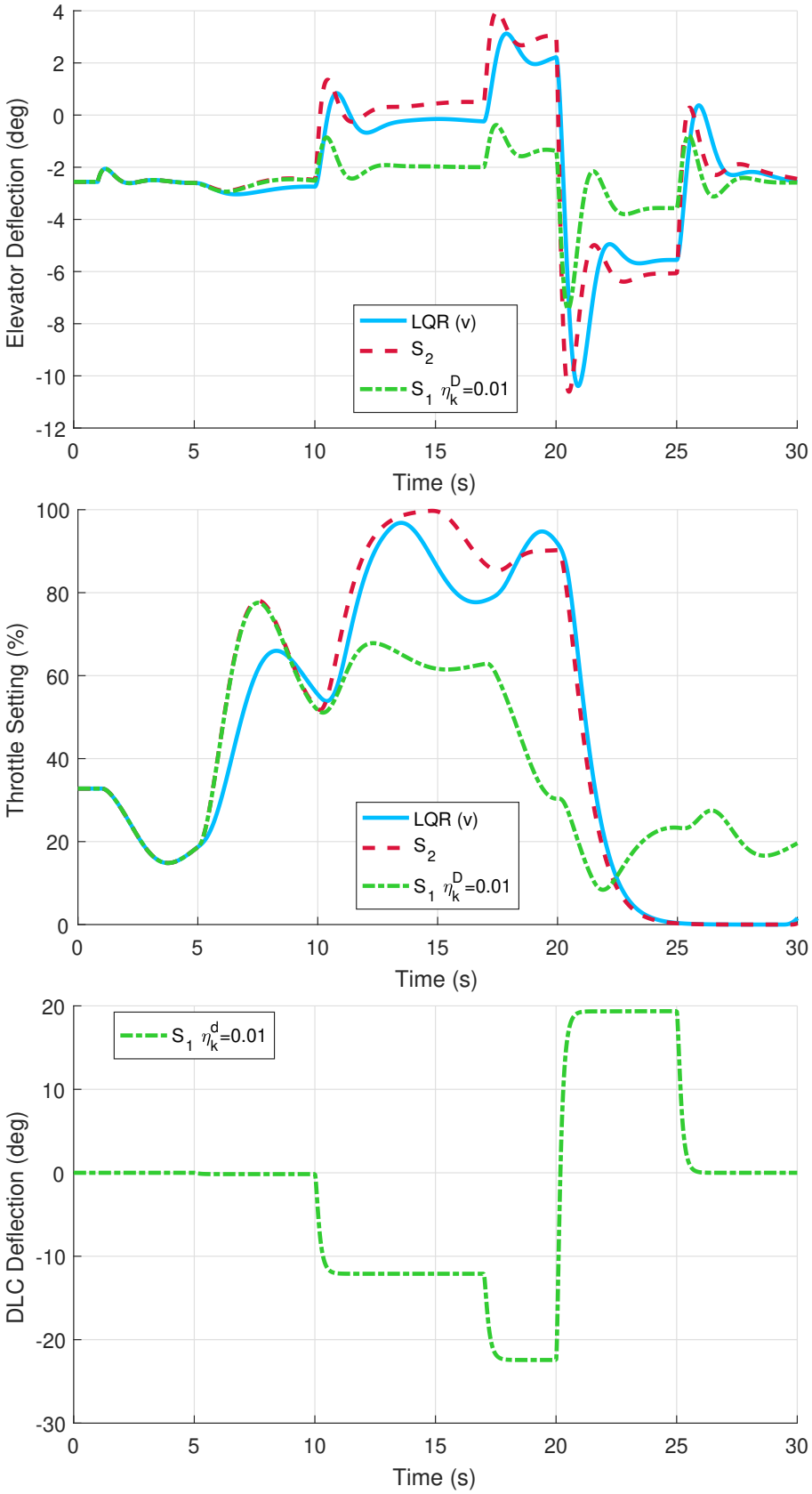

Figure 8.10: Control surface performance of the three controllers to a glide slope with disturbances.

8.4 X-Plane Simulations

To validate the performance results of $\boldsymbol{S}_1$ in numerical simulation, additional simulations using the X-Plane environment were conducted. These simulations aimed to verify the results shown in terms of accuracy as well as applicability to a more realistic plant model, with unmodelled non-linear dynamics. Within this section, all numerical results are indicated by "[N]" in figures, while X-Plane results are denoted by "[X]".

8.4.1 Simulation Comparison

First, to study the quality of the state space model subjected to control inputs, we compare the same scenario numerical and X-Plane environments. Figs. 8.11 and 8.12 show the resulting state and control inputs to a glide slope tracking manoeuvre under LQR control. Within the simulation, two adjustments are also made to the reference u command to excite the aircraft dynamics and allow for a good comparison.

The overall responses of the two different simulation environments are very similar, with the results being highly comparable. A more subtle point is to notice that in almost all instances the numerical simulation seems to have slightly faster dynamics, as the reference commands are reached more quickly. This suggests that the advantages of $\boldsymbol{S}_1$ displayed in numerical simulation may become more pronounced in the X-Plane environment. These results also serve as further validation of the system identification process, with the model yielding very good LQR performance, comparable to that of the ideal numerical simulation.

8.4.2 Glide Slope Tracking with Disturbances

The simulation conducted in Section 8.3.4 is reconstructed here, using similar disturbances as outlined in Table 8.2. The resulting states are given in Fig. 8.13 with the associated inputs in Fig. 8.14.

We see that the behaviour of the controllers is repeated in the X-Plane simulation, with $\boldsymbol{S}_1$ offering the fastest disturbance rejection. Furthermore, in cases where the throttle is saturated for the LQR and $\boldsymbol{S}_2$ controllers, the additional DLC flap allows $\boldsymbol{S}_1$ to track the references much more accurately. This is most noticeable in the large disparity between $\boldsymbol{S}_1$ throttle setting and the remaining controllers in Fig. 8.14. Another key feature here is the tighter regulation of pitch angle, θ. With $\boldsymbol{S}_1$ disturbance rejection active,the pitch angle is maintained much closer to the trim condition, as well as suffering far smaller magnitudes of deflection at the points where the disturbances are added.

Another key takeaway from these results is the excellent performance of both $\boldsymbol{S}_1$ and $\boldsymbol{S}_2$ disturbance observer based control schemes in general. This indicates that the model utilised for control design captures the steady state (as indicated in Section 8.4.1) and dynamic responses very well.

An additional feature of the X-Plane environment over the state space model is more realistic disturbance sources. The step disturbances studied so far offer good insight into the performance of the controller, but do not represent a truly realistic environment. In outdoor operation, step disturbances applied at discrete intervals directly on the disturbance channels are unlikely. To assess performance under more realistic circumstances, we must consider stochastic wind disturbances. The drawback of such comparisons is that direct comparison of responses is not sensible, as the disturbances will not be equal.

8.4.3 Glide Slope Tracking with Wind Gusts

To account for the stochastic nature of these disturbances, simulations were conducted for a longer period of time to allow for study of the average responses. Shown in Figs. 8.15 and 8.16 are the associated state and control responses for the three controller during

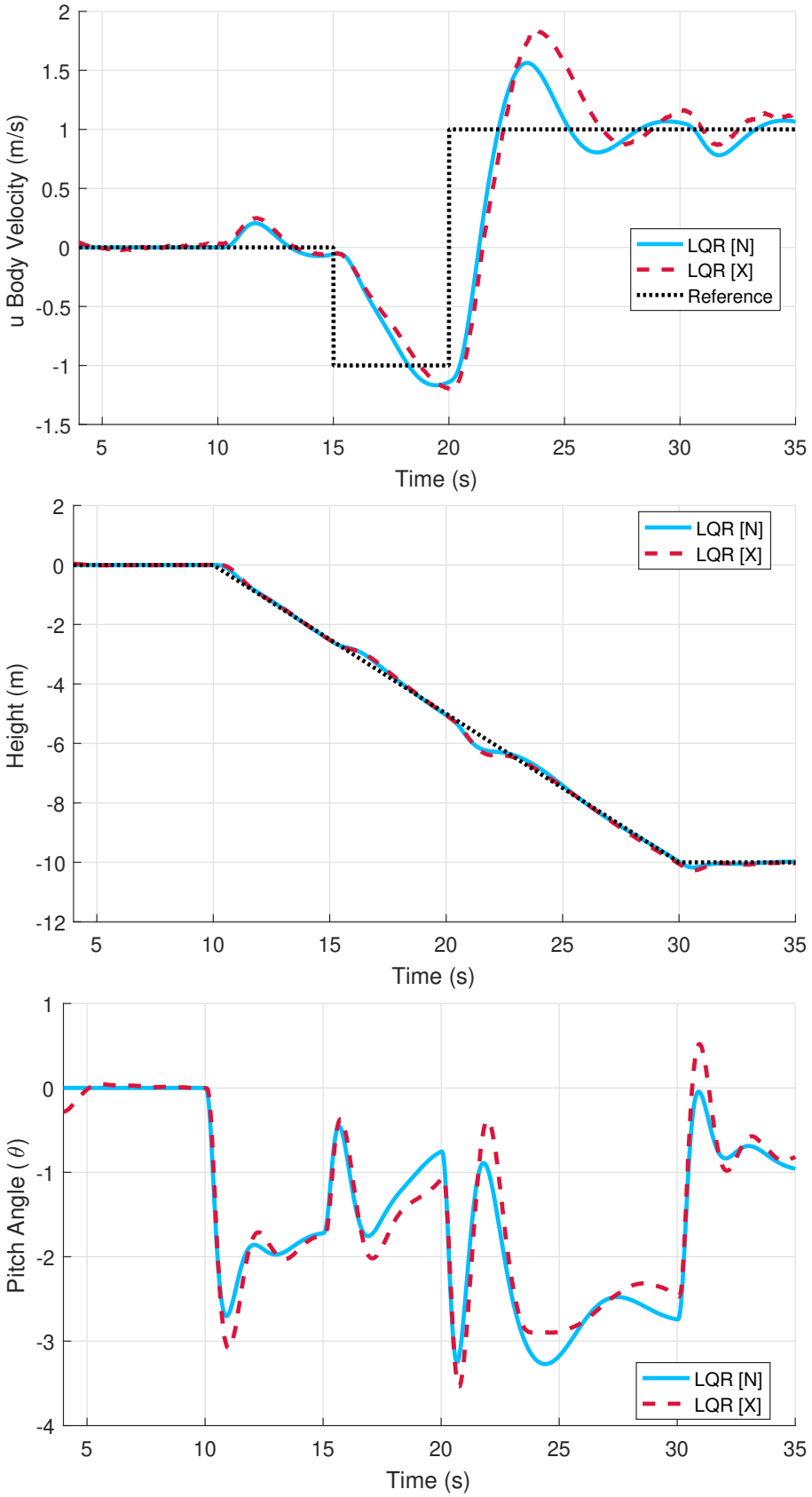

Figure 8.11: The resulting state comparisons of numerical modelling simulation compared to X-Plane.

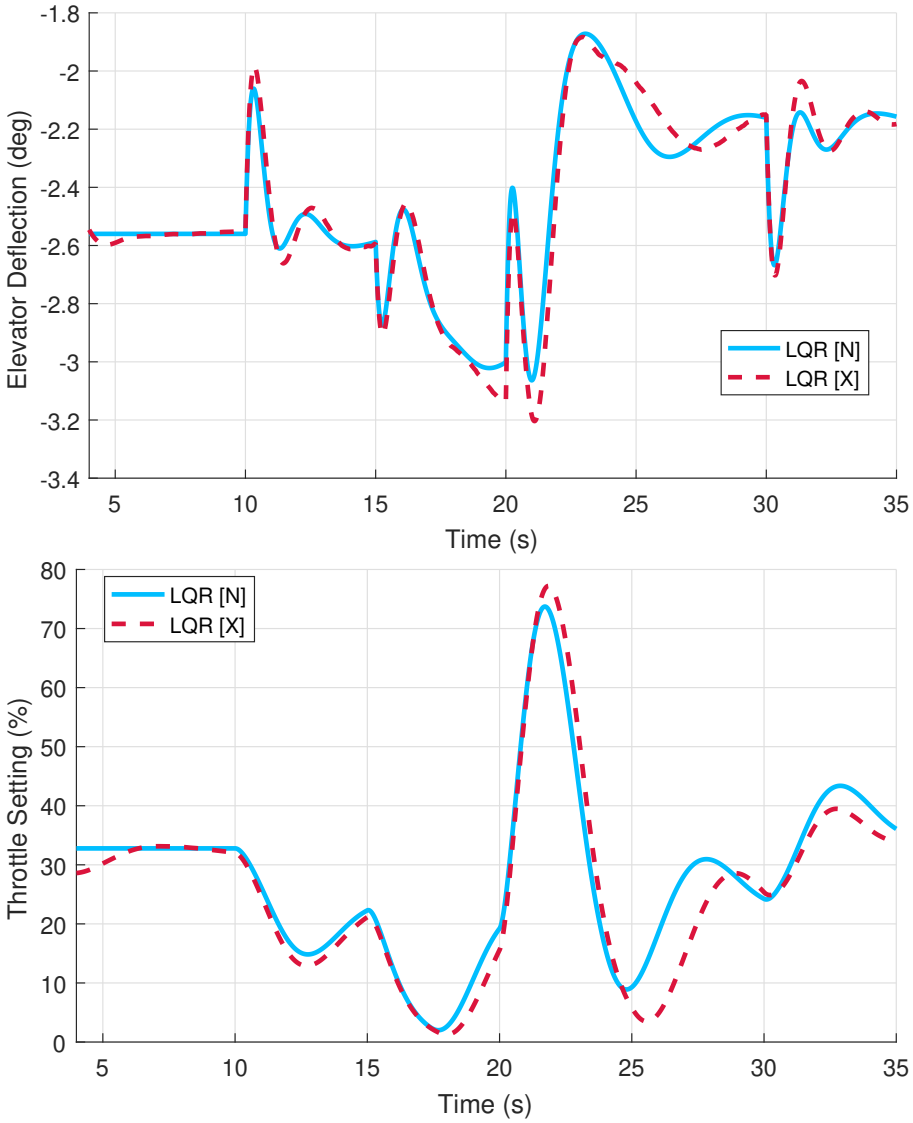

Figure 8.12: The resulting control action comparisons of numerical modelling simulation compared to X-Plane.

a 120s descent, under wind gust disturbances generated by X-Plane. Due to the noisy nature of the data, some statistical analysis was performed to compare the results. Two assessment criteria are used. First, the mean absolute error defined (for u) as

$$u_m = \frac{1}{n}\sum_{i=1}^{n}\left(|u_r(i) - u(i)|\right),$$

where n is the number of data points, $u_r(i)$ and $u(i)$ are the reference and measured values of u at sample i. The absolute value is taken to ensure that errors which oscillate about the reference values are detected. The mean absolute error gives a good measure of how closely a reference command is followed by a control scheme. To quantify the spread of the error, the variance is also considered, which is defined (for u) as

$$u_v = \frac{1}{n}\sum_{i=1}^{n}\left(u_r(i) - u(i)\right)^2,$$

where the variance highlights the spread of values around the mean. This is summarised in Table 8.3. Some interesting points are demonstrated in the results. First, we notice

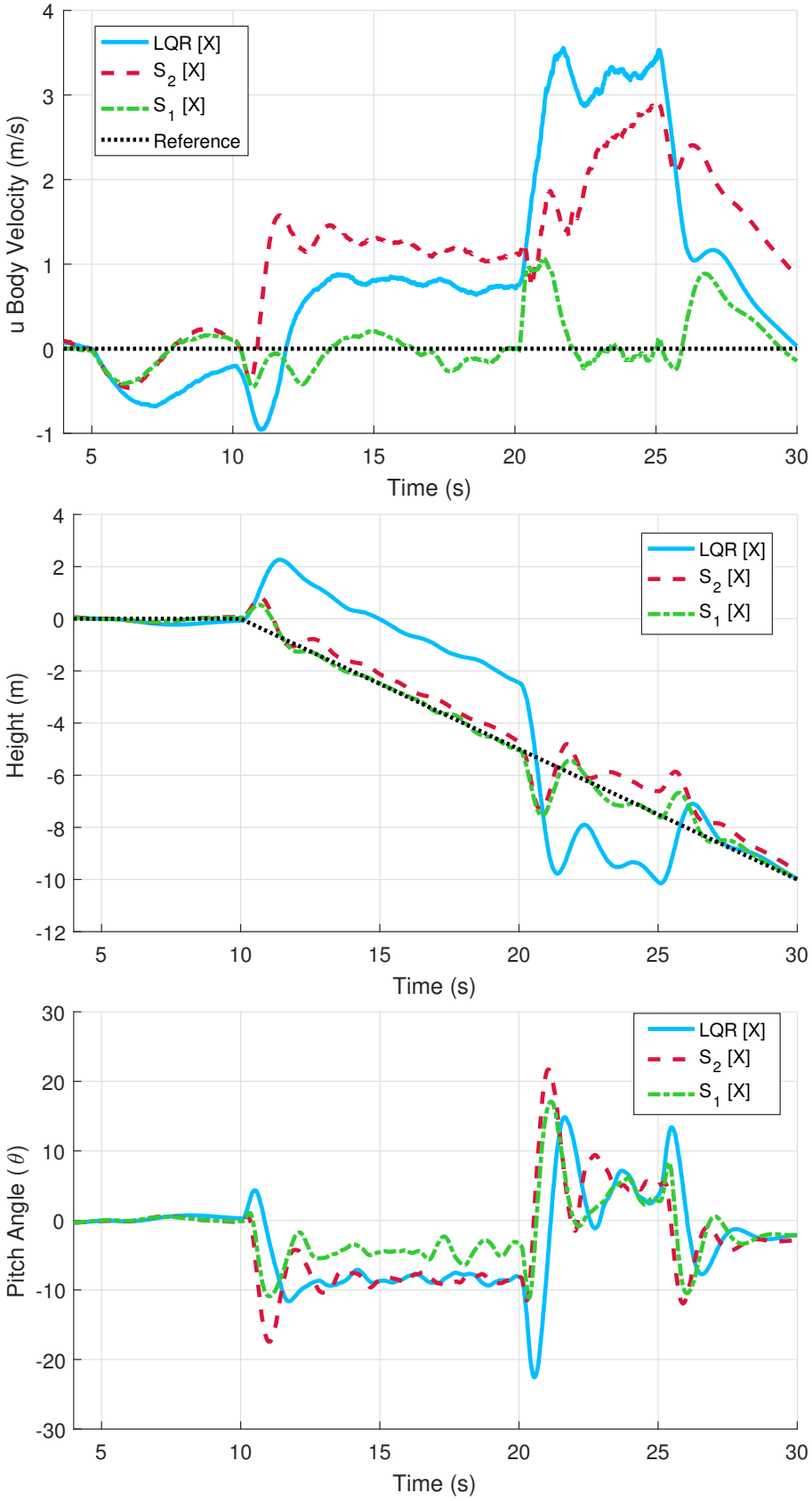

Figure 8.13: The recorded X-Plane state data for three controllers during a glide slope tracking manoeuvre with disturbances.

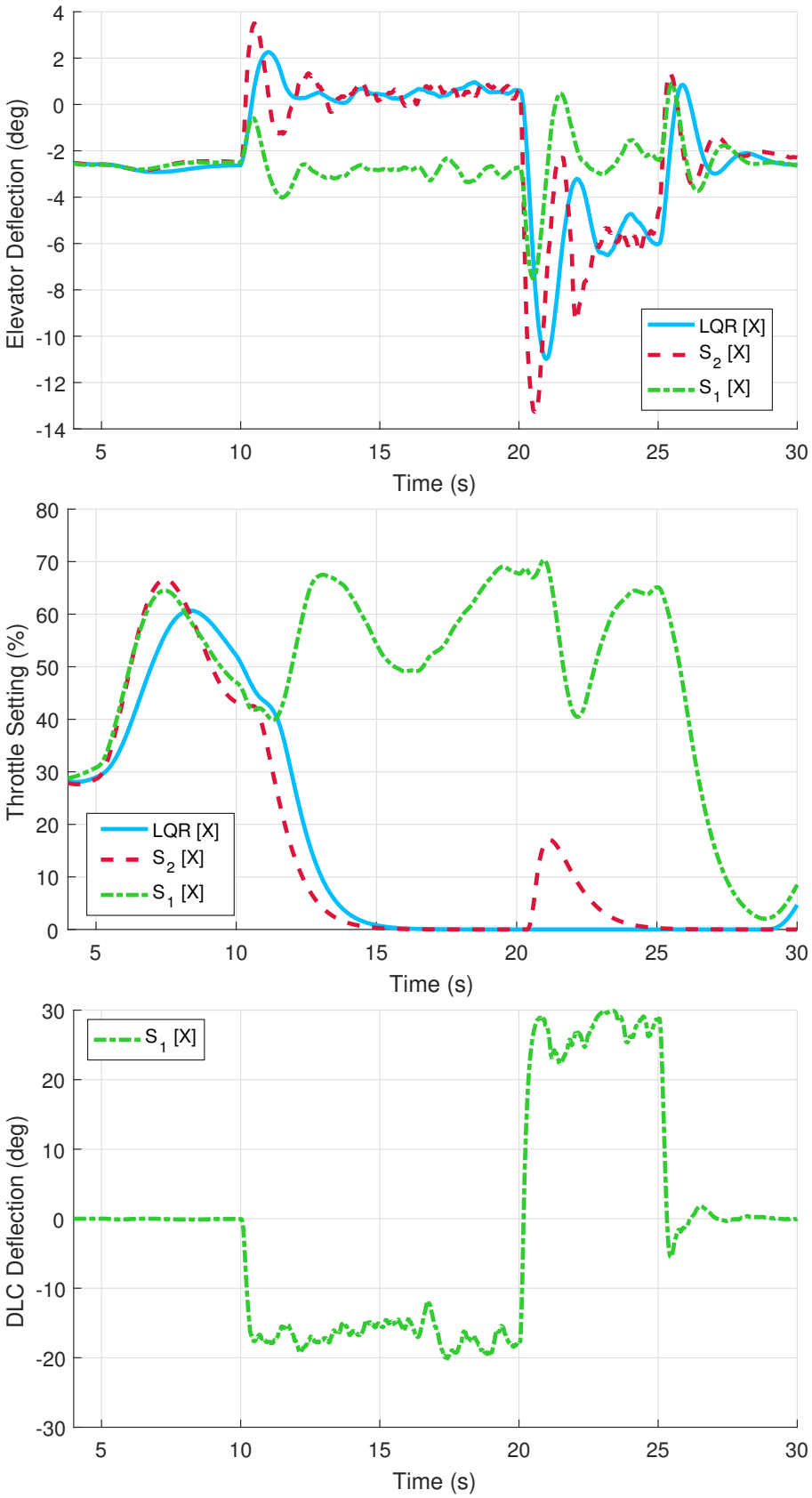

Figure 8.14: The X-Plane actuator states for three controllers during a glide slope tracking manoeuvre with disturbances.

Table 8.2: The disturbances and associated time at which they were applied when studying controller performance within X-Plane.

Disturbance	Time (s)	Values
u_d	5, 25	-1, 0
w_d	10, 20, 25	-20, 35, 0
q_d	17, 25	1, 0

Table 8.3: A comparison of the statistical performance analysis to the three controller types tracking a glide slope reference in X-Plane while subjected to stochastic gust disturbances.

	Mean Error			Variance		
	LQR	$\boldsymbol{S}_2$	$\boldsymbol{S}_1$	LQR	$\boldsymbol{S}_2$	$\boldsymbol{S}_1$
$u\ (m/s)$	1.57	1.89	1.04	0.97	1.48	0.88
$h\ (m)$	2.57	0.71	0.47	100.8	102.8	102.7
$\theta\ (deg)$	2.1	2.1	2.1	0.0030	0.0024	0.0015

that $\boldsymbol{S}_2$ offers the largest mean error in u tracking, while $\boldsymbol{S}_1$ offers the smallest; variance has similar characteristics. This appears to be a result of throttle saturation for $\boldsymbol{S}_2$. This is supported by the significantly lower mean error in h for $\boldsymbol{S}_2$ compared to the LQR.

For pitch angle, all three controllers have the same mean error. This is due to the change in aircraft attitude needed to track the glide slope reference; the magnitude of this change masks any information about the differences in the mean error. However, looking at the variance for pitch, we find further confirmation of previous data which has indicated that $\boldsymbol{S}_1$ offers far tighter regulation of the pitch angle.

The overall summary of the results is that $\boldsymbol{S}_2$ has resulted in slightly worse u tracking and regulation than the LQR, while yielding far better h tracking. $\boldsymbol{S}_2$ also results in more variance in both outputs being tracked, although offering some improvement in pitch angle variance. $\boldsymbol{S}_1$ offers the best mean error for both output variables, with less variance in u. For h tracking, $\boldsymbol{S}_1$ and $\boldsymbol{S}_2$ both offer slightly worse variance despite a lower mean error. This suggests that the additional variance is a result of the additional disturbance rejection action and is necessary for improved reference tracking. Overall, variance in h is very similar for all three controllers. For θ regulation, any difference in mean error is small enough to be negligible. In terms of variance however, $\boldsymbol{S}_2$ offers an improvement over the LQR, which is bettered further by $\boldsymbol{S}_1$.

The results have provided confirmation of the enhanced performance of $\boldsymbol{S}_1$ in two ways. First, performance has been validated with a realistic disturbance source. This proves that the observer is able to estimate disturbances in this realistic situation, which is achieved with a linear model of the non-linear aircraft dynamics. Additionally, the statistical analysis has demonstrated well the additional DLC benefit given by $\boldsymbol{S}_1$ over $\boldsymbol{S}_2$, with less error in both output variables. Additionally, $\boldsymbol{S}_1$ provides similar or less variance in the output variables, as well as less variance in the pitch angle state. This confirms numerically what has been demonstrated with previous simulations.

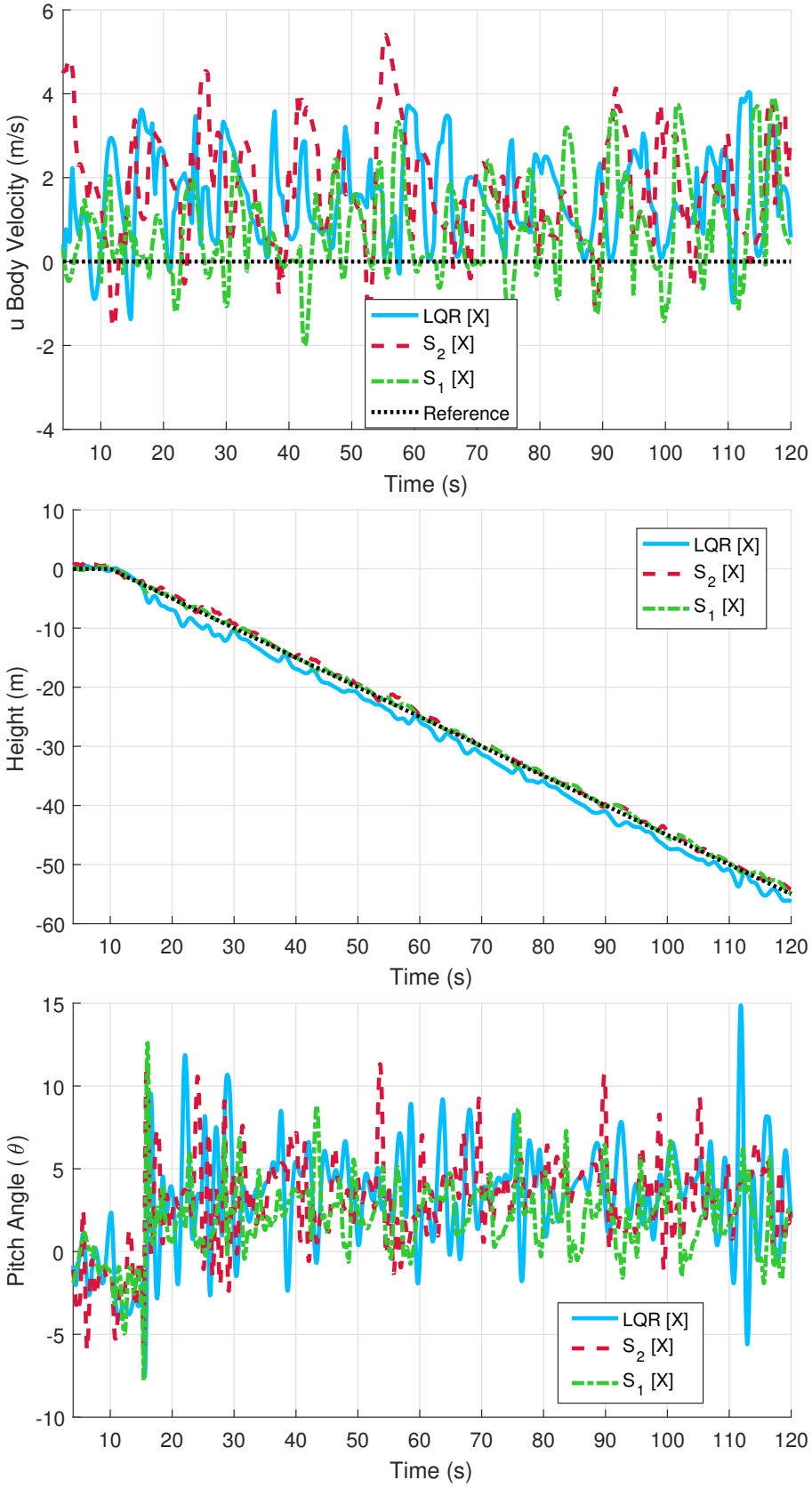

Figure 8.15: The recorded X-Plane states during an extended glide slope tracking manoeuvre with X-Plane gust disturbances active.

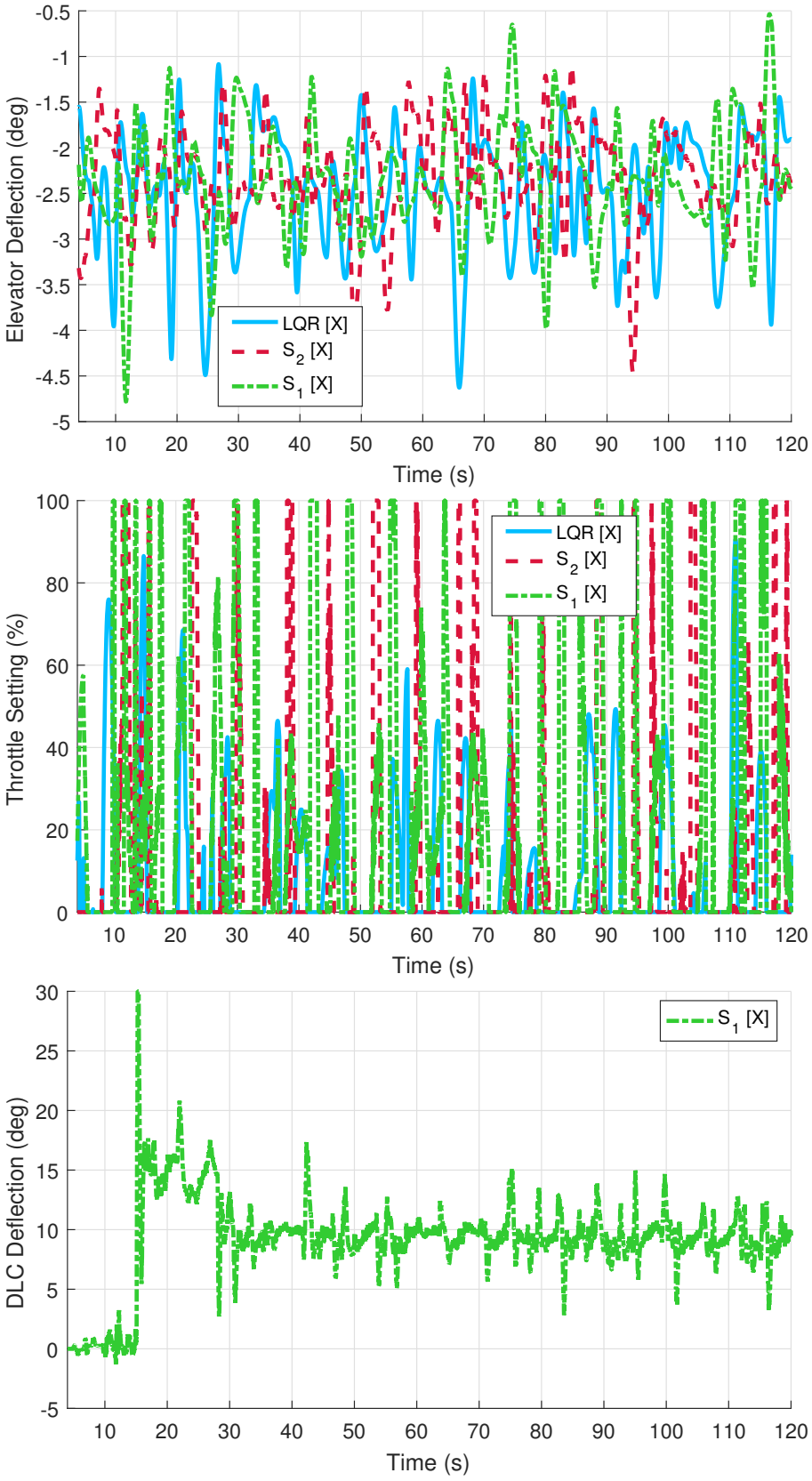

Figure 8.16: The X-Plane actuator states during an extended glide slope tracking manoeuvre with X-Plane gust disturbances active.

8.5 Conclusions

The work in this chapter has several important developments. A development on the previous reference tracking LQR methodology was presented, which allowed the system to accurately track non-continuous disturbances. This was intended to provide glide slope tracking for the aircraft in a landing scenario. A complication was described in comparing the standard (given by $\boldsymbol{S}_2$ in (8.4)) and DLC (given by $\boldsymbol{S}_1$ in (8.3)) enabled aircraft, as this would require separate baseline LQR controllers to be designed. This would then make fair and reasonable comparison of performance more difficult. It was decided that the same baseline LQR would be used for all three cases, with the DLC based disturbance observer being the only component of control with the ability to utilise the DLC flap.

The proposed DLC based disturbance observer controller has presented the over actuated case for a linear DOBC method. In Section 8.2.3, the issue with the previous method of calculating disturbance rejection gain for an over-actuated linear model was presented. By adapting methods from control allocation, it was demonstrated that the pseudoinverse method could be used to calculate the gain in the over actuated case. Further, using the weighted pseudoinverse allowed for selection of the resulting disturbance compensation gain. Simulations demonstrated that the weighting matrix resulted in the same response to disturbances using different control configurations, which is a key point with this method. It was also demonstrated that for the basic linear numerical simulation, the addition of the DLC flap provided minimal benefit to the system.

To realise the benefits of the DLC addition, it was necessary to include actuator dynamics in the model. The slow motor dynamics (compared to the servo actuators) limited the response rate of the $\boldsymbol{S}_2$ controller in terms of disturbance rejection. It was here that $\boldsymbol{S}_1$ was able to provide clear and significant benefits over $\boldsymbol{S}_2$ and the LQR, utilising the fast DLC dynamics to offer not only faster disturbance rejection but also increasing the magnitude of disturbances which could be rejected by the system. It was also shown in several simulations that the addition of the DLC flap allowed for tighter regulation of the pitch angle around the reference value in the presence of disturbances, which could have benefits during landing. The fact that the addition of the DLC flap yields better and faster disturbance rejection *and* improved pitch angle regulation show clearly that it has potential for improving landing robustness and safety for small UAVs.

The results demonstrated with numerical simulations were then validated with X-Plane simulations. The identified linear model was shown to match very well with the X-Plane simulation. It was then shown that the benefits which were demonstrated numerically transferred well to X-Plane, with $\boldsymbol{S}_1$ yielding very good performance. A final validation simulation was conducted using X-Plane generated stochastic disturbances. This simulation demonstrated that the designed observers were able to accurately estimate the disturbances even when subjected to entirely stochastic disturbances. Through statistical analysis of the resulting performance during an extended glide slope tracking manoeuvre, the benefits which had been identified previously were demonstrated clearly and numerically.

Overall, this chapter has presented a working solution to the calculation of disturbance rejection gain for a linear disturbance observer applied to an over actuated plant. It was shown that the weighted pseudoinverse allowed for selection of the control action used to reject a given disturbance. The end result, $\boldsymbol{S}_1$, was a disturbance observer which utilised the fast DLC actuator dynamics to improve performance over a non-DLC aircraft in glide slope tracking with disturbances. The method offers a means to improve landing safety and robustness for small UAVs, which are commonly fitted with flaps suitable for the application of the DLC technique. The presented results are likely to be more significant the larger the aircraft it is applied to, as the pitching dynamics tend to become slower, giving the additional DLC flap further benefit.

Chapter 9

Conclusions

The main contributions of this thesis are discussed here briefly, along with some additional discussion on possible future directions for this work.

9.1 Summary

This thesis outlined some of the difficulties faced by small fixed wing UAVs when operating outdoors. Through literature, the reasons for the sensitivity of such vehicles to external disturbances were identified. Operational considerations were outlined which would limit the direct application of optimal control techniques.

It was determined that the Disturbance Observer Based Control (DOBC) approach was a good candidate the reduce the effect of disturbances acting on these aircraft. Additionally, some limitations of previously developed methods were identified. In each case, a solution was proposed, studied and tested.

First, the effect of control saturation on the disturbance observer dynamics were studied. No previous work had solved the windup issue for disturbance observers in the presence of control saturation. It was also discussed in the literature review that, due to the unique characteristics of small UAVs, these aircraft were more likely to undergo control saturation in flight. An anti-windup compensator was designed based on the principles of classical anti-windup methods in control theory. Additionally, stability analysis of the proposed solution was conducted which proved that the proposed method accounted for the effect of windup on the estimation error dynamics. Through simulation, the potential risks to the aircraft were shown. It was also shown that the proposed method alleviated the windup effect entirely. With many safety considerations, a flight test was planned and conducted where the proposed solution was also shown to function as intended, entirely alleviating the effect of windup.

Continuing the study on the effect of actuator performance constraints on disturbance observers, actuator dynamics were considered. In control design, it is often assumed that the demanded action from a control scheme is equivalent to the applied action. Chapter 6 showed that, as the disturbance estimation dynamics of a disturbance observer become faster, the mismatch between demanded and applied control action could lead to instability within the observer. This places an upper bound on the disturbance observer gain which can be applied. Generally, a higher observer gain is preferable as it is correlated with disturbance rejection performance. By developing the disturbance observer to explicitly include actuator dynamics, this upper bound could be increased substantially (simulations demonstrated an increase by a factor of 16 with no degradation in performance). The resulting actuator augmented disturbance observer was able to greatly improve disturbance rejection performance compared to a baseline DOBC design, in both simulation and flight testing. This result is more notable considering the actuator bandwidth on a small UAV

is of an order of magnitude higher than full scale, hydraulically actuated aircraft (or any plant with low bandwidth actuators). The improvement in performance demonstrated on a small UAV would likely be even larger on such systems.

An investigation into the applicability of Direct Lift Control (DLC) was also conducted. It was hypothesised that the high bandwidth of small UAV actuators could be combined with DLC methods to offer improved disturbance rejection. In control design, a glide slope tracking problem was investigated, which required control of two output states. The inclusion of an additional control surface meant that the classical means of determining a disturbance attenuation gain could not be solved, as it required the inverse of a non-square system. A solution was proposed, by adapting methods from control allocation theory. By the nature of this system, a given disturbance could be rejected by a large set of control configurations. An additional development then allowed for designer selection on how disturbance rejection action should be allocated. Due to the slow response of the aircraft's motor, favouring the DLC control input allowed for improved disturbance rejection performance. This result was verified in an industry standard simulation environment.

During initial flight testing phases, a violent aircraft structural oscillation was identified. This oscillation limited progress on flight testing as it placed the aircraft at risk. An investigation was conducted which determined this aircraft oscillation was being excited by the various control systems. Due to the construction methods used for small UAVs, it is likely this is a feature not limited to the aircraft used for this thesis. For that reason, a solution which was generic enough to be widely applicable was needed. In literature, advanced methods for controlling such modes all required additional sensors or control surfaces as well as detailed modelling, so were not applicable. Older literature was found which presented the notch filter as a viable alternative. A basic model of the oscillations was also found in literature regarding missile dynamics. Through frequency domain analysis, the effect of this oscillation on the aircraft was studied. This analysis also indicated that the notch filter was a viable solution. A flight test program was planned. Through this flight test program, it was shown that the notch filter alleviated the effect of the structural oscillation and allowed for the operation of highly tuned control schemes being developed. The notch filter was also shown to have no noticeable impact on the performance of the controllers under investigation. Furthermore, the notch filter is simple enough that it could be applied to any small UAV suffering from this problem, requiring only the frequency of the oscillation for good performance.

As a conclusion for the entire thesis, it can be said that DOBC has successfully been applied to flight control of a small fixed wing UAV. The inclusion of DOBC methods were able to improve the performance of a baseline feedback controller. The novel contributions of this thesis have all had their roots in physical application and flight testing. Features such as actuator saturation and dynamics are often overlooked in literature and simulation, where their effects are assumed negligible. The structural oscillation and proposed solution would certainly not have been a feature of even very high fidelity simulations. The contributions herein facilitate the transition from theory to application.

9.2 Discussions on Future Work

During development of the ADOBC method in Chapter 6, it was shown that proper selection of the observer gain with respect to actuator position estimation was vital. The chosen gain had a clear impact on the disturbance estimation performance. A more rigorous method of selecting this gain would be beneficial. Although good results were obtained with manual tuning, this required time and effort. Additionally, ideal selection of this gain is subjective. As discussed in this work, the perceived ideal gain may shift depending on performance. There is potential for gain selection by studying the observer dynamics themselves. Theoretical methods such as pole placement may offer a more rigorous method of ensuring good dynamics separation of the two observers.

Considering the Actuator Augmented Disturbance Observer Based Control (ADOBC), it may be beneficial to investigate simpler means of reducing the destabilising effect of an observer without actuator dynamics explicitly considered. Some initial simulations studying saturation of the disturbance rejection action (e.g. limiting DOBC disturbance rejection action to 10% of the total control action available) have suggested that this may be a viable interim solution. This may offer a solution in cases where actuator dynamics are unknown or cannot be modelled.

A significant number of questions remain unanswered in regard to the structural oscillation problem. While the analysis conducted using missile flexing dynamics proved useful, this is clearly not the correct model. As discussed in Chapter 7, the witnessed oscillation is quite different from most classical problems in this area. A more thorough investigation of this oscillation to better understand it would be beneficial. Ground testing of the X8 structure should be conducted to determine if there are any corresponding natural modes in the detected frequency range. This would aid further investigations. Some study into the effect of actuators on this mode would also be beneficial. Using different servo actuators is easily achieved on the aircraft; choosing these to have different dynamics than the current servos would yield additional insight into the oscillation. It would also aid discussions on this topic if such oscillations could be identified in other small UAVs, as this might be a new and unexplored problem unique to this class of aircraft.

It was shown that the notch filter, when appropriately designed, was able to reduce the oscillation effect sufficiently for normal flight to resume. This solution was a good fit for the problem at hand, within the given time scale. There are many more options in this area. A more detailed investigation should be conducted into the performance effects of the notch filter. Comparison with some different methods of oscillation suppression would be very beneficial. On the design of the notch filter itself, there is potential for additional work. The filter used in this work was only implemented after numerous flight tests to identify the oscillation frequency. Given the simplicity in tuning the filter, it is very feasible that an active method could be developed to automatically tune this filter. This would allow the method to be deployed widely, only being activated and tuned when an aircraft requires it. This could improve flight safety of small UAVs in general.

Due to time constraints, it was not possible to conduct flight testing of the over actuated disturbance observer designed for the DLC configuration. The method demonstrated very favourable performance in simulation; other chapters demonstrated that the simulation results translated very well to flight test performance. However, as with the structural oscillation, it has been demonstrated herein that the numerical simulations cannot account for all dynamics. Flight testing of the proposed method would greatly improve the strength of the conclusions.

With more time, a flight test program would have been conducted to investigate the performance in landing scenarios. It is hoped that these flight tests would clearly demonstrate the performance benefit of DLC methods for small UAVs. Ideally, an improvement in landing accuracy and consistency would be demonstrated. Of arguably greater im-

portance, it might be possible to demonstrate a wider range of suitable flight conditions. Given the additional disturbance rejection capability and improved rejection performance, this is a reasonable outcome to expect. This could have benefits in many areas of UAV operations. Particularly, the safe deployment of search and rescue UAVs, which often operate in poor conditions, could be more easily obtained. Given the prevalence of servo actuated flaps on small UAVs, this method could see wide adoption if it was shown to yield tangible benefits.

An additional topic worthy of future consideration is the weighted pseudoinverse control allocation method used for the DLC controller. The chosen allocation method is one of the simpler methods, only allowing for control allocation which is precomputed. There exists a plethora of more advanced allocation methods for this topic. One of the most interesting options involve online optimisation methods which consider actuator saturation. It was shown many times in Chapter 8 that the additional DLC surface allows for the rejection of much larger disturbances without control saturation. It is therefore implied that through proper design of the allocation method, control saturation effects could be alleviated by the additional DLC flap. For example, if the control saturation term could be recomputed to act as a disturbance on the system, a control allocation method which alleviates this disturbance may be available. This would have wide implications for general small UAV flight control, as saturation is an ever present risk.

Some additional problems must also be overcome before this system is ready for flight testing. The most obvious of these is the sensory requirements of the DLC method. A means of measuring or observing the angle of attack is needed to obtain all states used in the current controller. An alternative for initial studies would be the development of a simpler model and control system, using only currently available sensors. Making use of the accelerometers aboard the aircraft would allow for a simpler implementation of the DLC method for vertical disturbance rejection. However this design would be more suited to rejection of gust accelerations rather than positional errors, as studied in this work. Such a method would still be expected to yield improved tracking performance as the effect of disturbances are still reduced.

Bibliography

[1] Thomas J Mueller and James D DeLaurier. Aerodynamics of small vehicles. *Annual Review of Fluid Mechanics*, 35(1):89–111, 2003.

[2] Simon Watkins, Juliette Milbank, Benjamin J. Loxton, and William H. Melbourne. Atmospheric winds and their implications for microair vehicles. *AIAA Journal*, 44(11):2591–2600, November 2006.

[3] Alexandru Brezoescu, Pedro Castillo, and Rogelio Lozano. Wind estimation for accurate airplane path following applications. *Journal of Intelligent & Robotic Systems*, 73(1-4):823–831, 2014.

[4] Hua Xiong, JQ Yi, GL Fan, and Feng-shui Jing. Anti-crosswind autolanding of uavs based on active disturbance rejection control. In *Proceedings of the Guidance, Navigation, and Control Conference. Toronto: AIAA*, pages 1–14, 2010.

[5] Jun Yang, Zhenhua Zhao, Shihua Li, and Wei Xing Zheng. Composite predictive flight control for airbreathing hypersonic vehicles. *International Journal of Control*, 87(9):1970–1984, 2014.

[6] Cunjia Liu, Wen-Hua Chen, and John Andrews. Tracking control of small-scale helicopters using explicit nonlinear mpc augmented with disturbance observers. *Control Engineering Practice*, 20(3):258–268, 2012.

[7] Karl Johan Astrom and Lars Rundqwist. Integrator windup and how to avoid it. In *American Control Conference, 1989*, pages 1693–1698. IEEE, 1989.

[8] Yu Luo, Andrea Serrani, Stephen Yurkovich, David B Doman, and Michael W Oppenheimer. Model predictive dynamic control allocation with actuator dynamics. In *American Control Conference, 2004. Proceedings of the 2004*, volume 2, pages 1695–1700. IEEE, 2004.

[9] Bernard Etkin. Turbulent wind and its effect on flight. *Journal of Aircraft*, 18(5):327–345, 1981.

[10] Walter Frost and Roland L Bowles. Wind shear terms in the equations of aircraft motion. *Journal of Aircraft*, 21(11):866–872, 1984.

[11] Frederic M Hoblit. *Gust loads on aircraft: concepts and applications*. Aiaa, 1988.

[12] Christopher D Regan and Christine V Jutte. Survey of applications of active control technology for gust alleviation and new challenges for lighter-weight aircraft. 2012.

[13] Pradeep R Ambati and Radhakant Padhi. A neuro-adaptive augmented dynamic inversion design for robust auto-landing. In *World Congress*, volume 19, pages 12202–12207, 2014.

[14] Hakim Bouadi and Félix Mora-Camino. Space-based nonlinear dynamic inversion control for aircraft continuous descent approach. In *Evolving and Adaptive Intelligent Systems (EAIS), 2012 IEEE Conference on*, pages 164–169. IEEE, 2012.

[15] Seid H Pourtakdoust, M Kiani, and A Hassanpour. Optimal trajectory planning for flight through microburst wind shears. *Aerospace Science and Technology*, 15(7):567–576, 2011.

[16] Sandeep S Mulgund and Robert F Stengel. Optimal nonlinear estimation for aircraft flight control in wind shear. *Automatica*, 32(1):3–13, 1996.

[17] Andy P Broeren and Michael B Bragg. Unsteady stalling characteristics of thin airfoils at low reynolds number. *Progress in astronautics and aeronautics*, 195:191–213, 2001.

[18] Peter Lissaman. Effects of turbulence on bank upsets of small flight vehicles. In *AIAA Aerospace Sciences Meeting Including The New Horizons Forum and Aerospace Exposition*, 2009.

[19] Mujahid Abdulrahim, Simon Watkins, Reuven Segal, Matthew Marino, and John Sheridan. Dynamic sensitivity to atmospheric turbulence of unmanned air vehicles with varying configuration. *Journal of aircraft*, 47(6):1873–1883, 2010.

[20] A Mohamed, R Clothier, S Watkins, R Sabatini, and M Abdulrahim. Fixed-wing mav attitude stability in atmospheric turbulence, part 1: Suitability of conventional sensors. *Progress in Aerospace Sciences*, 70:69–82, 2014.

[21] S. Watkins, M. Thompson, B. Loxton, and M. Abdulrahim. On low altitude flight through the atmospheric boundary layer. *International Journal of Micro Air Vehicles*, 2(2):55–68, 2010.

[22] Nabil Aouf, Benoit Boulet, and RM Botez. Robust gust load alleviation for a flexible aircraft. *Canadian Aeronautics and Space Journal*, 46(3):131–139, 2000.

[23] Robert G Cook, Rafael Palacios, and Paul Goulart. Robust gust alleviation and stabilization of very flexible aircraft. *AIAA journal*, 51(2):330–340, 2013.

[24] Boris Moulin and Moti Karpel. Gust loads alleviation using special control surfaces. *Journal of Aircraft*, 44(1):17–25, 2007.

[25] Kazuhide Okamoto and Takeshi Tsuchiya. Optimal aircraft control in stochastic severe weather conditions. *Journal of Guidance, Control, and Dynamics*, 39(1):77–85, 2016.

[26] Seungho Yoon, Youdan Kim, and Sanghyuk Park. Constrained adaptive backstepping controller design for aircraft landing in wind disturbance and actuator stuck. *International Journal of Aeronautical and Space Sciences*, 13(1):74–89, 2012.

[27] TE Disney. C-5a active load alleviation system. *Journal of Spacecraft and Rockets*, 14(2):81–86, 1977.

[28] J H Wykes, A S Morris, and C J Borland. B-1 structural mode control system. *AIAA Journal*, 1972.

[29] David Kaminski-Morrow. Airbus exploits a320 load-alleviation to offer higher mtow. Online Article. Accessed 10/08/2016.

[30] H Hönlinger, H Zimmermann, O Sensburg, and J Becker. Structural aspects of active control technology. In *AGARD CONFERENCE PROCEEDINGS AGARD CP*, pages 18–18. DTIC Document, 1995.

[31] Derek R Nelson, D Blake Barber, Timothy W McLain, and Randal W Beard. Vector field path following for miniature air vehicles. *IEEE Transactions on Robotics*, 23(3):519–529, 2007.

[32] Sikha Hota and Debasish Ghose. A modified dubins method for optimal path planning of a miniature air vehicle converging to a straight line path. In *American Control Conference, 2009. ACC'09.*, pages 2397–2402. IEEE, 2009.

[33] Alan L Jennings, Raűl Ordónez, and Nicola Ceccarelli. Dynamic programming applied to uav way point path planning in wind. In *Computer-Aided Control Systems, 2008. CACSD 2008. IEEE International Conference on*, pages 215–220. IEEE, 2008.

[34] N. Ceccarelli, J.J. Enright, E. Frazzoli, S.J. Rasmussen, and C.J. Schumacher. Micro uav path planning for reconnaissance in wind. In *American Control Conference, 2007. ACC '07*, pages 5310–5315, July 2007.

[35] Stephen Jackson, John Tisdale, Maryam Kamgarpour, Brandon Basso, and J Karl Hedrick. Tracking controllers for small uavs with wind disturbances: Theory and flight results. In *Decision and Control, 2008. CDC 2008. 47th IEEE Conference on*, pages 564–569. IEEE, 2008.

[36] Timothy G McGee and J Karl Hedrick. Path planning and control for multiple point surveillance by an unmanned aircraft in wind. In *2006 American Control Conference*, pages 6–pp. IEEE, 2006.

[37] Steven Mills, Nabil Aouf, and Luis Mejias. Image based visual servo control for fixed wing uavs tracking linear infrastructure in wind. In *Robotics and Automation (ICRA), 2013 IEEE International Conference on*, pages 5769–5774. IEEE, 2013.

[38] Cunjia Liu, Owen McAree, and Wen-Hua Chen. Path-following control for small fixed-wing unmanned aerial vehicles under wind disturbances. *International Journal of Robust and Nonlinear Control*, 23(15):1682–1698, 2013.

[39] Mohammad Sadraey and Richard Colgren. Robust nonlinear controller design for a complete uav mission. In *AIAA Guidance, Navigation, and Control Conference and Exhibit*, page 6687, 2006.

[40] Xilin Yang, Luis Mejias, and Timothy Molloy. A gust-attenuation controller for fixed-wing uavs during collision avoidance course. In *Digital Proceedings of the 2012 International Conference on Unmanned Aircraft Systems (ICUAS'12)*, 2012.

[41] Alexandru Brezoescu, Tadeo Espinoza, Pedro Castillo, and Rogelio Lozano. Adaptive trajectory following for a fixed-wing uav in presence of crosswind. *Journal of Intelligent & Robotic Systems*, 69(1-4):257–271, 2013.

[42] Jaime Rubio Hervas, Mahmut Reyhanoglu, and Hui Tang. Nonlinear automatic landing control of unmanned aerial vehicles on moving platforms via a 3d laser radar. In *AIP Conference Proceedings*, volume 1637, pages 907–917. AIP, 2014.

[43] Jaime Rubio Hervas, Mahmut Reyhanoglu, Hui Tang, and Erdal Kayacan. Nonlinear control of fixed-wing uavs in presence of stochastic winds. *Communications in Nonlinear Science and Numerical Simulation*, 33:57–69, 2016.

[44] Francisco Gavilan, JA Acosta, and Rafael Vazquez. Control of the longitudinal flight dynamics of an uav using adaptive backstepping. *IFAC Proceedings Volumes*, 44(1):1892–1897, 2011.

[45] Hua Xiong, Ruyi Yuan, Jianqiang Yi, Guoliang Fan, and Fengshui Jing. Disturbance rejection in uav's velocity and attitude control: Problems and solutions. In *Control Conference (CCC), 2011 30th Chinese*, pages 6293–6298. IEEE, 2011.

[46] Xun Wang, Weiwei Kong, Daibing Zhang, and Lincheng Shen. Active disturbance rejection controller for small fixed-wing uavs with model uncertainty. In *Information and Automation, 2015 IEEE International Conference on*, pages 2299–2304. IEEE, 2015.

[47] Daibing Zhang and Xun Wang. Autonomous landing control of fixed-wing uavs: from theory to field experiment. *Journal of Intelligent & Robotic Systems*, 88(2-4):619–634, 2017.

[48] Cunjia Liu and Wen-Hua Chen. Disturbance rejection flight control for small fixed-wing unmanned aerial vehicles. *Journal of Guidance, Control, and Dynamics*, pages 2810–2819, 2016.

[49] Liang-Liang Xie and Lei Guo. How much uncertainty can be dealt with by feedback? *IEEE Transactions on Automatic Control*, 45(12):2203–2217, 2000.

[50] Zhiqiang Gao. On the centrality of disturbance rejection in automatic control. *ISA transactions*, 53(4):850–857, 2014.

[51] Shihua Li, Jun Yang, Wen-Hua Chen, and Xisong Chen. *Disturbance Observer-Based Control: Methods and Applications*. CRC Press, 2014.

[52] Jingqing Han. From pid to active disturbance rejection control. *IEEE transactions on Industrial Electronics*, 56(3):900–906, 2009.

[53] CD Johnson. Real-time disturbance-observers; origin and evolution of the idea part 1: The early years. In *System Theory, 2008. SSST 2008. 40th Southeastern Symposium on*, pages 88–91. IEEE, 2008.

[54] C Johnson. Further study of the linear regulator with disturbances–the case of vector disturbances satisfying a linear differential equation. *IEEE Transactions on Automatic Control*, 15(2):222–228, 1970.

[55] CD Johnson. Accommodation of disturbances in optimal control problems. *International Journal of Control*, 15(2):209–231, 1972.

[56] Cn Johnson. Accomodation of external disturbances in linear regulator and servomechanism problems. *IEEE Transactions on automatic control*, 16(6):635–644, 1971.

[57] SangJoo Kwon and Wan Kyun Chung. A discrete-time design and analysis of perturbation observer for motion control applications. *IEEE Transactions on control systems technology*, 11(3):399–407, 2003.

[58] Jin-Hua She, Xin Xin, and Yaodong Pan. Equivalent-input-disturbance approach-analysis and application to disturbance rejection in dual-stage feed drive control system. *IEEE/ASME Transactions on Mechatronics*, 16(2):330–340, 2011.

[59] Wen-Hua Chen, Donald J Ballance, Peter J Gawthrop, and John O'Reilly. A nonlinear disturbance observer for robotic manipulators. *Industrial Electronics, IEEE Transactions on*, 47(4):932–938, 2000.

[60] Kiyoshi Ohishi, Masato Nakao, Kouhei Ohnishi, and Kunio Miyachi. Microprocessor-controlled dc motor for load-insensitive position servo system. *IEEE Transactions on Industrial Electronics*, (1):44–49, 1987.

[61] Takaji Umeno, Tomoaki Kaneko, and Yoichi Hori. Robust servosystem design with two degrees of freedom and its application to novel motion control of robot manipulators. *IEEE Transactions on Industrial Electronics*, 40(5):473–485, 1993.

[62] Han Jingqing. The" extended state observer" of a class of uncertain systems [j]. *Control and Decision*, 1, 1995. In Chinese.

[63] K Najim, D Hodouin, and A Desbiens. Adaptive control: state of the art and an application to a grinding process. *Powder Technology*, 82(1):59–68, 1995.

[64] Pradip K Sinha and Alexandre N Pechev. Model reference adaptive control of a maglev system with stable maximum descent criterion. *Automatica*, 35(8):1457–1465, 1999.

[65] Joao P Hespanha, Daniel Liberzon, and A Stephen Morse. Overcoming the limitations of adaptive control by means of logic-based switching. *Systems & control letters*, 49(1):49–65, 2003.

[66] Jun Yang, Wen-Hua Chen, Shihua Li, Lei Guo, and Yunda Yan. Disturbance/uncertainty estimation and attenuation techniques in pmsm drivesa survey. *IEEE Transactions on Industrial Electronics*, 64(4):3273–3285, 2017.

[67] Romeo Ortega and Mark W Spong. Adaptive motion control of rigid robots: A tutorial. In *Decision and Control, 1988., Proceedings of the 27th IEEE Conference on*, pages 1575–1584. IEEE, 1988.

[68] Wen-Hua Chen, Jun Yang, Lei Guo, and Shihua Li. Disturbance-observer-based control and related methodsan overview. *IEEE Transactions on Industrial Electronics*, 63(2):1083–1095, 2016.

[69] Wen-Hua Chen. Disturbance observer based control for nonlinear systems. *IEEE/ASME transactions on mechatronics*, 9(4):706–710, 2004.

[70] Lei Guo and Wen-Hua Chen. Disturbance attenuation and rejection for systems with nonlinearity via dobc approach. *International Journal of Robust and Nonlinear Control*, 15(3):109–125, 2005.

[71] Kyung-Soo Kim, Keun-Ho Rew, and Soohyun Kim. Disturbance observer for estimating higher order disturbances in time series expansion. *IEEE Transactions on automatic control*, 55(8):1905–1911, 2010.

[72] Kiyoshi Ohishi. Torque-speed regulation of dc motor based on load torque estimation. In *IEEJ International Power Electronics Conference, IPEC-TOKYO, 1983-3*, volume 2, pages 1209–1216, 1983.

[73] Kyung-Soo Kim and Keun-Ho Rew. Reduced order disturbance observer for discrete-time linear systems. *Automatica*, 49(4):968–975, 2013.

[74] Emre Sariyildiz and Kouhei Ohnishi. A guide to design disturbance observer. *Journal of Dynamic Systems, Measurement, and Control*, 136(2):021011, 2014.

[75] Carl J Kempf and Seiichi Kobayashi. Disturbance observer and feedforward design for a high-speed direct-drive positioning table. *IEEE Transactions on control systems Technology*, 7(5):513–526, 1999.

[76] Bin Yao, Mohammed Al-Majed, and Masayoshi Tomizuka. High-performance robust motion control of machine tools: an adaptive robust control approach and comparative experiments. *IEEE/ASME Transactions on Mechatronics*, 2(2):63–76, 1997.

[77] Yi Huang and Wenchao Xue. Active disturbance rejection control: methodology and theoretical analysis. *ISA transactions*, 53(4):963–976, 2014.

[78] Seung-Hi Lee, Young-Hoon Kim, and Sang-Eun Baek. Discrete-time robust tracking control using a state space disturbance observer. In *American Control Conference, 2000. Proceedings of the 2000*, volume 6, pages 4194–4198. IEEE, 2000.

[79] S-M Suh, CC Chung, and S-H Lee. Discrete-time track following controller design using a state-space disturbance observer. *Microsystem technologies*, 9(5):352–361, 2003.

[80] Qinglei Hu, Lihua Xie, Youyi Wang, and Chunling Du. Robust track-following control of hard disk drives using improved integral sliding mode combined with phase lead peak filter. *International Journal of Adaptive Control and Signal Processing*, 22(4):413–430, 2008.

[81] Seung-Hi Lee and Chung Choo Chung. Robust control using a state space disturbance observer. In *Decision and Control, 2003. Proceedings. 42nd IEEE Conference on*, volume 2, pages 1297–1302. IEEE, 2003.

[82] C Johnson. Optimal control of the linear regulator with constant disturbances. *IEEE Transactions on Automatic Control*, 13(4):416–421, 1968.

[83] Jun Yang, Wen-Hua Chen, and Shihua Li. Autopilot design of bank-to-turn missiles using state-space disturbance observers. 2010.

[84] Xinjiang Wei and Lei Guo. Composite disturbance-observer-based control and terminal sliding mode control for non-linear systems with disturbances. *International Journal of Control*, 82(6):1082–1098, 2009.

[85] Xinjiang Wei and Lei Guo. Composite disturbance-observer-based control and h control for complex continuous models. *International Journal of Robust and Nonlinear Control*, 20(1):106–118, 2010.

[86] Wen-Hua Chen. Nonlinear disturbance observer-enhanced dynamic inversion control of missiles. *Journal of Guidance, Control, and Dynamics*, 26(1):161–166, 2003.

[87] Jun Yang, Argyrios Zolotas, Wen-Hua Chen, Konstantinos Michail, and Shihua Li. Robust control of nonlinear maglev suspension system with mismatched uncertainties via dobc approach. *ISA transactions*, 50(3):389–396, 2011.

[88] Zhenxing Zhang, Shihua Li, and Sheng Luo. Terminal guidance laws of missile based on ismc and ndob with impact angle constraint. *Aerospace Science and Technology*, 31(1):30–41, 2013.

[89] Hao Lu, Cunjia Liu, Lei Guo, and Wen-Hua Chen. Flight control design for small-scale helicopter using disturbance-observer-based backstepping. *Journal of Guidance, Control, and Dynamics*, 2015.

[90] Luca Zaccarian and Andrew R Teel. *Modern anti-windup synthesis: control augmentation for actuator saturation*. Princeton University Press, 2011.

[91] Kevin Groves, Andrea Serrani, Stephen Yurkovich, Michael Bolender, and David Doman. Anti-windup control for an air-breathing hypersonic vehicle model. In *AIAA guidance, navigation, and control conference and exhibit*, page 6557, 2006.

[92] Andrea Serrani, Alicia M Zinnecker, Lisa Fiorentini, Michael A Bolender, and David B Doman. Integrated adaptive guidance and control of constrained nonlinear air-breathing hypersonic vehicle models. In *American Control Conference, 2009. ACC'09.*, pages 3172–3177. IEEE, 2009.

[93] Sophie Tarbouriech and Matthew Turner. Anti-windup design: an overview of some recent advances and open problems. *IET control theory & applications*, 3(1):1–19, 2009.

[94] Nicholas J Krikelis. State feedback integral control with intelligentintegrators. *International Journal of Control*, 32(3):465–473, 1980.

[95] Raymond Hanus, Michel Kinnaert, and J-L Henrotte. Conditioning technique, a general anti-windup and bumpless transfer method. *Automatica*, 23(6):729–739, 1987.

[96] PJ Campo, M Morari, and CN Nett. Multivariable anti-windup and bumpless transfer: A general theory. In *American Control Conference, 1989*, pages 1706–1711. IEEE, 1989.

[97] Kevin P Groves, David O Sigthorsson, Andrea Serrani, Stephen Yurkovich, Michael A Bolender, and David B Doman. *Reference command tracking for a linearized model of an air-breathing hypersonic vehicle*. Defense Technical Information Center, 2005.

[98] CJ Goh and TK Caughey. On the stability problem caused by finite actuator dynamics in the collocated control of large space structures. *International Journal of Control*, 41(3):787–802, 1985.

[99] M.V. Cook. *Flight Dynamic Principles 2nd Edition*. Elsevier, 2007.

[100] Theodore Von Karman. Progress in the statistical theory of turbulence. *Proceedings of the National Academy of Sciences*, 34(11):530–539, 1948.

[101] United States Department of Defence. Flying qualities of piloted aircraft. Technical report, United States Department of Defense, 1997.

[102] Jack W Langelaan, Nicholas Alley, and James Neidhoefer. Wind field estimation for small unmanned aerial vehicles. *Journal of Guidance, Control, and Dynamics*, 34(4):1016–1030, 2011.

[103] Lennart Ljung. *System Identification Toolbox User's Guide*. MathWorks, version 9.5 edition, 2016.

[104] Lennart Ljung. System identification. In *Signal analysis and prediction*, pages 163–173. Springer, 1998.

[105] Andrei Dorobantu, Austin Murch, Bérénice Mettler, and Gary Balas. System identification for small, low-cost, fixed-wing unmanned aircraft. *Journal of Aircraft*, 50(4):1117–1130, 2013.

[106] Jeff Craighead, Robin Murphy, Jenny Burke, and Brian Goldiez. A survey of commercial & open source unmanned vehicle simulators. In *Robotics and Automation, 2007 IEEE International Conference on*, pages 852–857. IEEE, 2007.

[107] Eduardo F Camacho and Carlos Bordons Alba. *Model predictive control*. Springer Science & Business Media, 2013.

[108] Navneet Kapoor and Prodromos Daoutidis. An observer-based anti-windup scheme for non-linear systems with input constraints. *International Journal of Control*, 72(1):18–29, 1999.

[109] Jean Smith, Jinya Su, Cunjia Liu, and Wen-Hua Chen. Disturbance observer based control with anti-windup applied to a small fixed wing uav for disturbance rejection. *Journal of Intelligent & Robotic Systems*, 88(2-4):329–346, 2017.

[110] Brian L Stevens, Frank L Lewis, and Eric N Johnson. *Aircraft control and simulation: dynamics, controls design, and autonomous systems*. John Wiley & Sons, 2nd edition edition, 1992.

[111] Frank L Lewis. *Applied optimal control & estimation: digital design & implementation*. Prentice Hall Englewood Cliffs, NJ, 1992.

[112] C Bohn and DP Atherton. An analysis package comparing pid anti-windup strategies. *IEEE Control Systems*, 15(2):34–40, 1995.

[113] Donny P Wang, Jonathan D Bartley-Cho, Christopher A Martin, and Brian J Hallam. Development of high-rate large-deflection hingeless trailing-edge control surface for the smart wing wind tunnel model. In *Smart structures and materials 2001: Industrial and commercial applications of smart structures technologies*, volume 4332, pages 407–419. International Society for Optics and Photonics, 2001.

[114] Jean Smith, Jun Yang, Cunjia Liu, and W-H Chen. Actuator dynamics augmented dobc for a small scale fixed wing uav. In *2018 IEEE International Conference on Industrial Technology*, pages LD–008362, 2018.

[115] Ira H Abbott. Pressure-distribution measurements of a model of a davis wing section with fowler flap submitted by consolidated aircraft corporation. Technical report, NATIONAL AERONAUTICS AND SPACE ADMIN LANGLEY RESEARCH CENTER HAMPTON VA, 1942.

[116] Kenneth L. Roger, Garold E. Hodges, and Larry Felt. Active flutter suppression - a flight test demonstration. *Journal of Aircraft*, 12(6), 1975.

[117] Robert H Scanlan and Robert Rosenbaum. *Introduction to the study of aircraft vibration and flutter*. Dover Publications, 1951.

[118] John H Wykes. Structural dynamic stability augmentation and gust alleviation of flexible aircraft. In *AIAA 5th Annual Meeting and Technical Display*. AIAA, October 1968.

[119] Irving Abel, Boyd Perry III, and Harold N Murrowf. Two synthesis techniques applied to flutter suppression on a flight research wing. *Journal of Guidance, Control, and Dynamics*, 1(5):340–346, 1978.

[120] E Nissim. Recent advances in aerodynamic energy concept for flutter suppression and gust alleviation using active controls. Technical report, NASA, 1977.

[121] A Behal, P Marzocca, VM Rao, and A Gnann. Nonlinear adaptive control of an aeroelastic two-dimensional lifting surface. *Journal of Guidance, Control, and Dynamics*, 29(2):382–390, 2006.

[122] DC Norman. Practical gust load alleviation and flutter suppression control laws based on a lqg methodology. In *Aerospace Sciences Meeting*, number 19. AIAA, AIAA, 1981.

[123] Sungsoo Na, Liviu Librescu, M Kim, I Jeong, and Pier Marzocca. Aeroelastic response of flapped-wing systems using robust estimation control methodology. *Journal of Guidance Control and Dynamics*, 29(1):199, 2006.

[124] M Tadi. State-dependent riccati equation for control of aeroelastic flutter. *Journal of Guidance Control and Dynamics*, 26(6):914–917, 2003.

[125] Vivek Mukhopadhyay. Historical perspective on analysis and control of aeroelastic responses. *Journal of Guidance Control and Dynamics*, 26(5):673–684, 2003.

[126] RT Haftka, JH Starnes Jr, and FW Barton. A comparison of two types of structural optimization procedures for satisfying flutter requirements. In *Structures, Structural Dynamics and Materials Conference*. AIAA, 1974.

[127] L Trame, L Williams, and R Yurkovich. Active aeroelastic oscillation control on the f/a-18 aircraft. In *Guidance, Navigation and Control Conference*, 1985.

[128] F Nesline and P Zarchan. A classical look at modern control for missile autopilot design. In *Guidance and Control Conference*, 1982.

[129] SE Talole, AA Godbole, JP Kolhe, and SB Phadke. Robust roll autopilot design for tactical missiles. *Journal of guidance, control, and dynamics*, 34(1):107, 2011.

[130] Anatole Verhaegen and Rafał Żbikowski. Aeroservoelastic modelling and control of a slender anti-air missile for active damping of longitudinal bending vibrations. *Aerospace Science and Technology*, 66:20–27, 2017.

[131] W. J. G. Pinsker. The control characteristics of aircraft employing direct-lift control. Technical report, Aerodynamis Department, Royal Aircraft Establishment, 1968.

[132] G. Sim and M. Onspaugh. Laboratory development of selected systems in the lockheed l-1011 tristar. In *3rd Aircraft Design and Operations Meeting*, page 782, Seattle, Washington, July 1971.

[133] L. O. Lykken and N. Shah. Direct lift control for improved automatic landing and performance of transport aircraft lowell. *Journal of Aircraft*, 9(5):325–332, 1972.

[134] Andreas Wildschek, Rudolf Maier, Martin Hromcik, Tomas Hanis, Alexander Schirrer, Martin Kozek, Christian Westermayer, and Mark Hemedi. Hybrid controller for gust load alleviation and ride comfort improvement using direct lift control flaps. In *Proceedings of Third European Conference for Aerospace Sciences (EUCASS)*, 2009.

[135] K-U Hahn and R Koenig. Attas flight test and simulation results of the advanced gust management system lars. In *Guidance, Navigation and Control Conference*, page 4343, 1992.

[136] Romain Merat. Study of a direct lift control system based on the a380 aircraft. In *46th AIAA Aerospace Sciences Meeting and Exhibit*, page 1432, 2008.

[137] Phuong Vu and Daniel J Biezad. Direct-lift design strategy for longitudinal control of hypersonic aircraft. *Journal of Guidance, Control, and Dynamics*, 17(6):1260–1266, 1994.

[138] Jie Huang. *Nonlinear output regulation: theory and applications*. SIAM, 2004.

[139] Tor A Johansen, A Cristafaro, KL Sørensen, Jakob M Hansen, and Thor I Fossen. On estimation of wind velocity, angle-of-attack and sideslip angle of small uavs using standard sensors. In *International Conference on Unmanned Aircraft Systems*, 2015.

[140] Tor A Johansen and Thor I Fossen. Control allocationa survey. *Automatica*, 49(5):1087–1103, 2013.

[141] Kenneth A Bordignon and Wayne C Durham. Closed-form solutions to constrained control allocation problem. *Journal of Guidance, Control, and Dynamics*, 18(5):1000–1007, 1995.

[142] Ola Härkegård and S Torkel Glad. Resolving actuator redundancy - optimal control vs. control allocation. *Automatica*, 41(1):137–144, 2005.